Kent Academic Repository

Williams, Marc Joseph (2015) *Engineering magnetic nanosystems for cancer diagnosis and treatment.* Doctor of Philosophy (PhD) thesis, University of Kent,.

Engineering magnetic nanosystems for cancer diagnosis and treatment

Marc Joseph Williams

A thesis submitted to the University of Kent
in the subject of Chemistry
for the degree of Doctor of Philosophy

School of Physical Sciences
University of Kent
England
5th August 2015

Declaration

I declare that the work presented in this thesis is my own work and has been written in my own words. Care has been taken to properly reference the work of others whenever required.

Date: 28th January 2015

Abstract

Iron oxide magnetic nanocomposites can be used for a variety of biomedical applications, including magnetic resonance imaging (MRI) and as site specific drug delivery systems. By functionalising the surface of the nanocomposite, other functions like cell labelling and targeting can also be realised. Several iron oxide nanocomposites were prepared through microwave assisted co-precipitation reactions, using polyelectrolytes and dopamine as surface stabilisers. This provided a highly magnetic and versatile foundation that could be used immediately in biological applications (such as MR imaging) but could also be further functionalised extending the applications of the material. Functionalisation was achieved via electrostatic interactions and carbodiimide coupling which led to the development of a multifunctional nanocomposite capable of supporting both fluorescent and targeting groups.

This work demonstrates that the construction of the nanocomposite is key to unlocking the biomedical potential of the material. HRTEM and SQUID results demonstrate the importance of microwave irradiation in the formation of highly crystalline materials. Microwave heating enhances crystal growth which improves the magnetisation values of the composite, to beyond materials prepared by traditional co-precipition methods. Polyelectrolytes can bestow excellent water stability on the particles, with the composite remaining in suspension for over 8 weeks. MRI measurements show that the high magnetism, combined with excellent water stability, translates into an effective MRI contrast agent, with the prepared composite out performing other commercial agents. Further functionalisation with fluorescent groups show other applications in cell labelling, and the addition of targeting groups can further enhance the selectivity of the composite.

This work results in the development of a highly magnetic, extremely water stable iron oxide foundation, that can immediately be used as a MRI contrast agent and can support multiple functional groups like fluorescent dyes and targeting groups.

Acknowledgements

There are just so many people to thank for all their help and support over the past 4 years and I'm so sorry if I have inadvertently left anyone out!

Firstly I would like to thank my parents, for all their love, support and help this is just as much as their thesis as it is mine. Also just as importantly, I would like to thank my supervisors Dr. Serena Corr and Dr. Donna Arnold for all of their help and guidance over the years. Thank you so much for both the opportunity and all the help that I have been given.

I have had the pleasure of working with so many people and groups, that have all helped me in my studies. Thanks to Kate for being the other madman stuck in the trenches with me and to Aaron, for not only living with me, but also putting up with my singing as I wrote my thesis! From old days I would like to thank the Corr group and in particular Chris, Charlie and Steve. I would also like to thank the current Corr Group up in Scotland and in particular Tom, for helping me run experiments, putting up with my silly questions and giving me a bed to crash on when needed. Thanks to the Arnold group (Laura, Chris and Dan) and Holder group (Liv, Christina, Danielle, Darren, Charlie and Gemma) for helping me when I was being dense and disorganised! Other students at Kent who I would like to thank are Hannah, Trevor and Ollie for putting up with me and helping me!

Thanks to the academics and the technical staff at the University of Kent for all of their help. More specifically the head technician J.J. for lending me obscure chemicals with absolutely minimal notice. Thanks to Iain Brown from the biosciences department for all his help with the TEM measurements ensuring my nanoparticles were more than just a smudge. I also would like thank Dr. Simon Holder and all of the other academics for all their support and kind comments.

Thanks to all of my collaborators as well. More specifically I would like to thank from the University of Strathclyde; Oonagh M. Collins and Edmund J. Cussen for the magnetisation data. From the University of Glasgow; Fraser J. Douglas and Donald MacLaren for the lovely HRTEM and SAED images. Jindrich Cinatl Jr., Dirk Krueger and Rafael T. M. de Rosales from Kings Col-

lege London for the MRI results and James D. Budge, Lara C. Sanders, Martin Michaelis and Mark Smales from the School of Biosciences at Kent for the cell testing results and confocal images.

I would also like to thank all my friends both at home (Lucy, Matt, James, Ben, Richard, and the rest of the werewolf crew), Canterbury (Toddy, Greg, Sarah, Clare, Ben, Mark and Sarah Warwick), family and last but not least Travis and Sparky, for ”helping” me write at the most inconvenient times.

Abbreviation list

AAS: Atomic absorption spectroscopy

ATA: 2-amino terephthalic acid

A-9-CA: Acridine-9-carboxylic acid

α-Fe_2O_3: Hematite

$CoFe_2O_4$: Cobalt Ferrite

$CuFe_2O_4$: Copper Ferrite

DCC: N,N'-Dicyclohexylcarbodiimide

DLS: Dynamic light scattering

DOX: Doxorubicin

EDCI: 1-Ethyl-3-(3-dimethylaminopropyl)carbodiimide

FA: Folic acid

γ-Fe_2O_3: Maghemite

Fe_3O_4: Magnetite

FTIR: Fourier transform infra-red spectroscopy

HOMO: Highest occupied molecular orbital

HRTEM: High resolution transmission electron microscopy

ICSD: Inorganic crystal structure database

LBL: Layer-By-Layer reaction

LUMO: Lowest unoccupied molecular orbital

$MnFe_2O_4$: Manganese Ferrite

MRI: Magnetic resonance imaging

M_s: Saturation magnetisation

Mwt: Molecular weight

NHS: N-Hydroxysuccinimide

NMR: Nuclear Magnetic Resonance spectroscopy

NMRD: Nuclear magnetic relaxation dispersion

PAA: Poly(acrylic acid)

pDADMAC: Poly(diallyldimethylammonium chloride)

PDI: Polydispersity index

PEG: Polyethylene glycol

PSSS: Poly(sodium-4-styrenesulfonate)

RES: Reticuloendothelial system

RhB: Rhodamine B

r_1: Transverse relaxivity

R_1: Transverse relaxation rate

r_2: Longitudial relaxivity

R_2: Longitudial relaxation rate

SAED: Selected area electron diffraction

SPP: Sodium polyphosphate

SQUID: Superconducting quantum interference device

TA: Terephthalic acid

TEM: Transmission electron microscopy

TGA: Thermogravimetric analysis

T_1: Transverse relaxation time

T_2: Longitudial relaxation time

UV-Vis: Ultraviolet-visible spectroscopy

XRD: X-ray diffraction

Contents

Chapter 1: Introduction

1.1 General introduction

The ’nano’ prefix has become an ubiquitous term in common parlance, with the latest must-have gadget being Apple’s iPod nano; yet nanotechnology has been used for centuries. An example of this is the Lycurgus cup, a Roman glass chalice containing both gold and silver dust which changes colour when light is shone through it. Unbeknownst to the Romans, they had actually prepared nanoparticles of gold and silver. While bulk gold and silver are shiny and metallic, these nanoparticles now take on size-dependant optical properties. Nanoparticles are typically below 100 nanometers in diameter, allowing researchers to work with particles with size dimensions on the molecular and cellular levels. One advantage of working at such small scales is that these particles may have unique properties when compared to their bulk equivalents.[1] In bulk materials, the majority of atoms exist within the volume of the material. In contrast, most atoms in nanoparticles are exposed at the surface. This high surface to volume ratio can play a huge role in changing the properties of nanoparticles.

1.2 Magnetic nanoparticles

The main aim of this work is to prepare a magnetic nanocomposite material, capable of both cancer diagnosis and treatment. Magnetic nanocomposites for biomedical applications commonly have a magnetic nanoparticle core, which can be made of various types magnetic material such as magnetite (Fe_3O_4),[2] maghemite (γ-Fe_2O_3)[3] or cobalt ferrite ($CoFe_2O_4$).[4] The magnetic core often needs to be stabilised so that it is biocompatible and does not oxidise or degrade. This stability can be achieved in several ways, for example by employing surfactants.[5–7] Once stabilised, other components can be attached to the nanoparticle to provide further functionality. The scope for magnetic nanoparticles in biomedical applications expands with this surface functionalisation, as a whole variety of compounds can be attached to the nanocomposite unlocking different functionalities.[8] Unlocking the potential of biomedical magnetic nanocomposites can be achieved though careful synthetic design. Each component added to the composite will not only bestow new functionality but also alter existing properties.

1.2.1 The spinel structure

The choice of magnetic core is very important as this governs the overall magnetic behaviour. Magnetite (Fe_3O_4) is a magnetic iron oxide which adopts an inverse spinel structure, a mineral class with the general formula $A^{2+}B_2{}^{3+}O_4{}^{2-}$. The iron cations in magnetite occupy 16 of the total 32 octahedral (A) sites and 8 of the 64 tetrahedral (B) sites, as shown in Figure 1.[9] Fe_3O_4 contains iron ions in two oxidation states, $Fe^{2+}Fe_2{}^{3+}O_4{}^{2-}$, where the Fe^{2+} ions occupy half of the octahedral sites while the Fe^{3+} ions fill the remaining octahedral sites and tetrahedral sites.[10,11] Different iron oxides can be prepared by substituting the Fe^{+2} ions with other similarly charged transition metals such as Co^{2+} or Mn^{2+}, with the transition metal used significantly altering the final properties of the iron oxide.[12,13] Maghemite (γ-Fe_2O_3) is another commonly prepared iron oxide nanoparticle. It is an oxidised form of magnetite, which is Fe deficient. The Fe^{2+} groups are oxidised into Fe^{3+} groups, and only $21\frac{1}{3}$ Fe^{3+} ions are distributed between the 16 octahedral and 8 tetrahedral sites resulting in the deficiency.[11]

1.2.2 Magnetic characteristics of iron oxide nanoparticles

Magnetism arises from the spin property of electrons. The combined spin and orbital motion of the individual electrons, dictates the overall magnetic moment of the atom.[16] An overall net magnetic moment will occur if there are unpaired electrons in the valence shell of the atom. The organisation of these unpaired electrons and their response to an external magnetic field are used to classify the types of magnetism the material displays. Single unpaired spins leads to diamagnetism (when spins oppose the applied field) and paramagnetism (when spins align and are proportional to the applied field), but the spins can also form ordered magnetic states generating a magnetic moment significantly

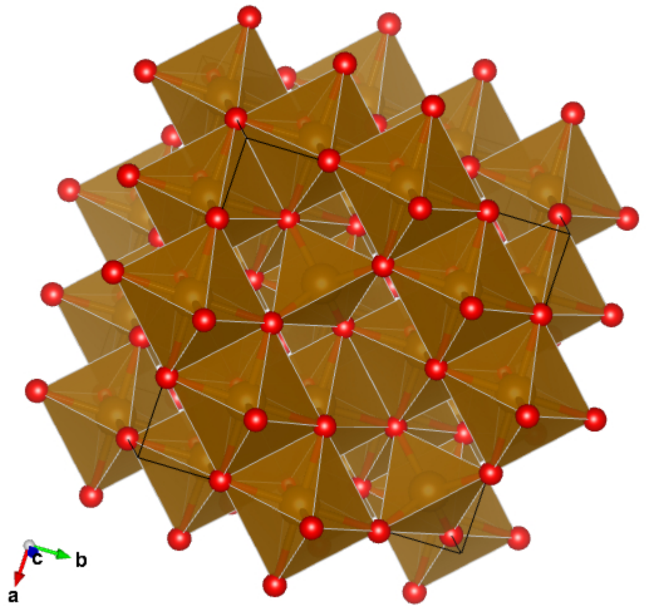

Figure 1: Magnetite crystal structure drawn using the VESTA program,[14] from the work by Fleet.[15] The iron atoms (brown) can be seen occupying some of the octahedral sites and tetrahedral sites in the crystal, which themselves are defined by the overall arrangement of oxygen atoms (red). For magnetite specifically, iron atoms occupy 16 of the 32 available octahedral sites and 8 of the 64 available tetrahedral sites. Half of these octahedral sites will be occupied with Fe^{2+} ions while the remaining octahedral sites and tetrahedral sites are occupied by Fe^{3+} ions resulting in an inverse spinel structure.[15]

stronger than the applied field. These ordered states occur from the formation of magnetic domains.

Individual magnetic moments can align parallel to each other, with large regions of parallel magnetic moments forming a magnetic domain. Domains form to reduce the internal energy of the material and contain magnetic spins that are all aligned in one direction.[17] Domains are separated by domain walls and may be aligned randomly in comparison to neighbouring domains, shown in Figure 2(b). When an external magnetic field is applied to a multi domain magnetic material such as this, the domains may align in the direction of the applied field. The degree of domain alignment is dependant on the strength of the applied field. As the strength of the applied field increases, all domains will irreversibly rotate to the crystallographic easy axis closest to the applied field direction (Figure 2(c)). Once all the moments are fully aligned in the direction of the field, the sample has reached its saturation magnetisation (M_s). The theoretical M_s values for some common magnetic materials are given in Table 1.

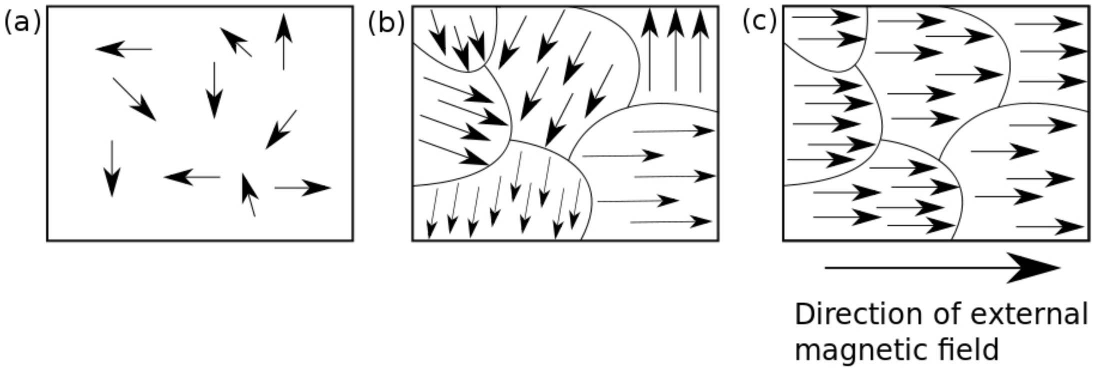

Figure 2: (a) Randomly aligned magnetic moments in a paramagnetic material in absence of a magnetic field. (b) Orientation of magnetic moments within the domains of an ordered magnetic material. The domains oppose each other when there is no external magnetic field. (c) Alignment of domains on application of an external magnetic field to reach saturation magnetisation.

Table 1: Theoretical magnetisation saturation (M_s) values for bulk iron oxides. Substituting the Fe^{2+} groups with other transition metals changes the magnetic properties of the material reflected in different theoretical M_s values.

Iron oxide	**M_s (emu g^{-1})**
Fe_3O_4[18]	92
$CoFe_2O_4$[19]	80
$CuFe_2O_4$[20]	55
$MnFe_2O_4$[13]	80

Magnetic materials can be classified according to how they respond to the application of an external magnetic field. Paramagnetic materials do not form domains. When an external magnetic field is removed thermal energy in the paramagnetic sample causes the moments to be randomly orientated again eliminating any residual magnetism. This causes the paramagnetic material to have little remanence or coercivity. Remanence relates to the residual magnetism of a magnetic material when the external field is removed, while coercivity is the applied magnetic field required to demagnetise the magnetic material. Low remanence and coercivity results in minimal residual magnetism which is desirable in the construction of biomedical agents as it reduces the risk of magnetic agglomeration and the formation of blood clots. The organisation of unpaired electrons into domains leads to other types of magnetic materials. In a ordered ferromagnetic material, the individual magnetic moments of the material align with the applied field and also with each other to form magnetic domains which may also align with the field. The existence of the domains generates a much stronger magnetic field in the material. When the field is removed, the thermal energy is not enough to randomly realign the domains, leading to residual magnetism and coercivity.[21] This residual magnetism may limit the use of bulk materials in biomedical applications, as it will cause the particles to aggregate with each other. In antiferromagnetic materials, the magnetic moments within the domains are aligned antiparallel to each other and cancel out, resulting in the magnetic domains displaying no net magnetisation. Ferrimagnetic materials consist of magnetic regions aligned antiparallel to each other but these regions are disproportionate to each other which causes only partial cancellation of the magnetic moment in the material. Néel observed this behaviour in Fe_3O_4.[22] The Fe^{3+} ions on the A and B sites cancel each other out, leaving only the the Fe^{2+} ions which are responsible for the observed magnetic moment.

The behaviour of materials in an applied external magnetic field can be studied using magnetisation curves. These are plots of magnetisation (M) against applied field strength (H) and an example for a ferromagnet is shown in Figure 3. Magnetisation curves give information about the coercivity and remanence of the sample. The magnitude of these properties may be determined from the hysteresis loop obtained during the measurement. The width of the loop relates to coercivity, with a wider loop requiring stronger external fields to demagnetise the material. The height of the hysteresis loop is an indication of the remanence of the material.

As the size of the ferro/ferrimagnetic material decreases, so do the number

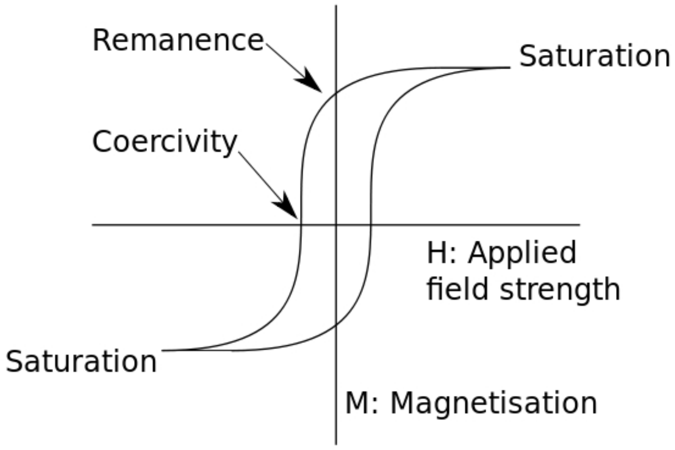

Figure 3: Magnetisation measurements that would be generated from a multi-domain ferromagnetic material. The ferromagnetic nature results in a hysteresis loop that defines the samples magnetisation saturation (maxima of M), remanence (value of M when H = 0) and coercivity (value of H when M = 0). Ferromagnetic materials produce a wide hysteresis loop due to a high coercivity and remanence.

of magnetic domains within the particle. If the particle decreases to a small enough size, it can become energetically unfavourable for multiple domains to exist. In this case, one single domain will exist and the particle will have a uniform magnetisation. A particle with a single domain is known as a superparamagnet. When this is exposed to an external magnetic field, the entire magnetic moment of the particle aligns parallel to the field as shown in Figure 4. When removed from the external field, the particles lose this alignment displaying no remanence or coercivity. This is advantageous for biomedical applications, as the uniformity within the domain ensures high magnetisation while the single domain ensures that particles will not agglomerate in the body through ferromagnetic attractions. To display superparamagnetic behaviour, the particles must be small enough to support a single domain and this size limit is defined as a critical diameter. Materials below this diameter will be superparamagnetic, while larger particles display ferromagnetic properties such as remanence. The critical diameter varies for the material, with magnetite nanoparticles being below 15 nm[19,23,24] making particle size a very important consideration in the construction of any magnetic nanocomposite.

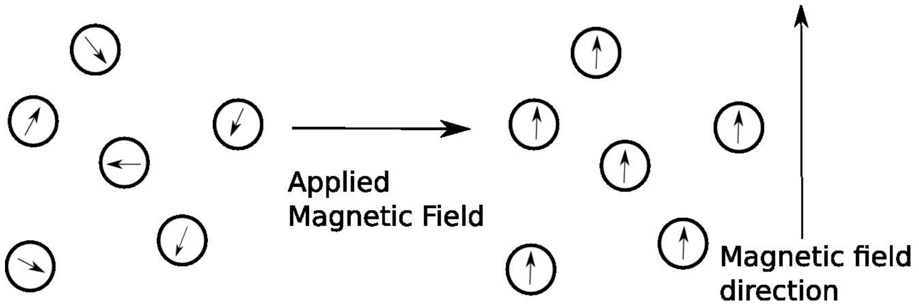

Figure 4: Schematic representation of superparamagnetic particles aligning with an external magnetic field. Arrows denote the magnetic moments of the individual particles. The domains of superparamagnetic material oppose each other under standard conditions. When an external magnetic field is applied, the superparamagnetic nanoparticles will align in the direction of the field. This alignment is lost when the external field is removed.

Utilising nanoscale materials means that more of the atoms in the crystal structure are exposed on the surface, making the formation of surface defects an extremely important consideration during synthesis. During crystal formation, incomplete/under coordinated areas on the crystal surface will form due to the lack of nearby ions. This breaks the symmetry on the surface, reduces the coordination sites of ions to the surface and leads to the existence of broken magnetic exchange bonds. These effects contribute to a misalignment of magnetic spins and are known as surface defects.[25] The existence of such surface defects reduces the saturation magnetisation since not all of the spins will align when exposed to an external magnetic field. These defects are more detrimental for nanoparticles, where a large number of atoms are exposed on the particle surface increasing the effect of surface defects. Therefore the synthesis method has to be carefully selected to ensure that the nanoparticles are small enough to be single domain while minimising surface defect formation.[26]

1.3 Preparation of iron oxide nanoparticles

Not only does the synthetic method reduce surface defect formation but also dictates other nanoparticle properties such as size and morphology. Controlling the individual steps of the synthesis method is fundamental to optimising the potential of these nanoparticles for biomedical applications and a number of methods are considered below.

1.3.1 Co-precipitation methods

In co-precipitation, crystal formation occurs from the addition of a concentrated base to a supersaturated solution of metal salts. For Fe_3O_4 nanoparticles, ferric (Fe^{3+}) and ferrous (Fe^{2+}) salts (i.e. chlorides, nitrates, sulphates) are dissolved in deoxygenated water in a stoichiometric ratio of 2:1 respectively. When dissolved, the iron salts undergo a deprotonation reaction to form iron hydroxides.[27] The addition of a concentrated base (i.e. NH_4OH, NaOH) to the saturated solution causes nucleation of magnetite seed particles.[28] The reaction is given as follows:

$$Fe^{2+} + 2Fe^{3+} + 8OH^{-} \rightarrow Fe_3O_4 + 4H_2O$$

Massart first reported this co-precipitation method for Fe_3O_4 but it has since been adopted to prepare a variety of other iron oxides by substituting the ferrous salt with other transition metal (II) ions.[28–30] The advantages of this method is that it is a quick, cheap and easy approach to preparing iron oxide nanoparticles in a scalable reaction. As the particles are prepared in water, stabilisation with hydrophilic platforms can be incorporated into the precipitation step, resulting in the formation of water stable magnetic nanoparticles (with the capacity for further functionalisation) in less than an hour *via* a one–pot reaction. Nanoparticles prepared in this manner tend to be 10 nm, but often display polydispersity, surface defects and M_s values of 45 emu g^{-1}, significantly lower than the theoretical bulk value of 98 emu g^{-1}.[31,32] The particle size and resulting magnetic properties can be affected by adjusting the experimental conditions (i.e. temperature, precursor, precipitating agent) and by considering the two stages of the co-precipitation reaction: nucleation and growth.[33–35] Nucleation is the formation of seed particles due to the addition of the base. When the base is added, the dissolved precursors react with each other to form very small iron oxide crystal seeds. If the crystal is too small, it is unstable and redissolves back into solution but when large enough the crystal is stable enough to start to grow and agglomerate. Growth is when the stable iron oxide seed particles agglomerate to form larger thermodynamically stable particles.[33] Control of these steps are needed to ensure a strong nucleation stage (to produce a large amount of crystals) with a short growth stage (to ensure the crystals remain small enough to be superparamagnetic).[34] This is illustrated by a LaMer diagram, shown in Figure 5, demonstrating how a strong nucleation step results in the formation of many small nanoparticles.[35]

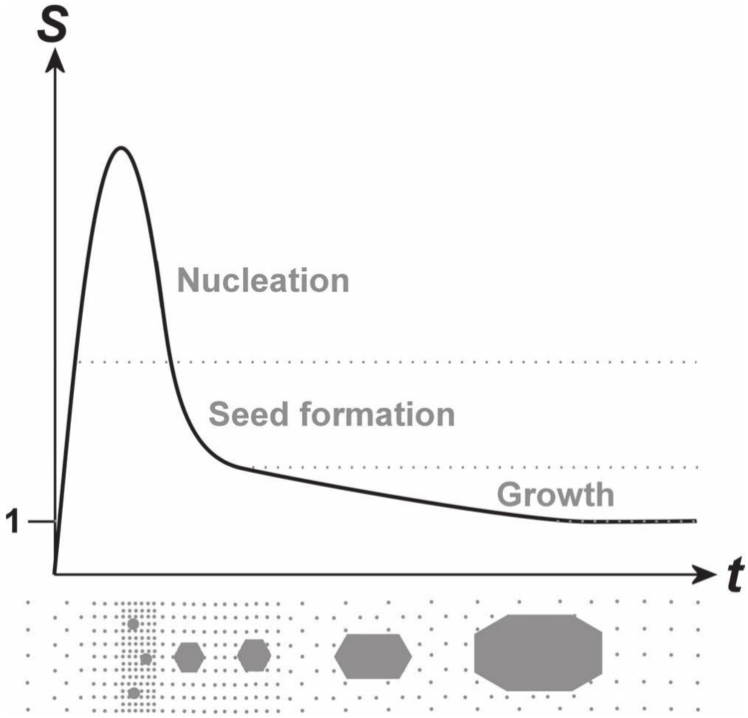

Figure 5: LaMer diagram illustrating the stages of nanocrystal formation and growth in a coprecipitation reaction.[35] Nucleation leads to the formation of many seed particles of a small size, but as the reaction continues, these particles decrease in number while increasing in crystallite size.

Pereira *et al.* have studied the effect of the base used to precipitate the iron oxide, replacing sodium hydroxide with isopropanolamine and diisopropanolamine, and have observed an increase in M_s values.[36] They attributed this magnetisation increase due to a decrease in the formation of surface defects. This occurs from the interactions of nitrogen and oxygen groups of the base with the under-coordinated sites on the iron oxide surface (figure 6). These surface defects form a magnetically dead layer which reduces M_s values. Minimising the formation of surface defects, reduces the formation of a magnetically dead surface layer, which will improve the overall magnetisation of the particles.

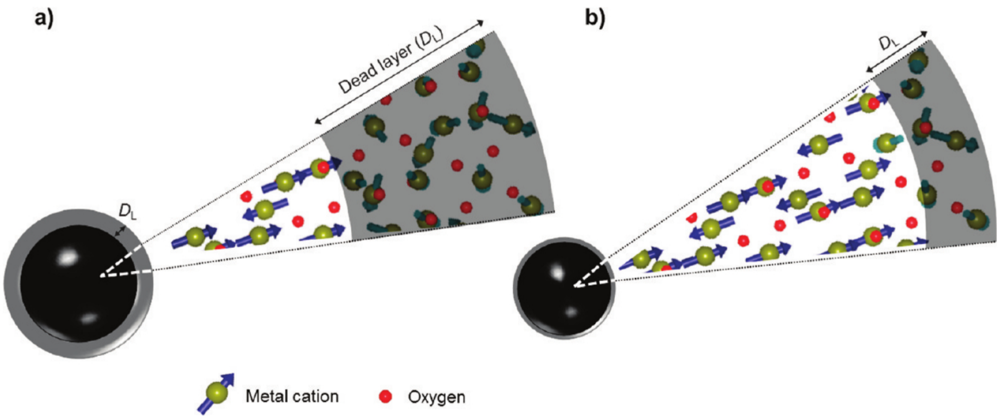

Figure 6: A schematic illustrating the effect of different bases on the formation of magnetically dead layers on iron oxides, based on the work by Pereira et al.[36] *Replacing sodium hydroxide with isopropanolamine and diisopropanolamine reduces the formation of surface defects, leading to an increase in magnetisation values.*

One of the attractive features of the co-precipitation approach is the ability to stabilise iron oxide nanoparticles with hydrophilic groups during the precipitation reaction. For example, charged groups of a hydrophilic stabiliser, such as a polyelectrolyte, can bind with the iron oxide surface as the particles are precipitated.[37,38] This is an extremely useful process as it allows for the development of a water stable magnetic nanocomposite in a single reaction step without any need for post processing. The formation of this water stable foundation allows the particles to be immediately used in biomedical applications or can allow further functionalisation through electrostatic interactions or aqueous coupling reactions.

1.3.2 High temperature decomposition methods

High temperature decomposition methods often afford highly crystalline, extremely uniform iron oxide nanoparticles. These particles are prepared by dissolving metal precursors such as oleates or acetylacetates in a high boiling solvent in the presence of a capping agent. This results in precursor decomposition and the formation of highly crystalline nanocrystals up to a few nanometers in size. This control over the resulting particle size through the careful selection of solvent and capping agent is a major advantage of this method.[39] Additionally, this method also minimises surface defect formation, enhancing the crystallinity of the iron oxide nanoparticles, which is reflected in high magnetisation values close to the theoretical bulk value (82 emu g^{-1} vs 98 emu g^{-1}).[2,39,40] Sun *et al.* have prepared 16 nm magnetite nanocrystals with hexagonal morphologies and have shown this method can be extended to provide a range of monodisperse nanoparticles with sizes as small as 4 nm (Figure 7).[2] The hexagonal morphology is indicative of highly crystalline materials, which is reflected in the nanoparticles having M_s values above 80 emu/g.[2,39] Bilecka *et al.* have introduced an additional microwave irradiation step to the high temperature decomposition reaction, reducing reaction times down to several minutes.[41] Masala and coworkers have demonstrated that this high temperature route can minimise the formation of surface defects when compared to aqueous methods.[42] They prepared $MnFe_2O_4$ nanoparticles *via* a high temperature decomposition reaction and compared them to particles formed in low temperature aqueous coprecipitation and reverse micelle reactions. They identify that the use of high temperatures allows for the controlled formation and growth of the particles which leads to less under co-ordinated surface sites. This reduces surface disorder but increases crystallinity, which they correlated to a significant increase in saturation magnetisation values. Comparing particles of a similar size, the high temperature decomposition iron oxides (4.6 nm) have significantly higher M_s values (50 emu g^{-1}) than those prepared by aqueous co-precipitation (13 emu g^{-1}; 3 nm) and reverse micelle methods (30 emu g^{-1}; 4 nm) which further illustrates this point.

One disadvantage of this approach is that the organic reaction conditions and use of hydrophobic capping groups requires post processing to remove the hydrophobic organic layer from the particles before they can be redispersed into aqueous solutions. Several groups have developed methods to deal with this. For example, Zhang *et al.* have developed a ligand exchange reaction to replace the hydrophobic surface coating with a polyelectrolyte.[43] The method ensures that the polyelectrolyte is firmly bound and provides a hydrophilic com-

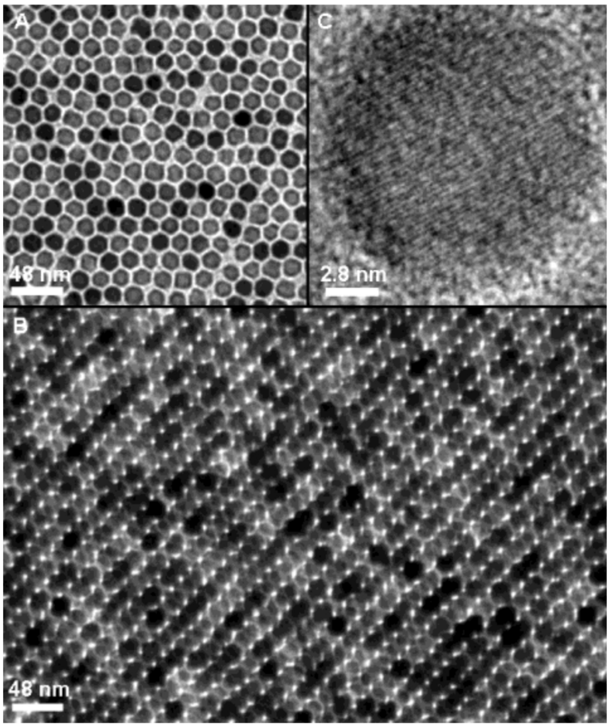

Figure 7: TEM images of Fe$_3$O$_4$ nanoparticles prepared by high temperature decomposition methods.[2] *Well defined particles with a hexagonal morphology can be observed.*

ponent to allow the particles to be redispersed into aqueous solutions, but this post processing adds extra steps and time to the reaction. Ge *et al.* also detailed a solvothermal method to stabilise iron oxide nanoparticles with polyelectrolyte to improve the stability of the particles in water but again the stabilisation step occurred post synthesis adding to the overall reaction time.[44]

1.3.3 Hydrothermal approaches

Hydrothermal methods work by sealing dispersions of the starting materials in a hydrothermal bomb and heating to high temperatures. In the case where water is used as the solvent, the combination of the high temperatures (374°C) and pressures (up to 220 bar) generated in the closed system leads to supercritical water.[45] In this state, water lacks surface tension but has a very high viscosity. This allows for normally insoluble compounds to now become highly soluble. The increased pressure means that reactions can be accessed at lower than normal reaction temperatures. Carvalho *et al.* have demonstrated that hydrothermal methods can be combined with co-precipitation techniques to further increase particle size (17-20 nm) and M$_s$ values (above 80 emu g^{-1}).[46] The advantage of this method is that the high reaction temperatures can increase crystallinity without the need for post processing to remove the organic components. Cai *et al.* prepared polyethyleneimine-Fe_3O_4 nanoparticles in a single step hydrothermal synthesis method, illustrating that this method can be combined with stabilisation and further functionalised with additional reactions.[47] Hydrothermal ageing can take several hours though and require high temperatures, therefore continuous hydrothermal systems can be prepared, allowing large scale production of nanoparticles as illustrated in the work by Barner *et al.*[48]

1.3.4 Microwave assisted reactions

Microwave irradiation presents an interesting alternative to traditional heating methods by offering rapid heating, controllability and faster reaction kinetics. Microwave heating has been used previously for organic reactions to reduce reaction times and suppress unwanted side reactions increasing the purity of the final product.[49] Microwave heating works on the principal of dielectric heating, which is the ability of a material to absorb microwave irradiation and convert it into heat. The heating mechanism relies on two principles: dipolar polarisation and ionic conduction. When exposed to electromagnetic microwave irradiation, charged groups such as dipoles or ions align with the incoming electric field of the radiation. This is an oscillating field, with the result that the ions or dipoles are constantly realigning with the field. When this oscillation is too quick for the ions and dipoles to align fully, lag occurs which results in resistive heating. This is measured as the amount of microwave energy that is absorbed by the sample and released as heat (the dielectric loss, ϵ''). The other heating mechanism is ionic conduction which is the collision of the oscillating charged particles (from the irradiation) which generates heat. This mechanism depends in part on the solvent used (for example, ionic liquids couple extremely well to the irradiation leading to excellent heat generation). The effectiveness of a solvent is dictated by the ratio between the dielectric constant (ϵ', the ability of the solvent to be polarised by the microwave irradiation) and the dielectric loss (ϵ''). This results in the dielectric loss tangent, $\tan\delta$, with a greater loss indicating a better microwave solvent. $\mathrm{Tan}\,\delta$ values over 0.5 are considered high microwave absorbing solvents (e.g. ethylene glycol, ethanol), having efficient microwave absorption allowing for rapid heating.[49]

Water is considered a medium microwave absorbing solvent with a $\tan\delta$ value of 0.123.[50] Water has a resonance frequency of 18 GHz, larger than the frequency of microwaves used in domestic/specialised systems (2.45 GHz).[50] While this is less effective at microwave heating than some other solvents, the use of water offers several advantages than other high absorbing solvents, especially in the preparation of biomedical agents. Some ionic liquids are organic solvents which may coat the particle surface requiring post processing to make the particles water stable. Utilising water as the solvent removes the need for post processing and can allow for *in situ* stabilisation. Additionally high microwave absorbing solvents heat up very rapidly which, while reducing reaction times, can lead to pressure spikes depending on the reaction. The slower ramping rate of heating water avoids this pressure spike, but utilising a medium absorbing solvent still allows faster heating than conventional heating methods. Komarneni *et al.* have demonstrated that water still reaches a desired temperature faster than conventional heating methods, showing the viability of the solvent in microwave reactions.[51] In addition to enhanced heating rates, microwave irradiation offers other advantages to conventional heating methods. Use of microwave systems allows for the *in situ* monitoring of reaction conditions such as temperature, internal pressure and microwave power. This improves reproducibility and safety, as digital limiters can be put in place to stop reactions from reaching dangerous conditions. There is also no contact between the heating element and the reaction mixture, which again minimises risk. Developments in microwave chemistry are improving the versatility of microwave systems, with current machines supporting a wide range of adaptors and expansions and can also be modified to have bigger reaction containers or auto samplers.

There have been only a few reports of incorporating microwave irradiation into iron oxide synthesis and the effectiveness of each approach. Enhanced growth and crystallinity is desirable, but care has to be taken that the particles do not grow too large. Khollam *et al.* combined the hydrothermal technique with microwave irradiation resulting in the formation of highly crystalline material with M_s values equivalent to high temperature decomposition methods.[52] However, these particles were sub-micron ferromagnets, making them too large and unsuitable for biomedical applications. Sreeja *et al.* incorporated microwave irradiation into the co-precipitation reaction of maghemite nanoparticles, noting an increase in the uniformity of the resulting particles.[53] Hong *et al.* also utilised microwave irradiation to age magnetite nanoparticles after they had been co-precipitated, which improved crystallinity and ensured the particles did not grow in size and become ferromagnetic.[54] They observed that ageing the nanoparticles improved crystallinity, with after two hours treatment highly crystalline nanoparticles with an M_s of $65.98\,\mathrm{emu\ g^{-1}}$ formed. Clearly, there is a great opportunity for developments in the microwave preparation of magnetic nanocomposite materials.

1.4 Biocompatibility of iron oxide nanoparticles

Biocompatibility is paramount in the construction of biomedical magnetic nanoparticles. A magnetic nanocomposite needs to be designed so that it is biocompatible with the body and can evade the biological elimination system in order to maximise their life span *in vivo*. Bare iron oxides can oxidise and degrade within cells damaging DNA causing mutations.[55,56] They are also unstable in aqueous solutions and will begin to cluster and agglomerate to exclude water. Stabilisation provides a hydrophilic coating for these particles minimising clustering. Clustering is undesirable as not only are larger particles more easily eliminated but agglomeration may lead to blocking of blood vessels. Another major consideration is particle lifespan. There are a magnitude of biological systems in place to eliminate foreign groups from the body. Therefore the magnetic composite needs to be designed to evade these mechanisms so it can reach the target site. One major elimination route is *via* the reticuloendothelial system (RES). The RES consists of specialised phagocytic cells that are associated with the liver, lymph nodes and spleen. When administered into the body, the RES coats the synthetic nanoparticles with proteins and glycoproteins based on their size and composition. This process is called opsonization and highlights the foreign nanoparticles to phagocytic cells. Once opsonized, macrophages and Kupffer cells of the RES engulf the nanoparticles and break them down. Larger particles ($>$200 nm) are more easily coated with proteins highlighting them for elimination much quicker than smaller particles.[57] Smaller particles are still susceptible to elimination as very small nanoparticles ($<$20 nm) can be filtered straight into urine from the kidneys without the need for opsonisation. These are depicted in Figure 8.[58] For access to diseased cells, there are reports of particles of up to 700 nm being able to penetrate the endothelium, but larger sizes may cause clotting in blood vessels and can increase opsonisation.[58,59] Sizes of between 30 and 150 nm have been reported to be the optimal size for magnetic nanocomposites as the particles are still small enough to be taken up by cells and will not be blocked in transit.[60,61]

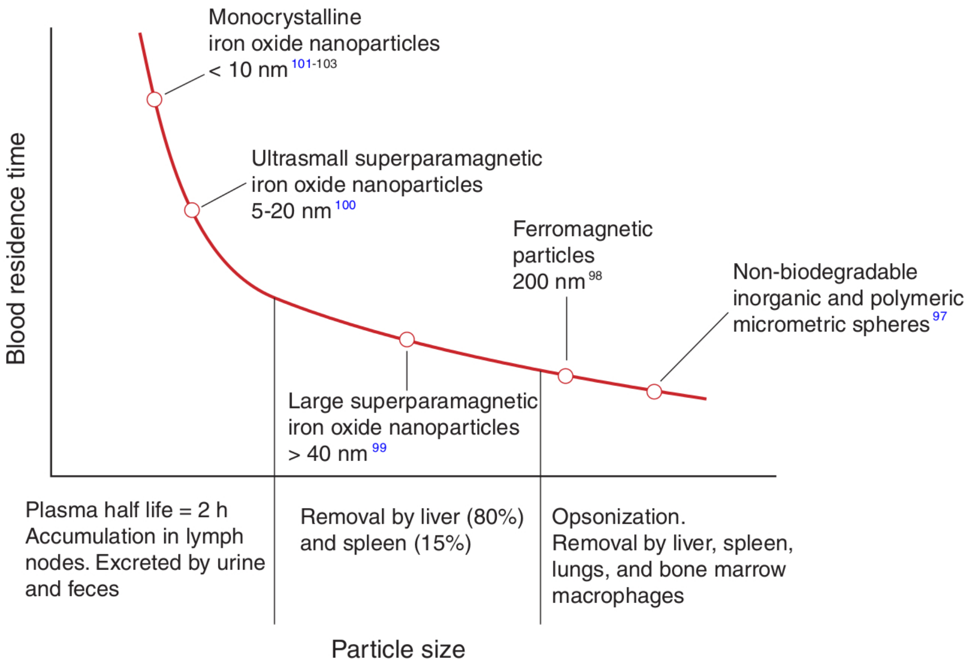

Figure 8: The fate of nanoparticles in the body based on size, with smaller particles lasting longer in the body as they can evade the reticuloendothelial system.[58] Particle size also effects elimination method, with larger particles being removed by opsonisation while smaller particles are filtered straight out of the bloodstream by the kidneys.

Surface charge and coating can have a great effect on evading RES and increasing the composites lifespan in the body. Hydrophobic surfaces are more easily coated with opsonisation proteins resulting in quicker elimination.[62] Gaur *et al.* reported that hydrophilic coatings can resist this process, thereby prolonging the particle life.[63] Regulating the surface charge is a key consideration, as highly positive coatings can attach non-specifically to cells whereas strongly negatively charged particles are more likely to be taken up by the liver.[61] The other significant consideration is the route of administration, as this can affect how the particles are processed and eliminated. Nanoparticles injected directly into the body are normally broken down by phagocytic cells, while oral administration exposes the particles to gastric acids which may reduce absorption.[58] When administered subcutaneously, the nanoparticles are transported through the lymphatic system and may be broken down there. This can be manipulated to ensure particles specifically reach lymphatic tumours.[64]

1.5 Stabilisation of iron oxide nanoparticles

Biological considerations illustrate that stabilisers are essential in the construction of biomedical magnetic nanocomposites. Not only do they ensure biocompatibility, but can also enhance existing properties and bestow new properties such as water stability and anchor points for further functionalisation. A wide range of materials can be used to stabilise iron oxide nanoparticles such as silica,[7,65,66] polymers/polyelectrolytes[37,67–69] and organic surfactants[6,70,71] with each stabiliser changing the particle size, morphology and properties. One common stabiliser is silica, as the silica layers are strongly bound to the iron oxide surface, are biocompatible and can allow for further surface functionalisation. Silica coatings are bound to the iron oxide surface through the condensation of orthosilicate groups with the iron groups on the surface.[7,72] A typical stabilisation reaction involves alkoxysilanes undergoing hydrolysis in solution. The unstable silane groups then undergo a condensation reaction with iron groups on the iron oxide surface forming an Fe-O-Si bond. This silica layer can then be further grown through additional condensation reactions, allowing the stabiliser thickness to be controlled.[66] The silica coating is covalently bound to the iron oxide surface minimising the risk of desorption. The ability to add and grow the initial silica layer allows for further functionalisation of the particles through the use of alkoxysilane linkers (i.e. 3-aminopropyltriethoxysilane). These linkers contain silicate groups that can condense on the silica surface and alternative functional groups to provide attachment points for other moieties. Chekina *et al.* have reported a method which binds amine groups to the silica surface *via* the Stöber method, which can be further functionalised using carbodiimide coupling.[73] McCarthy *et al.* illustrated a range of functionalisation reactions for silica coatings highlighting the versatility of this approach allowing for the development of multifunctional nanocomposites supporting multiple groups.[74] There are some caveats with silica stabilisers though as the stabilisation reaction has to be done separately post particle synthesis. Additionally, silica coatings have been shown to adversely effect magnetisation values by introducing a magnetically dead layer and increasing surface disorder with Park and coworkers reporting a decrease in magnetic properties from silica coated magnetite nanoparticles.[75] This is confirmed by Hui *et al.* who prepared a series of magnetite nanoparticles coated with silica layers of varying thickness noting a decrease in M_s values as layer thickness increases (with a decrease from 57.5 emu g^{-1} to 26 emu g^{-1} with a 20 nm silica layer).[76]

Polymers have traditionally been used to protect iron oxide nanoparticles and offer excellent water stability when bound. One example are polyelectrolytes, which consist of a series monomers that contain ionisable groups which disassociate in water leaving a charged chain. These charged chains can then bind to the iron oxide *via* electrostatic interactions between the monomers and oppositely charged surface ions.[77,78] The polyelectrolyte properties are dictated by the monomer composition and the chain length. Examples of polyelectrolytes are poly(sodium-4-styrene sulphonate),[37,38] poly(diallyldimethylammonium chloride)[79,80] and poly(acrylic acid).[81–83] Polyelectrolyte lengths can vary with chains of under 1,000 monomers to other chains over 1,000,000 monomers, with the larger lengths capable of supporting many iron oxide groups. The advantage of using polyelectrolytes is that they can be extremely hydrophilic with excellent water stability, with variable chain lengths allowing for further optimisation. Also, the electrostatic binding method can be performed simultaneously with precipitation, reducing reaction times and steps.

Polyelectrolytes are considered strong or weak based on their disassociation rate. Strong polyelectrolytes have easily ionisable groups that will disassociate under a wide range of conditions leaving a fully charged polyelectrolyte behind.[84,85] In the fully dissociated case, all monomers are exposed for binding with a repulsion effect between the charged monomers forcing the chain to adopt a linear conformation. Weak polyelectrolytes can be partially ionised in solution and the disassociation rate is greatly affected by experimental conditions such as pH.[86,87] This disassociation of the group then affects how the polyelectrolyte behaves in solution. Here, the binding sites are only partially exposed, with the non charged areas forming loops and folds as there is no repulsion forcing this conformation. The occurrence of these loops and folds increases the polyelectrolyte layer thickness, demonstrated in Figure 9. This can affect the composite size and ultimate use in biological applications, with larger materials more easily removed by the RES.

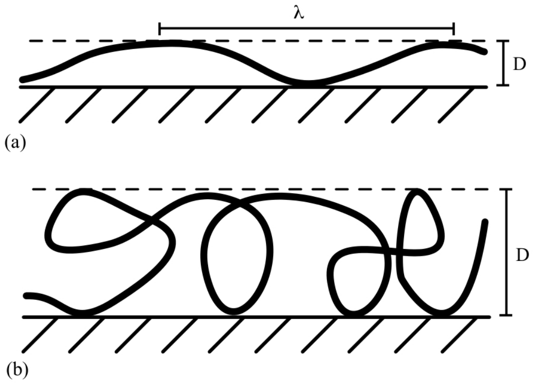

Figure 9: A schematic illustrating the differences in weak/strong polyelectrolytes on polyelectrolyte layer formation.[85] Strong polyelectrolytes adopt a linear conformation forming a flat surface on the substrate. The weak polyelectrolyte binds to the surface, but the formation of loops and folds results in the formation of a much thicker layer.

Polyelectrolytes have already been shown to be effective in the preparation of ferrofluids, with the work by Lin *et al.* stabilising magnetic nanoparticles with poly(acrylic acid).[81] They have developed a ferrofluid in a one step co-precipitation reaction that incorporated stabilisation into the precipitation stage. Light scattering techniques confirm that the material is water stable, with a hydrodynamic radius of 100 nm in neutral solutions. Polyelectrolyte-stabilised magnetic nanoparticles can also behave as promising MRI contrast agents.[37,38] Polyelectrolytes can also be used to stabilise iron oxide nanoparticles prepared from high temperature decomposition methods with the work by Zhang *et al.* and Ge *et al.* showing that hydrophobic iron oxide can be stabilised by hydrophilic polyelectrolyte and redispersed in solution.[43,44] Utilising a chain-based stabiliser rather than a layer-based coating will also affect M_s values and ultimately biological applications. Polyelectrolytes can limit crystal growth ensuring the particles are small enough to be superparamagnetic but also provide a magnetically dead layer that reduces M_s values.[69,81] The structural flexibility afforded by polyelectrolytes can also enhance biological applications. Attaching iron oxides to a chain, rather than fixing iron oxide clusters in an inorganic scaffold, allows the composite to adopt different conformations in solution.[7] As reported by several groups, when placed in an external magnetic polyelectrolyte stabilised magnetic nanocomposites form linear assemblies with a noticeable enhancement to MRI properties.[37,38,88]

Another common type of stabiliser is organic or fatty acids, such as oleic acid.[6,71] These possess long chains which can offer an organic environment for the entrapment and transport of hydrophobic drugs such as paclitaxel.[89] Ligand exchange can transfer these particles into water for subsequent biological use.[70,89] Another popular biocompatible stabiliser is dopamine which can bestow water stability on the iron oxide nanoparticles and can also be further functionalised through the amine group. Dopamine is an example of a catechol (1,2-dihydroxybenzene), with a terminal amine group. Catechols have a high affinity for iron oxide surfaces. Dopamine preferentially binds to under coordinated sites on the iron oxide surface via the hydroxide groups leading to the formation of a strong bidentate bond as shown in Figure 10.[90–94] The terminal amine can undergo a wide range of coupling reactions allowing for the attachment of groups that can extend the lifespan of the composite in the body such as polyethylene glycol,[95] fluorescent groups for imaging,[96] and chemotherapy agents for cancer treatment.[97]

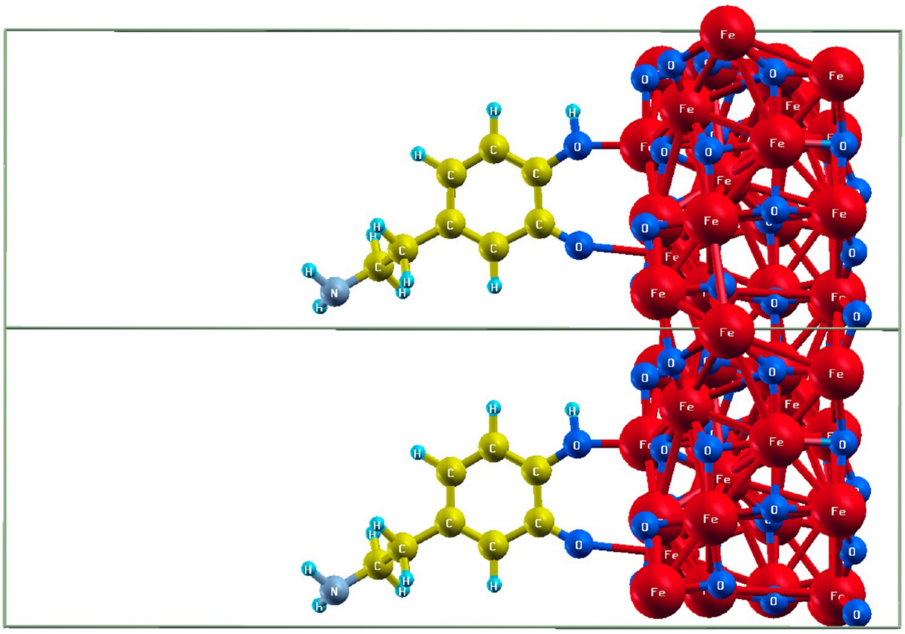

Figure 10: Dopamine binding to γ-Fe_2O_3 particle surfaces calculated by ab initio calculations by Fouineau et al.[93] *This illustrates the bidentate binding of the catechol group.*

1.6 Diagnostic and therapeutic applications

Through careful design and manipulation of the iron oxide core and surface coatings, these magnetic nanocomposites can be adapted to be used for a variety of biomedical applications, including magnetic resonance imaging, fluorescent labelling and site specific drug delivery systems.

1.6.1 Magnetic resonance imaging (MRI)

Magnetic nanoparticles have a key role in diagnostic purposes such as contrast agents for magnetic resonance imaging (MRI). MRI at its heart is a nuclear magnetic resonance experiment. It is a non-invasive imaging technique which works by manipulating the magnetic moments of protons within the body. Protons from water and lipids have very small magnetic moments. However, there is a very high concentration of protons in the body, which causes an overall net magnetisation that can be measured by MR imaging. When exposed to an external magnetic field, there is an alignment of the magnetic moments either parallel or anti-parallel to the external magnetic field. There is a slight difference in population between these two spins levels due to the anti-parallel alignment requiring slightly more energy. In MRI measurements, a radio frequency (rf) pulse is applied causing the aligned magnetic moments of the protons to become excited and de-align with the original applied field.[98] This pulse is calculated to be the energy difference between the two spin states, known as the Larmor frequency. Once the pulse is turned off, the spins will naturally realign with the applied field via longitudinal or transverse relaxation mechanisms.[99] Longitudinal relaxation is known as T_1 recovery or spin-lattice relaxation, where the energy from the excited nuclei is lost to the surroundings. Shorter T_1 relaxation times result in greater image intensity as the protons are relaxing faster between measurements.[100] Transverse relaxation is known as T_2 recovery or spin-spin relaxation and is the dissipation of energy from the interaction of the protons with other nuclei. Shorter T_2 relaxation times decrease signal intensity, increasing image contrast.[100] After multiple measurements, the difference in relaxation times between tissues provides an image, with areas of high proton concentration showing with a greater intensity.

The MR image can be improved with the use of contrast agents, which shorten the T_1 or T_2 relaxation times and improves the resolution of the image. Contrast agents are magnetic materials and the relaxation nature is determined by what relaxation time is more affected by the material, giving rise to T_1- or T_2-weighted contrast agents. The relaxation behaviour can be monitored experimentally using nuclear magnetic resonance dispersion (NMRD) profiles. Both the longitudinal (r_1) and transverse (r_2) relaxivities are calculated using the equation:

$$R_{i(obs)} = \frac{1}{T_{i(obs)}} = \frac{1}{T_{i(diam)}} + r_i C \tag{1}$$

where $1/T_{i(obs)}$ is the observed relaxation rate of the system (contrast agent plus solvent), $T_{i(diam)}$ is the relaxation time of diamagnetic contribution (i.e. the system without the contrast agent), C is concentration and r_i is the relaxivity.

The relaxivity is calculated for both longitudinal (i = 1) and transverse (i = 2) relaxation of the contrast agent and the ratio of the two relaxivities can be used to determine the effect of the contrast agent. For a contrast agent that improves T_1 signals, high r_1 relaxivities are required with a low r_2/r_1 ratio. For a T_2 contrast agent, high r_2 relaxivities and a high r_2/r_1 ratio are desired. Traditional T_1 MRI contrast agents are gadolinium-based compounds, whereas T_2 contrast agents tend to be iron oxide based.[101,102] Different MRI images can be taken of the body depending the weighting given on T_1 or T_2 measurements. There are many commercial MRI contrast agents available and their relaxivity values are given in Table 2. Key considerations for contrast agent behaviour are water stability and magnetic properties. High water stability ensures that the particles can be dispersed into solution, increasing the composites exposure to protons, while a high magnetic saturation ensures a stronger magnetic field is generated by the particles during the measurement. Exploring different synthesis methods and iron oxide compositions can tailor these properties to allow for the development of contrast agents.

Table 2: Relaxivities of commercially available iron oxide based contrast agents.[101,102] *Relaxivities in* mM^{-1} s^{-1}.

Name (Commerical)	**Coating type**	**r_1**	**r_2**
Ferumoxil (Lumirem)	Siloxane	3.2	72.0
Ferumoxide (Feridex)	Dextran	23.9	98.3
Ferucarbotran (Resovist)	Carboxydextran	25.4	151.0
Ferumoxtran (Sinerem)	Dextran	10.0	60.0
Feruglose (Clariscan)	Carbohydrate PEG	20.0	35.0

Na *et al.* have reported a contrast agent using iron oxide nanoparticles obtained from a high temperature decomposition method, stabilised with poly(acrylic) acid (PAA), PEG and catechol groups.[103] They observed that increasing the particle size improves r_2 relaxivity values. 23 nm particles had an r_2 value of 254 mM^{-1} s^{-1}, while 11 nm particles had r_2 values above most commercial agents at 181 mM^{-1} s^{-1}. Lee *et al.* have developed biocompatible iron oxide nanocubes, with a phospholipid coating.[104] The prepared nanocubes were biocompatible with MDA-MB-231 human breast cancer cells and displayed excellent M_s values (132.1 emu g^{-1}), reflected in strong r_2 values (324 mM^{-1} s^{-1}).The high relaxivity values allowed single cell imaging which is a promising avenue for the monitoring of transplanted cells. This work was further improved upon by Lee *et al.* who optimised the particle size.[105] They prepared 22 nm cubes with a relaxivity value of 761 mM^{-1} s^{-1}, one of the highest values found in the literature and over 6 times more effective than commercially available MRI contrast agents. They also found that as the nanoparticle size increased, r_2 values begin to decrease as the strong ferrimagnetic nature of the particles are enough to completely dephase the protons in water making them unsuitable for MRI analysis.

Relaxivity values are also greatly affected by the nature of the stabiliser. For example, Maity *et al.* have developed a one-pot coprecipitation method to prepare superparamagnetic iron oxide nanoparticles with a terephthalic acid, or 2-amino terephthalic acid, coating.[106] The particles had saturation magnetisation values of 74 emu g^{-1} but with r_2 values of 450.8 mM^{-1} s^{-1}, and 761 mM^{-1} s^{-1} for the 2-amino terephthalic acid and terephthalic acid coating respectively (Figure 11). The author attribute this increase to the stabiliser providing pathways allowing spin transfer from the superparamagnetic iron oxide to the protons surrounding the composite. They used a stabiliser containing diamagnetic spacers with π-conjugated bonds to provide the pathway to the surrounding protons. This indicates that the correct choice of stabiliser can also enhance relaxivity values alongside optimisation of the iron oxide core. Stabilisers can also improve relaxivity values by affecting the orientation or conformation of the magnetic nanoparticles. When bound to a polyelectrolyte chain for example, iron oxide nanoparticles are water stable and when exposed to a magnetic field the flexibility of the polyelectrolyte chain allows the particles to align with the external field leading to the formation of linear assemblies. This has been observed by several groups, with the adoption of a linear conformation increasing composite surface area which increases the amount of protons that can interact with the composite and therefore increasing relaxivity values.[37,38,88]

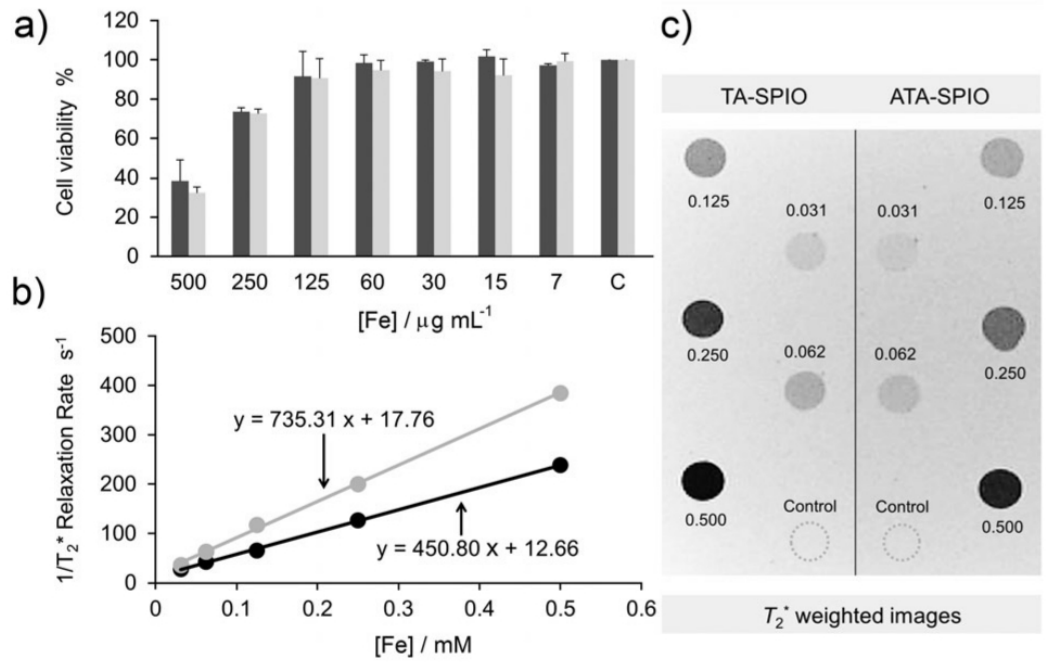

Figure 11: Cell testing and MRI measurements of iron oxide nanoparticles stabilised with terephthalic acid and 2-amino terephthalic acid by Maity et al.[106] *Cell testing shows no measurable toxicity (a), while increased transverse relaxation rates (b) and image darkening in phantom experiments (c) illustrate the increased effectiveness of the stabilised nanoparticles as a T_2 contrast agent.*

Utilising iron oxides as T_1 contrast agents over traditional gadolinium-based agents offers many advantages, the largest being reduced toxicity. Free gadolinium ions can chelate and precipitate in the blood making them very toxic, so they have to be protected before they can be used.[107] Iron oxide based materials have been shown to be far more biocompatible minimising this risk. Shen *et al.* developed ultra-small iron oxide nanoparticles to be used as T_1 contrast agents.[108] They observed that a smaller size, with decreasing magnetic properties and increasing surface defects, are key to suppressing the T_2 relaxation but maximising the T_1 relaxation. Fe_3O_4 nanoparticles, with sizes ranging form 1.9 to 13.8 nm, were prepared using sodium citrate as growth limiter to control particle size. The 1.9 nm particles had an M_s value of 4.54 emu g^{-1} but a r_2/r_1 ratio of 2.03 which is consistent with T_1 gadolinium based contrast agents. Sandiford *et al.* also designed iron oxide nanoparticles as T_1 contrast agents.[109] They prepared slightly larger nanoparticles of 5.5 nm which has a similar r_2/r_1 ratio 2.97 but were found to be better than commercial MRI contrast agents in general. The nanoparticles were synthesised using an organic technique and stabilised with PEG *via* a 1,1-bisphosphonate group which could then be labelled with the gamma-emitting isotope ^{99m}TC for dual imaging purposes.

Groups have worked towards the construction of contrast agents that can act as both T_1 and T_2 contrast agents. This is best illustrated in the work by Li *et al.* who prepared iron oxide nanoparticles *via* an aqueous coprecipitation method stabilised with poly(methacrylic acid).[110] These ultra-small nanoparticles had an average size of 3.3 nm and an M_s value of 16 emu g^{-1} with the resulting particles having an r_1 relaxivity value of 8.3 mM^{-1} s^{-1} and a r_2 relaxivity value of 35.1 mM^{-1} s^{-1}. *In vivo* T_1 and T_2 measurements confirm the particles can be used as a dual contrast agent.

1.6.2 Cell labelling and tracking

Functional groups can be bound to the surface of iron oxide based nanocomposites *via* exposed anchor groups which can be tailored depending on the desired application. An example of this is the attachment of fluorescent compounds which makes the nanocomposite suitable for confocal imaging, monitoring cell uptake and cell tracking. There are a vast range of fluorescent materials that can be bound to the composite such as organic dyes,[111–113] quantum dots,[114–116] and porphyirins.[117,118] Organic dyes mainly are used as they tend to be biocompatible and can easily be bound to magnetic nanoparticles through a variety of coupling reactions. There are a wide range of organic dyes that have been employed in biomedical applications including acridine orange,[112] Rhodamine B,[113,119] and fluorescein isothiocyanate.[120] Alternatives such as quantum dots can be tailored to fluoresce at different wavelengths but can be quite toxic.[121–123]

The attachment method of the moiety is key in the development of fluorescent nanoparticles. The group needs to be bound in such a way that it will not detach from the composite early, which could interfere with measurements or adversely affect the body. There are a number of approaches to attaching functional groups to magnetic nanocomposites. One example is to prepare a hollow vessel and load the fluorescent/functional group into the pores of the the vessel. This is illustrated in the work by Márquez *et al.* who filled hollow magnetite/silica spheres with Rhodamine B and measured the loading and release kinetics.[124] SEM images confirm the formation of hollow microspheres, while loading and release kinetics show that the material is contained in the silica shell with release dictated by environmental conditions such as pH and temperature. Foy and coworkers have prepared oleic acid coated magnetite nanoparticles and loading hydrophobic NIR (near infrared) dyes into the organic surface layer.[125] The composite was then bound to a block co-polymer to make the particles water stable and then exposed to MCF-5 xenograft breast tumours. They observed that the dye remained in the composite as the particles were taken up by the cells, which displayed increase fluorescence intensity, as shown in Figure 12.

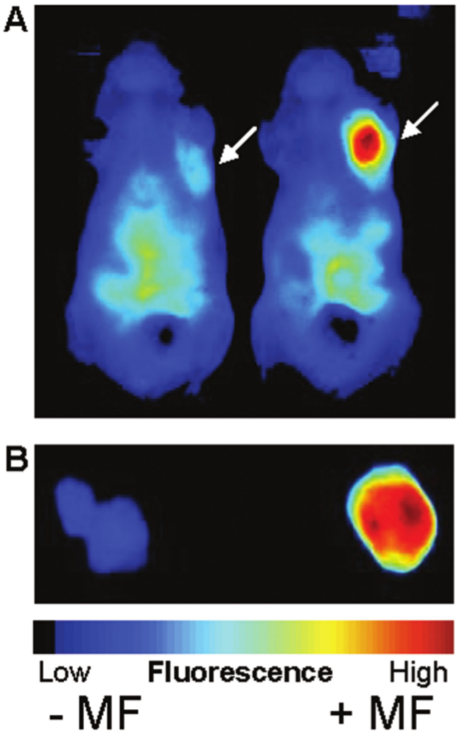

Figure 12: In vivo images of dye functionalised magnetic nanoparticles localised at a tumour site via magnetic targeting.[125] Nanocomposite concentration increases over time shown by an increase in fluorescence intensity.

An alternative approach is to attach the fluorescent group *via* electrostatic attractions. By mixing the charged fluorescent group with a stabiliser of the opposite charge, the dye can be bound to the material via electrostatic attractions.[126,127] The disadvantage of this approach is that the bound fluorescent group can disassociate from the composite releasing the dye early. Salgueiriño-Maceira *et al.* have bound quantum dots to the polyelectrolyte layer of a magnetic composite *via* electrostatic attractions and subsequently coated the composite with a silica layer to avoid desorption.[116] Guo took a different approach by depositing quantum dots directly on silica spheres containing magnetite nanoparticles and then protecting the overall composite with another silica layer to entrap the dye.[128] The addition of the silica layer did not diminish the composite fluorescence, as observed by confocal imaging. Another common method for grafting fluorescent groups to magnetic nanoparticles is through covalent coupling. Covalent coupling offers many advantages, one of which is the formation of a strong bond between the fluorescent group and the particle surface, which minimises early desorption. There are a wide range of possible covalent coupling reactions but a common method is carbodiimide coupling. This is a versatile binding method that allows the attachment of functional groups through the formation of an amide bond between amine and carboxylic acid groups. This is illustrated in the work by Hu *et al.* who have attached 9-amino acridine groups to PEG-stabilised Fe_3O_4 nanoparticles *via* carbodiimide coupling.[112] Qu *et al.* bound Fluorescein and Rhodamine B groups to iron oxide materials by carbodiimide coupling.[111] They demonstrated that a wide range of capping materials (including dopamine) can be used to bind fluorescent groups and that the carbodiimide coupling method allows the attachment of these groups through either the amine or carboxylic acid groups.

1.6.3 Site-specific drug delivery systems

Through functionalisation, one of the most promising applications for magnetic nanoparticles is the development of site-specific drug delivery systems. Chemotherapy is a very effective treatment against cancerous cells, destroying harmful cells or inhibiting tumour growth. The downside of this approach is that it can be non-specific, often targeting healthy cells alongside cancerous cells. Therefore, a carrier system is needed to transport these drugs to ensure they specifically target the afflicted cells. Magnetic nanoparticles are a very promising avenue for this, as the addition of the magnetic functionality allows them to be guided *in vivo* and held at the site by an external magnetic field.[129] This localises the drug, increasing its uptake into the cancerous cells at the target site while minimising the drugs effect on the surrounding healthy cells. There are many possible drugs to be used in chemotherapy such as Epirubicin,[130] Paclitaxel,[89,131] Doxorubicin,[132,133] RU 58668 (A steroid antiestrogen)[134] and Rapamycin[89] so developing a magnetic carrier is highly desirable to ensure that these compounds can be used to their full effect. An early example of magnetic drug targeting was reported by Lübbe *et al.* who bound the anti-cancer drug Epirubicin to magnetic nanoparticles that were coated with starch polymers.[130] Epirubicin (4'-epidoxorubicin) is an antibiotic that is used to treat tumours. The anionic phosphate groups of the starch polymers allowed for the electrostatic binding of the positively charged amino groups of the sugars in Epirubicin. Initially the study showed that the unloaded ferrofluid was biocompatible with no noticeable toxicity. The composite was then loaded, held over the tumour site with a magnetic field and after 7-14 days they found a visible change in the tumour which led to a complete loss of the tumour, illustrating the effectiveness of magnetic targeting. In a more recent example, the work by Zhou *et al.* illustrates the benefits of magnetic targeting by comparing doxorubicin (DOX) loaded magnetite nanoparticles to free doxorubicin.[133] The drug is bound to the PEG stabiliser on the iron oxide surface *via* an imine bond which can be broken under acidic conditions allowing for controlled release. They determined that at pH 7.4 DOX release was less than 10% (after 48 hours) but as the pH decreased to 5.4 this release increased to over 50% over 10 hours. The acidic environments of tumours allowed for a controlled release of the drug and reduced the risk of drug distribution to healthy sites. The nanocomposite-bound drug was found to be significantly more effective than the free DOX, demonstrating that not only does magnetic targeting minimise the risk of damaging healthy cells but lower concentrations of the drug can be used for magnetic targeting.

In addition to selectivity, another advantage of drug delivery systems is allowing for the distribution of hydrophobic drugs into cells. The magnetic carrier acts a hydrophilic platform, to which the drug can be bound and transported. For example RU 58668 is an effective anti-tumour steroid compound but is hydrophobic and cannot be distributed into aqueous cells without modification. Plassat *et al.* circumvented this issue by trapping RU 58668 into magnetic vesicles containing maghemite and rhodamine molecules.[134] The vesicles create an hydrophobic environment to contain the drug, while the hydrophilic shell and the magnetic particles allows the transport of the drug into the aqueous site. Electron microscopy and confocal imaging confirms the uptake and accumulation of the nanoparticles in MCF-7 cells under a 0.44 T magnet and tumour growth was inhibited from 40% to over 60% when magnetic targeting was employed. Poor dispersion can also be an issue for chemotherapy agents. For example, Paclitaxel is known to have poor solubility and requires a hydrophilic carrier. Dilnawaz *et al.* bound Paciltaxel to magnetic nanoparticles functionalised with glyceryl monooleate, making the overall composite hydrophilic.[89] The composite was also loaded with fluorescent groups and confocal microscopy confirmed uptake of the drug along with decreasing tumour size demonstrating the composites effectiveness as a drug delivery agent.

When the loaded composite reaches the targeted site, a reliable mechanism is needed to allow the release of drug so that it can interact with the cancerous cells. The release mechanism is based on how the drug is bound to the composite. One common method is to use the extreme environments of cancerous cells to increase the natural release of the drug. This is demonstrated in the work by Zhang *et al.* who prepared a hollow shell composite containing magnetite, silica and fluorescent $NaYF_4$ layers.[132] The chemotherapy agent DOX was loaded into the cavity and dispersed in tumour tissue, where it showed increased uptake by the cells and sustained release of the drug. Drug release increased with as the pH decreased, with the acidic environment of tumour cells allowing for selective release. This is echoed in the work by Yang *et al.* who loaded oleic acid stabilised iron oxide nanoparticles containing DOX groups into silica nanoparticles with a polymer containing pH sensitive groups.[135] The polymer then limited drug release under normal physiological cell conditions but accelerated drug release in acidic conditions. Hu *et al.* took a similar approach by developing a silica shell-like system that contains ibuprofen loaded magnetite particles, but surrounded the particles with a thermally responsive polymer to act as the release mechanism.[136] When heated, the silica shell ruptured releasing the drug. Not only do the trapped magnetite nanoparticles allow for magnetic targeting, but can also provide the heat to rupture the shell *via* hyperthermic heating. Transmission electron microscopy was used to to confirm this rupture and the release of the drug (Figure 13).

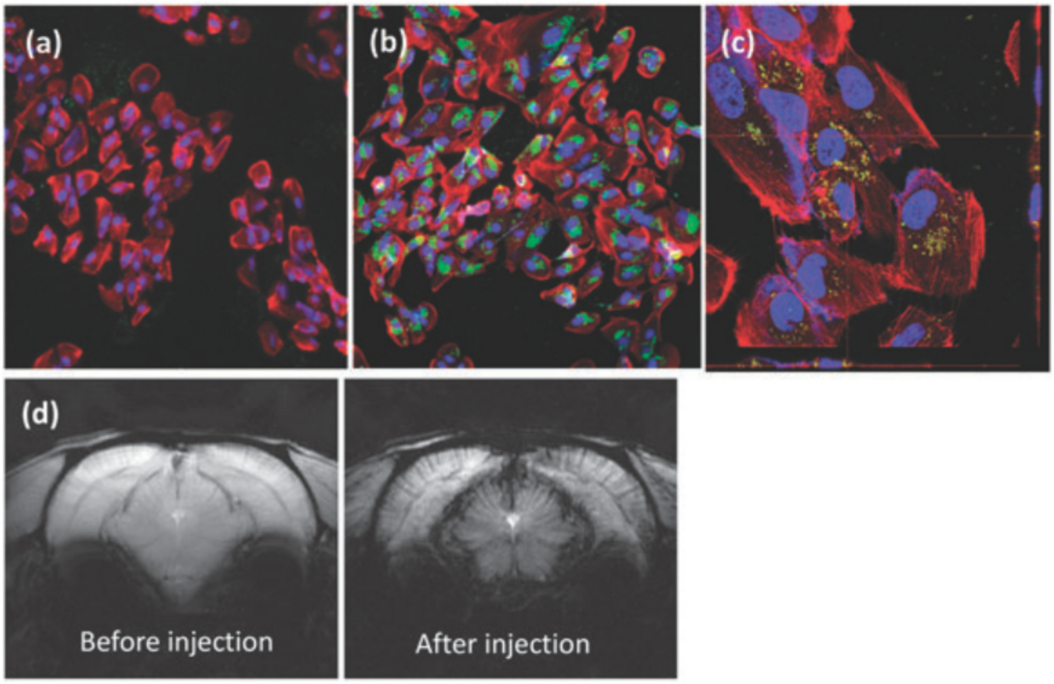

Figure 13: Confocal and MRI images of ruptured magnetic nanocomposites incubated with cells for 24 hr, showing the release of the trapped compound and darkening of the MR image.[136]

By attaching the drug to the composite *via* a specific type of bond, enzymes that are exclusive to or in higher concentration in cancerous cells can break that bond ensuring that the drug is only released where it is needed. This is illustrated in the work by Lee *et al.* who bound gemcitabine, a chemotherapy drug used in the treatment of pancreatic cancer, to iron oxide nanoparticles *via* a tetra peptide (GFLG) linker.[137] This bond can be cleaved by the enzyme cathepsin B, which is found in elevated concentrations in pancreatic tumour cells. The nanoparticles were taken up by the cells (confirmed by MR imaging) and tumour growth was inhibited by 50% indicating both the cleavage of the drug and effectiveness of the composite. Hwu *et al.* also bound Paclitaxel to magnetic nanoparticles *via* a Michael addition reaction using PEG with a phosphodiester as a linker.[131] This both enhanced the hydrophilicity of the composite while allowing a degree of selective targeting, as phosphate groups preferably bind to cancer cells and the enzyme phosphodiesterase (which will break the bond) is found in much higher concentrations in these cells. Experimental conditions showed that phosphodiesterase broke the bond holding the paclitaxel, relasing 91% of the drug over 10 days. The release was slow to begin with but after the 4th day drug release rapidly increased as the bonds became more exposed. Additionally this method resulted in very little free drug seen in the untargeted cells due to lower enzyme concentration. Lee *et al.* loaded DOX into a magnetic silica composite bound with cyclodextrin.[138] The cyclodextrin component blocks the pores that release the drug, which can be cleaved by glutathione. This is found at higher concentrations in cancer cells in comparison to healthy cells, and when exposed to cyclodextrin, the disulphide units within the blocker are cleaved, releasing the drug. Cell testing shows that without glutathione the drug is retained in the composite for 5 days. When added to cancer cells, the DOX is released quickly, as shown in a shrinking and ultimately death of the cancer cells within the same timeframe.

Magnetic targeting illustrates that chemotherapy agents can be localised within tumours, but selectivity can be improved further through the attachment of targeting groups to the nanocomposite. One common targeting group is folic acid, as folate receptors are over expressed in human cancer cells. Zhu *et al.* demonstrated the effectiveness of folic acid as the targeting group by binding it to hollow magnetite/silica spheres and monitoring their uptake into HeLa cells.[139] They observed the particles being primarily taken up by folic acid receptor endocytosis. They prepared hollow particles that could be loaded with DOX to cause cell death, with the folate groups ensuring that the particles are specifically taken up by tumour cells. Liong *et al.* also demonstrates the versatility of folic acid targeting, showing that folic acid bound magnetic nanocomposites can effectively guide Paclitaxel and Camptothecin (another chemotherapy drug) to cancerous cells.[140] There are many other examples of a wide range of chemotherapy agents specifically targeting cancerous cells through the use of folic acid functionalisation.[141–143] The combination of the folic acid targeting, drug delivery systems and attachment of luminescent groups has led to the development of multifunctional nanocomposites that can target, detect and treat cancerous cells. Lee *et al.* have prepared an iron oxide nanocomposite that was a drug delivery vehicle, a T_2 contrast agent (r_2: 76.2 mM^{-1} s^{-1}) and a fluorescent label.[144] Delivery of the chemotherapy agent was monitored *via* confocal imaging. MR images confirm the materials use as a contrast agent, while microscopy images show the cells had undergone apoptosis due to the DOX component. Wang *et al.* also developed a multifunctional treatment/diagnostic platform but incorporated targeting groups into the composite to ensure that the drug is distributed at the intended site.[145] They bound folic acid to the composite so it would be taken up by HeLa cells. Additionally they bound the photosensitive component aluminium phthalocyanine to the composite to destroy the cancerous cell through photodynamic therapy. Hu *et al.* developed nanocomposites with amiphilic diblock co-polymers which allowed for controlled release of Paclitaxel.[146] They additionally attached folic acid for specific targeting of cells and the magnetic components allowed for high r_2 relaxivities (121.1 mM^{-1} s^{-1}). Yang *et al.* also prepared a multifunctional nanocomposite, containing targeting ligands and DOX bound *via* linkers to a PEG coating.[147] The hydrophilic PEG layer enhanced water stability and the composites lifespan within the body, while the magnetic core showed good r_2 relaxivity values of 345.1 mM^{-1} s^{-1}. The chemotherapy agent was bound through a hydrazone linkage, which allowed the composite to be taken up through the folate receptors and cleaved within the cell ensuring no premature leakage.

1.7 Aims and objectives

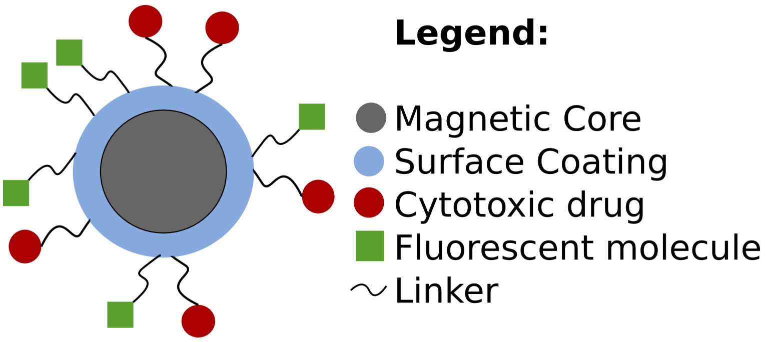

Figure 14: Schematic representation of the type of multifunctional nanocomposite prepared as part of this project. A magnetic core is coated with a protective stabiliser (shown in blue) which can support other functional groups such as drugs (red) or fluorescent moieties (green) via covalent coupling.

The ultimate aim of the current work was to prepare a highly magnetic, biocompatible, water stable iron oxide based nanocomposite with potential applications in fluorescent cell tracking, MR imaging and as a drug delivery system. A representation of such a multifunctional platform is shown in Figure 14. The literature has shown that careful design of the nanocomposite is key to unlocking the potential of iron oxide materials.

The scientific and technical objectives of this work was to prepare a series of iron oxide nanoparticles *via* a microwave assisted co-precipitation method, and to analyse these reactions to determine the best magnetic foundation for the composite. The synthesis method was explored in-depth with a particular focus on the effects of microwave irradiation on iron oxide formation, size, morphology and crystallinity. A highly effective, extremely water stable T_2 MRI contrast agent was developed through the stabilisation of iron oxide nanoparticles with polyelectrolytes. The properties of these polyelectrolytes was examined in detail (such charge and chain length), to maximise the potential of these materials as a MRI contrast agent. Ultimately, these pieces of work were combined to develop a multifunctional nanocomposite capable of supporting both fluorescent and targeting groups without any sacrifice to water stability and crystallinity. The prepared materials was characterised using a wide range of characterisation techniques (XRD, FTIR, Raman, TGA, DLS, UV-Vis, Fluorescence, AAS, NMR and SQUID measurements). The ultimate effectiveness of the materials was demonstrated through biological characterisation techniques such as MR imaging, confocal microscopy and cell testing.

The co-precipitation method was used over high temperature decomposition methods, as this enables the synthesis of particles over a very quick timeframe with simultaneous precipitation and stabilisation allowing the formation of water stable nanocomposites in a single step. This work distinguishes itself from traditional co-precipitation reactions in two major ways. Microwave irradiation was used to minimise surface defects formed from the co-precipitation process and to decrease reaction temperatures and times when compared to high temperature decomposition methods. Additionally dopamine and polyelectrolyte stabilisers was used to not only bestow excellent water stability, but to improve under co-ordinated surface sites further enhancing magnetisation values and provide anchoring points to allow for a wide range of functional groups to be attached to the nanocomposite.

This research lead to the development of a new family of multifunctional magnetic nanocomposites, which display excellent water stability coupled with strong magnetic properties and capability for further functionalisation in a quick, reproducible one step method. There has been little work incorporating microwave irradiation into the development iron oxide nanoparticles and there has yet to be a systematic study into the variation of charge and chain length of polyelectrolytes as a stabiliser to iron oxide nanoparticles which this work explores.

References

[1] Batlle, X.; Labarta, A. *J. Phys. D: Appl. Phys.* **2002**, *35*, R15–R42.

[2] Sun, S.; Zeng, H. *J. Am. Chem. Soc.* **2002**, *124*, 8204–8205.

[3] Teng, X.; Black, D.; Watkins, N. J.; Gao, Y.; Yang, H. *Nano Lett.* **2003**, *3*, 261–264.

[4] Khedr, M.; Omar, A.; Abdel-Moaty, S. *Colloids Surf., A* **2006**, *281*, 8–14.

[5] Si, S.; Kotal, A.; Mandal, T. K.; Giri, S.; Nakamura, H.; Kohara, T. *Chem. Mater.* **2004**, *16*, 3489–3496.

[6] Sahoo, Y.; Pizem, H.; Fried, T.; Golodnitsky, D.; Burstein, L.; Sukenik, C. N.; Markovich, G. *Langmuir* **2001**, *17*, 7907–7911.

[7] Philipse, A. P.; van Bruggen, M. P. B.; Pathmamanoharan, C. *Langmuir* **1994**, *10*, 92–99.

[8] Ito, A.; Shinkai, M.; Honda, H.; Kobayashi, T. *J. Biosci. Bioeng.* **2005**, *100*, 1–11.

[9] Thapa, D.; Kulkarni, N.; Mishra, S. N.; Paulose, P. L.; Ayyub, P. *J. Phys. D: Appl. Phys.* **2010**, *43*, 195004.

[10] Cornell, R. M.; Schwertmann, U. *The Iron Oxides:Structure, Properties, Reactions, Occurrences and Uses*; Wiley-VCH, 2003.

[11] West, A. R. *Solid State Chemistry and its Applications Second Edition*; Wiley, 2014.

[12] Kim, Y.; Kim, D.; Lee, C. S. *Physica B* **2003**, *337*, 42–51.

[13] Tang, Z. X.; Sorensen, C. M.; Klabunde, K. J.; Hadjipanayis, G. C. *J. Appl. Phys.* **1991**, *8*, 5279–5281.

[14] Momma, K.; Izumi, F. *J. Appl. Crystallogr.* **2011**, *44*, 1272–1276.

[15] Fleet, M. E. *Acta. Cryst.* **1981**, *B37*, 917–920.

[16] Jiles, D. *Introduction to magnetism and magnetic materials*; Chapman and Hall, 1991.

[17] Weiss, P. *Compt. Rend.* **1906**, *143*, 1136.

[18] Woo, K.; Hong, J.; Choi, S.; Lee, H.-W.; Ahn, J.-P.; Kim, C. S.; Lee, S. W. *Chem. Mater.* **2004**, *16*, 2814–2818.

[19] Maaz, K.; Mumtaz, A.; Hasanain, S.; Ceylan, A. *J. Magn. Magn. Mater.* **2007**, *308*, 289–295.

[20] Roy, S.; Ghose, J. *J. Appl. Phys.* **2000**, *87*, 6226–6228.

[21] Rana, S.; Gallo, A.; Srivastava, R. S.; Misra, R. *Acta Biomater.* **2007**, *3*, 233–242.

[22] Kodama, R. *J. Magn. Magn. Mater.* **1999**, *200*, 359–372.

[23] Morais, P.; Garg, V.; Oliveira, A.; Silva, L.; Azevedo, R.; Silva, A.; Lima, E. *J. Magn. Magn. Mater.* **2001**, *225*, 37–40.

[24] Goya, G. F.; Berquó, T. S.; Fonseca, F. C.; Morales, M. P. *J. Appl. Phys.* **2003**, *94*, 3520–3528.

[25] Batle, X.; Pérez, N.; Guardia, P.; Iglesias, O.; Labrta, A.; Bartolomé, F.; García, L. M.; Bartolomé, J.; Roca, A. G.; Morales, M. P.; Serna, C. J. *J. Appl. Phys.* **2011**, *109*, 07B524.

[26] Battle, X.; Labarta, A. *J. Phys. D: Appl. Phys.* **2002**, *35*, R15–R42.

[27] Gupta, A. K.; Gupta, M. *Biomaterials* **2005**, *26*, 3995–4021.

[28] Massart, R. *IEEE Trans. Magn.* **1981**, *Mag-17*, 1247–1248.

[29] Komarneni, S.; D'Arrigo, M. C.; Leonelli, C.; Pellacani, G. C.; Katsuki, K. *J. Am. Ceram. Soc.* **1998**, *81*, 3041–3043.

[30] Li, F.; Liu, J.; Evans, D. G.; Duan, X. *Chem. Mater.* **2004**, *16*, 1597–1602.

[31] Mikhaylova, M.; Kim, D. K.; Bobrysheva, N.; Osmolowsky, M.; Semenov, V.; Tsakalakos, T.; Muhammed, M. *Langmuir* **2004**, *20*, 2472–2477.

[32] Morel, A.-L.; Nikitenko, S. I.; Gionnet, K.; Wattiaux, A.; Lai-Kee-Him, J.; Labrugere, C.; Chevalier, B.; Deleris, G.; Petibois, C.; Brisson, A.; Simonoff, M. *ACS Nano* **2008**, *2*, 847–856.

[33] Tromp, R. M.; Hannon, J. B. *Surf. Rev. Lett.* **2002**, *9*, 1565–1593.

[34] Park, J.; Privman, V.; Matijević, E. *J. Phys. Chem. B* **2001**, *105*, 11630–11635.

[35] Polarz, S. *Adv. Funct. Mater.* **2011**, *21*, 3214–3230.

[36] Pereira, C.; Pereira, A. M.; Fernandes, C.; Rocha, M.; Mendes, R.; Fernández-García, M. P.; Guedes, A.; Tavares, P. B.; Grenèche, J.-M.; Araújo, J. P.; Freire, C. *Chem. Mater.* **2012**, *24*, 1496–1504.

[37] Corr, S. A.; Gun'ko, Y. K.; Tekoriute, R.; Meledandri, C. J.; Brougham, D. F. *J. Phys. Chem. C* **2008**, *112*, 13324–13327.

[38] Corr, S. A.; Byrne, S. J.; Tekoriute, R.; Meledandri, C. J.; Brougham, D. F.; Lynch, M.; Kerskens, C.; O'Dwyer, L.; Gun'ko, Y. K. *J. Am. Chem. Soc.* **2008**, *130*, 4214–4215.

[39] Sun, S.; Zeng, H.; Robinson, D. B.; Raoux, S.; Rice, P. M.; Wang, S. X.; Li, G. *J. Am. Chem. Soc.* **2004**, *126*, 273–279.

[40] Tian, Y.; Yu, B.; Li, X.; Li, K. *J. Mater. Chem.* **2011**, *21*, 2476–2481.

[41] Bilecka, I.; Djerdj, I.; Niederberger, M. *Chem. Commun.* **2008**, 886–888.

[42] Masala, O.; Seshadri, R. *Chem. Phys. Lett.* **2005**, *402*, 160–164.

[43] Zhang, T.; Ge, J.; Hu, Y.; Yin, Y. *Nano. Lett.* **2007**, *7*, 3203–3207.

[44] Ge, J.; Hu, Y.; Biasini, M.; Dong, C.; Guo, J.; Beyermann, W. P.; Yin, Y. *Chem. Eur. J.* **2007**, *13*, 7153–7161.

[45] Reverchon, E.; Adami, R. *J. Supercrit. Fluid.* **2006**, *37*, 1–22.

[46] Carvalho, M. D.; Henriques, F.; Ferreira, L. P.; Godinho, M.; Cruz, M. M. *J. Solid State. Chem.* **2013**, *201*, 144–152.

[47] Cai, H.; An, X.; Cui, J.; Li, J.; Wen, S.; Li, K.; Shen, M.; Zheng, L.; Zhang, G.; Shi, X. *ACS Appl. Mater. Inter.* **2013**, *5*, 1722–1731.

[48] de Tercero, M. D.; Bruns, M.; Martínez, I. G.; Türk, M.; Fehrenbacher, U.; Jennewein, S.; Barner, L. *Part. Part. Syst. Charact.* **2013**, *30*, 229–234.

[49] Bilecka, I.; Niederberger, M. *Nanoscale* **2010**, *2*, 1358–1374.

[50] Gabriel, C.; Gaberiel, S.; Grant, E. H.; Halstead, B. S. J.; Mingos, D. M. P. *Chem. Soc. Rev.* **1998**, *7*, 213–223.

[51] Komarneni, S.; Katsuki, H. *Pure Appl. Chem.* **2002**, *74*, 1537–1543.

[52] Khollam, Y.; Dhage, S.; Potdar, H.; Deshpande, S.; Bakare, P.; Kulkarni, S.; Date, S. *Mater. Lett.* **2002**, *56*, 571–577.

[53] Sreeja, V.; Joy, P. A. *Mater. Res. Bull.* **2007**, *42*, 1570–1576.

[54] Hong, R.; Pan, T.; Li, H. *J. Magn. Magn. Mater.* **2006**, *303*, 60–68.

[55] Mahmoudi, M.; Simchi, A.; Milani, A. S.; Stroeve, P. *J. Colloid. Interf. Sci.* **2009**, *336*, 510–518.

[56] Karlsson, H. L.; Cronholm, P.; Gustafsson, J.; Möller, L. *Chem. Res. Toxicol.* **2008**, *21*, 1726–1732.

[57] Neuberger, T.; Schöpf, B.; Hofmann, H.; Hofmann, M.; von Rechenberg, B. *J. Magn. Magn. Mater.* **2005**, *293*, 483–496.

[58] Arruebo, M.; Fernández-Pacheco, R.; Ibarra, M. R.; Santamaría, J. *Nanotoday* **2007**, *2*, 22–32.

[59] Moghimi, S. M.; Hunter, A. C.; Murray, J. C. *Pharmacol. Rev.* **2001**, *53*, 283–318.

[60] Debbage, P.; Jaschke, W. *Histochem. Cell Biol.* **2008**, *130*, 845–875.

[61] Berry, C. C. *J. Phys. D: Appl. Phys.* **2009**, *42*, 224003.

[62] Berry, C. C.; Curtis, A. S. G. *J. Phys. D: Appl. Phys.* **2003**, *36*, 198–206.

[63] Gaur, U.; Sahoo, S. J.; De, T. K.; Ghosh, P.; Maitra, A.; Ghosh, P. K. *Int. J. Pharm.* **2000**, *202*, 1–10.

[64] Brigger, I.; Dubernet, C.; Couvreur, P. *Adv. Drug Deliver. Rev.* **2002**, *54*, 631–651.

[65] Sun, Y.; Duan, L.; Guo, Z.; DuanMu, Y.; Ma, M.; Xu, L.; Zhang, Y.; Gu, N. *J. Magn. Magn. Mater.* **2005**, *285*, 65–70.

[66] Lu, Y.; Yin, Y.; Mayers, B. T.; Xia, Y. *Nano Lett.* **2002**, *2*, 183–186.

[67] Chatterjee, J.; Haik, Y.; Chen, C. *J Magn. Magn. Mater.* **2001**, *225*, 21–29.

[68] Lutz, J.-F.; Stiller, S.; Hoth, A.; Kaufner, L.; Pison, U.; Cartier, R. *Biomacromolecules* **2006**, *7*, 3132–3138.

[69] Si, S.; Kotal, A.; Mandal, T. K.; Giri, S.; Nakamura, H.; Kohara, T. *Chem. Mater.* **2004**, *16*, 3489–3496.

[70] Jain, T. K.; Morales, M. A.; Sahoo, S. K.; Leslie-Pelecky, D. L.; Labhasetwar, V. *Mol. Pharm.* **2005**, *2*, 194–205.

[71] Zhang, L.; He, R.; Gu, H.-C. *Appl. Surf. Sci.* **2006**, *253*, 2611–2617.

[72] Stöber, W.; Fink, A.; bohn, E. *J. Colloid Interface Sci.* **1968**, *26*, 62–69.

[73] Chekina, N.; Horák, D.; Jendelová, P.; Trchová, M.; Beneš, M. J.; Hrubý, M.; Herynek, V.; Turnovcová, K.; Suková, E. *J. Mater. Chem.* **2011**, *21*, 7630–7639.

[74] McCarthy, S. A.; Davies, G.-L.; Gun'ko, Y. K. *Nat. Protoc.* **2012**, *7*, 1677–1693.

[75] Park, J. C.; Gilbert, D. A.; Liu, K.; Louie, A. Y. *J. Mater. Chem.* **2012**, *22*, 8449–8454.

[76] Hui, C.; Shen, C.; Tian, J.; Bao, L.; Ding, H.; Li, C.; Tian, Y.; Shiab, X.; Gao, H.-J. *Nanoscale* **2010**, *3*, 701–705.

[77] Dobrynin, A. V.; Colby, R. H.; Rubinstein, M. *Macromolecules* **1995**, *28*, 1859–1871.

[78] Dobrynin, A. V.; Rubinstein, M. *Prog. Polym. Sci.* **2005**, *30*, 1049–1118.

[79] Mattison, K. W.; Dubin, P. L.; Brittain, I. J. *J. Phys. Chem. B.* **1998**, *102*, 3830–3836.

[80] Notley, S. M.; Norgren, M. *Biomacromolecules* **2008**, *9*, 2081–2086.

[81] Lin, C.-L.; Lee, C.-F.; Chiu, W.-Y. *J. Colloid. Interf. Sci.* **2005**, *291*, 411–420.

[82] Ge, J.; Hu, Y.; Biasini, M.; Dong, C.; Guo, J.; Beyermann, W. P.; Yin, Y. *Chem. Eur. J.* **2007**, *13*, 7153–7161.

[83] Na, H. B.; Palui, G.; Rosenberg, J. T.; Ji, X.; Grant, S. C.; Mattoussi, H. *ACS Nano* **2012**, *6*, 389–399.

[84] Blaakmeer, J.; Böhmer, M. R.; Stuart, M. A. C.; Fleer, G. J. *Macromolecules* **1990**, *23*, 2301–2309.

[85] Netz, R. R.; Andelman, D. *Phys. Rep.* **2003**, *380*, 1–95.

[86] Cranford, S. W.; Ortiz, C.; Buehler, M. J. *Soft Matter* **2010**, *6*, 4175–4188.

[87] Yoo, D.; Shiratori, S. S.; Rubner, M. F. *Macromolecules* **1998**, *31*, 4309–4318.

[88] Park, J.-H.; von Maltzahn, G.; Zhang, L.; Schwartz, M. P.; Ruosahti, E.; Bhatia, S. N.; Sailor, M. J. *Adv. Mater.* **2008**, *20*, 1630–1635.

[89] Dilnawaz, F.; Singh, A.; Mohanty, C.; Sahoo, S. K. *Biomaterials* **2010**, *31*, 3694–3706.

[90] Gu, H.; Yang, Z.; Gao, J.; Chang., C. K.; Xu, B. *J. Am. Chem. Soc.* **2004**, *127*, 34–35.

[91] Xu, C.; Xu, K.; Gu, H.; Zheng, R.; Liu, H.; Zhang, X.; Guo, Z.; Xu, B. *J. Am. Chem. Soc.* **2004**, *126*, 9938–9939.

[92] Chen, L. X.; Liu, T.; Thurnauer, M. C.; Csencsits, R.; Rajh, T. *J. Am. Chem. Soc.* **2004**, *126*, 9938–9939.

[93] Fouineau, J.; Brymora, K.; Ourry, L.; Mammeri, F.; Yaacoub, N.; Calvayrac, F.; Ammar-Merah, S.; Greneche, J.-M. *J. Phys. Chem. C* **2013**, *117*, 14295–14302.

[94] Amstad, E.; Gillich, T.; Bilecka, I.; Textor, M.; Reimhult, E. *Nano Lett.* **2009**, *9*, 4042–4048.

[95] Xie, J.; Xu, C.; Kohler, N.; Hou, Y.; Sun, S. *Adv. Mater* **2007**, *19*, 3163–3166.

[96] Goldmann, A. S.; Schödel, C.; Walther, A.; Yuan, J.; Loos, K.; Müller, A. H. E. *Macromol. Rapid Commun.* **2010**, *31*, 1608–1615.

[97] Garlyyev, B.; Durmus, Z.; Kemikli, N.; Sozeri, H.; Baykal, A. *Polyhedron* **2011**, *30*, 2843–2848.

[98] McRobbie, D. W.; Moore, E. A.; Graves, M. J.; Prince, M. R. *MRI From Picture to Proton*; Cambridge University Press, 2007.

[99] Sun, C.; Lee, J. S.; Zhang, M. *Adv. Drug. Deliv. Rev.* **2008**, *60*, 1252–1265.

[100] Lauffer, R. B. *Chem. Rev.* **1987**, *87*, 901–927.

[101] Wang, Y.-X. J. *Quant. Imaging Med. Surg.* **2011**, *1*, 35–40.

[102] Wang, Y.-X. J.; Hussain, S. M.; P.Krestin, G. *Eur. Radiol* **2001**, *11*, 2319–2331.

[103] Na, H. B.; Palui, G.; Rosenberg, J. T.; Ji, X.; Grant, S. C.; Mattoussi, H. *ACS Nano.* **2012**, *6*, 389–399.

[104] Kee, N.; Kim, H.; Choi, S. H.; Park, M.; Kim, D.; Kim, H.-C.; Choi, Y.; Lin, S.; Kim, B. H.; Jung, H. S.; Kim, H.; Park, K. S.; Moon, W. K.; Hyeon, T. *PNAS* **2011**, *108*, 2662–2667.

[105] Lee, N.; Choi, Y.; Lee, Y.; Park, M.; Moon, W. K.; Choi, S. H.; Hyeon, T. *Nano Lett.* **2012**, *12*, 3127–3131.

[106] Maity, D.; Zoppellaro, G.; Sedenkova, V.; Tucek, J.; Safarova, K.; Polakova, K.; Tomankova, K.; Jiwoky, C.; Stollberger, R.; Machala, L.; Zboril, R. *Chem. Commun.* **2012**, *48*, 11398–11400.

[107] Shellock, F. G.; Kanal, E. *J. Magn. Reson. Imaging* **1999**, *10*, 477–484.

[108] Shen, L.; Bao, J.; Wang, D.; Wang, Y.; Chen, Z.; Ren, L.; Zhou, X.; Ke, X.; Chen, M.; Yang, A. *Nanoscale* **2013**, *5*, 2133–2141.

[109] Sandiford, L.; Phinikaridou, A.; Protti, A.; Meszaros, L. K.; Cui, X.; Yan, Y.; Frodsham, G.; Williamson, P. A.; Gaddum, N.; Botnar, R. M.; Green, M. A.; de Rosales, R. T. M. *ACS Nano* **2013**, *7*, 500–512.

[110] Li, Z.; Yi, P. W.; Sun, Q.; Lei, H.; Zhao, H. L.; Zhu, Z. H.; Smith, S. C.; Lan, M. B.; Lu, G. Q. M. *Adv. Funct. Mater.* **2012**, *22*, 2387–2393.

[111] Qu, H.; Caruntu, D.; Liu, H.; O'Connor, C. J. *Langmuir* **2011**, *27*, 2271–2278.

[112] Hu, F.; Li, Z.; Tu, C.; Gao, M. *J. Colloid. Interf. Sci.* **2007**, *311*, 469–474.

[113] Das, M.; Mishra, D.; Dhak, P.; Gupta, S.; Maiti, T. K.; Basak, A.; Pramanik, P. *Small* **2009**, *5*, 2883–2893.

[114] Corato, R. D.; Bigall, N. C.; Ragusa, A.; Dorfs, D.; Genovese, A.; Marotta, R.; Manna, L.; Pellegrino, T. *ACS Nano* **2011**, *5*, 1109–1121.

[115] Liu, B.; Xie, W.; Wang, D.; Huang, W.; Yu, M.; Yao, A. *Materials Letters* **2008**, *62*, 3014–3017.

[116] Salgueiriño-Maceira, V.; Correa-Duarte, M. A.; Spasova, M.; Liz-Marzán, L. M.; Farle, M. *Adv. Funct. Mater.* **2006**, *16*, 509–514.

[117] Nowostawka, M.; Corr, S.; Byrne, S. J.; Conroy, J.; Volkov, Y.; Gun'ko, Y. K. *J. Nanobiotechnology* **2011**, *9*, 1–12.

[118] Kemikli, N.; Kavas, H.; Kazan, S.; Baykal, A.; Ozturk, R. *J. Alloy Compd.* **2010**, *502*, 439–444.

[119] Sahoo, Y.; Goodarzi, A.; Swihart, M. T.; Ohulchanskyy, T. Y.; Kaur, N.; Furlani, E. P.; Prasad, P. N. *J. Phys. Chem. B* **2005**, *109*, 3879–3885.

[120] Yang, H.-H.; Zhang, S.-Q.; Chen, X.-L.; Zhuang, Z.-X.; Xu, J.-G.; Wang, X.-R. *Anal. Chem.* **2004**, *76*, 1316–1321.

[121] Alivisatos, A. P.; Gu, W.; Larabell, C. *Annu. Rev. Biomed. Eng.* **2005**, *7*, 55–76.

[122] Jaiswal, J. K.; Mattoussi, H.; Mauro, J. M.; Simon, S. *Nat. Biotechnol.* **2003**, *21*, 47–51.

[123] Larson, D. R.; Zipfel, W. R.; Williams, R. M.; Clark, S. W.; Bruchez, M. P.; Wise, F. W.; Webb, W. W. *Science* **2003**, *300*, 1434–1436.

[124] Márquez, F.; Herrera, G. M.; Campo, T.; Cotto, M.; Duncongé, J.; Sanz, J. M.; Elizalde, E.; Perales, O.; Morant, C. *Nanoscale Res. Lett.* **2012**, *7*, 210.

[125] Foy, S. P.; Manthe, R. L.; Foy, S. T.; Dimitrijevic, S.; Krishnamurthy, N.; Labhasetwar, V. *ACS Nano* **2010**, *4*, 5217–5224.

[126] Hong, X.; Li, J.; Wang, M.; Xu, J.; Guo, W.; Li, J.; Bai, Y.; Li, T. *Chem. Mater.* **2004**, *16*, 4022–4027.

[127] Kang, J.; Dähne, L. *Langmuir* **2011**, *27*, 4627–4634.

[128] Guo, J.; Yang, W.; Wang, C.; He, J.; Chen, J. *Chem. Mater.* **2006**, *18*, 5554–5562.

[129] Dobson, J. *Drug Dev. Res.* **2006**, *67*, 55–60.

[130] Lübbe, A. S.; Bergemann, C.; Huhnt, W.; Fricke, T.; Riess, H.; Brock, J. W.; Huhn, D. *Cancer Res* **1996**, *56*, 4694–4701.

[131] Hwu, J. R.; Lin, Y. S.; Josephrajan, T.; Hsu, M.-H.; Cheng, F.-Y.; Yeh, C.-S.; Su, W.-C.; Shieh, D.-B. *J. Am. Chem. Soc.* **2009**, *131*, 66–68.

[132] Zhang, F.; Braun, G. B.; Pallaoro, A.; Zhang, Y.; Shi, Y.; Cui, D.; Moskovits, M.; Zhao, D.; Stucky, G. D. *Nano. Lett.* **2012**, *12*, 61–67.

[133] Zhao, Z.; Huang, D.; Yin, Z.; Chi, X.; Wang, X.; Gao, J. *J. Mater. Chem.* **2012**, *22*, 15717–15725.

[134] Plassat, V.; Willhelm, C.; Marsaud, V.; Ménager, C.; Gazeau, F.; Renoir, J.-M.; Lesieur, S. *Adv. Funct. Mater.* **2011**, *21*, 83–92.

[135] Yang, S.; Chen, D.; Li, N.; Mei, X.; Qi, X.; Li, H.; Xu, Q.; Lu, J. *J. Mater. Chem.* **2012**, *22*, 25345–25361.

[136] Hu, S.-H.; Chen, Y.-Y.; Liu, T.-C.; Tung, T.-H.; Liu, D.-M.; Chen, S.-Y. *Chem. Commun.* **2011**, *47*, 1776–1778.

[137] Lee, G. Y.; Qian, W. P.; Wang, L.; Wang, Y. A.; Staley, C. A.; Satpathy, M.; Nie, S.; Mao, H.; Yang, L. *ACS Nano* **2013**, *26*, 2078–2089.

[138] Lee, J.; Kim, H.; Kim, S.; Lee, H.; Kim, J.; Kin, N.; Park, H. J.; Choi, E. K.; Lee, J. S.; Kim, C. *J. Mater. Chem.* **2012**, 14061–14067.

[139] Zhu, Y.; Fang, Y.; Kaskel, S. *J. Phys. Chem. C* **2010**, *114*, 16382–16388.

[140] Liong, M.; Lu, J.; Kovochich, M.; Xia, T.; Ruehm, S. G.; Nel, A. E.; Tamanoi, F.; Zink, J. I. *ACS Nano* **2008**, *2*, 889–896.

[141] Wu, H.; Liu, G.; Zhang, S.; Shi, J.; Zhang, L.; Chen, Y.; Chen, F.; Chen, H. *J. Mater. Chem.* **2011**, *21*, 3037–3045.

[142] Maeng, J. H.; Lee, D.-H.; jung, K. H.; Bae, Y.-H.; Park, I.-S.; Jeong, S.; Jeon, Y.-S.; Shim, C.-K.; Kim, W.; Kim, J.; Lee, J.; Kee, Y.-M.; Kim, J.-H.; Kim, W.-H.; Hong, S.-S. *Biomaterials* **2010**, *31*, 4995–5006.

[143] Kaaki, K.; Hervé-Aubert, K.; Chiper, M.; Shkilnyy, A.; Soucé, M.; Benoit, R.; Paillard, A.; Dubois, P.; Saboungi, M.-L.; Chourpa, I. *Langmuir* **2012**, *28*, 1496–1505.

[144] Lee, J. E.; Lee, N.; Kim, H.; Kim, J.; Choi, S. H.; Kim, J. H.; Kim, T.; Song, I. C.; Park, S. P.; Moon, W. K.; Hyeon, T. *J. Am. Chem. Soc.* **2010**, *132*, 552–557.

[145] Wang, F.; Chen, X.; Zhao, Z.; Tang, S.; Huang, X.; Lin, C.; Cai, C.; Zheng, N. *J. Mater. Chem.* **2011**, *21*, 11244–11252.

[146] Hu, J.; Qian, Y.; Wang, X.; Liu, T.; Liu, S. *Langmuir* **2012**, *28*, 2073–2082.

[147] Yang, X.; Grailer, J. J.; Rowland, I. J.; Javadi, A.; Hurley, S. A.; Matson, V. Z.; Steeber, D. A.; Gong, S. *ACS Nano* **2010**, *4*, 6805–6817.

Chapter 2 Experimental procedures

2.1 Characterisation techniques

2.1.1 X-ray diffraction (XRD)

XRD analyses the crystal structure of the material allowing for determination of atom positions and unit cell parameters. This information can distinguish different iron oxides and information can be gleaned on crystallite sizes. Crystalline materials consist of atoms arranged in repeating ordered patterns resulting in a lattice. X-rays interact with these atoms and may be diffracted, as depicted in Figure 15. Most of the scattered X-rays cancel each other out through destructive interference, but a few of the scattered waves are constructive and add to each other. This can be detected and used in crystal assignment, according to Bragg's law:

$$n\lambda = 2dsin\theta \tag{2}$$

where n is an integer, λ is the wavelength of X-ray irradiation used, d is the distance between lattice planes and θ is the angle between the X-ray and the scattering plane. According to this law, the constructively scattered X-rays are related to the size and shape of the unit cell (as the *d* component relates to the spacing between the planes of the lattice) allowing multiple scattered waves to form diffraction peaks which can be used to calculate the crystallographic parameters of the unit cell. In an XRD measurement, electrons are generated from a source (a filament, the cathode) and are fired at a metal anode at high speeds (i.e. Cu, Mo) ionising the metals and generating X-rays. The X-rays then hit the target and scatter forming destructive and constructive waves, with the constructively scattered waves detected. Measurements are taken leading to the formation of a diffraction pattern, with the individual peaks relating to lattice planes in the crystal structure. By assigning these planes, the shape and size of unit cell can be determined which is an indicator on the identity the material. Substitution of atoms within the crystal structure will slightly change the parameters of the unit cell, and the different atoms themselves will cause a slight change in the scattering angles of X-rays resulting in a shifting of the diffraction peaks. This shifting effect can be used to distinguish materials with similar crystal structures.[1,2] X-ray diffraction and the use of Bragg's law in crystal structure determination is especially significant as this is the 100th anniversary of the award of the Noble Prize for Physics to Sir William Lawrence Bragg and Sir William Henry Bragg for their pioneering work in crystallography.

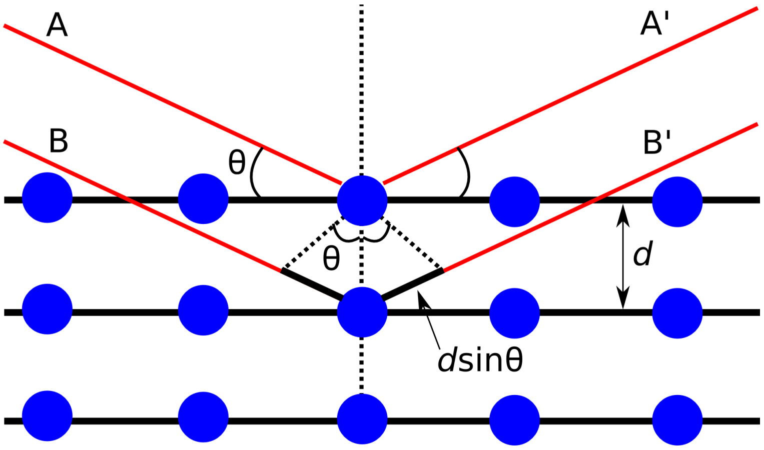

Figure 15: Diffraction of X-rays within a lattice structure. Destructive waves will cancel each other out but constructive waves can be detected and measured. According to Bragg's law, these constructive waves are specific to the lattice spacings and can be used to determine the crystal structure of a material. A and B are incident X-rays, A' and B' are the diffracted rays.

XRD can also be used to calculate the primary particle size of nanoscale materials. The primary particle size is the average crystallite size calculated from the XRD broadening and is representative of the sample tested in the XRD. The XRD primary particle size was compared to the observed particle sizes measured from TEM images. Paul Scherrer observed that when the particle size is very small (less than 200 nm), the scattered X-rays undergo a broadening effect, which translates into broad peaks in the X-ray diffraction pattern.[3] This peak broadening can be measured and the Scherrer equation can be used to calculate the average primary particle size.

$$T = \frac{K\lambda}{\beta cos\theta} \tag{3}$$

where T is the crystallite size, K is the shape factor of the particle, λ is the X-ray wavelength, β is the line broadening at half intensity (FWHM) and θ is the Bragg angle of a peak. The Scherrer equation is effective at calculating the primary particle size, but is limited to uniform well defined particles, as irregular particle shapes will affect the shape factor, resulting in a unreliable measurement.[4] Other factors can also contribute to peak broadening such as strain, and instrumental broadening. Instrument broadening can occur in several ways (i.e. from the X-ray source profile, optics) and can increase the width of the peaks, therefore resulting in a discrepancy between the actual crystallite size and that predicted by the Scherrer formula. Unfortunately, instrumental broadening was not taken into account for these results, which is reflected in part in the differences between the TEM and XRD results. As such the XRD Scherrer broadening values gives an average crystal size representative of the entire sample, while the TEM measurements will account for individual particle morphology and give a size distribution of the particles. X-ray diffraction patterns were collected using a Bruker D8 X-ray Diffractometer. A standard measurement took 4 hours 30 minutes, between 20 to 70^0 2θ. The X-ray wavelength was 1.5408Å using a copper source (40kV, 40 mA). Several samples in chapter 5 (sample B and sample E in figure 54) and chapter 6 (Mag/Dop/PSSS in figure 85 and the microwave assisted co-precipitated microwaved Mag/PSSS/Dop/A-9-CA/FA sample in figure 88) were measured at the University of Glasgow using a Panalytical X'Pert. A standard measurement took 2 hours, between 20 to 80^0 2θ. The X-ray wavelength was 1.5408Å using a copper source (40kV, 40 mA).

2.1.2 Selected area electron diffraction (SAED)

SAED is a crystallographic technique similar to XRD that gives information about crystal structure. This technique is incorporated into electron microscopy systems and substitutes X-ray radiation with an electron beam. The wavelength of the electron beam used in TEM measurement is on the same order of magnitude as the interplanar spacing of the crystal causing the crystal lattice to act as a diffraction grating, scattering the beam. This scattering is still bound by Bragg diffraction, with the scattering angles characteristic to the crystal structure. The scattered beam hits a detector, with the signal recorded as a spot. Multiple measurements are taken at various angles to obtain multiple diffraction spots relating to the unit cell of the crystal. Measurements at different angles are not necessarily needed though if the sampling area contains numerous randomly orientated nanocrystals. The resulting pattern is a series of concentric circles made up of these diffraction spots, with each circle indicative of a lattice plane.[5,6] SAED measurements were collected on a FEI Tecnai TF20 instrument fitted with a field emission gun, operated at 200 keV, at the University of Glasgow, by Fraser J. Douglas and Donald MacLaren.

2.1.3 Vibrational spectroscopy

Vibrational spectroscopy is a technique which measures the interaction of chemical bonds with radiation of specific wavelengths. Chemical bonds are capable of absorbing radiation, which will excite the molecule. The nature of the excitation (and which groups are affected) is dependant on the wavelength of light used. Infra-red and visible light causes the bonds within the structure to vibrate. This vibration can be a bending or stretching of the bond which is either symmetrical or anti symmetrical to the molecule as a whole and is specific to that type of bond. This specificity allows chemical bonds to be assigned to these vibrations, multiple vibrations results in a pattern that is unique to a chemical structure. Two vibrational spectroscopy techniques have been employed here: infra-red (IR) spectroscopy and Raman spectroscopy. The two methods are complementary as the measurable vibrations are dictated by selection rules, with one method being able to detect vibrations that the other cannot. IR absorption causes a change of charge separation in polar molecules. Therefore IR light is only absorbed if the molecule has a permanent dipole moment. Raman spectroscopy depends on the polarisability of molecule and relates to how the molecules polarisability can be deformed.

IR spectroscopy measures the absorption of light by the sample. In a standard FTIR measurement, a sample is exposed to a range of IR wavelengths. Some of this light is absorbed by the sample and the remaining light hits the detector and compared with a full reference beam. The wavelengths of the infra-red light that is shone on the sample changes slightly and another measurement is taken. This is repeated and a spectrum is produced containing multiple absorptions. These absorptions can be assigned to chemical bonds which can be used in identifying the composite. The IR instrument used for analysis is the Shimadzu IRAffinity-1. Dried powders were characterised using the golden gate bridge component. All measurements were taken over a range of 400-4000 cm^{-1} with a resolution of 1 cm^{-1} for 256 scans. A background spectrum was taken before every session using the parameters above to eliminate interfering signals from atmospheric H_2O and CO_2.

Raman spectroscopy measurements involve exciting the sample with a laser of a specific wavelength within the visible light range of the electromagnetic spectrum. The sample is excited by the light and releases an inelastic scattered photon of a different energy, either higher (anti-Stokes) in energy, or lower (Stokes) in energy to the excitation wavelength (Rayleigh line). This photon is detected and the difference between the excitation wavelength is characteristic of the vibrational mode that was excited by the light, allowing the peaks to be assigned to a chemical structure. Raman measurements were collected using a Horiba Jobin Yvon LabRAMHR system. The system was calibrated with a silica standard and samples were focuses using 50x objective lens. For sample measurements, a spatula tip of the dried powder was placed on a aluminium tray (aluminium is Raman invisible). All samples were tested with the 35 mW 637 nm (red) laser using a 10% and 25% filter. Acquisition time was 3 seconds with a total of 30 acquisitions for each measurement. An average measurement took 90 seconds and each sample was tested multiple times.

2.1.4 Thermogravimetric analysis (TGA)

TGA can be used to identify and quantify the organic components of the nanocomposite. TGA measurements involve monitoring a samples mass over a range of increasing temperatures. The principal behind TG analysis is that as a multicomponent material is heated, the individual components will degrade and vaporise, decreasing the sample mass. The decomposition temperatures of the components are specific to the material and the individual mass losses of specific components can be identified. This leads to the formation of a multistep TGA profile with each step relating to a specific component of the composite. In addition to identifying the individual component, the mass loss of the steps can be used to quantify how much material is bound to the composite. During a measurement, the sample is heated in a sealed chamber with the internal environment determined by the gas cylinder attached to the machine. Therefore the environment the sample is heated in can be controlled, which can be used to induce transitions such as oxidation during the measurement.[7] Attaching a compressed air cylinder to the machine will cause the sample to oxidise during heating, whereas if a oxygen free gas is used (i.e. nitrogen or argon), the oxidation of the sample can be limited. High temperature transitions such as oxidation occur over a specific temperature range and can cause the sample to change in mass, which will be reflected as a mass gain/loss in the TGA profile. This change can then be cross referenced with similar TGA profiles in the literature and can give an indication on the transformation of the material when heated in certain atmospheres. TGA measurements were done on a Netsch STA 409 PC Luxx. All measurements were performed in an air environment unless specified otherwise. 25 mg of the dried powder was heated in a alumina crucible to 700°C with a ramp of 3 °C/min.

2.1.5 Nuclear magnetic resonance (NMR) spectroscopy

NMR spectroscopy can be used to identify the chemical structure of the organic stabiliser materials and to confirm the formation of coupling bonds (i.e. amide bonds). ^{1}H NMR spectroscopy measures the magnetic moment of protons in a sample. The magnetic moment generated by a proton is very small but in a sample there is a very large amount of protons, causing the small magnetic spins to generate a significant net signal which can be measured. In a measurement, the spins are aligned with an external field and a radio pulse is used to excite/knock the signals off the applied axis. The spins will then realign to this applied field and this relaxation process is measured. The resulting signal can then be interpreted and assigned to a chemical structure, based on the chemical shifting of the peaks. NMR data was collected using a JEOL ECS spectrometer (400 MHz). Single pulse ^{1}H NMR data at 25°C was collected of the samples. All samples were dissolved in D_2O solvent, with TMS used as a reference peak. Data were collected and analysed using the Jeol Delta software package

2.1.6 Transmission electron microscopy (TEM)

Electron microscopy can be employed to identify and measure particle morphology and size. TEM is ideal for nanoparticle analysis as image resolution is high enough to allow crystallite size and morphology measurements. TEM images are obtained by firing an electron beam through a sample. The beam passes through thin areas of the sample while the dense areas absorb more of the beam. The electrons that pass through then hit a detector creating an image, with the areas that absorbed the beam generating contrast. As such the prepared samples need to be thin enough to allow passage of the electrons and of low concentrations so clustering does not obscure the particles. The samples were measured on a JEOL JEM (200-fx) at 120 kV. Dry samples were dispersed in ethanol and sonicated for 15 minutes. A drop of the solution was then transferred onto a carbon coated copper grid, covered and left to dry overnight for analysis. For water based samples, 100 μL was dispersed in 3 mL millipore water. A drop of this solution was placed on a carbon coated copper grid, covered and left to dry overnight. Samples exposed to a magnetic field were prepared in the same way but was left to dry over a 2 T magnetic block overnight. Images were taken at 100x, 200x and 40000x magnification. Particle sizing was done using the ImageJ software and for every sample 100 particles were measured to calculate an average size and standard deviation. High resolution TEM were performed on a FEI Tecnai TF20 instrument fitted with a field emission gun, operated at 200 keV at the University of Glasgow, by Fraser J. Douglas and Donald MacLaren. HR-TEM samples were prepared by dispersing the sample in deionised water and dropping the solution onto an amorphous holey carbon coated grid.

2.1.7 Dynamic light scattering (DLS)

DLS measures the hydrodynamic radius and clustering of particles in solution. Knowledge of cluster size and the size distribution profiles can infer water stability and determine the particles suitability for biomedical applications. DLS measurements work by tracking the movement and speed of particles in solution using a laser. In solution the particles undergo Brownian motion (the random movement of particles due to the interaction of other particles). A DLS measurement takes multiple scans of the sample in quick succession and compares the images to track the movement and speed of the particles in solution. The Stokes-Einstein equation defines the relationship between particle size and speed, with smaller particles moving faster than larger particles.

$$D = \frac{k_B T}{6\pi\eta r} \tag{4}$$

where D is the diffusion constant, k_B is the Boltzmann constant, T is temperature, η is the dynamic viscosity and r is radius of the particles. Using this equation it can be calculated that larger particles have lower diffusion coefficients, resulting in slower movement in solution. DLS utilises this principle by measuring the movement and speed of particles throughout a series of measurements. If there has been large particle movement between the scans, this indicates fast unimpeded movement (due to high diffusion coefficients) and that the particles are quite small. The reverse is true with larger particles, with little movement indicating a small diffusion coefficient. The detection of this particle movement is done through the scattering of light by the particles in solution. In a measurement a laser is shone into the solute and suspended particles will deflect this light into a detector. This is recorded as a light spot in an image. For a suspension, there will be a large amount of scattering resulting in a speckle pattern consisting of light and dark spots. Multiple patterns are collected and compared. If there is correlation between the patterns, large particle sizes can be inferred from this. Inversely if there is little correlation between the patterns, then significant particle movement must be causing this variation suggesting smaller particle sizes. Algorithms are then applied to the correlation between the signals to calculate the size distribution.

The DLS instrument used for analysis was a Zeta sizer nano series (Nano-ZS) manufactured by Malvern Instruments. All samples were tested in disposable low volume plastic cuvettes (1 mL) at 25°C. A single measurement consists of between 12-20 scans (which was determined by the software). Each measurement was repeated 3 times and averages were calculated from the results. Samples were measured repeatedly over several months to determine the effect of time on water stability and the hydrodynamic radius of the sample. All measurements passed software quality checks, unless noted otherwise.

2.1.8 Zeta potentials

Zeta potential measurements can be used to additionally confirm particle water stability. Zeta potentials are a measure of a particles surface charge which can provide information on clustering. When dispersed in solution, the particles are either positively or negatively charged ions. The particles attract solvent ions of opposite charge, leading to the formation of an electrical double layer (Figure 16). Solvent ions that are close to the surface are strongly bound to the particle forming the inner Stern layer, while solvent ions further away are only loosely bound. Loosely bound ions in this area form the second outer layer, called the diffuse layer. Ions within this diffuse layer will still move with the particle in the solution, but ions at a distance beyond this layer are unaffected by the particles' charge. The boundary to the diffuse layer and beyond is known as the slipping plane and the potential that exists at the slipping plane is the zeta potential of the particle. This is a measure of the potential difference between the particles diffuse layer and the dispersion medium, with the potential varying depending on the distance between the slipping plane and the particle surface. A particle with a high surface charge will have a greater effect on solvent ions in solution, resulting in a larger slipping plane and therefore increasing the zeta potential. If this zeta potential is a high value, the particles in solution will tend to repel each other and not cluster and flocculate. If the zeta potential is low, then there is not this repulsion force, that will stop clustering. The dividing line where the zeta potential is large enough to repel neighbouring particles is accepted at above +30 mV or below -30 mV.[8]

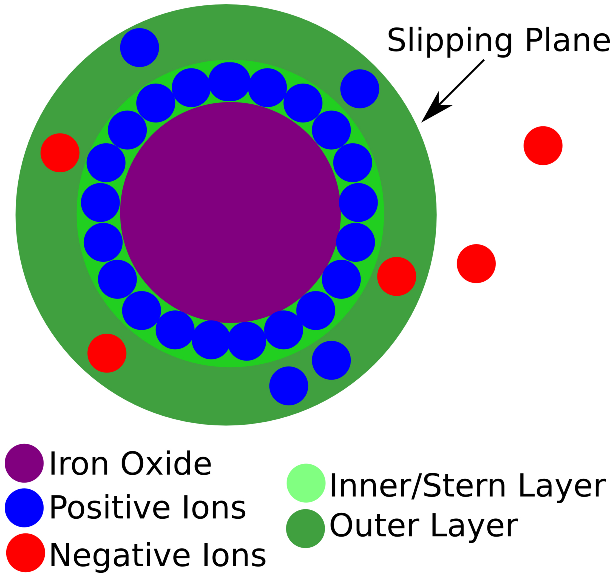

Figure 16: When dispersed in solution, an electrical double layer forms around the particle. For a negatively charged iron oxide nanoparticles, initially a strongly bound positively charged solvent layer forms on the particle surface. This charge then attracts oppositely charged solvent ions to form a weakly bound outer layer, and an overall electrical double layer. Beyond this double layer, the charged solvent ions are not attracted to the iron oxide. The boundary between the outer layer and beyond is known as the slipping plane. The potential of the slipping plane is the zeta potential of the particle.

A particles zeta potential is measured using electrophoresis. A specialist zeta cell containing two electrodes is filled with the tested suspension. A electrical current is passed through the cell, causing the charged particles to move to the opposite electrode. The movements of the particles are measured with a laser. Particles with a greater zeta potential move faster than the particles with a lower zeta potential. Zeta potentials were measured on a zeta sizer nano series (Nano-ZS) manufactured by Malvern Instruments. Samples were tested in a disposable folded capillary zeta cell. Each measurement consisted of 12 runs and 3 measurements for each sample with averages being calculated from these measurements.

2.1.9 Biological cell testing

Toxicity studies were undertaken at the School of Biosciences at the University of Kent and performed on UKF-NB-3 neuroblastoma cells, primary human retinal pigment epithelial cells (RPE) and Primary human fibroblasts (HFF). Measurements were taken by James D. Budge, Lara C. Sanders, Martin Michaelis and Mark Smales. Dispersions were incubated with these cells with increasing concentration for one week. The aim was to ensure that the nanocomposite base was non toxic and biocompatible with a wide range of cells. An MTT dye assay was then used to determine the cell viability after one week. UKF-NB-3 cells were cultivated in IMDM supplemented with 10% foetal calf serum (FCS), 100 IU/mL penicillin, and 100 mg/mL streptomycin. Retinal pigment epithelial cells were cultured in DMEM supplemented with 20% FCS, 100 IU/mL penicillin, and 100 mg/mL streptomycin. Fibroblasts were cultured in DMEM supplemented with 10% FCS, 100 IU/mL penicillin, and 100 mg/mL streptomycin. All cells were cultivated at 37°C in humidified 5% CO_2.[9,10] Cell viability upon the addition of nanoparticle preparations at different concentrations was determined by the 3-(4,5-dimethylthiazol-2-yl)-2,5-diphenyltetrazolium bromide (MTT) dye reduction assay after 120 h of incubation.[9,10]

2.1.10 Magnetic property measurements

The magnetic properties of the nanocomposites were determined using a Superconducting QUantum Interference Device (SQUID). SQUIDs are capable of detecting very small changes in magnetisation values while being able to work in a range of external magnetic fields at a variety of temperatures. This allows the accurate assessment of the nanoparticles magnetic properties in a variety of external conditions. A SQUID magnetometer works on the principle of a Josephson junction to detect the changes in magnetisation. The Josephson effect is a supercurrent, a current that flows indefinitely without the addition of a voltage. The Josephson junction is constructed from two superconductors separated by a thin layer. In a SQUID measurement, the sample is passed through the coils containing the supercurrent, under an applied magnetic field. The magnetic flux of the tested sample will affect this supercurrent. A change in magnetic flux of the sample causes a proportional change in the current of the superconducting loop. The voltage of the current is monitored which allows changes in magnetisation to be equated to changes in voltage. Under standard conditions the current is split equally between the system. With the addition of the samples magnetic field, this current will begin to favour one side of the system and starts to split causing different voltage readings throughout the system. This change of voltage is recorded with a sensitive detector, allowing SQUIDs to detect very small changes in magnetisation. SQUID measurements were taken at the University of Glasgow and at the University of California, Santa Barbara on a Quantum Design SQUID magnetometer by Serena A. Corr, Oonagh M. Collins and Edmund J. Cussen. Samples were immobilised within wax to stop particle agitation during measurements. Measurements involved several cycles collecting data between 20 x 10^3 G to -20 x 10^3 G. All samples were tested at both 300 K and 10 K, to observe magnetic properties.

2.1.11 Atomic absorption spectroscopy (AAS)

AAS determines the elemental composition and concentrations of metal ions in a composite. AAS can be used to calculate the iron concentrations of dispersions, which can then be used alongside MRI testing to calculate relaxivity values for the dispersions. AAS works on calculating the absorption of light by vaporised metals and correlating this to the Beer-Lambert law so a concentration can be calculated. The sample is prepared by dissolving completely in acid and then vaporised using a flame atomiser, freeing the metal ions. Now in the gas state, the metal ions can be excited by light. Excitation of the particles is due to the absorption of light with a wavelength specific to the metal that is being excited (for example, for iron detection a lamp with a wavelength of 302.1 nm is needed). The AAS used was an AAnalyst 800 manufactured by Perkin Elmer. For all samples a calibration curve made up of five iron standards (ranging from 1-10 ppm) with concentrations and absorptions calculated before the measurement. AAS samples were made from the final washings of the samples with 5 drops of HCl added to 1 mL of the washing. The sample was then heated and evaporated to form a concentrated liquid. Millipore water was then added to the sample and evaporated off another 3 times. The final concentrated liquid was then diluted with millipore water (25 mL) and transferred into a volumetric flask for later use. Iron samples were tested with the 302.1 nm wavelength lamp with a slit width of 0.2 nm.

2.1.12 MRI measurements

MRI measurements allow for determination of relaxivities of the magnetic nanocomposites to evaluate their efficacy as contrast agents. MR imaging was performed at Kings College London by Jindrich Cinatl Jr., Dirk Krueger and Rafael T. M. de Rosales with a standard extremity flex coil on a clinical 3T MRI scanner (Achieva, Philips Healthcare, Best, The Netherlands). T_2 was determined with a 2D multi-spin-echo sequence. The acquired imaging data was transferred to a computer running Matlab and analysed using an in-house Matlab tool to obtain the relaxation time, T_2, for each Fe concentration. Excel was used to plot the relaxation rate, R_2, over the concentration and the relaxivity value was determined using linear regression.

2.1.13 UV-Vis and fluorescence spectroscopy

UV-Vis spectroscopy measures the excitation of electrons by the absorption of light, whereas fluorimetry detects the emission of energy as photons by the excited electrons returning back to the ground state. Materials that are conjugated contain π or non bonding electrons which can absorb ultra-violet to visible light. When exposed to this light, the electrons absorb this energy and become excited, promoting them to higher orbitals. This is the transition from the highest occupied molecular orbital (HOMO) to the lowest unoccupied molecular orbital (LUMO). The wavelength required for this transition relates to the energy gap between the HOMO and LUMO states, with a larger gap requiring longer wavelengths to excite. The electrons cannot maintain this excited state and will decay back down to a ground state, releasing this energy in a variety of processes, which is measured by fluorescence spectroscopy. UV-Vis spectroscopy looks at the transition of the electron from the ground state to the excited state. The absorbance of light by a sample is dictated by the Beer lambert law (which is related to the concentration of fluorescent groups within the sample), which outlines the selection rules to determine which electronic transitions are allowed and which are forbidden. A scanning monochromator allows specific wavelengths to be used, allowing a measurement to cycle through a range of wavelengths. As absorption follows the Beer-Lambert law, samples must be diluted before measurement as the law only works with low concentrations of samples (below an absorbance of 1). Additionally, scattering of light by inorganic groups can affect UV-Vis measurements, limiting its application with nanocomposites containing inorganic cores.[11,12] All UV-Vis measurements were performed on a UNIcam UV-500 containing a deuterium (200-400 nm) and tungsten lamp (300-700 nm) with lamp change at 325 nm. All samples were measured in a low volume glass cuvette (1 mL) and the system was dual beam requiring a second matching cuvette filled with a standard/blank to be in at all times. Measurements were taken between 200-600 nm, with a resolution of 4 nm and a normal scan speed. All samples were tested in (or diluted with) millipore water unless stated otherwise.

Fluorometry was used to observed the energy release from the transition of excited electrons back to the ground state. Fluorescence is the release of this excited energy as a photon and can be measured using a fluorimeter. The wavelength emitted through this energy release is specific to the fluorophore that is used, allowing fluorimetry to be used as an identification technique confirming the binding of fluorescent groups. This technique can also measure any quenching effects from attaching fluorescent groups to the magnetic nanocomposites. Quenching can occur with magnetic materials and can reduce the fluorescence of materials which is undesirable. The unpaired electrons in the magnetic core provide an alternative pathway for the excitation energy to dissipate into. This reduces energy that can be released by the fluorophore as a photon reducing the overall fluorescence. Weak fluorescence can limit the materials use in biological applications such as confocal imaging, but this effect can be limited through the careful use of spacers to separate the magnetic component from the fluorescent component. Two types of measurements can be taken with a fluorimeter, an excitation scan and a emission scan. An emission scan maps the emission of photons from fluorophores by exciting the sample at a specific wavelength. Using the absorption maxima obtained from UV-Vis spectroscopy, the sample is excited at a specific wavelength and detectors within the fluorimeter track the emission of the sample, to determine the optimal emission wavelength. The other type of scan is an excitation spectrum and is the opposite to an emission spectrum. With this the detection wavelength is kept constant (the emission wavelength) and the excitation wavelengths are cycled to measure the absorption of the sample. As such an excitation spectrum can be similar to a UV-Vis absorption spectrum. Excitation measurements are also unaffected by light scattering from the inorganic cores, allowing for excitation measurements for materials with inorganic cores.[12] All measurements were performed on a FluoroMax-2 manufactured by Jobin YVON SPEX Instruments S.A. The dispersions collected from the composites were tested in a clear 4 sided quartz curvette. Emission and excitation spectra were obtained for all samples, 20 measurements were taken for each spectrum with the results averaged out. Excitation and emission slit widths were set to 2 nm.

2.1.14 Confocal imaging

Confocal microscopy allows for the imaging of fluorescent materials. Traditionally fluorescent microscopy methods involves exciting the entire sample with a low wavelength light and then detecting the higher wavelength emission. Confocal imaging follows the same principle but differs in two different ways. Instead of flooding the entire sample with light (which can interfere with measurements), the sample is instead excited by a single beam of light, which limits the unwanted excitation and emission of neighbouring areas. Confocal imaging also uses a spatial pinhole over the detector to limit the background light from hitting the detector. The aim is to limit fluorescence of the sample in areas out of focus of the microscope as these will adversely effect the image. This results in improved resolution and contrast of the image, but the point excitation method can only measure a small area requiring scanning of the image. Confocal measurements were taken at the University of Kent by James D. Budge, Lara C. Sanders, Martin Michaelis and Mark Smales to monitor the uptake of fluorescent nanoparticles into UKF-NB-3 neuroblastoma cells. Multiple images at varying depths were taken to confirm particle distribution throughout the cell. UKF-NB3 cells were seeded at 2 x 10^5 cells/well in a 24 well plate, containing a coverslip in each well, and grown at 37°C for 48 hours. Rhodamine conjugated nanoparticles were diluted to 0.099 mg/L iron concentration in media, 1 mL added to appropriate wells and incubated for 3 hours before aspirating and fixing with methanol at -20°C for 5 minutes. Coverslips were mounted using mowiol and anti-fade and slides examined using a Leica confocal laser scanning (TCS 4; x 63 oil lens) microscope.

2.2 Materials and equipment

Hydrochloric acid, potassium dihydrogen phosphate, dipotassium hydrogen phosphate and sodium chloride were acquired from Fisher Scientific. All other chemicals were obtained from Sigma Aldrich. All water used was millipore water, obtained from a Barnstead easy pure II machine by Thermo Scientific. The microwave synthesiser used was a CEM Discover SP. The centrifuge used was a Sanyo Centaur 2 MSE. Air sensitive reactions were performed using a Schlenk line, using N_2 gas to provide the inert atmosphere. Toxic or air sensitive materials were prepared in a glove box and stored in sealed Schlenk tubes. The glove box used is an MBraun Labstar. Powders were stored in glass vials filled with nitrogen before and after the addition of the powder. Water washings were stored in 50 mL centrifuge tubes.

2.3 Synthetic procedures for chapter 3

2.3.1 Deoxygenated water

Millipore water (100 mL) was heated to boiling in a round bottom flask using a heating mantle. The sample was then taken off the heat and left to cool naturally for over 3 hours with nitrogen gas bubbled into the water at a slow but constant rate. Once cooled, the nitrogen flow was stopped and the flask was sealed with parafilm. The water was used within 3 days after preparation.

2.3.2 Microwave heating water reactions

Deoxygenated water (22.5 mL) was transferred into a microwave vessel (30 mL) with magnetic fleas and sealed using a plastic cap. The system was then programmed to heat the sample to 150°C with the power set to 10 W. The sample was given 20 minutes ramping time, 5 minutes reaction time and then cooled naturally (with none of the samples taking longer than 40 minutes to cool). The measurement was repeated with the power increasing by 10 W increments, with the final measurement heating at 150 W. 15 measurements were taken in total.

2.3.3 Microwave assisted synthesis of magnetite nanoparticles

Iron (III) chloride hexahydrate (2.700 g, 10 mmol) and iron (II) chloride tetrahydrate (0.990 g, 5 mmol) were dissolved in deoxygenated water (12.5 mL) and stirred for 15 minutes. An orange solution formed. The solution was heated to 80°C in an oil bath. Ammonium hydroxide (10 mL, 28-30%) was injected into the heated solution forming a jet black precipitate. The solution was stirred for 20 minutes. The suspension was transferred into a microwave tube (30 mL) and sealed with a rubber cap. The tube was heated by microwave radiation to 150°C at 100 W for 20 minutes (including an additional 10 minutes allocated by the instrument for temperature ramping). Once cooled the sample was washed by magnetic decantation with millipore water (30 mL x 5) and ethanol (20 mL). The black powder was stored in a glass vial and the washings were discarded.

2.3.4 Microwave assisted synthesis of cobalt ferrite nanoparticles

Cobalt (II) nitrate hexahydrate (1.4582 g, 5 mmol) and iron (II) chloride tetrahydrate (1.981 g, 10 mmol) were weighed out in a glove box. Cobalt (II) nitrate hexahydrate is toxic, therefore these materials were weighed out in a glove box to minimise particle exposure. These were then dissolved in deoxygenated water (12.5 mL) and stirred for 15 minutes. An wine red solution formed. The solution was heated to 80°C in an oil bath. Ammonium hydroxide (10 mL, 28-30%) was injected into the heated solution forming a jet black precipitate. The solution was stirred for 20 minutes. The suspension was taken out of the oil bath and left to cool for 10 minutes. The suspension was then transferred into a microwave tube (30 mL) and sealed with a rubber cap. The tube was heated by microwave radiation to 150°C at 100 W for 20 minutes (including an additional 10 minutes allocated by the instrument for temperature ramping). Once cooled the sample was washed by magnetic decantation with millipore water (30 mL x 5) and ethanol (20 mL). The black powder was stored in a glass vial and the washings were discarded.

2.3.5 Microwave assisted synthesis of copper ferrite nanoparticles

Copper (II) chloride dihydrate (0.851 g, 5 mmol) and iron (II) chloride tetrahydrate (1.985 g, 10 mmol) were dissolved in deoxygenated water (12.5 mL) and stirred for 15 minutes. A lime green solution formed. The solution was heated to 80°C in an oil bath. Ammonium hydroxide (10 mL, 28-30%) was injected into the heated solution forming a dark black precipitate. The solution was stirred for 20 minutes. The suspension was taken out of the oil bath and left to cool for 10 minutes. The suspension was then transferred into a microwave tube (30 mL) and sealed with a rubber cap. The tube was heated by microwave radiation to 150°C at 100 W for 20 minutes (including an additional 10 minutes allocated by the instrument for temperature ramping). Once cooled the sample was washed by magnetic decantation with millipore water (30 mL x 5) and ethanol (20 mL). The black powder was stored in a glass vial and the washings were discarded.

2.3.6 Microwave assisted synthesis of manganese ferrite nanoparticles

Manganese (II) chloride tetrahydrate (0.989 g, 5 mmol) and iron (III) chloride hexahydrate (2.701 g, 10 mmol) were dissolved in deoxygenated water (12.5 mL) and stirred for 15 minutes. An dark orange solution formed. The solution was heated to 80°C in an oil bath. Ammonium hydroxide (10 mL, 28-

30%) was injected into the heated solution forming a black precipitate. The solution was stirred for 20 minutes. The suspension was taken out of the oil bath and left to cool for 10 minutes. The suspension was then transferred into a microwave tube (30 mL) and sealed with a rubber cap. The tube was heated by microwave radiation to 150°C at 100W for 20 minutes (including an additional 10 minutes allocated by the instrument for temperature ramping). Once cooled the sample was washed by magnetic decantation with millipore water (30 mL x 5) and ethanol (20 mL). The black powder was stored in a glass vial and the washings were discarded.

2.3.7 One pot microwave assisted synthesis of iron oxide nanoparticles

Urea (0.719 g, mmol) was dissolved in deoxygenated water (12.5 mL) and and stirred for 15 minutes. Iron (III) chloride hexahydrate (2.700 g, 10 mmol) and iron (II) chloride tetrahydrate (0.990 g, 5 mmol) were then dissolved in the urea solution. An orange solution formed. The solution was transferred into a microwave tube (30 mL) and sealed with a rubber cap. The tube was heated by microwave radiation to 150°C at 100W for 20 minutes (including 10 minutes for temperature ramping). Once cooled a brick red precipitate formed. The sample was washed by magnetic decantation with millipore water (30 mL x 5) and ethanol (20 mL). The red powder was stored in a glass vial and the washings were discarded.

2.4 Synthetic procedures for chapter 4

2.4.1 Microwave assisted synthesis of magnetite nanoparticles stabilised with poly(sodium 4-styrenesulfonate)

Iron (III) chloride hexahydrate (2.700 g, 10 mmol) and iron (II) chloride tetrahydrate (0.990 g, 5 mmol) were dissolved in deoxygenated water (12.5 mL) and stirred for 15 minutes. An orange solution formed. Poly(sodium-4-styrenesulfonate) (0.1 g, 1.4μmol, 70,000 Mwt) was then added to the iron chloride solution. The solution was heated to 80°C in an oil bath. Ammonium hydroxide (10 mL, 28-30%) was injected into the heated solution forming a jet black precipitate. The solution was stirred for 20 minutes. The suspension was taken out of the oil bath and left to cool for 10 minutes. The suspension was then transferred into a microwave tube (30 mL) and sealed with a rubber cap. The tube was heated by microwave radiation to 150°C at 100W for 20 minutes (including an additional 10 minutes allocated by the instrument for temperature ramping). Once cooled the sample was washed by magnetic decantation with millipore water (30 mL x 5) and ethanol (20 mL). After the second water washing a stable suspension formed. The black powder was stored in a glass vial and the third, forth and fifth washing was stored in a centrifuge tube and kept stationary. The other washings were discarded.

2.4.2 Microwave assisted synthesis of magnetite nanoparticles stabilised with sodium polyphosphate

Iron (III) chloride hexahydrate (2.700 g, 10 mmol) and iron (II) chloride tetrahydrate (0.990 g, 5 mmol) were dissolved in deoxygenated water (12.5 mL) and stirred for 15 minutes. An orange solution formed. Sodium polyphosphate (0.1 g, 1 μmol, 100,000 Mwt) was then added to the iron chloride solution. The solution was heated to 80°C in an oil bath. Ammonium hydroxide (10 mL, 28-30%) was injected into the heated solution forming a jet black precipitate. The solution was stirred for 20 minutes. The suspension was taken out of the oil bath and left to cool for 10 minutes. The suspension was then transferred into a microwave tube (30 mL) and sealed with a rubber cap. The tube was heated by microwave radiation to 150°C at 100W for 20 minutes (including an additional 10 minutes allocated by the instrument for temperature ramping). Once cooled the sample was washed by magnetic decantation with millipore water (30 mL x 5) and ethanol (20 mL). After the second water washing a stable suspension formed. The black powder was stored in a glass vial and the third, forth and fifth washing was stored in a centrifuge tube and kept stationary. The other washings were discarded.

2.4.3 Microwave assisted synthesis of Fe_3O_4/poly(sodium 4-styrenesulfonate) nanoparticles functionalised with Rhodamine B

Iron (III) chloride hexahydrate (2.700 g, 10 mmol) and iron (II) chloride tetrahydrate (0.990 g, 5 mmol) were dissolved in deoxygenated water (12.5 mL) and stirred for 15 minutes. An orange solution formed. Poly(sodium-4-styrenesulfonate) (0.1 g, 1.4 μmol, 70,000 Mwt) was then added to the iron chloride solution. The solution was heated to 80°C in an oil bath. Ammonium hydroxide (10 mL, 28-30%) was injected into the heated solution forming a jet black precipitate. The solution was stirred for 20 minutes. The suspension was taken out of the oil bath and left to cool for 10 minutes. The suspension was then transferred into a microwave tube (30 mL) and sealed with a rubber cap. The tube was heated by microwave radiation to 150°C at 100W for 20 minutes (including an additional 10 minutes allocated by the instrument for temperature ramping). Once cooled the sample was washed by magnetic decantation with millipore water (30 mL x 2) and redispersed into millipore water (30 mL). Rhodamine B (0.005 g, 0.01 mmol) was dissolved in millipore water (10 mL) and then added to the iron oxide solution. This was left to stir for 1 hour. The solution was drained and then washed by magnetic decantation with millipore water (30 mL x 5) and ethanol (20 mL). A water stable suspension formed immediately. The black powder was stored in a glass vial and the third, forth and fifth washing were stored in a centrifuge tube and kept stationary. The other washings were discarded.

2.5 Synthetic procedures for chapter 5

2.5.1 Microwave assisted synthesis of magnetite nanoparticles stabilised with poly(acrylic acid)

Iron (III) chloride hexahydrate (2.700 g, 10 mmol) and iron (II) chloride tetrahydrate (0.990 g, 5 mmol) were dissolved in deoxygenated water (12.5 mL) and stirred for 15 minutes. An orange solution formed. Poly(acrylic acid) (0.1 g) was then added to the iron chloride solution. Three different stabilisers were tested:

Table 3: The PAA polyelectrolyte sizes and classifications used to stabilise iron oxide particles in chapter 5

Polyelectrolyte name	Polyelectrolyte Mwt	Sample name
V. Low Mwt	1,800	Sample A
High Mwt	400,000-500,000	Sample B
V. High Mwt	1,250,000	Sample C

The solution was heated to 80°C in an oil bath. Ammonium hydroxide (10 mL, 28-30%) was injected into the heated solution forming a jet black precipitate. The solution was stirred for 20 minutes. The suspension was taken out of the oil bath and left to cool for 10 minutes. The suspension was then transferred into a microwave tube (30 mL) and sealed with a rubber cap. The tube was heated by microwave radiation to 150°C at 100W for 20 minutes (including an additional 10 minutes allocated by the instrument for temperature ramping). Once cooled the sample was washed by magnetic decantation with millipore water (30 mL x 5) and ethanol (20 mL). After the second water washing a stable suspension formed. The black powder was stored in a glass vial and the third, forth and fifth washing were stored in a centrifuge tube and kept stationary. The other washings were discarded.

2.5.2 Microwave assisted synthesis of magnetite nanoparticles stabilised with poly(diallyldimethylammonium chloride)

Iron (III) chloride hexahydrate (2.700 g, 10 mmol) and iron (II) chloride tetrahydrate (0.990 g, 5 mmol) were dissolved in deoxygenated water (12.5 mL) and stirred for 15 minutes. An orange solution formed. Poly(diallyldimethylammonium chloride) (0.1 g) was then added to the iron chloride solution. Three different stabilisers were tested:

Table 4: The pDADMAC polyelectrolyte sizes and classifications used to stabilise iron oxide particles in chapter 5

Polyelectrolyte name	**Polyelectrolyte Mwt**	**Sample name**
Low Mwt	<100,000	Sample D
Medium Mwt	100,000-200,000	Sample E
High Mwt	400,000-500,000	Sample F

The solution was heated to 80°C in an oil bath. Ammonium hydroxide (10 mL, 28-30%) was injected into the heated solution forming a jet black precipitate. The solution was stirred for 20 minutes. The suspension was taken out of the oil bath and left to cool for 10 minutes. The suspension was then transferred into a microwave tube (30 mL) and sealed with a rubber cap. The tube was heated by microwave radiation to 150°C at 100W for 20 minutes (including an additional 10 minutes allocated by the instrument for temperature ramping). Once cooled the sample was washed by magnetic decantation with millipore water (30 mL x 5) and ethanol (20 mL). After the second water washing a stable suspension formed. The black powder was stored in a glass vial and the third, forth and fifth washing were stored in a centrifuge tube and kept stationary. The other washings were discarded.

2.6 Synthetic procedures for chapter 6

2.6.1 Phosphate buffer solution

Potassium dihydrogen phosphate (0.023 g, 0.169 mmol), dipotassium hydrogen phosphate (0.023 g, 0.132 mmol) and sodium chloride (0.876 g, 14.9 mmol) was dissolved in millipore water (100 ml).

2.6.2 EDCI coupling of dopamine to poly(acrylic acid) using organic solvents

1-Ethyl-3-(3-dimethylaminopropyl)carbodiimide (EDCI) (0.321 g, 1.67 mmol) was dissolved in dimethylformamide (10 mL) and triethylamine (18 mL). A cloudy white suspension formed. The solution was cooled in an ice bath.

Poly(acrylic acid) (0.973 g, 0.54 mmol, 1800 Mwt) was added to the solution. This solution was heated to 80°C and took 20 minutes to fully dissolve. In a separate container, dopamine hydrochloride (0.473 g, 2.5 mmol) was dissolved in dimethylformamide (10 mL) and triethylamine (18 mL). This was stirred for 30 minutes and then N-hydroxysuccinimide (0.037 g, 0.32 mmol) was added. The solutions were mixed and left to heat at 80°C for 5 days.The solution changed to a dark red colour after 24 hours. This colour lightened after 48 hours and a dark brown sludge formed. After 5 days, the solution was evaporated using a rotary evaporator leaving behind a viscous dark brown liquid. This was stored in a glass vial under nitrogen

2.6.3 EDCI coupling of dopamine to poly(acrylic acid) using water

Poly(acrylic acid) (0.218 g, 0.12 mmol, 1800 Mwt) and 1-Ethyl-3-(3-dimethylaminopropyl) carbodiimide (EDCI) (0.173 g, 0.9 mmol) were dissolved in phosphate buffer solution (30 mL). Dopamine hydrochloride (0.171 g, 0.9 mmol) was then added to form a cloudy white solution. The pH of the solution was 6 and needed no further adjustment. The solution was stirred for 48 hours. The solution was then purified with dialysis and the excess solvent was evaporated to leave a white powder.

2.6.4 Co-precipitation of Fe_3O_4 nanoparticles stabilised with dopamine

Iron (III) chloride hexahydrate (2.700 g, 10 mmol) and iron (II) chloride tetrahydrate (0.990 g, 5 mmol) were dissolved in deoxygenated water (12.5 mL) and stirred for 15 minutes. An orange solution formed. Dopamine hydrochloride (0.100 g, 0.52 mmol) was then added to the iron chloride solution. The solution then changed to a dark green colour. The solution was heated to 80°C in an oil bath. Ammonium hydroxide (10 mL, 28-30%) was injected into the heated solution forming a jet black precipitate. The solution was stirred for 20 minutes. Once cooled the sample was washed by magnetic decantation with millipore water (30 mL x 5) and ethanol (20 mL). After the second water washing a stable suspension formed. The black powder was stored in a glass vial and the third, forth and fifth washing were stored in a centrifuge tube and kept stationary.

The other washings were discarded.

2.6.5 Co-precipitation of Fe_3O_4 nanoparticles stabilised with a dopamine/poly (acrylic acid) composite prepared in organic solvents

Iron (III) chloride hexahydrate (2.700 g, 10 mmol) and iron (II) chloride tetrahydrate (0.990 g, 5 mmol) were dissolved in deoxygenated water (12.5 mL) and stirred for 15 minutes. An orange solution formed. The dopamine/poly(acrylic acid) composite (0.100 g, 1,800 Mwt PAA) was then added to the iron chloride solution. A brown precipitate appeared to form with the addition of the stabiliser. The solution was heated to 80°C in an oil bath. Ammonium hydroxide (10 mL, 28-30%) was injected into the heated solution forming a jet black precipitate. The solution was stirred for 20 minutes. Once cooled the sample was washed by magnetic decantation with millipore water (30 mL x 5) and ethanol (20 mL). After the second water washing a stable suspension formed. The black powder was stored in a glass vial and the third, forth and fifth washing were stored in a centrifuge tube and kept stationary. The other washings were discarded.

2.6.6 Co-precipitation of Fe_3O_4 nanoparticles stabilised with a dopamine/poly (acrylic acid) composite prepared in water

Iron (III) chloride hexahydrate (2.700 g, 10 mmol) and iron (II) chloride tetrahydrate (0.990 g, 5 mmol) were dissolved in deoxygenated water (12.5 mL) and stirred for 15 minutes. An orange solution formed. The dopamine/poly(acrylic acid) composite (0.100 g, 1,800 Mwt PAA) was then added to the iron chloride solution. The solution then changed to a dark green colour. The solution was heated to 80°C in an oil bath. Ammonium hydroxide (10 mL, 28-30%) was injected into the heated solution forming a jet black precipitate. The solution was stirred for 20 minutes. Once cooled the sample was washed by magnetic decantation with millipore water (30 mL x 5) and ethanol (20 mL). After the second water washing a stable suspension formed. The black powder was stored in a glass vial and the third, forth and fifth washing were stored in a centrifuge tube and kept stationary. The other washings were discarded.

2.6.7 Co-precipitation of Fe_3O_4 nanoparticles stabilised with dopamine/acridine-9-carboxylic acid composite

Iron (III) chloride hexahydrate (2.700 g, 10 mmol) and iron (II) chloride tetrahydrate (0.990 g, 5 mmol) were dissolved in deoxygenated water (12.5 mL) and stirred for 15 minutes. An orange solution formed. Dopamine hydrochloride (0.100 g, 0.52 mmol) was then added to the iron chloride solution. The solution then changed to a dark green. The solution was heated to 80°C in an oil bath. Ammonium hydroxide (10 mL, 28-30%) was injected into the heated solution forming a jet black precipitate. The solution was stirred for 20 minutes. Once cooled the sample was washed by magnetic decantation with millipore water (30 mL x 2) until the solution was pH 7. In a separate round bottom flask acridine-9-carboxylic acid (0.015 g, 0.06 mmol) was dissolved in phosphate buffer (30 mL). 1-Ethyl-3-(3-dimethylaminopropyl)carbodiimide (EDCI) (0.173 g, 0.9 mmol) was then added to the solution. This solution was then added to the iron oxide suspension and was left to stir for 24 hours in the dark. The solution was then drained and the precipitate was washed with millipore water (30 mL x 5) and ethanol (20 mL). A stable suspension formed with the first water washing. The black powder was stored in a glass vial and all washings were collected and stored in a centrifuge tubes. A second sample was prepared where the sample was washed with phosphate buffer solution after the conjugation of acridine-9-carboxylic acid. All 5 phosphate buffer washings were collected and stored.

2.6.8 Acridine-9-carboxylic acid standard

Acridine-9-carboxylic acid was dissolved in millipore water (0.010 g, 0.044 mmol). 5 drops of hydrochloric acid was added to the solution to help dissolve the solid.

2.6.9 Preparation of folic acid/N-hydroxysuccinimide composite via an carbodiimide coupling reaction

Folic acid (2.0 g, 4.5 mmol) was dissolved in dry dimethylformamide (75 mL). N,N'-Dicyclohexylcarbodiimide (0.62 g, 3 mmol) and N-hydroxysuccinimide (0.51 g, 4.4 mmol) were then dissolved in the solution and left to stir for 24 hours in the dark. A viscous yellow solution formed. This was then filtered using a Buchner funnel to leave a clear yellow solution. This was then precipitated in diethyl ether to form an orange precipitate. This was dried in a vacuum oven at room temperature. The resulting product was stored in a glass vial under nitrogen.

2.6.10 Functionalisation of magnetite/dopamine nanoparticles with a folic acid/ N-hydroxysuccinimide composite

Iron (III) chloride hexahydrate (2.700 g, 10 mmol) and iron (II) chloride tetrahydrate (0.990 g, 5 mmol) were dissolved in deoxygenated water (12.5 mL) and stirred for 15 minutes. An orange solution formed. Dopamine hydrochloride (0.100 g, mmol) was then added to the iron chloride solution. The solution colour changed to a dark green. The solution was heated to 80°C in an oil bath. Ammonium hydroxide (10 mL, 28-30%) was injected into the heated solution forming a jet black precipitate. The solution was stirred for 20 minutes. The precipitate was washed with millipore water (30 mL) twice and then redispersed in phosphate buffer (20 mL). The folic acid/N-hydroxysuccinimide composite (0.080 g) was sonicated in phosphate buffer (10 mL) for 15 minutes. The folic acid composite was then added to the iron oxide solution and was left to stir overnight. The solution was then drained and the precipitate was then washed with millipore water (30 mL x 5) and ethanol (20 mL). A stable suspension formed with the first water washing. The black powder was stored in a glass vial and all washings were collected and stored in a centrifuge tubes.

2.6.11 Co-precipitation of Fe_3O_4 nanoparticles stabilised with dopamine and poly(sodium-4-styrenesulfonate) simultaneously

Iron (III) chloride hexahydrate (2.700 g, 10 mmol) and iron (II) chloride tetrahydrate (0.990 g, 5 mmol) were dissolved in deoxygenated water (12.5 mL) and stirred for 15 minutes. An orange solution formed. Dopamine hydrochloride (0.100 g, mmol) and poly(sodium-4-styrenesulfonate) (0.100 g, 1.4 μmol, 70,000 Mwt) were then added to the iron chloride solution. The solution then changed to a dark green. The solution was heated to 80°C in an oil bath. Ammonium hydroxide (10 mL, 28-30%) was injected into the heated solution forming a jet black precipitate. The solution was stirred for 20 minutes. Once cooled the sample was washed by magnetic decantation with millipore water (30 mL x 5) and ethanol (20 mL). After the third water washing a stable suspension formed. The black powder was stored in a glass vial and the third to fifth washings were stored in a centrifuge tube and kept stationary. The other washings were discarded.

2.6.12 Co-precipitation of Fe_3O_4 nanoparticles functionalised with poly(sodium-4-styrenesulfonate), dopamine, acridine-9-carboxylic acid and folic acid.

Iron (III) chloride hexahydrate (2.700 g, 10 mmol) and iron (II) chloride tetrahydrate (0.990 g, 5 mmol) were dissolved in deoxygenated water (12.5 mL) and stirred for 15 minutes. An orange solution formed. Dopamine hydrochloride (0.100 g, 0.52 mmol) and poly(sodium-4-styrenesulfonate) (0.100 g, 1.4 μmol, 70,000 Mwt) were then added to the iron chloride solution. The solution then changed to a dark green colour. The solution was heated to 80°C in an oil bath. Ammonium hydroxide (10 mL, 28-30%) was injected into the heated solution forming a jet black precipitate. The solution was stirred for 20 minutes. Once cooled the sample was washed by magnetic decantation with millipore water (30 mL x 2) until the solution was pH 7. In a separate round bottom flask, acridine-9-carboxylic acid (0.015 g, 0.067 mmol) was dissolved in phosphate buffer (30 mL).1-Ethyl-3-(3-dimethylaminopropyl)carbodiimide (EDCI) (0.173 g, 0.9 mmol) was then added to the solution. This solution was then added to the iron oxide suspension and was left to stir for 24 hours in the dark. This solution was then added to the iron oxide suspension and was left to stir for 24 hours in the dark. The solution was drained using magnetic separation and then redispersed in phosphate buffer (20 mL). The folic acid/N-hydroxysuccinimide composite (0.080 g) was sonicated in phosphate buffer (10 mL) for 15 minutes. The folic acid composite was then added to the iron oxide solution and was left to stir overnight. The solution was then drained and the precipitate was then washed with millipore water (30 mL x 5) and ethanol (20 mL). A stable suspension formed with the first water washing. The black powder was stored in a glass vial and all washings were collected and stored in a centrifuge tubes.

2.6.13 Microwave-assisted co-precipitation of Fe_3O_4 nanoparticles functionalised with poly(sodium-4-styrenesulfonate), dopamine, acridine-9-carboxylic acid and folic acid

Iron (III) chloride hexahydrate (2.700 g, 10 mmol) and iron (II) chloride tetrahydrate (0.990 g, 5 mmol) were dissolved in deoxygenated water (12.5 mL) and stirred for 15 minutes. An orange solution formed. Dopamine hydrochloride (0.100 g, 0.52 mmol) and poly(sodium-4-styrenesulfonate) (0.100 g, mmol) were then added to the iron chloride solution. The solution then changed to a dark green. The solution was heated to 80°C in an oil bath. Ammonium hydroxide (10 mL, 28-30%) was injected into the heated solution forming a jet black precipitate. The solution was stirred for 20 minutes. The suspension was taken out of the oil bath and left to cool for 10 minutes. The suspension was then transferred into a microwave tube (30 mL) and sealed with a rubber cap. The tube was heated by microwave radiation to 150°C at 100W for 20 minutes (including an additional 10 minutes allocated by the instrument for temperature ramping). Once cooled the sample was washed by magnetic decantation with millipore water (30 mL x 2) until the solution was pH 7. In a separate round bottom flask, acridine-9-carboxylic acid (0.015 g, 0.067 mmol) was dissolved in phosphate buffer (30 mL).1-ethyl-3-(3-dimethylaminopropyl)carbodiimide (EDCI) (0.173 g, 0.9 mmol) was then added to the solution. This solution was then added to the iron oxide suspension and was left to stir for 24 hours in the dark. The solution was drained using magnetic separation and then redispersed in phosphate buffer (20 mL). The folic acid/N-hydroxysuccinimide composite (0.080 g) was sonicated in phosphate buffer (10 mL) for 15 minutes. The folic acid composite was then added to the iron oxide solution and was left to stir overnight. The solution was then drained and the precipitate was then washed with millipore water (30 mL x 5) and ethanol (20 mL). A stable suspension formed with the first water washing. The black powder was stored in a glass vial and all washings were collected and stored in centrifuge tubes.

References

[1] Li, F.; Liu, J.; Evans, D. G.; Duan, X. *Chem. Mater.* **2004**, *16*, 1597–1602.

[2] Gomes, J.; Sousa, M.; Tourinho, F.; Itri, M.-F. R.; Depeyrot, J. *J. Magn. Magn. Mater.* **2005**, *289*, 184–187.

[3] Patterson, A. L. *Phys. Rev.* **1939**, *56*, 978–982.

[4] Weidenthaler, C. *Nanoscale* **2011**, *3*, 792–810.

[5] Daou, T. J.; Pourroy, G.; Bégin-Colin, S.; Grenèche, J. M.; Ulhaq-Bouillet, C.; Legaré, P.; Bernhardt, P.; Leuvrey, C.; Rogez, G. *Chem. Mater.* **2006**, *18*, 4399–4404.

[6] Sun, S.; Zeng, H.; Robinson, D. B.; Raoux, S.; Rice, P. M.; Wang, S. X.; Li, G. *J. Am. Chem. Soc.* **2004**, *126*, 273–279.

[7] Mazo-Zuluaga, J.; Barrero, C. A.; Díaz-Terán, J.; Jerez, A. *Hyperfine Interact* **2003**, *148*, 153–161.

[8] Cunningham, D.; Littleford, R. E.; Smith, W. E.; Lundahl, P. J.; Khan, I.; McComb, D. W.; Graham, D.; Laforest, N. *Faraday Discuss.* **2006**, *132*, 135–145.

[9] Michaelis, M.; Paulus, C.; Löschmann, N.; Dauth, S.; Stange, E.; Doerr, H. W.; Nevels, M.; Jr., J. C. *Cell. Mol. Life Sci* **2011**, *68*, 1079–1090.

[10] Michaelis, M.; Rothweiler, F.; Agha, B.; Barth, S.; Voges, Y.; Löschmann, N.; von Deimling, A.; Breitling, R.; Doerr, H. W.; Rödel, F.; Speidel, D.; Jr., J. C. *Cell Death Dis.* **2012**, *3*, e294.

[11] Salgueiriño-Maceira, V.; Correa-Duarte, M. A.; Spasova, M.; Liz-Marzán, L. M.; Farle, M. *Adv. Funct. Mater.* **2006**, *16*, 509–514.

[12] Hu, F.; Li, Z.; Tu, C.; Gao, M. *J. Colloid. Interf. Sci.* **2007**, *311*, 469–474.

Chapter 3: Iron oxide Synthesis

3.1 General introduction and objectives

The magnetic property of nanoparticles is an important consideration for their use in biomedical applications, such as magnetic hyperthermia, MR imaging, targeted drug delivery and cell tracking.[1–4] Small superparamagnetic nanoparticles are promising candidates for use in the diagnosis and treatment of cancerous areas. These single domain magnetic nanoparticles are advantageous as while the individual domain is strongly magnetic, the particles themselves do not retain any residual magnetism outside an applied magnetic field. This allows the particles to be highly magnetic when needed, but prevents agglomeration and clotting through residual magnetic attractions. Optimising the resulting magnetic properties is therefore desirable and may be achieved by tailoring the synthesis method. High temperature solvothermal methods are traditionally used to prepare highly crystalline and magnetic materials.[5–8] Aqueous methods allow for the formation of water stable nanoparticles in a simple and often shorter timeframe. However, the crystallinity of these particles often suffers compared to the high temperature organic routes.[9,10] The aim of this chapter is to develop an aqueous-based route to preparing highly crystalline iron oxide nanoparticles which will bypass the need for additional post-synthesis work up required with organic methods. To accomplish this, microwave irradiation will be incorporated into the traditional co-precipitation method. Given that microwave heating works through the dielectric heating effect, the entire reaction should heat quickly and at a uniform rate. Here, a fast nucleation step, where iron oxide seeds form on addition of base, will be followed by a controlled growth step under microwave heating to improve crystallinity while maintaining the small particle size. This co-precipitation method is versatile and can be used to prepare a wide range of iron oxides.

Magnetite and several other iron oxides will be prepared and characterised to determine if the microwave assisted co-precipitation method can be modified to maximise particle crystallinity and hence magnetic properties. A series of spinel oxides will be prepared including cobalt ferrite ($CoFe_2O_4$), copper ferrite ($CuFe_2O_4$) and manganese ferrite ($MnFe_2O_4$). The major objective of this work is to optimise the synthesis method to develop a highly magnetic foundation which can be built upon to prepare water stable, biocompatible magnetic nanocomposites.

3.2 Characterisation of iron oxide nanoparticles

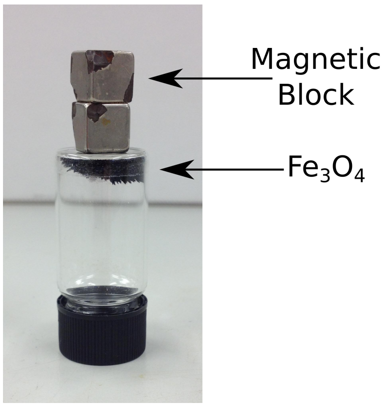

Figure 17: Magnetically responsive Fe_3O_4 nanoparticles from microwave assisted co-precipitation.

Iron oxide nanoparticles were prepared via a microwave assisted co-precipitation method. Briefly, seed particles were precipitated from a saturated solution of metal chlorides by the addition of a base, before being treated with microwave irradiation for 20 minutes at 150°C. In order to determine the best microwave reaction conditions for preparing iron oxides, several optimisation reactions were performed. Heating is key to controlling crystal growth, so exploration of heating ranges and times is essential in understanding the formation of highly crystalline iron oxides. A standard 20 minute co-precipitation reaction was performed at a series of temperatures (50, 75, 100, 125, 150, 175°C) to establish the minimum temperature needed to form magnetically responsive iron oxide nanoparticles. Too low temperatures (less than 125°C) led to an incomplete reaction with the formation of a red/brown powder (indicating oxidation). Above 125°C a magnetically responsive black powder formed (Figure 17), 150°C was chosen as the reaction temperature, as it ensures the consistent formation of a magnetic powder without heating to excessive temperatures. The reaction time for the 150°C co-precipitation reaction was also varied (5, 10, 15, 20, 25, 30 minutes) to determine the best heating time. Again, too short reaction times lead to the formation of a non magnetic red powder. 20 minutes was found to be sufficient time to produce jet black magnetic iron oxide powders without excessive reaction times.

The reaction conditions was further optimised by adjusting the heating rate and microwave system settings. Digital heating methods allows greater control over the systems heating rate and can monitor the internal conditions of a reaction. Time taken for the system to reach temperature is the ramping time. Rapid ramping times can cause pressure increases/spikes within the vessel which can also affect the reaction. Ramping times (and therefore frequency of pressure spikes) are controlled by the microwave power of a system which is variable. The higher the microwave power, the quicker the heating time and the larger the pressure increase. Therefore the optimal power setting needs to be determined to ensure quick ramping times without generating excessive pressures. The optimal microwave power was determined through a series of heating reactions on blank water samples. 15 reactions were undertaken, which involved heating a blank water sample to 150°C while varying the microwave power (10-150W, with measurements in 10 W increments (figure 18)). Reaction temperature was monitored using infrared (IR) thermometers to allow for non-invasive, volume independent measurements. Once at temperature, power would be cut or cycled to minimise heat loss and ensure a consistent temperature. It was observed that at lower powers, the system could not reach the 150°C temperature needed for the co-precipitation reaction. Above 70 W the system could reach the temperature, with the ramping time needed to reach the temperature decreasing as power increases. At high powers (above 100 W) this decrease in ramping time is minimal.

The heating power above 70 W needs to be further optimised as higher powers can decrease ramping times needed, but consideration also has to be made for the pressure within the vessel. The addition of metal chlorides and ammonium hydroxide will generate increased pressure during the reaction and pressure spikes can occur with fast ramping times. High pressures can damage the reaction vessel and can be a serious safety hazard, so microwave systems have safety cut-offs to prevent the reaction going over 300 PSI. If broken the system turns off the heating element and stops the reaction prematurely which can result in a brick red non magnetic sample. Figure 19 compares the blank water reaction against a standard iron oxide co-precipitation reaction heated to 150°C at 100 W. The addition of reaction materials causes a significant increase in pressure, with the pressure at the peak of the reaction over double the pressure of the water reaction. At 100 W the pressure in a vessel is significantly below the safety limits, ensuring that any pressure spike will not trip the cut off ending the reaction early. Higher powers can be used, but consistency is essential to ensure the formation of a crystalline magnetic material. A power setting of 100 W ensures that the sample will heat quickly, but also goes to completion.

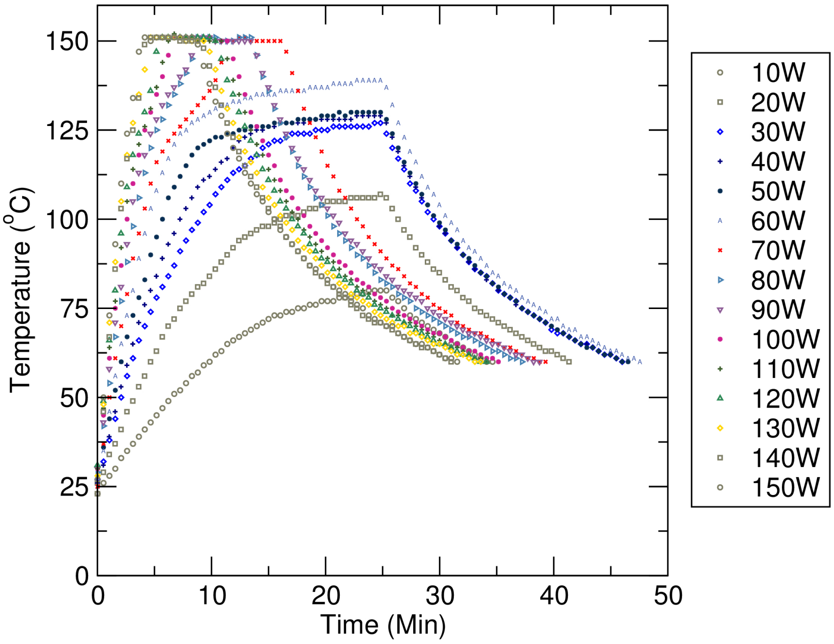

Figure 18: Microwave heating profiles for blank water samples at varying microwave powers (10-150W). 70°C is the base power needed to heat the samples up to the target temperature (150°C), with powers above this reducing the ramping time needed.

From these optimisation reactions, the reaction conditions for all subsequent co-precipitation reactions was chosen to be 150°C at 100 W for 20 minutes. For all prepared samples, a black, magnetically responsive precipitate formed (Figure 17). The dried powders were characterised with XRD, FTIR, Raman, TEM and SQUID measurements.

3.2.1 Structural characterisation

Powder XRD patterns were collected of the ferrite nanoparticles to confirm the spinel structure and to calculate the average primary particle size using the

Scherrer equation. Figure 20 shows the patterns for magnetite (red), cobalt ferrite (green), copper ferrite (blue) and manganese ferrite (yellow), alongside the ICSD standard for magnetite (purple).

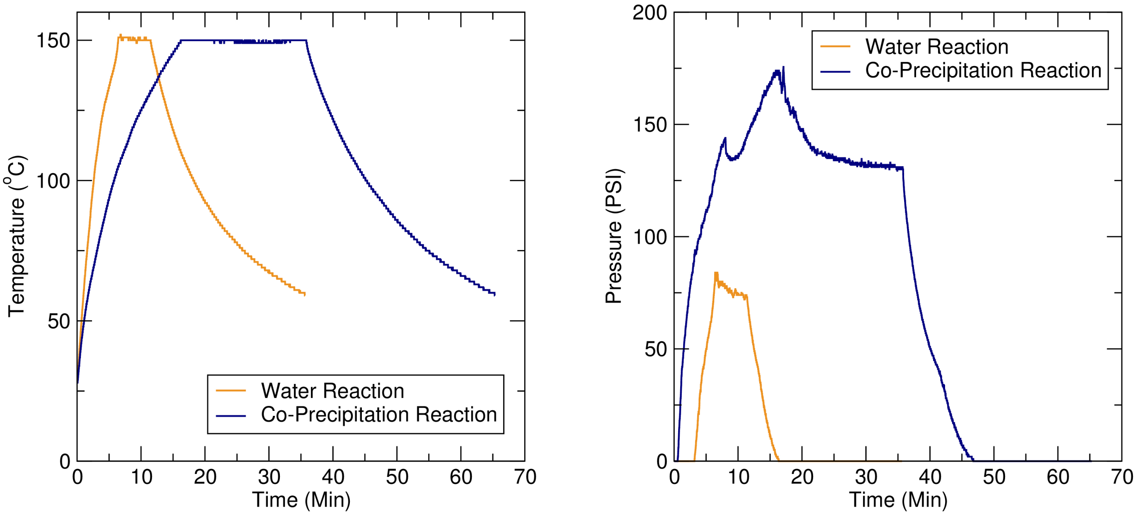

Figure 19: Heating profiles for a blank water reaction (orange) and a typical coprecipitation iron oxide reaction (blue). Upon addition of ammonia and starting materials ramping times and internal pressures increases. At 100 W, the co-precipitation reaction can still reach the optimum temperature of 150° C while remaining under the safety pressure limits.

The magnetite pattern matches that of the standard from the ICSD database and to previously reported patterns of magnetite.[9,11–14] All other ferrite samples also display the spinel pattern but a shifting of the peaks is also observed. This shifting of the peaks is due in part to the change in lattice parameters from both substituting the Fe^{2+} ions with other transition metal ions. Substituting the M^{+2} ion will vary the ionic radius of the ions in the crystal structure changing the unit cell size slightly. This changes the overall lattice parameters causing the X-rays to diffract at a slightly different angle, which is reflected by a shifting in the peaks. Lee *et al.* substituted Fe^{2+} groups with a variety of transition metals, observing that the varying ionic radii along with the metal distribution in the spinel structure causes this shifting effect.[15] Gomes *et al.* observed that by increasing the ionic radii of the M^{2+} ions, this results in a greater distortion in the packing of the oxygen ions increasing the lattice parameters, and therefore showing a greater shifting effect.[16] This effect can be seen in the prepared sample with the difference between the $MnFe_2O_4$ (largest ionic radii) and $CuFe_2O_4$ (smallest ionic radii) samples. All patterns agree with standards from the ICSD database.[16–18] The broad XRD peaks indicate the formation of nanoparticles and the average sizes has been calculated using the Scherrer equation. These results are detailed in Table 7. The magnetite nanoparticles were the smallest in size at 11.2 nm with the cobalt ferrite nanoparticles being the largest at 24.7 nm.

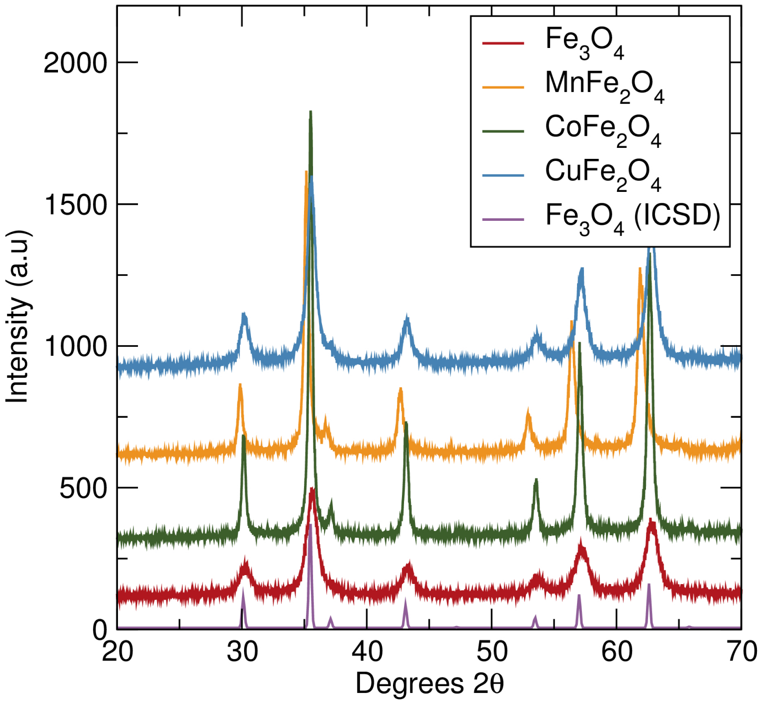

Figure 20: XRD patterns of ferrite nanoparticles synthesised via a microwave assisted coprecipitation method. All samples share the same inverse spinel crystal structure but peak shifting distinguishes the samples. An ICSD standard for magnetite (purple) is included, with this and all of the other samples agreeing with the respective ICSD standards.[11,16–18]

Often, it can be difficult to distinguish between different iron oxide nanoparticles using powder XRD, e.g. the patterns for magnetite (Fe_3O_4) and maghemite (γ-Fe_2O_3) are very similar. Therefore, FTIR and Raman spectroscopy have been employed to further investigate these particles, since different metal-oxygen bonds will have different vibrational energies.[15,19] Figure 21 shows the FTIR measurements of the ferrite nanoparticles.

Magnetite displays an Fe-O stretch at 560 cm^{-1}.[7,20] A similar stretch is observed for all other ferrite samples, with a shift in the peak position due to the substitution of Fe^{2+} ions for another transition metal. This substitution retains the iron oxide inverse spinel structure but by changing the ionic radius it alters bond lengths and how the bond absorbs infra-red energy. This change in absorption results in a slight shifting effect of this metal oxygen bond. Lee *et al.* observed that the signal shifts to a higher frequency due to the greater bond strength of the metal oxygen bond.[15] This is reflected in the FTIR results with the manganese ferrite shifting to a lower wavelength. Manganese ions have the largest ionic radius of the tested transition metals, causing it to form the weakest bond resulting in a shift to lower wave numbers. This shifting effect has been confirmed by other groups with the patterns matching reports in the literature.[21–23]

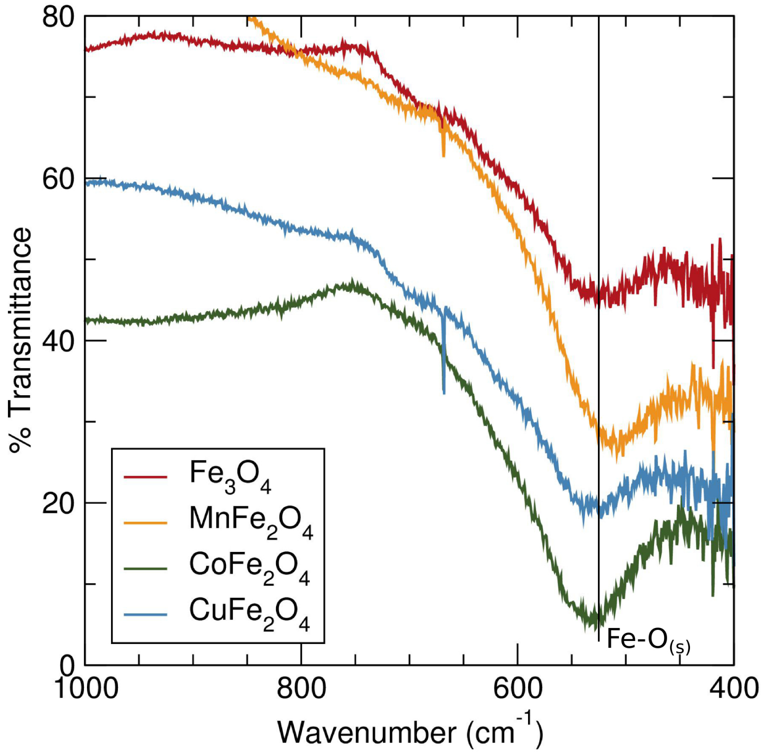

Figure 21: IR spectra of magnetite (red), manganese ferrite (yellow), cobalt ferrite (green) and copper ferrite (light blue).

In order to obtain Raman data, the measurement was carried out using a 637 nm red laser with a 10% filter. Care must be taken in performing these measurements, as heating and eventual oxidation of the particles can occur upon excessive laser exposure. To demonstrate this, an initial measurement was collected at a laser power of 35 mW for 90 seconds. The samples were then exposed to the laser for 3 minutes and then re-measured, with the results for magnetite shown in Figure 22. Initially, the sample gives four peaks at 186, 364, 503 and 696 cm^{-1} (Table 5). These bands occur due to specific vibrations within the crystal structure, which can be associated to bonds using group theory. Gasparov *et al.* determined that the unit cell for magnetite crystals consists of 56 atoms with the smallest (Bravais) cell containing 42 vibrational modes. 5 of these modes are Raman active: A_{1g}, E_g and three T_{2g} modes.[24] Each of these modes contain several symmetry elements that make a bond in the crystal structure and are assigned Mulliken symbol (i.e. A_{1g}, E_g) to represent these combined symmetry elements.

Four of these modes can be observed in the collected magnetite pattern. The broad band at around 696 cm^{-1} is an A_{1g} band, characteristic of magnetite.[24–27] This vibration is specific to the arrangement of oxygen groups in the spinel structure and is the strongest band in the spectrum.[24,28] The band at 503 cm^{-1} relates to the E_g mode and is the bond between the oxygen groups and the B site (Fe^{2+} and Fe^{3+}) in the inverse spinel structure. The final two bands are at 186 and 364 cm^{-1} relating to the T_{2g} mode. This is from the vibrations of the bonds between the oxygen atoms and the iron groups in the A site of the spinel (Fe^{3+}). Gasparov *et al.* predicted these bands to be at 193 and 310 cm^{-1} , with the discrepancy/shifting in the observed pattern indicating powder oxidation.[24] The oxidised variant maghemite, has a T_1 Raman band at 350 cm^{-1} due to the increased oxidised Fe^{3+} content. The observed band is closer to the maghemite assignment suggesting that the particles contains mixed magnetite and maghemite phases, due to the presence of bands relating to both iron oxide types. This mixed phase is supported by the very slight brown colour of the powder in the microscopy image (Figure 23(a)).

After continual exposure to the laser (Figure 22(b)), significant changes are noted. As observed from the microscope images, the black/brown powder turns red (Figure23(b)) and the broad magnetite/maghemite peaks disappear to be replaced by several sharp peaks. The peak positions (Table 5) and the red powder are characteristic of the iron oxide hematite (α-Fe_2O_3), which has a significantly more complex structure with 7 active Raman peaks (five E_g bands and two A_{1g} bands).[28] These peaks are accounted for and in good agreement with hematite patterns found in the literature.[25,26,29] The small shoulder on the 607 cm^{-1} E_g band is an LO (Longitudinal optical) E_u vibration from residual maghemite, indicating that the sample can be oxidised further.[25,29]

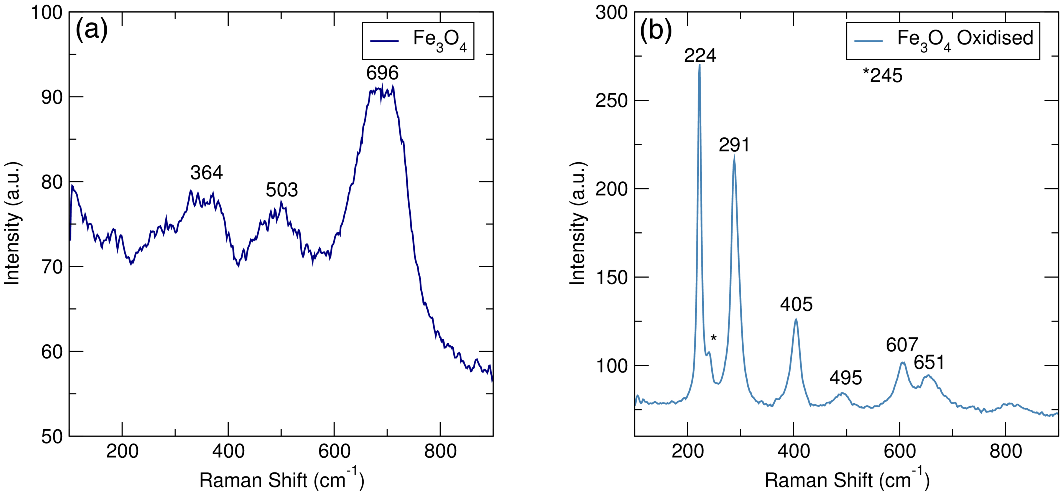

Figure 22: Raman spectrum of Fe_3O_4 nanoparticles before (a) and after (b) continuous exposure to the Raman laser. Prior to prolonged laser exposure, a mixture of magnetite and maghemite peaks can be seen, while after exposure the pattern matches that of hematite (an oxidised ferrite).

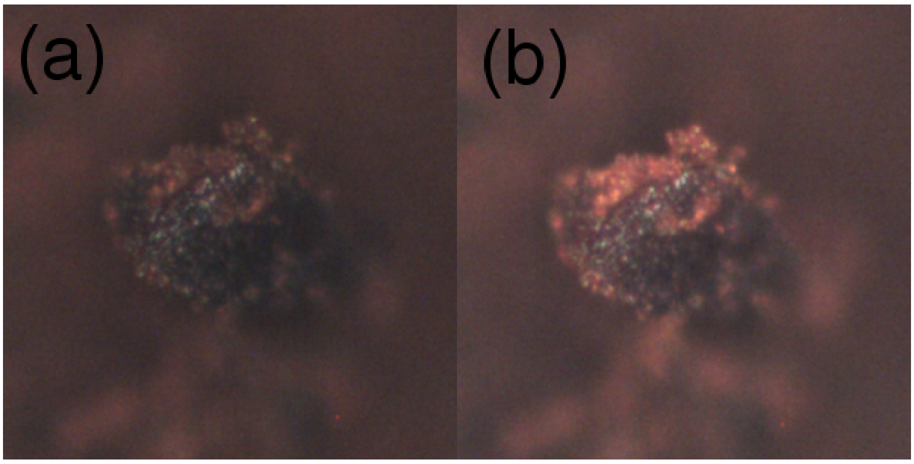

Figure 23: Microscope images of magnetite nanoparticles before (a) and after (b) exposure to a higher power laser. The brown/red colour of the particles before the measurement (left) suggest a slight oxidation of the sample. After prolonged exposure to the stronger laser (right), the formation of red areas confirms oxidation into hematite.

Table 5: Raman peak and vibrational mode assignment for magnetite nanoparticles before and after oxidation by the laser. Before oxidation, the sample displays magnetite (A_{1g}) and magnetite/maghemite vibrational modes (V. mode) such as E_g and T_{2g}. After continual exposure to the laser, sharp hematite bands appear suggesting oxidation.[25,29]

Pre Oxidation		**Post Oxidation**	
Raman Shift (cm^{-1})	**V. mode**	**Raman Shift (cm^{-1})**	**V. mode**
364	E_g	224	A_{1g}
503	T_{2g}	245	E_g
696	A_{1g}	291	E_g
		405	E_g
		495	A_{1g}
		607	E_g
		651	E_u

All other ferrite samples display a similar spectrum, containing A_{1g} bands and a mixture of E_g/T_{2g}/T_1 bands suggesting that the powder is mixed phase containing maghemite impurities (Figure 24 and Table 6). Substitution of the Fe^{2+} ion with transition metal ions will change the bond lengths of the crystal structure and how the Raman waves scatter from the bonds. The spinel structure and bond types are retained but the expanded/compressed lattice dimensions cause a shifting of the peaks. All samples have a strong broad A_{1g} bands characteristic of the oxygen packing in the ferrite structure. The cobalt ferrite sample starts showing a large number of sharp peaks indicating that the sample has partly oxidised into hematite. The specific cobalt ferrite peaks are noted at 670 (A_{1g}), 394 and 460 cm^{-1} corresponding to literature values for $CoFe_2O_4$.[19,30–32] However, the sharp bands at 218, 277 and 593 cm^{-1} correspond to hematite.[25,26,29] Complete oxidation would remove the A_{1g} band suggesting only partial oxidation of the sample. The copper ferrite sample shows a pattern similar to magnetite, with an E_g band at 510 cm^{-1} and two T_{2g} bands at 187 and 350 cm^{-1}. The presence of the T_{2g} bands indicate a mixed material containing both magnetite and maghemite (with the 350 cm^{-1} band possibly being a T_1 maghemite band). Little shifting is seen for the copper ferrite sample making it difficult to distinguish from the magnetite sample.[33] The manganese ferrite sample only has two Raman bands, the A_{1g} band at $622\,\mathrm{cm}^{-1}$ and the T_{2g} band at $322\,\mathrm{cm}^{-1}$. Significant shifting of these bands can be seen when compared to the magnetite pattern highlighting the effect of manganese doping with the shifting of the A_{1g} band. This pattern and assignment agrees with previous literature reports for manganese ferrite.[19,25]

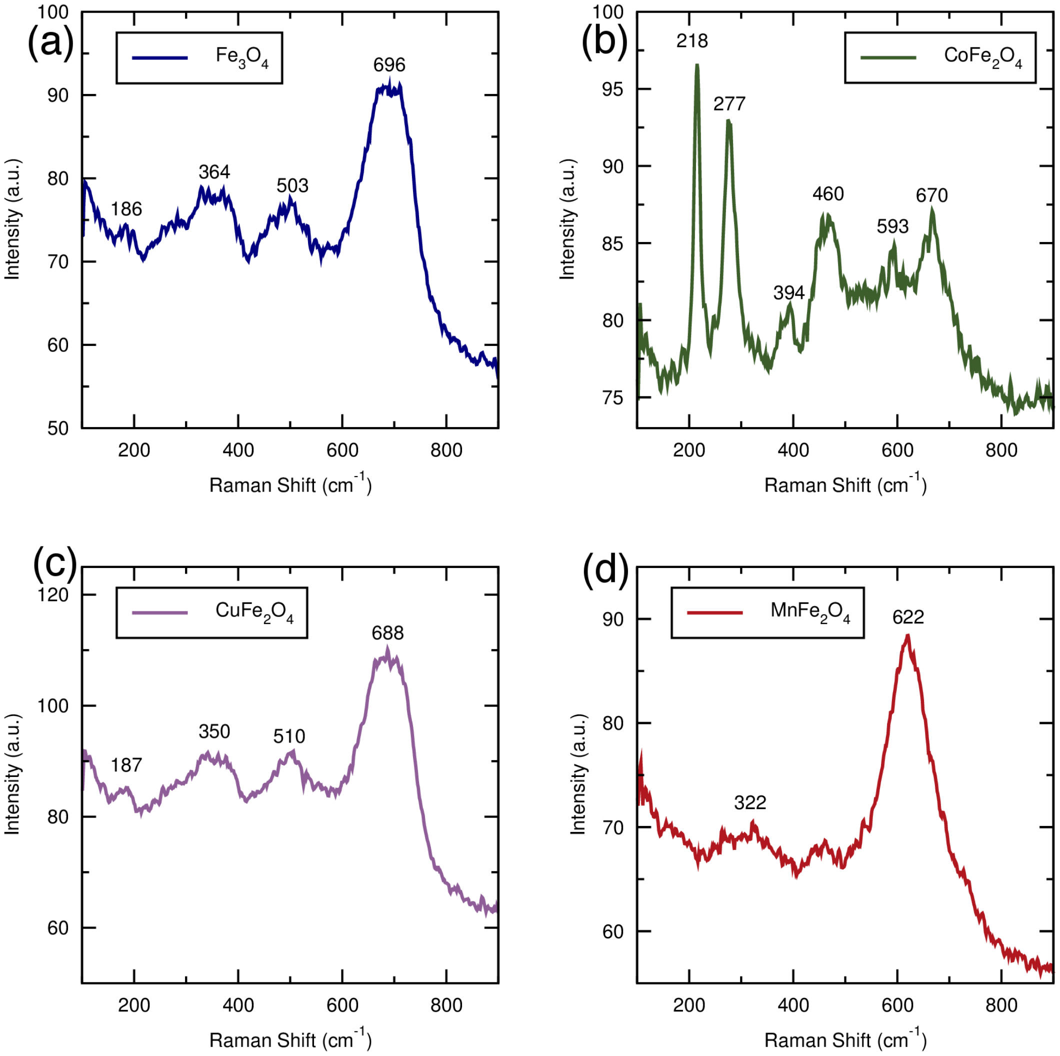

Figure 24: Raman spectra of (a) magnetite, (b) cobalt ferrite, (c) copper ferrite and (d) manganese ferrite, with all samples displaying typical ferrite bands.

Table 6: Raman peak and vibrational mode assignment for transition metal ferrite particles. Between the common peaks of E_g and A_{1g} shifting of the peaks positions can be observed, which can be used to distinguish the particles from each other.

Sample	**T_{2g} (1)**	**E_g**	**T_{2g} (2)**	**A_{1g}**
Fe_3O_4		364	503	696
$CoFe_2O_4$		394	460	670
$CuFe_2O_4$	187	350	510	688
$MnFe_2O_4$		322		622

3.2.2 Particle size and crystallinity

The primary particle sizes for all samples were measured from 100 particles using TEM and are shown in Figure 25 and Table 7. Aggregation is noted for all samples, due to drying effects from preparing the grids. Great variation can be seen in particle size and morphology between the samples. The magnetite nanoparticles are smallest in size and distribution (12 ± 2 nm). All other particles have larger sizes, with greater size distributions also noted (Figure 26). The largest of the particles is cobalt ferrite with an average size of 40.4 nm ± 24.7 nm and a wide size variance with some individual particles being over 70 nm in size. When compared to the Scherrer XRD measurements, both results show an increase in particle size. There is a slight agreement between the results although the TEM images show a greater size increase for the cobalt ferrite and manganese ferrite sample, than with the Scherrer measurements.

Table 7: Average particle sizes calculated from the TEM images (n=100) and XRD patterns. Both types of characterisation results show an increase in nanoparticle size in comparison to magnetite.

Sample	**TEM Size (S.D) (nm)**	**XRD Scherrer (nm)**
Magnetite	12.1 (1.99)	11.2
Cobalt Ferrite	40.4 (14.93)	24.7
Copper Ferrite	18.9 (3.01)	14.8
Manganese Ferrite	37.9 (7.02)	23.7

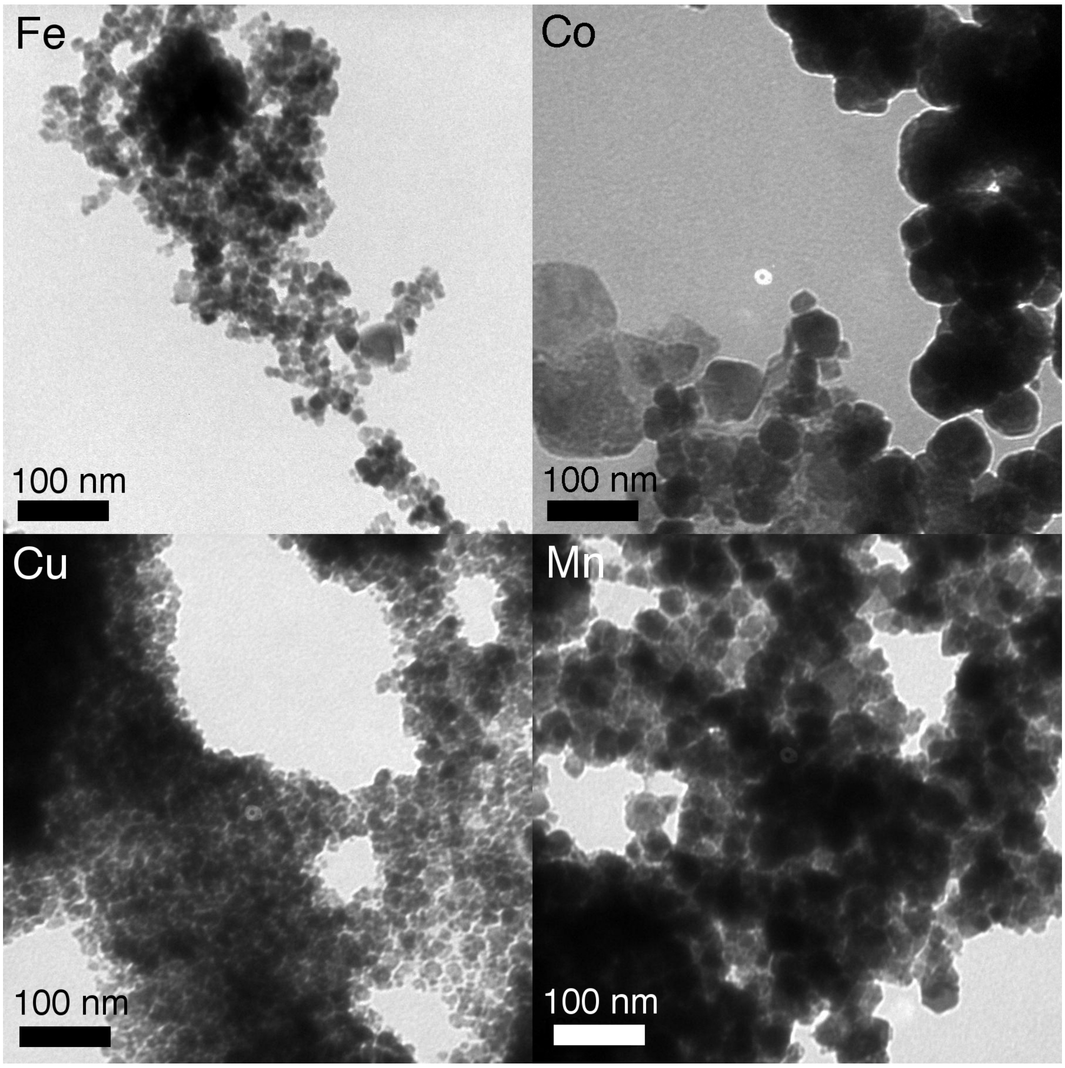

Figure 25: TEM images taken of magnetite, cobalt ferrite, copper ferrite and manganese ferrite. Clustering can be seen in all samples from drying effects. Magnetite, Cobalt, manganese ferrite begin to show a hexagonal morphology, whereas the copper nanoparticles are much smaller in size and more ill defined.

Given the small size and uniformity of the magnetite nanoparticles, high resolution electron microscopy images were recorded to further examine these nanoparticles. Figure 27 confirms the formation of single crystal nanoparticles. The particles take a hexagonal morphology, with a monodisperse size and shape distribution. The hexagonal morphology is associated with a high crystallinity and is commonly seen in high temperature solvothermal synthesis methods.[5,6] Interplanar distances were also measured using HRTEM, with the distances further characteristic of the inverse spinel structure.[7,34] The SAED pattern obtained is characteristic for magnetite with the diffraction spots corresponding to the spinel structure. The lattice patterns calculated from the images agree with previous XRD results and SAED patterns of magnetite found within the literature.[6,34]

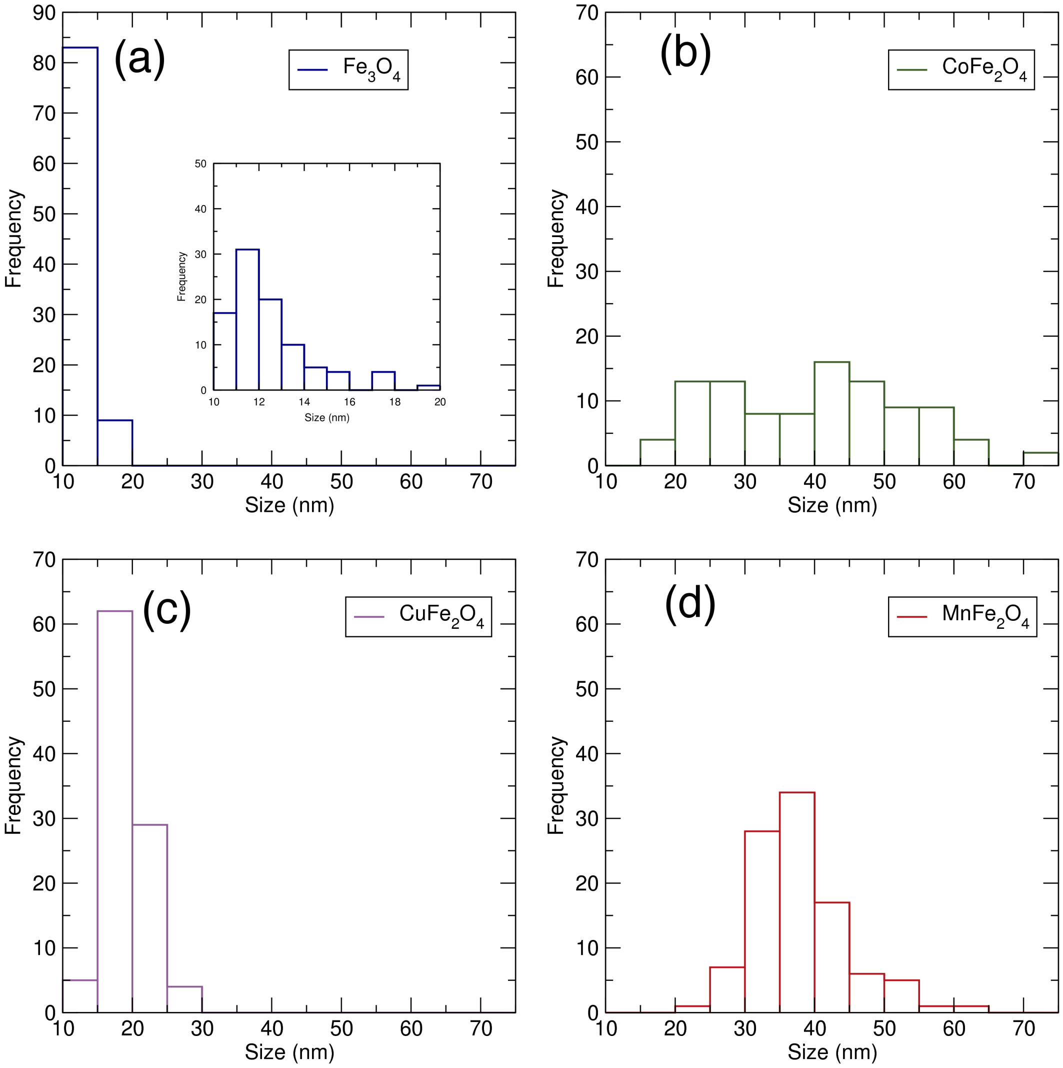

Figure 26: Histograms of the primary particle sizes of (a) magnetite, (b) cobalt ferrite, (c) copper ferrite and (d) manganese ferrite dried in ambient conditions (n=100). Magnetite shows the smallest size distribution of all the ferrites, while cobalt ferrite has the largest.

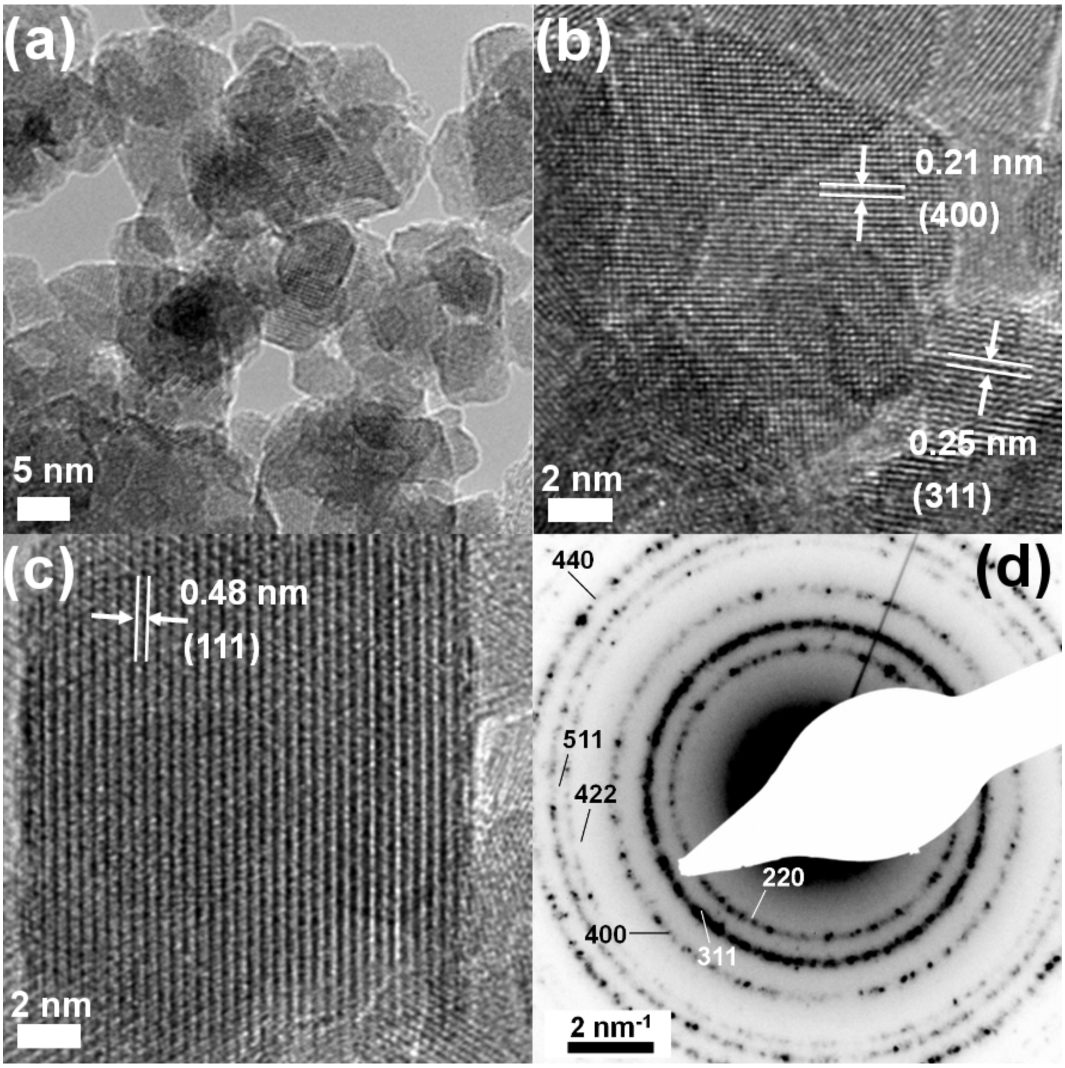

Figure 27: High resolution TEM images (image a-c) and SAED image (image d) of magnetite nanoparticles. Well defined highly crystalline magnetite particles were observed that formed traditional hexagonal morphologies. Lattice spacings and SAED measurements confirm the identity of the magnetite core.

3.2.3 Magnetic property measurements

The magnetic properties of the ferrite nanoparticles were measured using SQUID magnetometry, with magnetisation curves obtained at 300K and 10K in a magnetic field of up to 5 x10^4 G and are plotted in Figures 28 and 29. In ordered materials (e.g. ferromagnets), where the individual magnetic moments can align parallel with each other to form magnetic domains, all domains can be aligned in the same direction as an applied external magnetic field. This can be experimentally observed in the form of M-H curves, where M is the magnetisation and H is the applied magnetic field strength. Often, for ferro- and ferrimagnetic materials, there is a hysteresis noted in this curve, which provides information on the coercivity (the applied magnetic field required to demagnetise the sample) and the remanence (the residual magnetism of the material once the applied magnetic field has been removed). The high residual magnetism of ferromagnetic bulk materials and resulting magnetic attractions can lead to agglomeration. Changes in particle size can drive large changes in the M-H curve behaviour. One important example of this is the case of superparamagnetic single-domain particles, which are of the order of 10 nm, where all spins therein aligned parallel or anti-parallel to the easy axis. This magnetic anisotropy is a result of the spins aligning along a preferred crystallographic direction.

At 300K, the magnetite sample does not display a hysteresis loop, showing negligible coercivity and remanence (Figure 28(a)). This behaviour is indicative of superparamagnetic single domain magnetic nanoparticles.[35–38] The saturation magnetisation (M_s) of the magnetite sample at 300 K is 65.2 emu/g and is unsaturated up to fields of 5 x10^4 G, further characteristic of superparamagnetic material.[9,35] The M_s value is a measure of the magnetic spin and domain strength within the particles. Saturation is reached when all of the magnetic spins within the domain are aligned in respect to an external magnetic field. The higher the value, the stronger the external magnetic field needs to be to align the spins, meaning more spins within the domain and therefore a stronger magnetic domain. The stronger the domain, the greater magnetic field generated by the particles when used in biological applications. For paramagnetic/superparamagnetic materials, saturation cannot be reached even at high applied fields. This is due to ambient thermal energy causing the spins in paramagnetic/single domain materials to agitate and become slightly misaligned with the applied field. Magnetic spins in multi domain materials require more energy to agitate than the ambient thermal energy, eliminating this misalignment, causing the material to magnetically saturate in weak external magnetic fields. The saturation point can therefore be an additional approach to distinguishing between ferromagnetic and superparamagnetic material. Optimisation of the particles magnetism is essential, as a strong magnetic domain increases MRI efficacy, while superparamagnetism eliminates the risk of agglomeration/clotting.

Figure 29(a) shows the same sample but measured at 10 K. The M_s value increases and now the particles start to display residual magnetism, with a slight hysteresis noted. This hysteresis forms due to the low thermal energy being unable to randomise the magnetic spins when removed from the external field. The particles are still not completely saturated even when cooled, further confirming the particles superparamagnetic nature. This is due to the single domain structure causing a slight misalignment of magnetic moments with the external field. As the sample is cooled these spins remained slightly misaligned stopping complete saturation.[9,35] Very high external fields are needed to fully align the individual (paramagnetic) moments to the external field.

This superparamagnetic behaviour is desirable for biomedical applications as the particles show no residual magnetism, eliminating the risk of magnetic agglomeration when in the body. The critical diameter for magnetite is reported to be between 10 and 15 nm.[35,39] TEM images and XRD measurements show that the particle size is below this critical diameter which is reflected in superparamagnetic curves in the SQUID measurements.

The M_s values for these magnetite nanoparticles are below the theoretical maximum for bulk magnetite, most likely due to some spin disorder on the particle surface.[10] However, the values obtained here have higher M_s values than those observed for magnetite nanoparticles synthesised by traditional co-precipitation methods (M_s = 40-50 emu/g).[9,10] The improved M_s values are due to the use of microwave irradiation during particle synthesis. Microwave irradiation promotes crystal growth and reduces surface defects/spin disorder. As the particles are single domain, high crystallinity is essential to the formation of this domain. Surface defects introduced from stunted crystal growth, introduces spin disorder reducing the alignment of magnetic moments within the domain, lowering M_s values. Highly crystalline nanoparticles have very few surface defects which is reflected in improved M_s values. High temperatures are one of the more common methods to limit defect formation. Magnetite particles

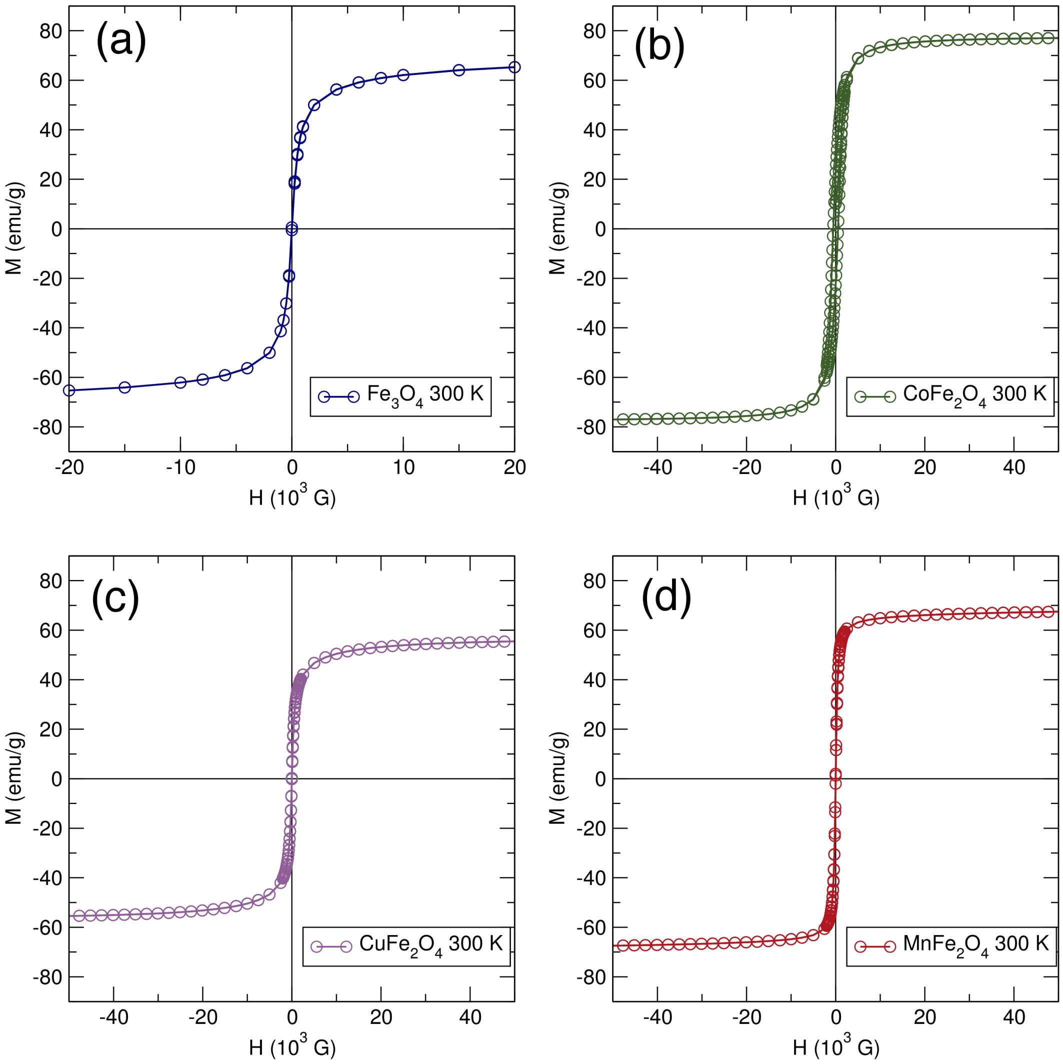

Figure 28: Magnetic measurements of (a) magnetite, (b) cobalt ferrite, (c) copper ferrite and (d) manganese ferrite at 300 K. Magnetite and copper ferrite samples display no hysteresisand do not saturate, indicating superparamagnetism, whereas cobalt and manganese ferrite show ferromagnetic properties.

prepared by high temperature solvothermal methods display high crystallinity due to heating and as a result, high magnetisation values (60-85 emu/g).[5–8] Microwave irradiation achieves the same effect on crystal growth as conventional heating methods, but can be incorporated into co-precipitation reactions to produce highly crystalline water stable materials. This high degree of crystallinity is confirmed from previous HRTEM images, and is reflected in the increased M_s values.

The other iron oxide samples showed varying magnetic properties, based on their size and morphology. The largest of the particles was cobalt ferrite

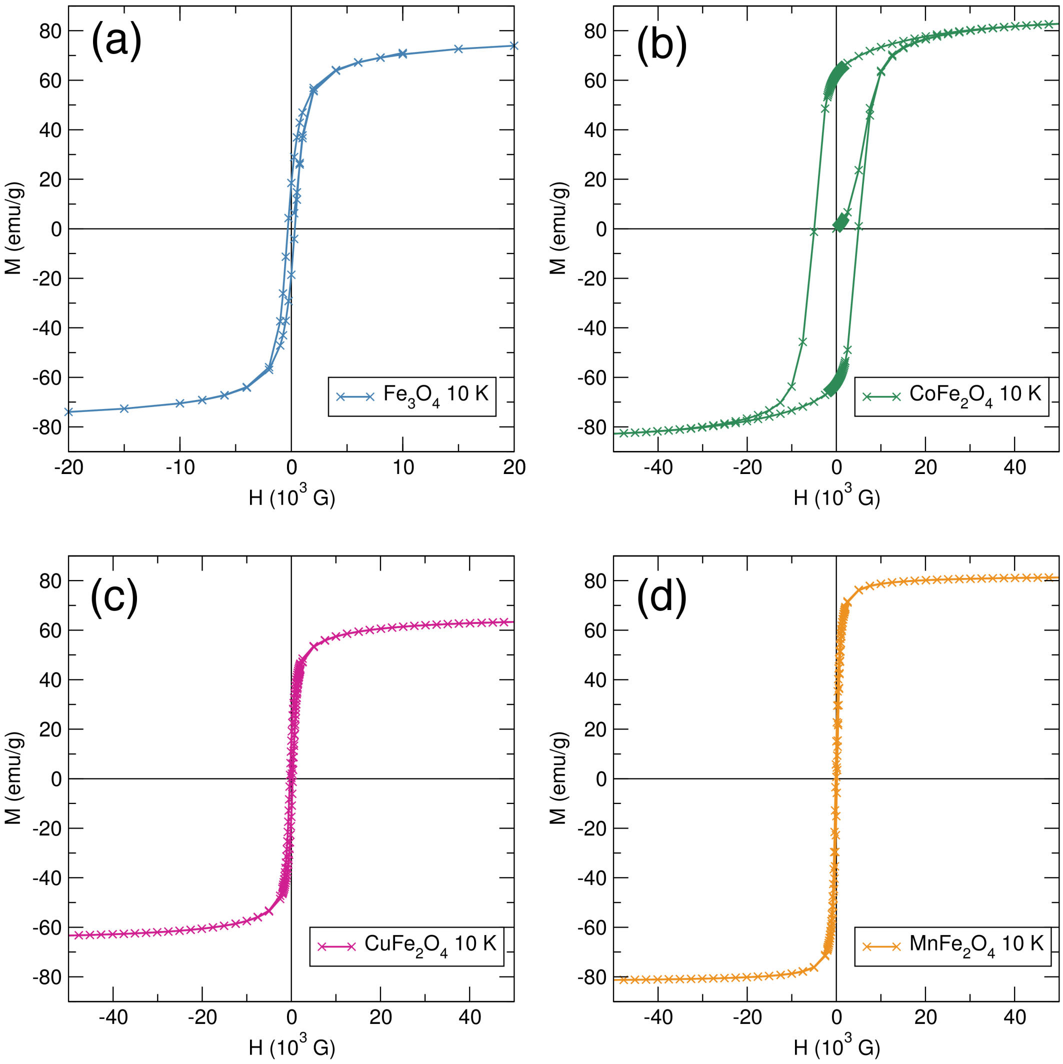

Figure 29: Magnetic measurements of (a) magnetite, (b) cobalt ferrite, (c) copper ferrite and (d) manganese ferrite at 10 K. All samples display hysteresis in their profiles.

(40.4 nm) with the increased size reflecting very high M_s values and the observation of a hysteresis and residual magnetism (figure 28 (b)). The particles were above the critical diameter and too large to be single domain (determined by Maaz *et al.* as 28 nm).[40] Multiple domains increase the energy requirements to randomise the magnetic spins above the ambient thermal energy, resulting in ferromagnetic properties. This is problematic for biomedical applications as under normal conditions the particles will agglomerate through magnetic attractions which can cause clotting. The hexagonal morphology of the particles shown in TEM images indicate that the particles are very crystalline. This results in the cobalt ferrite nanoparticles having the highest M_s values of all the samples (table 8). When compared to other reports of cobalt ferrite in the literature, the prepared particles show slightly higher magnetisation values to the literature; 58.3-68 emu/g.[40,41] The magnetisation values are close to the theoretical maximum for bulk cobalt ferrite (80.8 emu/g), illustrating that microwave irradiation enhances cobalt ferrite crystal growth. The literature also demonstrates how to prepare particles below the critical diameter. Kim *et al.* observed that higher temperatures promoted crystal growth and therefore an increase in particle sizes.[41] Rajendran *et al.* managed to prepare superparamagnetic cobalt ferrite nanoparticles using a low temperature method that were 6nm in size.[42] These particles displayed superparamagnetic properties, supporting the relationship between heat and particle size.

The small size and poorly defined particle morphology of the copper ferrite nanoparticles is reflected in the lowest M_s values of all of the samples (figure 28 (c)). The ill defined morphology suggests multiple defects within the crystal which reduces domain strength and M_s values. The particles display no residual magnetism or coercivity which is characteristic of superparamagnetism.[35–38] Copper ferrite is classified as a soft magnet with a theoretical maximum of 55 emu/g, so the lower values of between 25-35 emu/g were to be expected.[43–45] The effect of microwave irradiation is clearly seen with the the prepared particles having an saturation magnetisation much greater than other reported samples and very close to the theoretical maximum.[43–45] The high M_s values are due to the Fe^{3+}/Fe^{2+} content in the iron oxide. The particles were prepared from copper (II) chloride dihydrate and iron (II) chloride tetrahydrate. During synthesis the Fe^{2+} ions will oxidise into the Fe^{3+} ions (which with the Cu^{2+} ions) form the $A^{2+}B_2{}^{3+}O_4{}^{2-}$ spinel structure of copper ferrite. This oxidation of the iron ions depends on the reaction environment though, with many co-precipitation techniques oxidising the Fe^{2+} precursor by bubbling air through the starting solution.[46,47] In the reaction detailed in this chapter, this induced oxidation was limited from the extensive use of air sensitive techniques (such as using a schlenk line and deoxygenated water), leading to the copper ferrite particles being precipitated from a mixture of Fe^{2+} and Fe^{3+} ions. This results in the final spinel structure containing a mixture of Fe^{3+}, Fe^{2+} and Cu^{2+} ions and making it non stoichiometric copper ferrite. Thapa *et al.* prepared a similar material with increasing Fe^{2+} concentrations noting that the replacement of Fe^{3+} ions with Fe^{2+} ions caused a significant increase in M_s values for copper ferrite.[48] This can be seen with this sample with a saturation value very close to the theoretical maxiumum indicating non-stoichmeteric copper ferrite nanoparticles. This altered stoichiometery was also observed in the Raman/FTIR/XRD patterns with the lack of peak shifting expected from the copper groups (figures 24, 21 and 20). The larger morphologies and decreased M_s values indicate that there is a copper component to the particles. Even with optimisation, pure copper ferrite nanoparticles are restricted by the theoretical bulk M_s maximum of 55 emu/g limiting their application in comparison to the other iron oxide particles.

Interestingly, the manganese ferrite nanoparticles were larger in size than magnetite, but with similar M_s values (figure 28 (d)). The theoretical maximum for manganese ferrite was calculated to be 80 emu/g with the prepared particles very close to this value (66.9 emu/g) due to increased crystal growth from microwave irradiation. The particles did not exhibit hysteresis even at room temperature, indicating the particles are superparamagnetic. When compared to the literature, Deraz *et al.* prepared particles of a similar size (34 nm) and M_s values, identifying that the particles are multi domain, with very small coercivity and remanence values.[49] The formation of multiple domains are responsible for the particles high magnetisation values, which are close to the bulk value. Tang *et al.* notes a similar occurrence with smaller 25 nm particles, which are close to bulk value but display a slight remanence.[50] This remanence and coercivity is lost when the particles are below 10nm indicating that the particles prepared in this chapter are above the single domain critical diameter, which risks the formation of multi domain particles.[50,51] For the sample in this chapter, microwave irradiation resulted in the formation of particles close to their bulk values, but the increased particle size is undesirable, as the literature suggests the onset of ferromagnetic behaviour from the size increase (despite the lack of hysteresis on the SQUID results) which will ultimately limit biological applications.

Table 8: Magnetisation saturation values for iron oxides at 300K and 10K. The larger particles tended to show higher M_s values. Upon cooling the M_s values for all samples increased. Microwave irradiation shows in increase in M_s values for all samples bringing them close to their theoretical bulk M_s values

Sample	Theoretical M_s Values 300K	This Chapter Size (nm)	This Chapter M_s (Emu/g) 300K	This Chapter M_s (Emu/g) 10K	Literature Values Size (nm)	Literature Values M_s (Emu/g) 300K
Magnetite	92[52]	12	65.2	81	8[10]	51[10]
Cobalt Ferrite	80[40]	40	76.4	82.7	25[40]	68[40]
Copper Ferrite	55[43]	18	55.1	63.2	20[45]	32.8[45]
Manganese Ferrite	80[50]	37.9	66.9	80.1	25[50]	68[50]

The literature illustrates that manganese ferrite shows enhanced properties as an MRI contrast agent, so optimisation of the particles, is needed to unlock this potential.[51,53,54] Reports by other groups suggest that prolonged heating does not cause a significant increase in particle size but will improve superparamagnetic properties.[22,55] Kodama *et al.* notes that a longer ageing step during synthesis can reduce the formation of surface defects.[22] Chen *et al.* also noted that prolonged digestion times produces smaller particles guaranteeing them to be superparamagnetic.[55] This can be applied to the method listed in this chapter by prolonging the conventional and microwave heating steps.

3.3 Attempted one pot microwave synthesis of Fe_3O_4 nanoparticles

Figure 30: Non-magnetic, red precipitate obtained from the one step urea based co-precipitation reaction.

The results have shown that incorporating microwave irradiation into the co-precipitation reaction results in highly magnetic iron oxide nanoparticles. An attempt was made to make the synthetic process a single-step, one-pot reaction. To do this, urea was added to the metal chloride solution instead of ammonia as a base. The aim here was that as the vessel was heated and as the reaction progressed, the urea would break down to form an *in situ* base, which would precipitate the nanoparticles. However, instead of a black, magnetically responsive powder characteristic of magnetite, a non-magnetic red powder (figure 30) was obtained using this method, which was characterised with XRD, FTIR and Raman spectroscopy.

3.3.1 Powder characterisation

Figure 31 shows substantial changes in the powder XRD pattern for this sample. Peak broadening allows the particle size to be calculated using the Scherrer equation. The nanoparticles were significantly larger than bare magnetite nanoparticles with an average size of 26.37 nm. The peak positioning is characteristic of the hexagonal hematite structure, and agrees with the ICSD standard for hematite.[56]

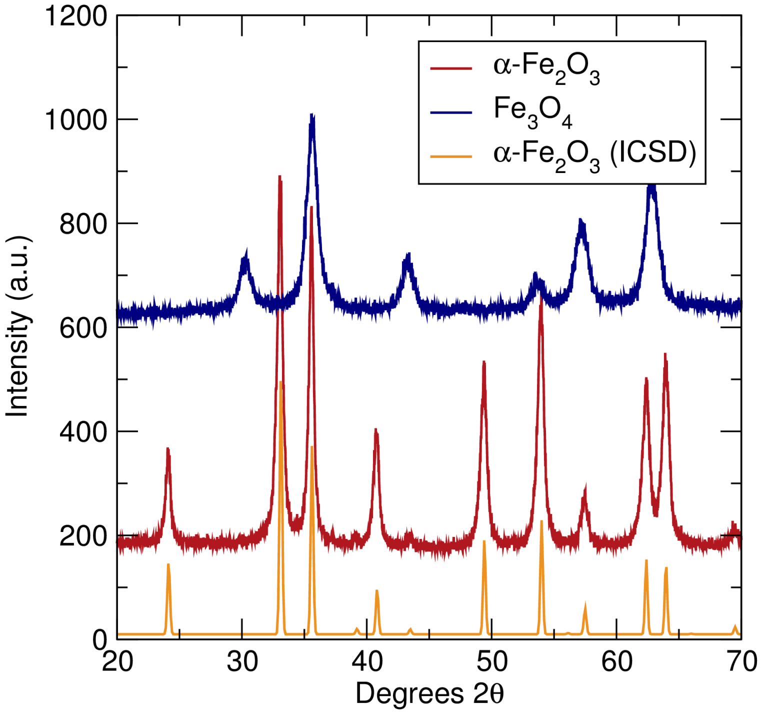

Figure 31: XRD pattern of iron oxide nanoparticles synthesised via a microwave assisted coprecipitation method using urea (red). The original magnetite peaks are shown in blue. Peak positions are characteristic of hematite and match the ICSD standard for hematite (yellow).[56]

The FTIR measurement also highlights the differences between magnetite and red powder (figure 32). The iron oxide peak shifted to a lower wavenumber (515 cm^{-1}) and a second peak formed (425 cm^{-1}). These peaks are characteristic of hematite (which is also brick red in colour) which agrees with the literature.[28,29] Chernyshova *et al.* have assigned the two peaks as the asymmetrical A_{2u}/E_u modes at 425 cm^{-1} and the mode E_u at 515 cm^{-1}.[29] Hematite (Fe_2O_3) is an oxidised form of iron oxide, containing only Fe^{3+} groups with both of the above modes relating to the Fe-O bonds in the crystal structure.

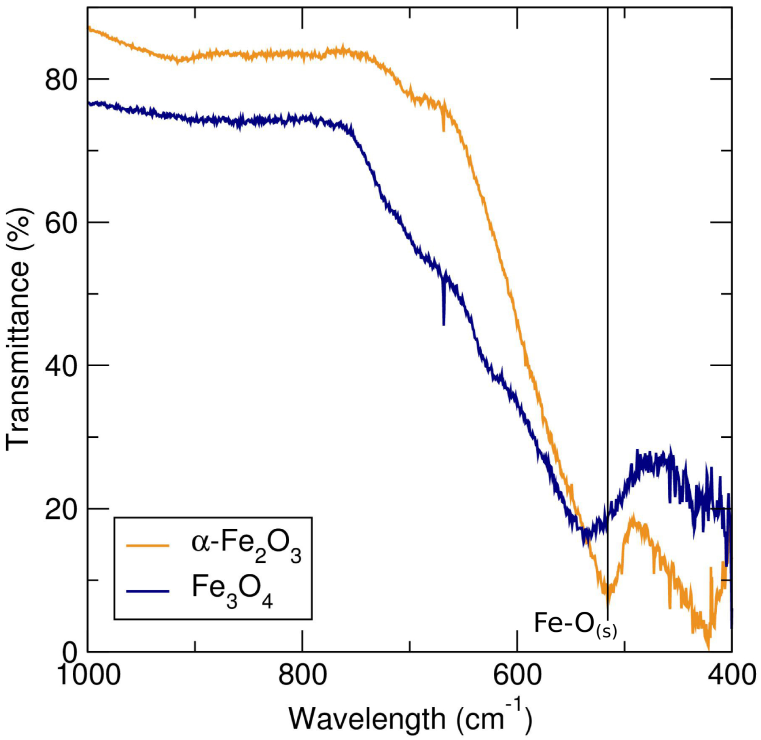

Figure 32: FTIR Spectra of iron oxide nanoparticles synthesised in a co-precipitation reaction using urea (yellow) or the standard ammonium hydroxide (blue). The ammonium hydroxide reaction shows the characteristic magnetite stretch at 560 cm^{-1} (blue) whereas the urea reaction shows two peaks at 425 cm^{-1} and 515 cm^{-1} which is characteristic of hematite.[29]

Raman spectroscopy of the powder confirms the samples identity as hematite (figure 33 and table 9). It has been observed that hematite has 7 active bands (five E_g bands and two A_{1g} bands) which are all accounted for in the spectrum below.[29] These bands all relate to iron oxygen bonds within the structure. The initial Raman spectrum is almost identical to the oxidised magnetite sample with the formation of several intense sharp peaks (figures 22 (b) and 33). After continual exposure to the laser, the pattern does not change but the measurement area darkens indicating burning (figure 34). The persistence of the sharp peaks after heating, further confirms that the powder is hematite. These peaks also match with hematite patterns found within the literature.[25,29] The metastable maghemite impurity at 650 cm^{-1} is absent for the hematite sample confirming complete formation of hematite from the urea based reaction.

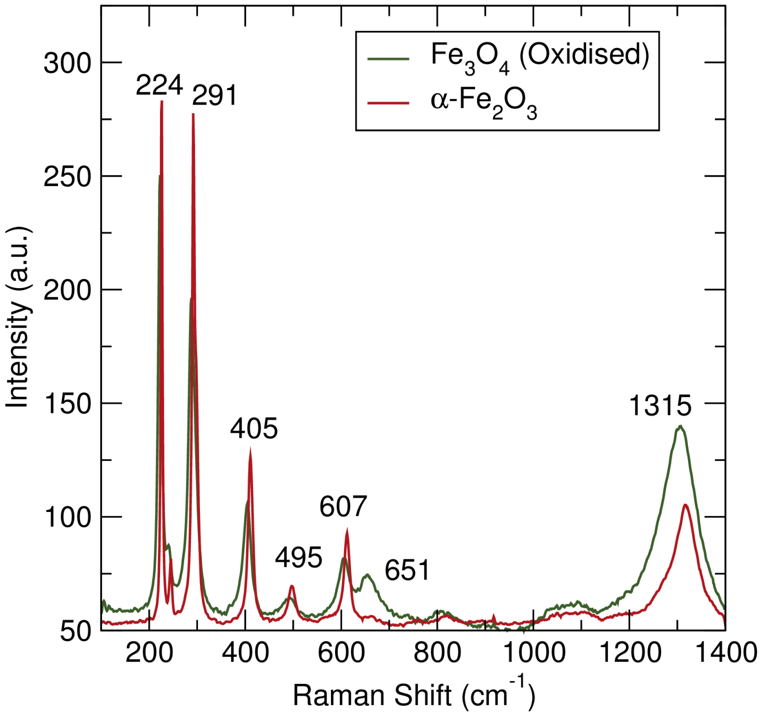

Figure 33: Raman spectra of iron oxide nanoparticles (green) after exposure to a higher power laser and iron oxide particles prepared via a urea based coprecipitation reaction (red, along with peak assignments). After significant exposure to the Raman laser, the spectrum changes significantly to match the hematite sample. A small shoulder remains in the oxidised sample though which is due to a maghemitite impurity.

Table 9: Raman peak and vibrational mode assignment for hematite nanoparticles. The absence of the metastable maghemite impurity at 651cm^{-1} suggests complete transition the iron oxide particles into the hematite crystal structure.

Raman Shift (cm^{-1})	**Vibrational mode**
224	A_{1g}
245	E_g
291	E_g
405	E_g
495	A_{1g}
607	E_g
651	E_u

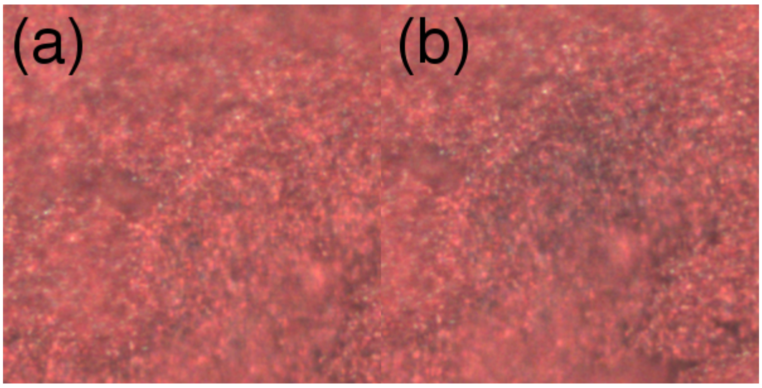

Figure 34: Microscope images of hematite nanoparticles before (a) and after (b) exposure to a higher power laser. The red colour of the powder is characteristic of hematite. After exposure to the laser a darkening of the sample can be seen due to burning.

3.4 Discussion and conclusions

This approach details a co-precipitation method that is quick and simple, which can prepare iron oxide nanoparticles with a similar crystallinity/magnetisation as the iron oxides prepared by solvothermal methods. The TEM and SQUID results show that the incorporation of microwave irradiation is responsible for this increase in crystallinity. This is confirmed by other groups incorporating microwave irradiation into their reactions.[57–59] Many groups found that microwave irradiation enhanced crystal growth to such a degree that particles size increased significantly leading to ferromagnetism.[57,58] Hong *et al.* separated microwave irradiation from the precipitation step to age the nanoparticles afterwards ensuring the particles remain superparamagnetic.[59] They observed that 2 hours ageing improved crystallinity (resulting in a M_s of 70.48 emu/g) while retaining a particle size (9nm) below the critical diameter. The method used in this chapter, utilises ageing to prepare particle of a similar crystallinity and size but demonstrates that similar results can be achieved within in a much shorter timeframe (20 minutes).

Comparing the synthesised iron oxides, the magnetite sample appears to be most suitable for biomedical applications. This sample has the smallest particle size while having the highest magnetisation values and displaying superparamagnetic behaviour. Both the copper and cobalt ferrite samples were unsuitable for biomedical use, with the copper ferrite sample having the lowest magnetisation of all of the samples. The cobalt ferrite sample was the opposite displaying significant ferromagnetism due to the large particle size. Further optimisation would either sacrifice crystallinity (for cobalt ferrite) or significantly alter the particle stoichiometry (for copper ferrite). The most promising alternative is manganese ferrite which has a similar M_s value to magnetite, but further optimisation needs to be made before the particles are suitable for biomedical applications. The larger particle size increases the chance of oponization and elimination from the body. Optimisation of the synthesis method through increased heating times can circumvent these problems leading to the development of a manganese ferrite nanoparticle with enhanced MRI properties and equivalent M_s values to microwave assisted prepared magnetite nanoparticles.[51,53,54]

The other focus of this chapter is the development of a one-pot microwave assisted co-precipitation reaction utilising urea as a base. The method used in this chapter caused the iron oxide to oxidise into the magnetically non responsive hematite. Several groups have avoided the formation of hematite in urea based co-precipitation methods by adjusting the reaction conditions.[60–62] One notable example is the work by Lian *et al.* which undertook a similar co-precipitation reaction but repeated the reaction in both a sealed vessel (as with this chapter) and under reflux.[60] When heated in a sealed vessel hematite forms but when heated under reflux, this oxidation is avoided (forming magnetite). Oxidation was attributed to the carbon dioxide formed from the decomposition of urea. The carbon dioxide formed interacts with the iron groups in a closed vessel oxidising the Fe^{2+} groups forming hematite. Heating the sample under reflux though, stops CO_2 from oxidising the iron oxides. The microwave system can be adapted to support reflux experiments providing a possible way to circumvent the oxidation of the nanoparticles, allowing the development of this one pot synthesis method.

From the results of this chapter, it is clear that microwave assisted coprecipitated magnetite nanoparticles are an excellent foundation for the development of biomedical magnetic nanocomposites. These particles display a high crystallinity with very high M_s values at room temperature without any sacrifice to size or superparamagnetism. In addition to a strong magnetic foundation, the other advantage of using the co-precipitation technique is that stabilisation and functionalisation of the iron oxide can be done simultaneously with precipitation. This allows for the development of water stable functionalised nanocomposites in a single reaction without any addition to the synthesis time. Previous work by the group demonstrates this by stabilising magnetite with the polyelectrolyte PSSS.[63,64] Future work will be to incorporate this stabilisation step into the microwave assisted coprecipitation reaction to prepare water stable highly magnetic nanoparticles that can be used in biomedical applications such as MR imaging.

References

[1] Berry, C. C.; Curtis, A. S. G. *J. Phys. D: Appl. Phys.* **2003**, *36*, 198–206.

[2] Gupta, A. K.; Gupta, M. *Biomaterials* **2005**, *26*, 3995–4021.

[3] Mornet, S.; Vasseur, S.; Grasset, F.; Veverka, P.; Goglio, G.; Demourgues, A.; Portier, J.; Pollert, E.; Duguet, E. *Prog. Solid. State. Ch.* **2006**, *34*, 237–247.

[4] Neuberger, T.; Schöpf, B.; Hofmann, H.; Hofmann, M.; von Rechenberg, B. *J. Magn. Magn. Mater.* **2005**, *293*, 483–496.

[5] Sun, S.; Zeng, H. *J. Am. Chem. Soc.* **2002**, *124*, 8204–8205.

[6] Sun, S.; Zeng, H.; Robinson, D. B.; Raoux, S.; Rice, P. M.; Wang, S. X.; Li, G. *J. Am. Chem. Soc.* **2004**, *126*, 273–279.

[7] Tian, Y.; Yu, B.; Li, X.; Li, K. *J. Mater. Chem.* **2011**, *21*, 2476–2481.

[8] Hou, Y.; Yu, J.; Gao, S. *J. Mater. Chem.* **2003**, *13*, 1983–1987.

[9] Mikhaylova, M.; Kim, D. K.; Bobrysheva, N.; Osmolowsky, M.; Semenov, V.; Tsakalakos, T.; Muhammed, M. *Langmuir* **2004**, *20*, 2472–2477.

[10] Morel, A.-L.; Nikitenko, S. I.; Gionnet, K.; Wattiaux, A.; Lai-Kee-Him, J.; Labrugere, C.; Chevalier, B.; Deleris, G.; Petibois, C.; Brisson, A.; Simonoff, M. *ACS Nano* **2008**, *2*, 847–856.

[11] Fleet, M. E. *Acta. Cryst.* **1981**, *B37*, 917–920.

[12] Mahmoudi, M.; Simchi, .; Milani, A. S.; Stroeve, P. *J. Colloid. Interf. Sci.* **2009**, *336*, 510–518.

[13] Cheng, F.-Y.; Su, C.-H.; Yang, Y.-S.; Yeh, C.-S.; Tsai, C.-Y.; Wu, C.-L.; Wu, M.-T.; Shieh, D.-B. *Biomaterials* **2005**, *26*, 729–738.

[14] Kim, D. K.; Zhang, Y.; Voit, W.; Rao, K. V.; Muhammed, M. *J Magn. Magn. Mater.* **2001**, *225*, 30–36.

[15] Li, F.; Liu, J.; Evans, D. G.; Duan, X. *Chem. Mater.* **2004**, *16*, 1597–1602.

[16] Gomes, J.; Sousa, M.; Tourinho, F.; Itri, M.-F. R.; Depeyrot, J. *J. Magn. Magn. Mater.* **2005**, *289*, 184–187.

[17] Antic, B.; Kremenović, A.; Nikolic, A. S.; Stoiljkovic, M. *J. Phys. Chem. B* **2004**, *108*, 12646–12651.

[18] Ferreira, T.; Waerenborgh, J.; Mendonça, M.; Nunes, M.; Costa, F. *Solid State Sci.* **2003**, *5*, 383–392.

[19] Valdés-Solís, T.; Tartaj, P.; Marbán, G.; Fuertes, A. B. *Nanotechnology* **2007**, *18*, 145603.

[20] Zaitsev, V. S.; Filimonov, D. S.; Presnyakov, I. A.; Gambino, R. J.; Chu, B. *J. Colloid Interf. Sci.* **1999**, *212*, 49–57.

[21] Ponhan, W.; Maensiri, S. *Solid State Sci.* **2009**, *11*, 479–484.

[22] Kodama, T.; Ookubo, M.; Miura, S.; Kitayama, Y. *Mater. Res. Bull.* **1996**, *31*, 1501–1512.

[23] Naseri, M. G.; Saion, E. B.; Ahangar, H. A.; Shaari, A. H.; Hashim, M. *J. Nanomater* **2010**, *2010*, 1–8.

[24] Gasparov, L. V.; Arenas, D.; Choi, K.-Y.; Güntherodt, G.; Berger, H.; Forro, L.; Margaritondo, G.; Struzhkin, V. V.; Hemley, R. *J. Appl. Phys.* **2005**, *97*, 10A922.

[25] Shebanova, O. N.; Lazor, P. *J. Solid State Chem.* **2003**, *174*, 424–430.

[26] de Faria, D. L. A.; Silva, S. V.; de Oliveira, M. T. *J. Raman Spectrosc.* **1997**, *28*, 873–878.

[27] Shebanova, O. N.; Lazor, P. *J. Raman Spectrosc.* **2003**, *34*, 845–852.

[28] Chamritski, I.; Burns, G. *J. Phys. Chem. B* **2005**, *109*, 4965–4968.

[29] Chernyshova, I. V.; Hochella, M. F.; Madden, A. S. *Phys. Chem. Chem. Phys.* **2007**, *9*, 1736–1750.

[30] Soler, M.; Melo, T.; da Silva, S.; Lima, E.; Pimenta, A.; Garg, V.; Oliveira, A.; Morais, P. *J. Magn. Magn. Mater.* **2004**, *272–276*, 2357–2358.

[31] Qu, Y.; Yang, H.; Yang, N.; Fan, Y.; Zhu, H.; Zuo, G. *Mater. Lett.* **2006**, *60*, 3548–3552.

[32] da Silva, S. W.; Melo, T. F. O.; Soler, M.; Lima, E.; da Silva, M. F.; Morais, P. C. *IEEE. T. Magn.* **2003**, *39*, 2645–2647.

[33] Varshney, D.; Yogi, A. *Mater. Chem. Phys.* **2010**, *123*, 434–438.

[34] Daou, T. J.; Pourroy, G.; Bégin-Colin, S.; Grenèche, J. M.; Ulhaq-Bouillet, C.; Legaré, P.; Bernhardt, P.; Leuvery, C.; Rogez, G. *Chem. Mater.* **2006**, *18*, 4399–4404.

[35] Goya, G. F.; Berquó, T. S.; Fonseca, F. C.; Morales, M. P. *J. Appl. Phys.* **2003**, *94*, 3520–3528.

[36] Lu, A.-H.; Salabas, E. L.; Schüth, F. *Angew. Chem., Int. Ed.* **2007**, *46*, 1222–1244.

[37] Pankhurst, Q. A.; Connolly, J.; Jones, S. K.; Dobson, J. *J. Phys. D: Appl. Phys.* **2003**, *36*, R167–R179.

[38] Pankhurst, Q. A.; Thanh, N. K. T.; Jones, S. K.; Dobson, J. *J. Phys. D: Appl. Phys.* **2009**, *42*, 224001.

[39] Morais, P.; Garg, V.; Oliveira, A.; Silva, L.; Azevedo, R.; Silva, A.; Lima, E. *J. Magn. Magn. Mater.* **2001**, *225*, 37–40.

[40] Maaz, K.; Mumtaz, A.; Hasanain, S.; Ceylan, A. *J. Magn. Magn. Mater.* **2007**, *308*, 289–295.

[41] Kim, Y. I.; Kim, D.; Lee, C. S. *Physica B* **2003**, *337*, 42–51.

[42] Rajendran, M.; Pullar, R.; Bhattacarya, A.; Das, D.; Chintalapudi, S.; Majumdar, C. *J. Magn. Magn. Mater.* **2001**, *232*, 71–83.

[43] Roy, S.; Ghose, J. *J. Appl. Phys.* **2000**, *87*, 6226–6228.

[44] Jiang, J. Z.; Goya, G. F.; Rechenberg, H. R. *J. Phys.: Condens. Matter* **1999**, *11*, 4063–4078.

[45] Goya, G.; Rechenberg, H. *Nanostruct. Mater.* **1998**, *10*, 1001–1011.

[46] Tao, S.; Gao, F.; Liu, X.; Sørensen, O. T. *Mater. Sci. Eng.* **2000**, *B77*, 172–176.

[47] Despax, C.; Tailhades, P.; Baubet, C.; Villette, C.; Rousset, A. *Thin Solid Films* **1997**, *293*, 22–28.

[48] Thapa, D.; Kulkarni, N.; Mishra, S. N.; Paulose, P. L.; Ayyub, P. *J. Phys. D: Appl. Phys.* **2010**, *43*, 195004.

[49] Deraz, N. M.; Shaban, S. *J. Anal. Apply. Pyrolysis* **2009**, *86*, 173–179.

[50] Tang, Z. X.; Sorensen, C. M.; Klabunde, K. J.; Hadjipanayis, G. C. *J. Appl. Phys.* **1991**, *8*, 5279–5281.

[51] Lu, J.; Ma, S.; Sun, J.; Xia, C.; Liu, C.; Wang, Z.; Zhao, X.; Gao, F.; Gong, Q.; Song, B.; Shuai, X.; Ai, H.; Gu, Z. *Biomaterials* **2009**, *30*, 2919–2928.

[52] Woo, K.; Hong, J.; Choi, S.; Lee, H.-W.; Ahn, J.-P.; Kim, C. S.; Lee, S. W. *Chem. Mater.* **2004**, *16*, 2814–2818.

[53] Lee, J.; Huh, Y.; Jun, Y.; Seo, J.; Jang, J.; Song, H.; Kim, S.; Cho, E.; Yoon, H.; Suh, J.; Cheon, J. *Nat. Med.* **2007**, *13*, 95–99.

[54] Tromsdorf, U. I.; Bigall, N. C.; Kaul, M. G.; Bruns, O. T.; Nikolic, M. S.; Mollwitz, B.; Sperling, R. A.; Reimer, R.; Hohenberg, H.; Parak, W. J.; Fŏrster, S.; Beisiegel, U.; Adam, G.; Weller, H. *Nano Lett.* **2007**, *7*, 2422–2427.

[55] Chen, J. P.; Sorensen, C. M.; Klabunde, K. J.; Hadjipanayis, G. C.; Devlin, E.; Kostikas, A. *Phys. Rev. B* **1996**, *54*, 9288–9296.

[56] Blake, R. L.; Hessevick, R. E.; Zoltai, T.; Finger, L. W. *Am. Mineral.* **1966**, *51*, 123–129.

[57] Khollam, Y.; Dhage, S.; Potdar, H.; Deshpande, S.; Bakare, P.; Kulkarni, S.; Date, S. *Mater. Lett.* **2002**, *56*, 571–577.

[58] Wang, W.-W.; Zhu, Y.-J.; Ruan, M.-L. *J. Nanopart. Res.* **2007**, *9*, 419–426.

[59] Hong, R.; Pan, T.; Li, H. *J. Magn. Magn. Mater.* **2006**, *303*, 60–68.

[60] Lian, S.; Wang, E.; Kang, Z.; Bai, Y.; Gao, L.; Jiang, M.; Hu, C.; Xu, L. *Solid State Commun.* **2004**, *129*, 485–490.

[61] Cheng, W.; Tang, K.; Qi, Y.; Sheng, J.; Liu, Z. *J. Mater. Chem.* **2010**, *20*, 1799–1805.

[62] Liao, X.; Zhu, J.; Zhong, W.; Chen, H.-Y. *Mater. Lett.* **2001**, *50*, 341–346.

[63] Corr, S. A.; Gun’ko, Y. K.; Tekoriute, R.; Meledandri, C. J.; Brougham, D. F. *J. Phys. Chem. C* **2008**, *112*, 13324–13327.

[64] Corr, S. A.; Byrne, S. J.; Tekoriute, R.; Meledandri, C. J.; Brougham, D. F.; Lynch, M.; Kerskens, C.; O’Dwyer, L.; Gun’ko, Y. K. *J. Am. Chem. Soc.* **2008**, *130*, 4214–4215.

Chapter 4: Polyelectrolyte stabilised magnetic nanoparticles

4.1 General introduction and objectives

Chapter 3 demonstrated that microwave heating combined with traditional aqueous co-precipitation methods allows for the fast and easy synthesis of highly crystalline magnetic nanoparticles. The particles obtained are single domain and superparamagnetic, making them ideal candidates for further development as MRI contrast agents. This chapter aims to prepare a magnetic nanocomposite using these magnetite cores, stabilised with a hydrophilic coating in the form of a polyelectrolyte. These polyelectrolytes will be bound to the nanoparticle surface to bestow water stability on the magnetic cores. A polyelectrolyte is a charged polymer, where multiple charged groups along the polymer chain can act as binding sites for surface iron atoms and the resulting polyelectrolyte-nanoparticle composite is water stable. Such binding is depicted in Figure 35.

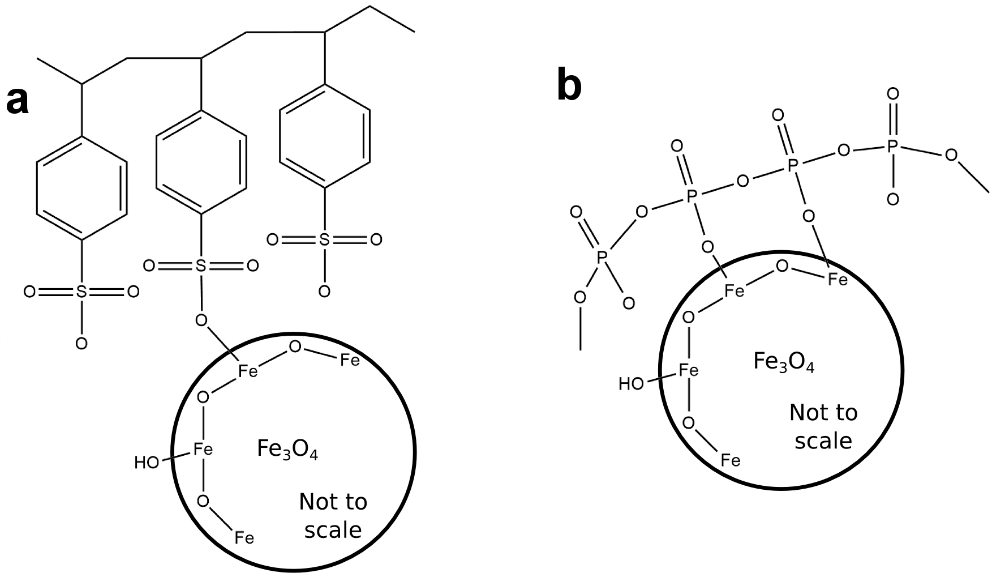

PSSS-stabilised iron oxide **SPP-stabilised iron oxide**

Figure 35: Schematic of the proposed one pot co-precipitation and stabilisation reaction of magnetite nanoparticles with poly(sodium-4-styrenesulfonate) (PSSS) and sodium polyphosphate (SPP) showing multiple possible binding groups to iron oxide surface.

The stability could be enhanced by the accompanying electrostatic interactions between the nanoparticle surface and the polyelectrolyte. Other possible interactions could occur through cross linking of neighbouring polyelectrolyte strands. The final composite will be a hydrophilic polyelectrolyte platform that supports multiple magnetite nanoparticles, allowing the normally unstable iron oxide cores to be dispersed in water. The type of polyelectrolyte employed could also affect the properties of the final nanocomposites by altering the surface chemistry of the magnetic core.[1,2]

Two different polyelectrolytes were investigated and the proposed reactions are shown in Figure 36. Poly(sodium-4-styrene sulfonate) (PSSS) is a negatively charged polyelectrolyte which binds through a sulfonate group to iron atoms on the magnetite surface. Previous work has demonstrated PSSS as an effective stabiliser for the preparation of stable iron oxide nanoparticles using a traditional coprecipitation approach.[3,4] To date, microwave approaches to enhancing the crystallinity and water stability have not been explored. This is the major aim of the current chapter. Sodium polyphosphate, also a negatively charged polyelectrolyte, was investigated to check the effect, if any, of the nature of the polyelectrolyte on the resulting particles. This is the first investigation of the use of this polyelectrolyte for the stabilisation of iron oxide nanoparticles for biomedical applications.

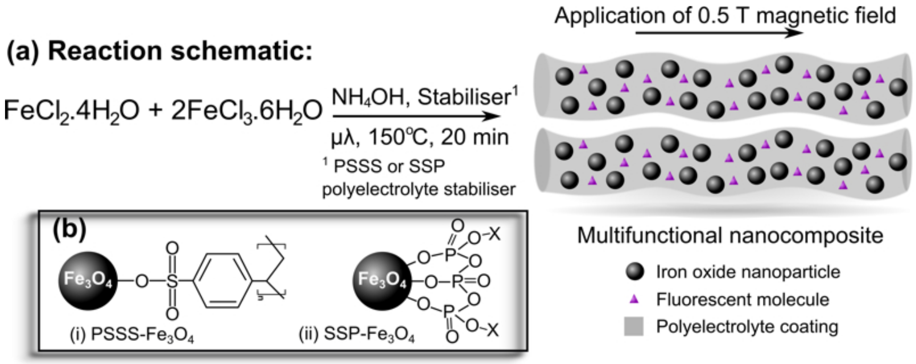

Figure 36: A schematic illustrating a nanocomposite comprised of iron oxide nanoparticles, with a polyelectrolyte stabiliser (PSSS or SPP). Also included in this scheme is the proposed incorporation of a fluorescent molecule during the coating process (Rhodamine B).

4.2 Characterisation of polyelectrolyte-Fe_3O_4 nanocomposites

A similar microwave-assisted method to that developed in Chapter 3 has been employed and is depicted in Figure 36. Here, the polyelectrolyte is added to the starting iron chloride solution, so that as the particles are precipitated they are simultaneously stabilised. The precipitated nanoparticles were washed several times with water and finally with acetone, with the dried powder characterised using XRD, TGA, HRTEM and SQUID measurements. The water stable washings were retained and characterised using FTIR, DLS, TEM and AAS. Cytotoxicity and MR efficacy were also investigated.

4.2.1 Structural characterisation

Powder XRD patterns were collected to characterise the iron oxide core and to calculate the average crystallite size using the Scherrer equation. The patterns for PSSS-Fe_3O_4 (blue line) and SPP-Fe_3O_4 (purple line) are shown in Figure 37, together with unfunctionalised Fe_3O_4 nanoparticles prepared using the same method but without the addition of polyelectrolyte (yellow line). The patterns collected match that of the magnetite standard from the ICSD database and to previously reported XRD patterns of Fe_3O_4.[5–9] The broad peaks observed indicate small particles, with crystallite sizes calculated from the Scherrer equation as 16.1 nm for PSSS-Fe_3O_4 and 10.9 nm for SPP-Fe_3O_4 (in comparison to microwave-assisted bare magnetite, with a size of 11.2 nm). This difference in calculated size indicates the polyelectrolyte stabiliser may have an effect on the primary particle size.

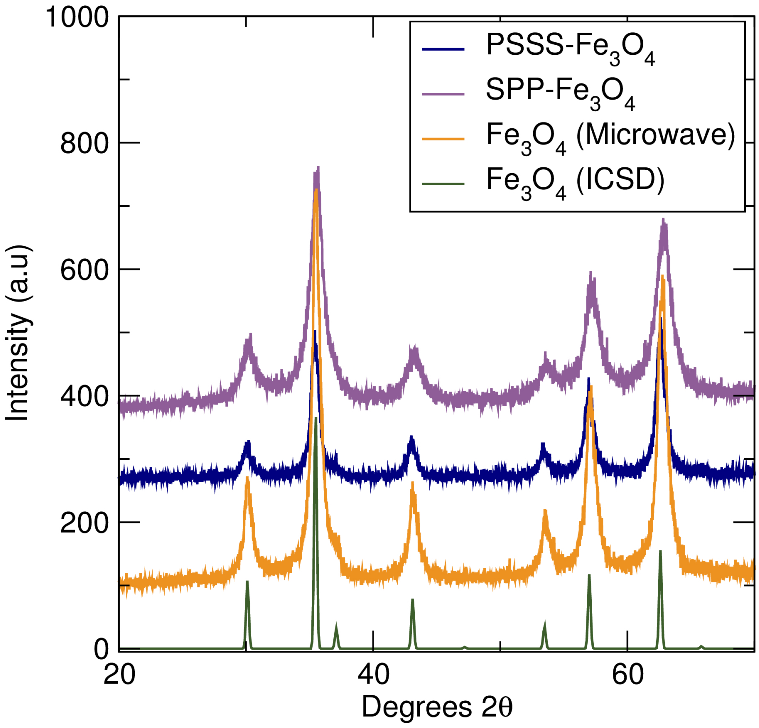

Figure 37: XRD patterns for stabilised samples using microwave assisted coprecipitation: bare magnetite (orange), PSSS-labelled magnetite (navy) and SSP-labelled magnetite (purple). For comparison, a standard pattern of magnetite from the ICSD database (green) is also included.[5]

4.2.2 Surfactant characterisation

FTIR spectroscopy and TGA were used to confirm the presence of the polyelectrolyte coating on the nanoparticle surface. Both samples gave an Fe-O stretch at 533 cm^{-1} and a smaller O-H broad absorption at 3400 cm^{-1} due to water physically adsorbed on the particle surface. In the case of PSSS-Fe$_3$O$_4$, an Fe-O-S stretch is noted at 669 cm^{-1} (Figure 38 (a)), which indicates the binding of the charged sulfonate group of PSSS to the magnetite surface through the surface iron atoms. The sulfonate group also gives S-O stretches at 830 and 775 cm^{-1} and R-SO$_2$-OR stretches at 1405, 1160 and 1115 cm^{-1}. The aromatic group of the polyelectrolyte gives a broad C-C stretch at 1610 cm^{-1}. The C-H bonds in the alkane backbone gives a broad stretch at 2991 cm^{-1} which begin to merge with the O-H peaks. All of these stretches observed here are in good agreement with similar stretches reported in the literature.[3,4,10]

In the case of the SPP-Fe_3O_4 sample (Figure 38b), an Fe-O-P stretch is observed at 992 cm^{-1}.[11,12] This indicates binding of the polyelectrolyte through the phosphate groups to surface iron atoms. Asymmetric vibrations of the phosphate backbone are observed at 869 cm^{-1} (P-O-P bond) and at 1255 cm^{-1} (O-P-O bond). Terminal phosphate groups, which are indicative of free (i.e., unbound to the nanoparticle surface) SPP, are represented by a stretch at 1085 cm^{-1}. Broadening of the peaks is due to the use of a long chain polyelectrolyte, as the repeating signals of the bridging phosphate groups interfere with each other, resulting in a broadening effect. Gong *et al.* undertook an extensive study into phosphate chains and the effect of binding and pH in ATR-FTIR measurements.[13] They identified that the free P-O signal (1085 cm^{-1}), shifts to lower wavenumbers when it forms a P-OH group or binds to a metallic surface. Gosh *et al.* confirmed that this shifting effect occurs when bound to iron oxides.[14] The shifting of the 1255 cm^{-1} peak in the SPP-Fe_3O_4 sample prepared here to the lower wavelength of 950 cm^{-1} is indicative of this binding effect. As the peak is shifted, it begins to overlap with the stretches assigned to the phosphate backbone (869 cm^{-1}) leading to the formation of the large peak rather than the series of smaller individual signals, also contributing to this broadening effect.

TGA was also used to further confirm the presence of the polyelectrolyte coating on the magnetic cores. Samples were measured in air. Bare magnetite presents a single mass loss of 3.4% between 60°C and 160°C due to the removal of solvent molecules (water and acetone) trapped on the iron oxide surface from the washing of the samples (Figure 39, yellow line). The mass increase between 200-300°C is due to oxidation of the Fe^{2+} ions in the magnetite core from being heated in air. When heated, these groups are oxidised into Fe^{3+} groups, transitioning the core into maghemtite (γ-Fe_2O_3) and after prolonged oxidation into hematite (α-Fe_2O_3). The brick red colour of the heated sample indicates complete oxidation of Fe^{2+} to Fe^{3+} and this transition is similar to previous reports of TGA measurements by other groups.[15,16] They have observed a mass gain in the TGA measurements due to the oxidation of Fe^{2+} groups, and confirmed the transformation of the powder into hematite at

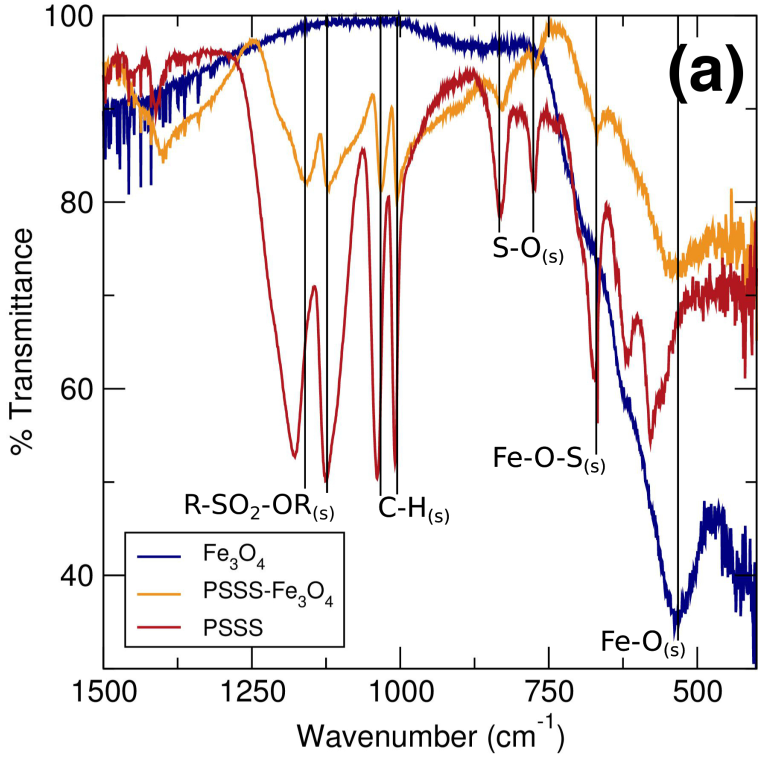

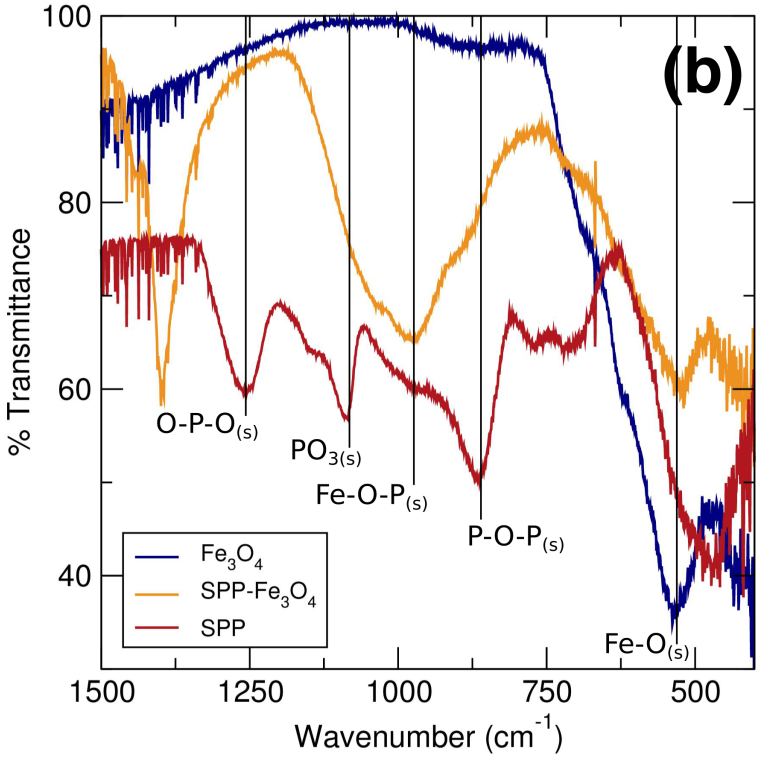

Figure 38: FTIR spectra of (a) PSSS-Fe$_3$O$_4$ (yellow), bare Fe$_3$O$_4$ (blue) and PSSS (red). the magnetic nanocomposite stabilised with PSSS (yellow), bare magnetite (blue) and unbound PSSS (red). (b) FTIR spectra of SPP-Fe$_3$O$_4$ (yellow), bare Fe$_3$O$_4$ (blue) and SPP (red).

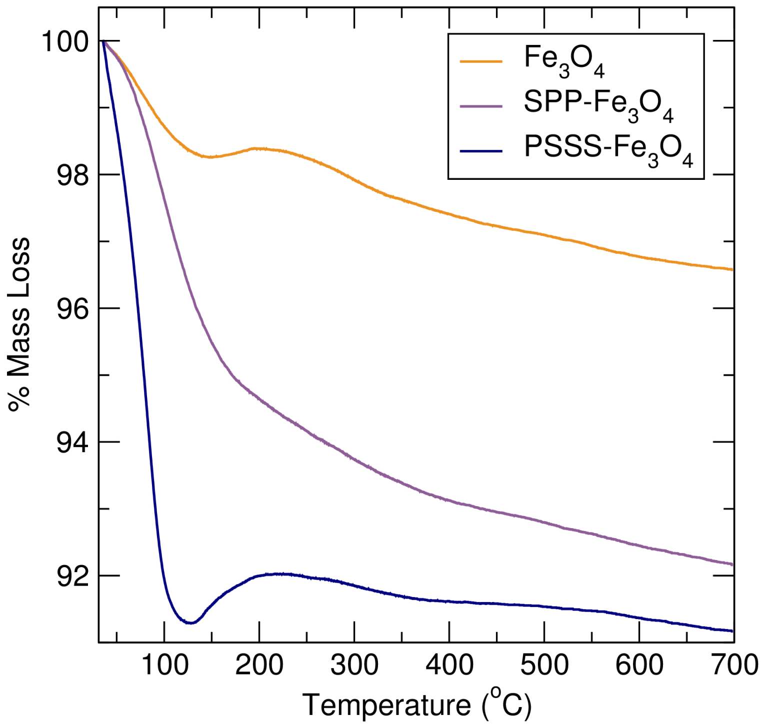

Figure 39: Thermogravimetric analysis for both magnetite (yellow), PSSS stabilised magnetite (blue) and SPP stabilised magnetite (purple) samples measured in air. The PSSS and SPP stabilised samples show large mass losses (9.3% and 7.8% respectively), with the heavier PSSS polyelectrolyte showing the greater mass loss. All samples show a mass increase at 200° C due to the oxidation of the magnetite cores from being measured in air.

high temperatures. The stabilised samples have a much greater mass loss due to removal of the polyelectrolyte. In the case of PSSS-Fe_3O_4, there is a loss of 9.3% due to removal of the polyelectrolyte stabiliser while for SPP-Fe_3O_4 this is lower at 7.8%.

4.2.3 Particle size and crystallinity

Electron microscopy was used to examine the size of the iron oxide nanoparticles and to determine the effects of microwave irradiation and choice of polyelectrolyte stabiliser on the resulting particle morphology. Primary particle sizes were measured over 100 particles from TEM images of samples dried in ambient conditions (see Figures 40 to 42 and Table 10). Aggregation was observed in all samples dried under ambient conditions. This is due to drying effects from preparing the grids and in the case of polyelectrolyte stabilised samples the presence of the stabiliser may also cause aggregation.[17] The primary particle sizes for all samples were less than 15 nm, placing them within the critical size diameter for a single domain iron oxide nanoparticle. The effect of the polyelectrolyte can be seen in the variation between primary particle sizes, with the PSSS sample (13.4 nm) being slightly larger than bare magnetite (12.1 nm). SPP-Fe_3O_4 particles are significantly smaller (10.9 nm). The measured sizes are in good agreement with the Scherrer broadening sizes calculated from the XRD patterns.

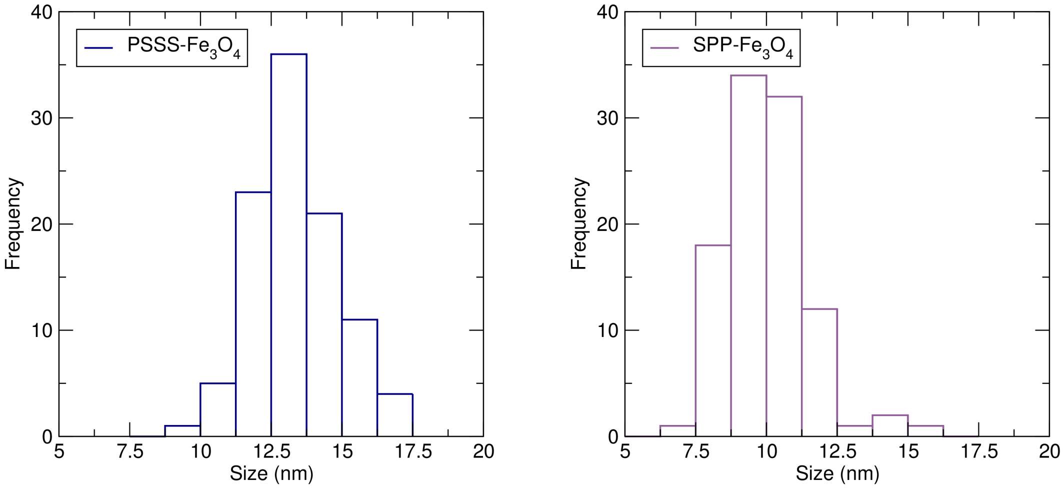

Figure 40: Histograms of the primary particle sizes of PSSS-stabilised magnetite (blue) and SPP-stabilised magnetite (purple) calculated from TEM images of the particles dried in ambient conditions (N=100). PSSS-Fe_3O_4 particles are larger in size but with a narrower size distribution, whereas SPP-Fe_3O_4 particles are smaller but larger in spread.

High resolution electron microscopy images in Figure 41 show that single crystal magnetite nanoparticles form regardless of the stabiliser used. However, the stabiliser has a significant effect on the resulting morphology and crystallinity of the magnetic core. The PSSS stabilised nanocomposites (figure 41 (a), (c)) appear highly crystalline in nature and are slightly larger than either the pure Fe_3O_4 (Chapter 3) or the SPP-Fe_3O_4 sample. The particle shape is regular and faceted. The SPP nanocomposites (figure 41 (b), (d)) are much more irregular in shape and less defined. The lattice spacings in the HRTEM images are characteristic of magnetite crystals and that combined with the SAED measurements further confirms the magnetite identity of the core. The SAED results agrees with previous XRD results and other SAED magnetite patterns presented in the literature.[15,18]

Table 10: Particle sizes calculated from TEM images, where N = 100 particles. The primary particle sizes were calculated from grids dried under ambient conditions. The assembly widths were also measured from particles dried in the 0.5T external field. The polyelectrolyte employed significantly affects primary particle size and the formation of these assemblies.

Stabiliser	**Particle size** (nm)	**S.D.** (nm)	**Assembly width** 0.5T field (nm)	**S.D.** (nm)
PSSS-Fe_3O_4	13.4	1.5	61.6	18.2
SPP-Fe_3O_4	10.9	1.4	477.7	167.5

When exposed to an 0.5 T external magnetic field, the PSSS-Fe_3O_4 nanocomposites form roughly linear assemblies aligned with the applied field. SPP-Fe_3O_4, on the other hand, displays a minimal response (Figures 42 and 43). The PSSS assemblies were a few particles wide but typically over 500 nanometers in length. This behaviour is likely due to the nature of the polyelectrolytes employed. PSSS is a strong polyelectrolyte that is fully deionised in the basic solutions that the particles were precipitated in.[19–22] When fully deionised, this has two effects. Firstly, all sulfonate sites are available for binding. Additionally, the charged sulfonate groups will tend to repel each other forcing the polyelectrolyte to adopt a linear shape.[23,24] When the polyelectrolyte is saturated with magnetite nanoparticles, the remaining unbound sulfonate groups repel each other promoting the formation of a linear structure. After washing until neutral, the free sulfonate groups are no longer charged, do not repel each other and the entire nanocomposite can aggregate when dried under ambient conditions (Figure 42 b). In the presence of an external magnetic field, the nanocomposite can then realign into chains, which may be aided by cross linking of neighbouring PSSS chains. The linear assembly will have a much greater surface area than a larger cluster such as SPP-Fe_3O_4 (Figure 42 d, e). This is an interesting consideration for MR efficacy, since a higher surface area linear assembly should interact with more of the surrounding protons thereby enhancing contrast agent effectiveness.

The SPP stabilised sample clustered and agglomerated, with a slight orientation to the external magnetic field instead of forming narrow linear assemblies. This is due to SPP being a weak polyelectrolyte and is not completely disassociated in the basic solution that the particles are precipitated in.[21,25,26] This blocks binding sites and reduces the repulsion between monomer groups. Ultimately this stops the formation of linear assemblies, instead promoting the formation of loops and curls in the polyelectrolyte which causes clustering and the formation of a thicker polyelectrolyte layer.[21,27–29] Additionally the restricted binding sites means that less magnetite is bound to each polyelectrolyte chain making the overall chain less responsive in an external magnetic field.

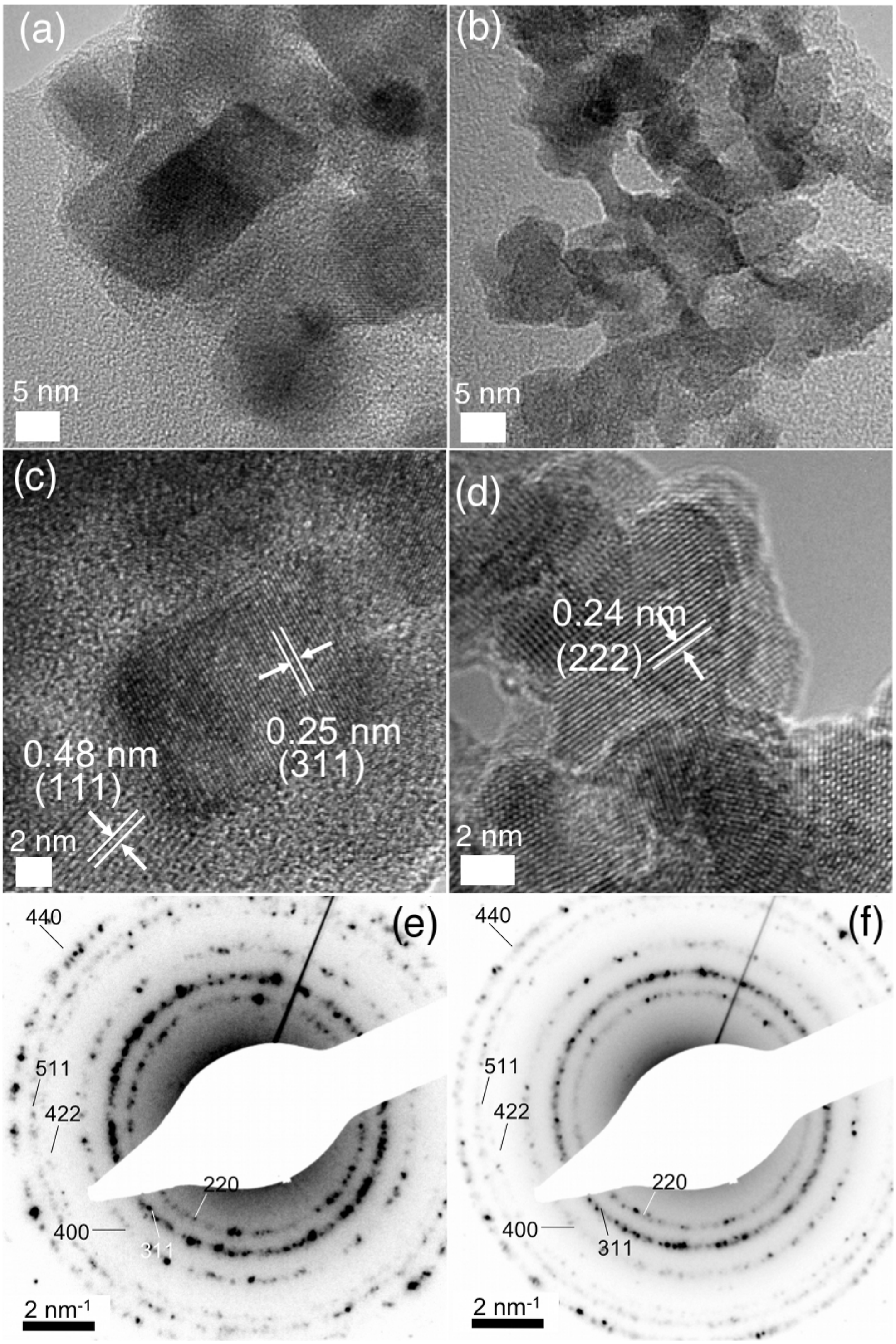

Figure 41: High resolution TEM images (images a-d) and SAED images (images e and f) were taken of both the PSSS (images a, c and e) and SPP (images b, d and f) stabilised samples. Lattice spacings and SAED measurements confirm the magnetite core.

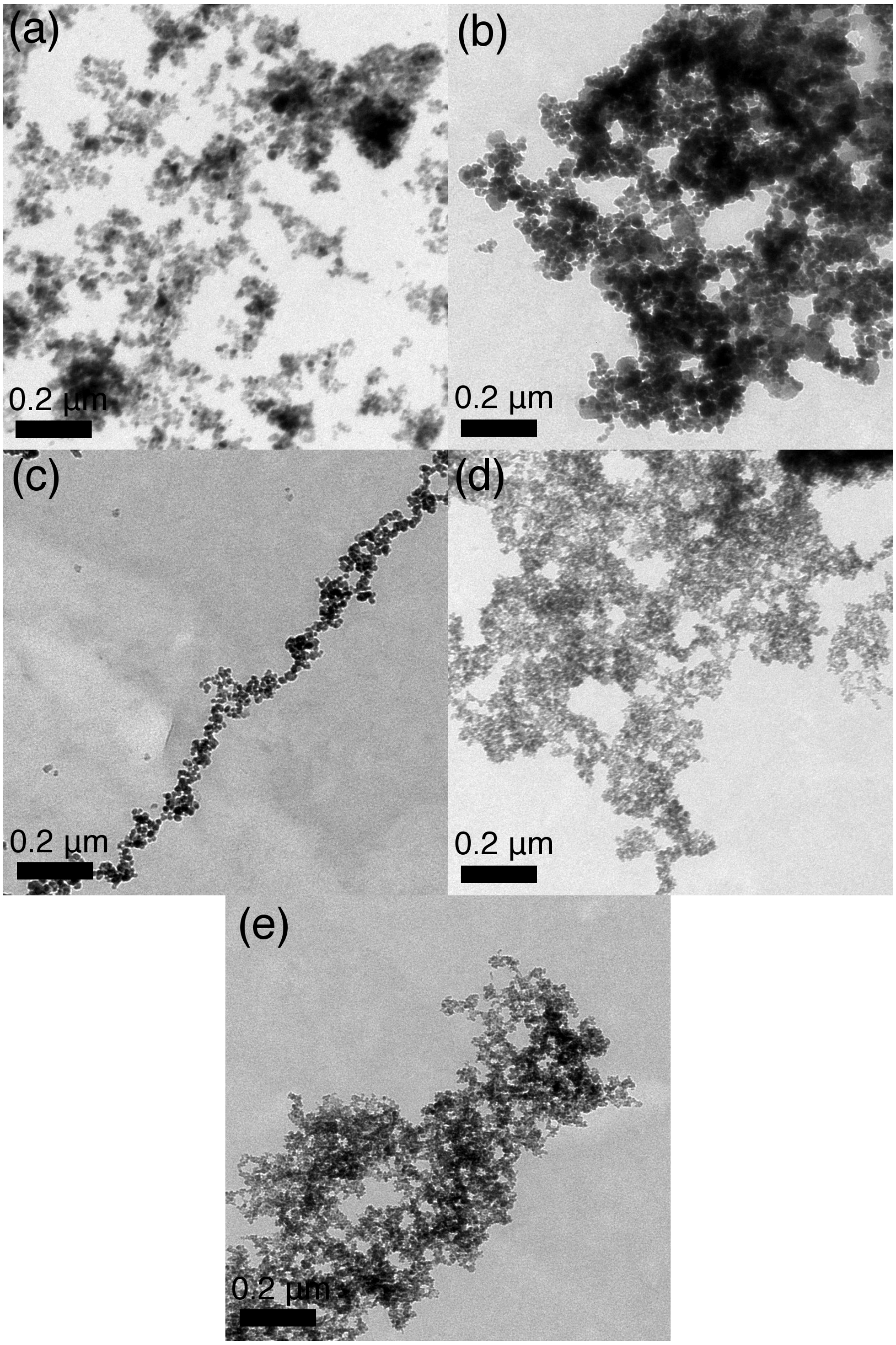

Figure 42: TEM images of (a) bare magnetite nanoparticles, (b) PSSS-Fe_3O_4 *dried in ambient conditions, (c) PSSS-*Fe_3O_4 *dried in an external 0.5 T magnetic field, (d) SPP-*Fe_3O_4 *dried in ambient conditions and (e) SPP-*Fe_3O_4 *dried in an external 0.5 T magnetic field. Clustering observed under ambient conditions for both samples, while the PSSS sample forms thin linear assemblies in a magnetic field.*

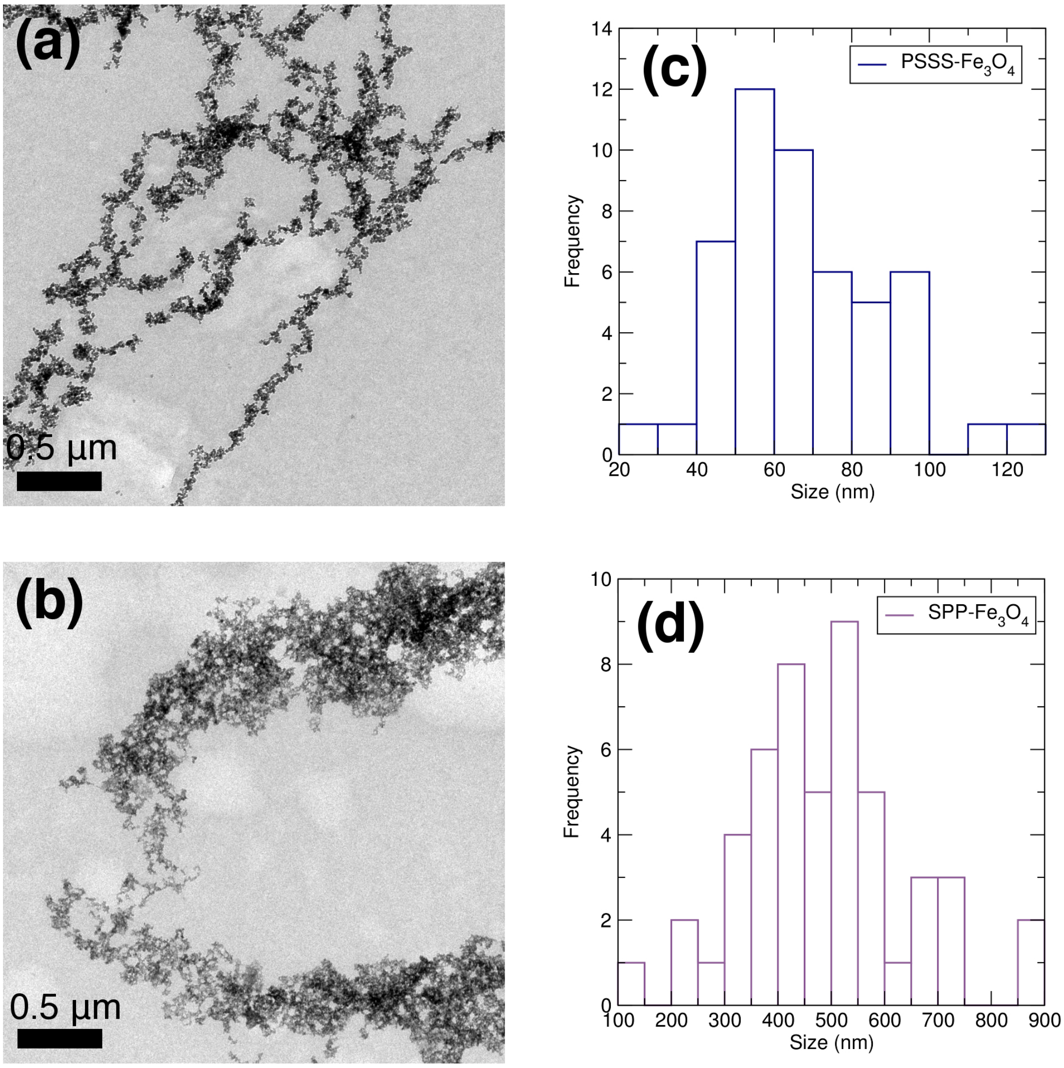

Figure 43: TEM images (a, c) and histograms (b, d) of PSSS-Fe_3O_4 and SPP-Fe_3O_4 nanocomposites, respectively, dried in an external magnetic field. The PSSS composite forms thin linear assemblies, which are several particles wide whereas the SPP samples formed much larger aggregates normally over 200 nm in size

4.2.4 Suspension behaviour

DLS was used to determine how the composites behave and aggregate in water suspensions. The addition of the polyelectrolyte coating provides a hydrophilic layer for the nanoparticles, allowing dispersion in aqueous suspension. As the particles are washed to neutral and as pH 7 is approached, they become more readily dispersed in water. Stability in this case was defined as a suspension of particles which remained in water without precipitating after sitting on a 0.5 T magnet overnight. At pH 7, very stable suspensions of iron oxide nanoparticles in water were obtained. The suspension behaviour of each washing was characterised using DLS and the results are presented in Table 11.

Table 11: DLS measurements of the PSSS-Fe_3O_4 nanocomposite. Slight differences can be seen between the polyelectrolyte types, with the SPP based samples having a larger hydrodynamic radius due to polyelectrolyte folding and looping. Zeta potentials (Z. Po.) indicate a high water stability

Sample	**Dispersion 3**		**Dispersion 4**		**Dispersion 5**		**Z. Po.**
	Z-Average (d.nm)	**PDI**	**Z-Average** (d.nm)	**PDI**	**Z-Average** (d.nm)	**PDI**	(mV)
PSSS-Fe_3O_4	166	0.248	82.78	0.111	94.7	0.097	-41.5
SPP-Fe_3O_4	171.5	0.262	137.1	0.204	104.9	0.158	-48.2

As the suspensions approach neutrality, the Z-averages and polydispersity indices (PDIs) decrease and cluster distribution shifts to monomodal (Figure 44). Clusters with a Z-average of around 100 nm are observed for both samples at pH 7. Although the Z-averages for both final dispersions are similar, there is a large difference in the PDIs, which may be attributed to the behaviour of the polyelectrolyte. In weak polyelectrolytes, such as SPP, the presence of loops and folds in the stabiliser results in the formation of a thicker polyelectrolyte layer.[21,27–29] Netz *et al.* explored the absorption mechanics of weak polyelectrolytes, detailing how the weak polyelectrolyte chain is more flexible (due to less repulsion between monomers), and therefore more susceptible to forming loops and folds in solution.[24] Several groups have measured this thickness increase experimentally using ellipsometery.[21,30,31] In all measurements, it was found that the weak polyelectrolyte forms thicker layers (with a greater variance in size) than strong polyelectrolytes (which take a linear conformation due to monomer repulsion and therefore lie flat on the particle surface). This local clustering of the polyelectrolyte results in a more polydisperse and slightly larger nanocomposite. Manipulating the formation of loops and curls is commonly done in the development and tailoring of layer-by-layer nanocomposites as it allows for the development of pH responsive polyelectrolyte films.[27,30] For most biomedical applications, it is desirable for the particles to be 200 nm or less, with the nanocomposites discussed within this chapter in this size range.[32–34] Both samples display enhanced water stability by staying in suspension for over a month, even in the presence of an external 0.5 T magnetic field. The final PSSS-Fe_3O_4 suspension was extremely stable staying in suspension for several months. This enhanced stability compared to particles prepared without the additional microwave step suggests that these suspensions show good promise as contrast agents for MR imaging.

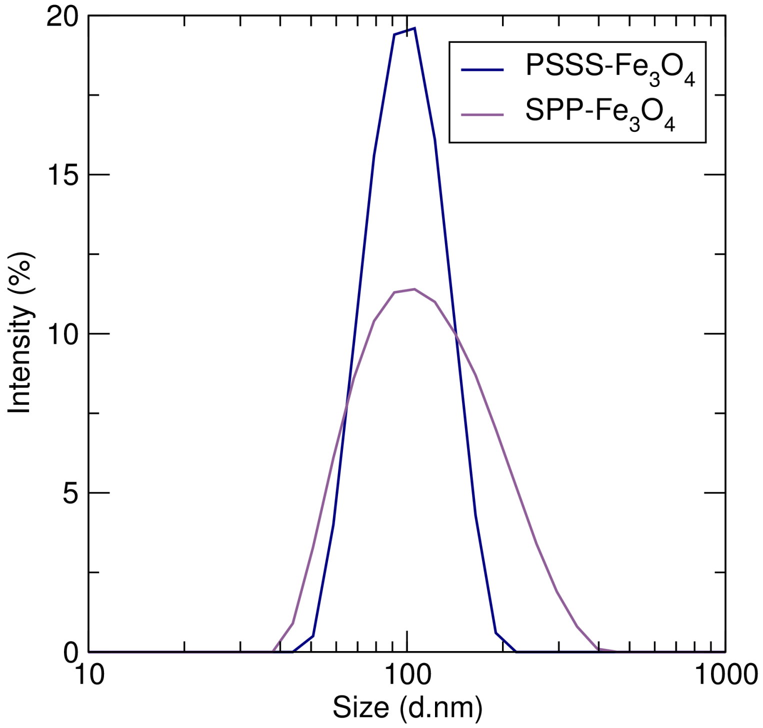

Figure 44: Size distribution of PSSS-Fe_3O_4 and SPP-Fe_3O_4 in aqueous suspension measured at pH 7 using DLS. The PSSS stabilised sample showed a smaller size distribution as the polyelectrolyte will not fold or curl to the same extent as SPP.

The surface charge of the particles was also measured using DLS. This technique measures the zeta potential of particles in suspension, which is an indicator of possible agglomeration/clustering. The zeta potential is based on the surface charge of particles and how water molecules are attracted and dragged by the particle surface. Zeta potentials below -30 mV or above 30 mV are considered water stable and will show little agglomeration.[35] Bare magnetite has a charge (-12.5 mV) and which is reflected by its high instability in water. When stabilised with polyelectrolytes, the zeta potentials for both composite types increases to over -40 mV again further supporting the high water stability.

4.2.5 Magnetic property measurements

The magnetic properties of the nanocomposites were measured using a SQUID and magnetisation curves recorded at 300 K and 10 K in a magnetic field of up to 2 x 10^4 G are shown in Figure 45. From Figure 45, it can be seen that there is negligible coercivity and remanence noted at 300 K, indicative of superparamagnetic, single-domain iron oxide particles. The magnetisation is unsaturated up to 2 T, even at 10 K. Uncoated magnetite prepared using similar microwave-assisted methods gives a saturation magnetisation of 65.2 emu/g at 300 K, as discussed in Chapter 3.[36] While this is lower than the theoretical value for bulk magnetite of 98 emu/g (most likely due to spin disorder on the particle surface), this value is higher than the previously reported saturation magnetisation values for aqueous routes to iron oxide nanoparticles (40-50 emu/g).[4,37] By employing polyelectrolytes as stabilisers here, it is observed that primary particle sizes and morphologies change and this, in turn, has a marked effect on the resulting magnetic properties. The SPP-stabilised particles have a reduced M_S value of 49.7 emu/g at 300 K (Figure 45c). The PSSS-stabilised samples, on the other hand, have an M_S value of 71.8 emu/g at 300 K (Figure 45a). While this value is still lower than that of the theoretical value for bulk magnetite, this can be explained by a reduction in M_S due to the presence of the nonmagnetic polyelectrolyte stabiliser.[18] Interestingly, the magnetisation value here is significantly higher that M_S values previously obtained from NMRD data for PSSS-stabilised Fe_3O_4 (30-50 emu/g) prepared without the additional microwave synthesis step.[38]

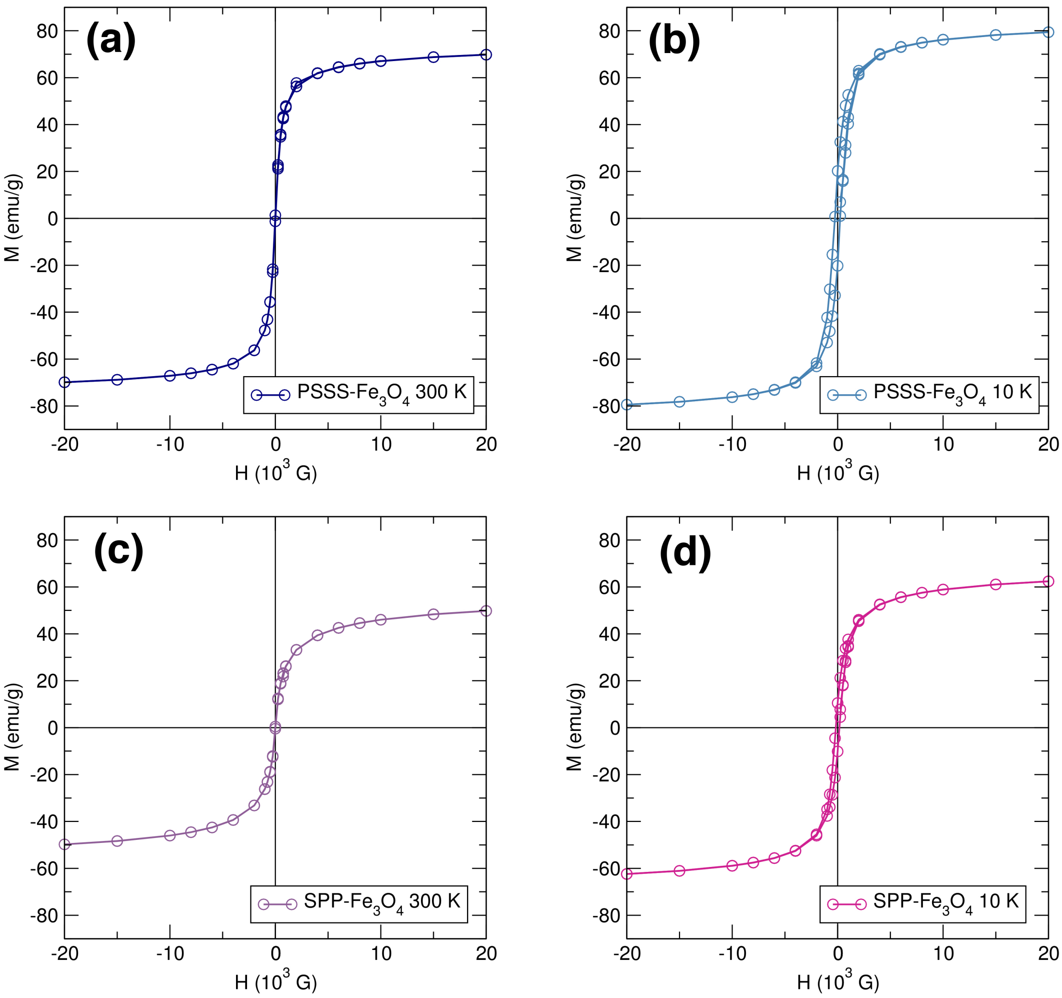

Figure 45: Magnetic hysteresis loops of PSSS-Fe_3O_4 at (a) 300 K and (b) 10 K and SPP-Fe_3O_4 at (c) 300 K and (d) 10 K.

The saturation magnetisation value is greatly affected by crystallinity of the sample. A greater saturation magnetisation value means that particles will generate a stronger magnetic moment when placed in an external magnetic field. The stronger the moment, the more protons will be affected by the composite. The differences in M_S observed here relate to interaction of the polyelectrolyte with the iron oxide surface, which can either increase or decrease surface disorder. Disorder in the crystal structure results in a magnetically ”dead” layer which does not contribute to the overall magnetisation. TEM images of PSSS-Fe_3O_4 show well-defined particles of high crystallinity, which is reflected in the higher M_S values. Given the M_S value for PSSS-Fe_3O_4 is higher that bare magnetite, this indicates that the PSSS coating can actually improve the crystallinity of the magnetite surface. The opposite is true for SPP-Fe_3O_4, where TEM showed the nanoparticles were poorly defined and this is reflected in the lower M_S values. The samples were cooled to 10K and displayed the expected behaviour, with neither reaching saturation (this is also indicative of superparamagnetism). Hysteresis loops are observed at lower temperatures, which indicate residual magnetism. This is expected as at the lower temperatures there is not enough thermal energy for the magnetic spins to randomly align during the measurement, resulting a small degree of residual magnetism. The PSSS-Fe_3O_4 sample has a similar M_S value to that reported for particles prepared using high temperature decomposition routes and organic solvents (80 emu/g).[39] The method here has the added advantage over these high temperature route in that the particles can be dispersed in aqueous suspension without the need for any post processing, vital for use as a contrast agent for MR imaging. This high magnetisation may influence the MRI properties of the composite, as the magnetic core can interact more effectively with surrounding water molecules for greater imaging efficacy.

4.2.6 Determination of iron concentration

Before we can evaluate the MR efficacy of these stable suspensions, the concentration of iron in each suspension must be accurately determined. Using AAS, this can be determined reliably. Iron standards were prepared from a iron standard (obtained from sigma aldrich) diluted with millipore water to form 7 standards with concentrations of 1, 1.5, 2, 2.5, 5, 7.5 and 10 ppm. Using the calibration curve, the concentration of iron in stable suspensions of PSSS-Fe_3O_4 and SPP-Fe_3O_4 were calculated. The PSSS sample displayed the best water stability and the neutral suspension had the highest iron concentration of 6.09 mg/l in comparison to SPP with 5.09 mg/l.

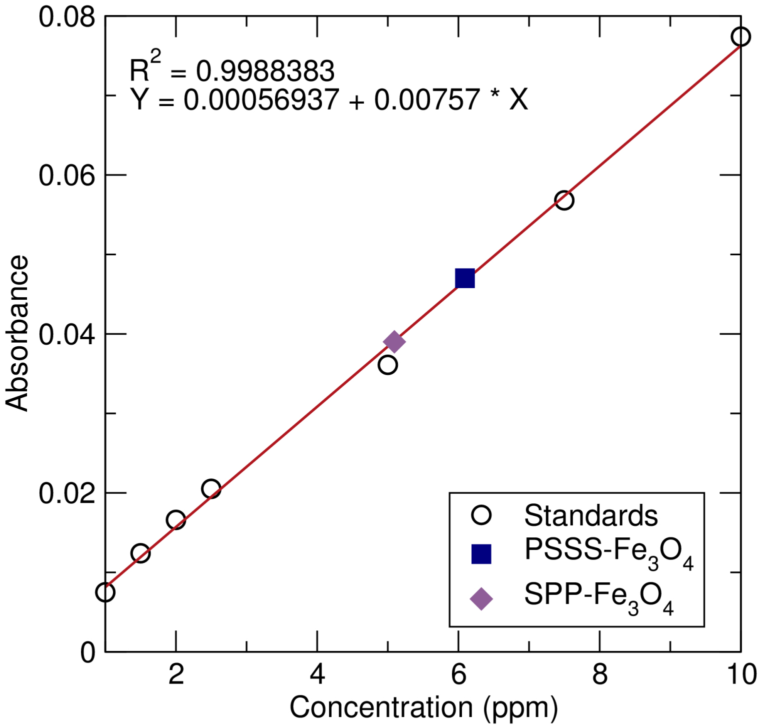

Figure 46: The iron content of the PSSS (square) and SPP (diamond) stabilised nanocomposites plotted with the calibration standards (circle). Iron concentration increased with the washings with the final PSSS sample displaying the highest concentration of 6.09 mg/l

4.3 Biomedical applications

To evaluate any potential cell toxicity and contrast agent efficacy, the neutral suspensions of PSSS-Fe_3O_4 and SPP-Fe_3O_4 were examined. These suspensions were tested in live cells to ensure biocompatibility and with an MRI scanner to determine their ultimate relaxivities.

4.3.1 Live cell testing

The effect of stabiliser on cell toxicity was examined by cell viability studies on suspensions of the polyelectrolyte-stabilised particles co-incubated at increasing concentrations (0.001 μg to 1000 μg) with a range of cell lines and these results are depicted in Figure 47. Regardless of the stabiliser employed, all nanoparticle suspensions tested were found to be non-toxic to three different mammalian cell lines. This is determined by the fact they did not affect the viability of UKF-NB-3 neuroblastoma cells, primary human retinal pigment epithelial (RPE) cells, or primary human foreskin fibroblasts (HFF) even in concentrations up to 1 mg iron/l. The non-toxicity of these suspensions is promising for their ultimate biomedical application.

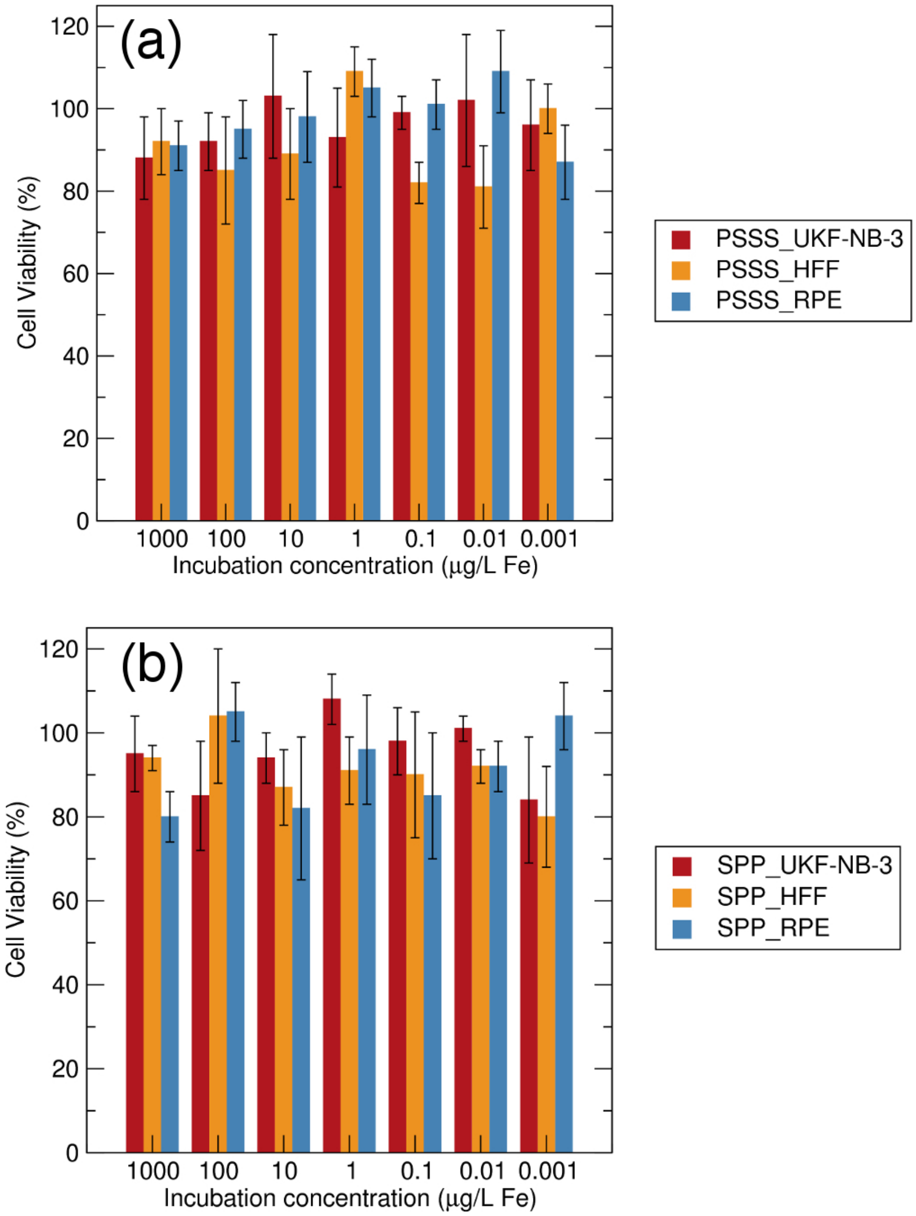

Figure 47: Cytotoxicity profiles of (a) PSSS and (b) SPP stabilised nanocomposites in UKF-NB-3 neuroblastoma cells, primary human retinal pigment epithelial (RPE) cells and primary human foreskin fibroblasts (HFF). There was minimal cell death with the nanocomposites at concentrations of up to 1 mg/L.

4.3.2 Magnetic resonance imaging testing

Stable neutral suspensions of PSSS-Fe_3O_4 and SPP-Fe_3O_4 were tested in a 3 T clinical MRI scanner with increasing Fe concentrations. As the samples increased in concentration a darkening of the image is observed, indicating that the composites shorten relaxation times (characteristic of transverse relaxation). The PSSS based nanocomposites showed the greatest darkening effect. The r_2 values of the composites were calculated to be 69.2 mM^{-1} s^{-1} and 39.9 mM^{-1} s^{-1} for the PSSS and SPP sample respectively. This indicates that the high crystallinity of the PSSS sample resulted in a highly magnetic, water stable nanocomposite that is reflected in very strong r_2 values. Another factor that further enhances the contrast effect of the PSSS composite is the formation of a thin linear assembly in magnetic fields (seen in the TEM images, figure 43). The formation of this linear assembly gives the composite a greater surface area allowing a larger portion of the water protons to interact with the magnetite cores. This effect further enhances the r_2 values of the composite. The nanocomposites are in line with commercial MRI contrast agents but the advantage of this work is that the nanoparticles are prepared and stabilised in less than an hour in a scalable one pot reaction.[40,41]

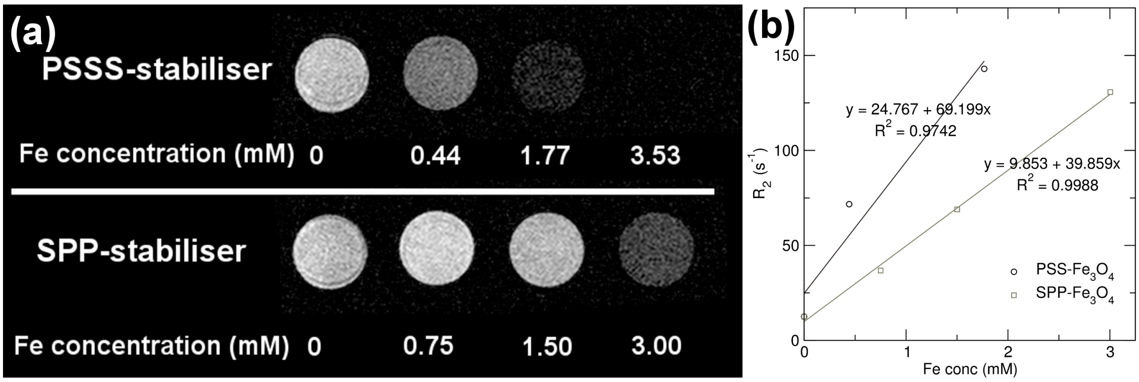

Figure 48: T_2-weighted MR images of PSSS stabilised and SPP stabilised magnetite nanoparticles. As concentration increases a darkening of the image can be observed. The PSSS-Fe_3O_4 displayed the best properties with an r_2 value of 69.2 mM^{-1} s^{-1} whereas the SPP-Fe_3O_4 composites had an r_2 value of 39.9 mM^{-1} s^{-1}.

The observed r_2 values for the SPP-Fe_3O_4 suspension are lower than for PSSS-Fe_3O_4. This can be explained by the ill-defined, poorly crystalline particle shape which leads to lower magnetisation values and the formation of large clustered material. Improved MRI properties from linear assemblies have been observed previously by the group.[3,4] Park *et al.* also observed this effect from the linear assemblies of magnetic nanoparticles.[42] They prepared dextran coated iron oxide nanoparticles in the form of a linear assembly (”nanoworms”) and compared them with unorganised magnetic nanoparticles and commercial agents. In all cases, the ”nanoworms” proved to have a higher M_S and relaxivity values than the other samples. They also associated this enhanced relaxivity with the assembly having a greater surface area allowing increased magnetic interactions with the surrounding water protons. Even with the reduced values, the SPP nanocomposites can still be used as an MRI contrast agent with a significant darkening effect seen at low concentrations

4.4 Fluorescent-magnetic nanocomposites

The MRI results demonstrate that the biocompatible PSSS-stabilised nanocomposites make excellent contrast agents with high r_2 values. In order to explore the possibility of engineering a multimodal platform capable of MR imaging and fluorescent imaging (for cell labelling and tracking), the fluorescent dye Rhodamine B was incorporated into the nanocomposite. Fluorescent labelled PSSS-Fe_3O_4 was prepared by the addition of Rhodamine B to the PSSS polyelectrolyte solution before particle precipitation, where association is driven by the electrostatic interactions between the dye and the polyelectrolyte. The composite was characterised with FTIR, DLS, UV-Vis and fluorescence spectroscopy and cellular uptake was observed using confocal imaging.

4.4.1 FTIR and DLS measurements

FTIR spectroscopy was used to confirm the addition of the Rhodamine B moiety to the nanocomposite (figure 49 (a)). Rhodamine B was added at very low quantities and gives weak signals which interact with the polyelectrolyte stretches. The C=C bonds of Rhodamine B give a characteristic broad stretch at 1410 cm^{-1}. The C=C Rhodamine B stretches occur in the same region as the C=C bonds in the polyelectrolyte stabiliser. These signals interact causing a broadening and intensity increase in the C=C stretch. Persistence of the stretches associated with PSSS and Fe-O shows that the addition of Rhodamine B does not have a drastic effect on the existing nanocomposite.

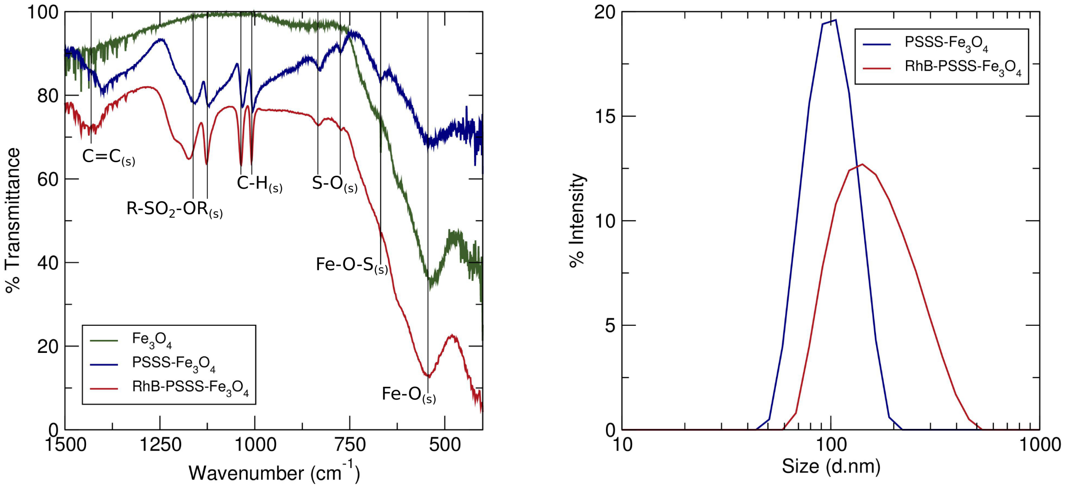

Figure 49: (Left) IR spectra of the magnetite nanoparticles (green) stabilised with PSSS (blue) and PSSS-Rhodamine B (red). (Right) DLS measurements of PSSS-stabilised and PSSS-Rhodamine B nanocomposites, in aqueous suspension. The fluorescent composite has a slightly greater size distribution.

DLS was used to identify any changes in suspension behaviour by the addition of the fluorescent groups. As the sample is washed, the cluster distribution becomes monomodal, similar to the non-fluorescent samples (figure 49 (b)). The addition of Rhodamine B increases the Z-averages and PDI values for all of the dispersions (Table 12). This increase in cluster size still makes the particles viable for biomedical applications.[32–34] The fluorescent sample displays extremely high water stability, staying in suspension for over two months. Zeta potentials for the fluorescent nanocomposite was extremely high (-55.8mV) again further supporting the high water stability.

UV-Vis spectroscopy was used to study the optical properties of the nanocomposites and to identify the excitation wavelength of Rhodamine B. Absorbance peaks for Rhodamine B are hidden due to scattering of light by the magnetic particles in suspension, with only a slight response seen at 230 nm (figure 50). A broad bump between 300-450 nm and a small peak at 230 nm is expected from the Rhodamine B group (Figure 50).

Table 12: DLS measurements of the PSSS stabilised and PSSS-rhodamine B nanocomposite dispersions. The Rhodamine B functionalised sample had slightly larger Z-average and PDI values than traditional PSSS-stabilised samples due to the increased size from the rhodamine B. Zeta potentials (Z. Po. indicate a high water stability, despite the composite supporting additional groups.

Sample	**Dispersion 3**		**Dispersion 4**		**Dispersion 5**		**Z. Po.**
	Z-Average (d.nm)	**PDI**	**Z-Average** (d.nm)	**PDI**	**Z-Average** (d.nm)	**PDI**	(mV)
PSSS-Fe$_3$O$_4$	166	0.248	82.78	0.111	94.7	0.097	-41.5
RhB-PSSS-Fe$_3$O$_4$	166	0.248	140.8	0.116	148.9	0.142	-55.8

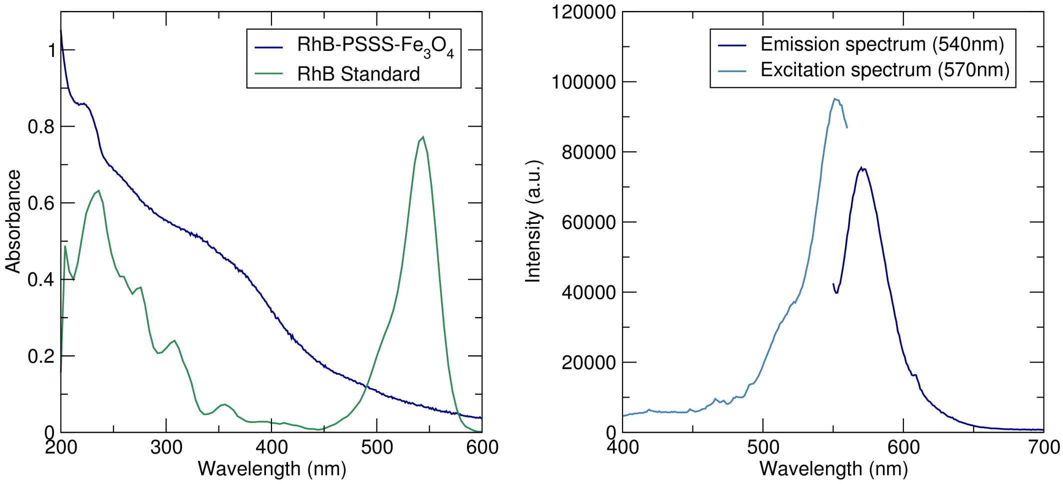

Figure 50: (Left) UV-Vis spectra of Rhodamine B standard (green) and RhB-PSSS-Magnetite (blue). Scattering of light by the nanoparticles suppresses the Rhodamine B signal with a sight response at 230 nm. (Right) Emission (navy) and Excitation (light blue) spectra of PSSS-magnetite functionalised with Rhodamine B. The characteristic emission and excitation peaks of Rhodamine B confirm the success of the functionalisation reaction.

Fluorescence spectroscopy was used to further characterise the nanocomposites, with the measurements unaffected by light scattering from the particles. An excitation and emission spectrum was taken for the final dispersion. Characteristic Rhodamine B peaks can be seen in both the excitation and emission spectra confirming the presence of the fluorescent group in the composite. The PSSS-Fe_3O_4-RhB nanocomposite shows an emission peak at 570 nm and a excitation peak at 540 nm, which agrees with the characteristic peaks of Rhodamine B.[43,44] The persistence of fluorescence peaks in the dispersion after multiple washes indicate that the Rhodamine B molecules are securely coupled to the nanocomposite.

4.4.2 Confocal imaging

After confirming the fluorescent nature of the nanocomposite, confocal imaging was employed to determine the cellular uptake of the composite and the materials effectiveness as a fluorescent label. Suspensions of PSSS-Fe_3O_4 and SPP-Fe_3O_4 were introduced to cultures of UKF-NB-3 neuroblastoma cells and multiple images were taken to confirm uptake and labelling.

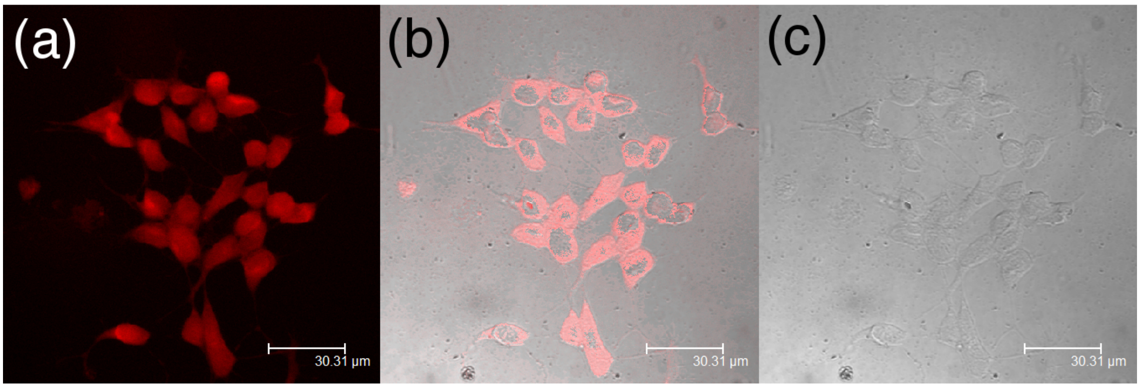

Figure 51: Confocal imaging of RhB-PSSS-Magnetite nanoparticles. Image (a) is the fluorescent particles, image (c) is of the cells without the fluorescent imaging while image (b) is an overlay of the fluorescent image with the cells showing the internalisation of the particles.

Images at a fixed depth show the uptake of the composite by the cells. The fluorescence emission of the nanocomposite is intense enough to identify and distinguish the individual cells from each other (Figure 51). Figure 52 confirms the uptake of the nanocomposite by the cells, showing that the fluorescent nanocomposite is dispersed throughout the cells at varying depths, rather than being trapped on the cell surface. These images demonstrate the nanocomposites suitability as a fluorescent label, which combined with the earlier MR images, confirm that the composite can be used as a dual imaging agent.

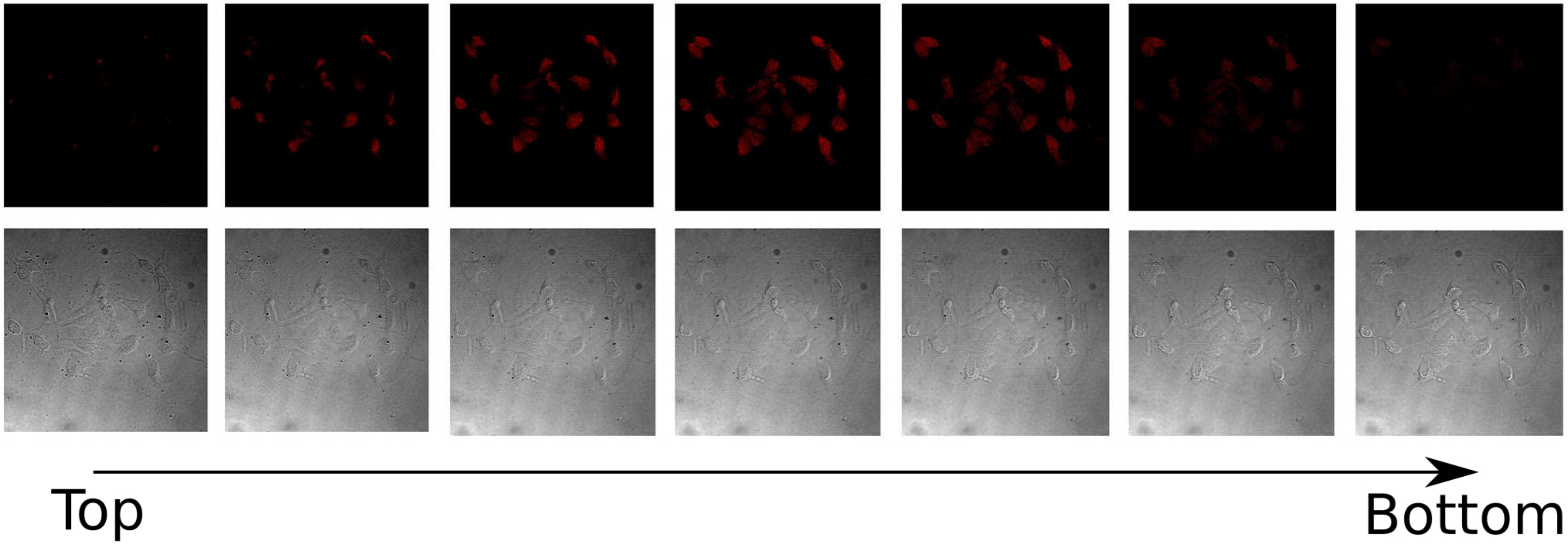

Figure 52: Z-Scan images of the confocal measurements of Rhodamine B functionalised PSSS-Fe_3O_4 nanoparticles. The depth of the images increases from left to right. The persistence of the fluorescent groups in the images confirm that the particles were internalised by the cells rather than trapped on the cell surface.

4.5 Discussion and conclusions

The method outlined in this chapter successfully demonstrates the use of microwave irradiation for the synthesis and stabilisation of magnetic nanoparticles. This approach results in a highly crystalline, extremely water stable and biocompatible iron oxide based nanocomposites. These multifunctional nanocomposites can be prepared in under an hour, with applications in both MR and confocal imaging. Two factors are responsible for the efficacy of these particles, microwave irradiation and the polyelectrolyte stabiliser itself. The previous chapter already demonstrated the effect of microwave irradiation on particle crystallinity, and this work explores the link between crystallinity and polyelectrolyte stabilisation

Previous work by the group and other researchers demonstrated the *in situ* stabilisation of iron oxide nanoparticles using the co-precipitation method, noting changes to magnetisation values from stabilisation.[4,45–47] HRTEM images in this chapter show that the stabiliser has a great effect on particle crystallinity. SQUID measurements then link these changes in crystallinity to magnetisation values, which is ultimately reflected in the MRI measurements. The two polyelectrolytes demonstrate how the stabiliser can either enhance (PSSS), or limit (SPP) particle crystallinity. The literature further confirms this link, with Lin *et al.* observing a crystallinity decrease from another polyelectrolyte stabiliser (PAA). The stabiliser reduced the saturation magnetisation of the particles from 50 emu/g to 35 emu/g. They determined that the polyelectrolyte acted as a template limiting crystal growth.[46] Itoh *et al.* expands on this through correlating an increase surface anisotropy with the binding of the SPP coating.[47] The specific effect of the stabiliser on crystallinity is unique to the material used though, with examples of organic stabilisers (such as dopamine) improving crystallinity.[48,49] These stabilisers coordinate and repair surface defects, to increase crystallinity and magnetisation values of the particles. This can be observed with the PSSS-Fe_3O_4 sample, which had a higher magnetisation value than bare magnetite. This highlights the importance of the stabiliser in the nanoparticle design.

Stabilisers not only positively effect crystallinity, but can also improve particle MRI efficacy in other ways. One stabiliser of interest is terephthalic acid, which has been shown to enhance the iron oxide contrast effect, independent of particle crystallinity. Maity *et al.* prepared an terephthalic acid stabilised iron oxide nanocomposite, and reported one of the highest iron oxide based MRI relaxivity values in the current literature.[50] The prepared particles were stabilised (*in situ*) with 2-amino terephthalic acid and terepthalic acid within the space of 2 hours. The particles had strong magnetisation values (M_s: 73.6 and 74.3 emu g^{-1} respectively) but the r_2 values for the particles are some of the highest values reported (450.8 and 735.3 mM^{-1} s^{-1} respectively). These high relaxivity values were ultimately reflected in both MRI measurements and images showing a great contrast effect. They attribute this increase to the structure of the stabiliser. Terephthalic acid and 2-amino terephthalic acid stabilisers contain π-conjugation paths that allow spin transfer from electrons in the magnetic core to the neighbouring water molecules. This allows a greater distribution of the charge to a larger group of neighbouring protons through this direct link. This work is interesting, and combining the terepthalic acid stabiliser, with microwave irradiation and PSSS might be able to further optimise MRI relaxivity values.

The other essential element of this synthesis process is microwave irradiation. Microwave heating has been shown to further enhance the particle crystallinity in tandem with the stabiliser (PSSS), or minimise the growth inhibition from less suitable stabiliser materials. Microwave irradiation promotes crystal growth, resulting in highly crystalline particles similar to solvothermal methods. This method though allows the particles to be redispersed into water immediately after precipitation avoiding the need for post processing (common with high temperature decomposition methods).[18,39,51,52] Post processing results in long multistep methods and the ligand exchange process can further reduce magnetisation values.[53,54] The method outlined here, combines precipitation and stabilisation into a single step, with the correct choice of stabiliser minimising surface defect formation through *in situ* stabilisation. The method presented here also enables functionalisation to occur simultaneously with precipitation and stabilisation. A variety of other approaches can be used to bind

Rhodamine B to magnetite but this approach offers speed and simplicity. While microwave irradiation allows stabilisation/functionalisation with little sacrifice to magnetic properties.

Both polyelectrolytes allow for biocompatible, water stable nanoparticles which show good promise as MRI contrast agents. The results show that PSSS is the optimal stabilise though, as the coating further enhances crystal growth and makes the nanocomposite extremely stable in suspension. These differences between the samples underlies how essential the polyelectrolyte is on the composites properties. Not only does the polyelectrolyte bestow water stability but can also have a significant effect on the particle size, morphology and magnetic properties. Further work will continue to explore polyelectrolyte properties by looking at chain length and polyelectrolyte mass in addition to binding groups.

References

[1] Gao, J.; Ran, X.; Shi, C.; Cheng, H.; Cheng, T.; Su, Y. *Nanoscale* **2013**, *5*, 7026–7033.

[2] Si, S.; Kotal, A.; Mandal, T. K.; Giri, S.; Nakamura, H.; Kohara, T. *Chem. Mater.* **2004**, *16*, 3489–3496.

[3] Corr, S. A.; Gun'ko, Y. K.; Tekoriute, R.; Meledandri, C. J.; Brougham, D. F. *J. Phys. Chem. C* **2008**, *112*, 13324–13327.

[4] Corr, S. A.; Byrne, S. J.; Tekoriute, R.; Meledandri, C. J.; Brougham, D. F.; Lynch, M.; Kerskens, C.; O'Dwyer, L.; Gun'ko, Y. K. *J. Am. Chem. Soc.* **2008**, *130*, 4214–4215.

[5] Fleet, M. E. *Acta. Cryst.* **1981**, *B37*, 917–920.

[6] Mikhaylova, M.; Kim, D. K.; Bobrysheva, N.; Osmolowsky, M.; Semenov, V.; Tsakalakos, T.; Muhammed, M. *Langmuir* **2004**, *20*, 2472–2477.

[7] Mahmoudi, M.; Simchi, A.; Milani, A. S.; Stroeve, P. *J. Colloid. Interf. Sci.* **2009**, *336*, 510–518.

[8] Cheng, F.-Y.; Su, C.-H.; Yang, Y.-S.; Yeh, C.-S.; Tsai, C.-Y.; Wu, C.-L.; Wu, M.-T.; Shieh, D.-B. *Biomaterials* **2005**, *26*, 729–738.

[9] Kim, D. K.; Zhang, Y.; Voit, W.; Rao, K. V.; Muhammed, M. *J Magn. Magn. Mater.* **2001**, *225*, 30–36.

[10] Cirtiu, C. M.; Raychoudhury, T.; Ghoshal, S.; Moores, A. *Colloid Surface. A* **2011**, *390*, 95–104.

[11] Lefêvre, G. *Adv. Colloid Interfac.* **2004**, *207*, 109–123.

[12] Parikh, S. J.; Chorover, J. *Langmuir* **2006**, *22*, 8492–8500.

[13] Gong, W. *Int. J. Miner. Process.* **2001**, *63*, 147–165.

[14] Ghosh, G.; Panicker, L.; Ningthoujam, R. S.; Barick, K. C.; Tewari, R. *Colloid Surface B* **2013**, *103*, 267–274.

[15] Daou, T. J.; Pourroy, G.; Bégin-Colin, S.; Grenèche, J. M.; Ulhaq-Bouillet, C.; Legaré, P.; Bernhardt, P.; Leuvrey, C.; Rogez, G. *Chem. Mater.* **2006**, *18*, 4399–4404.

[16] Mazo-Zuluaga, J.; Barrero, C. A.; Díaz-Terán, J.; Jerez, A. *Hyperfine Interact.* **2003**, *148–149*, 4399–4404.

[17] Goya, G. F.; Berquó, T. S.; Fonseca, F. C.; Morales, M. P. *J. Appl. Phys.* **2003**, *94*, 3520–3528.

[18] Sun, S.; Zeng, H.; Robinson, D. B.; Raoux, S.; Rice, P. M.; Wang, S. X.; Li, G. *J. Am. Chem. Soc.* **2004**, *126*, 273–279.

[19] Dobrynin, A. V.; Colby, R. H.; Rubinstein, M. *Macromolecules* **1995**, *28*, 1859–1871.

[20] Dobrynin, A. V.; Rubinstein, M. *Prog. Polym. Sci.* **2005**, *30*, 1049–1118.

[21] Yoo, D.; Shiratori, S. S.; Rubner, M. F. *Macromolecules* **1998**, *31*, 4309–4318.

[22] Kolarik, L.; Furlong, D. N.; Joy, H.; Struijk, C.; Rowe, R. *Langmuir* **1999**, *15*, 8265–8275.

[23] Blaakmeer, J.; B ohmer, M. R.; Stuart, M. A. C.; Fleer, G. J. *Macromolecules* **1990**, *23*, 2301–2309.

[24] Netz, R. R.; Andelman, D. *Phys. Rep.* **2003**, *380*, 1–95.

[25] Cranford, S. W.; Ortiz, C.; Buehler, M. J. *Soft Matter* **2010**, *6*, 4175–4188.

[26] Apaydin, K.; Laachachi, A.; Bour, J.; Toniazzo, V.; Ruch, D.; Ball, V. *Colloid Surface A* **2012**, *415*, 274–280.

[27] Shiratori, S. S.; Rubner, M. F. *Macromolecules* **2000**, *33*, 4213–4219.

[28] van de Steeg, H. G. M.; Stuart, M. A. C.; de Keizer, A.; Bijsterbosch, B. H. *Langmuir* **1992**, *8*, 2538–2546.

[29] der Schee, H. A. V.; Lyklema, J. *J. Phys. Chem.* **1984**, *88*, 6661–6667.

[30] Itano, K.; Choi, J.; Rubner, M. F. *Marcomolecules* **2005**, *38*, 3450–3460.

[31] Choi, J.; Rubner, M. F. *Macromolecules* **2005**, *38*, 116–124.

[32] Laurent, S.; Forge, D.; Port, M.; Roch, A.; Robic, C.; Elst, L. V.; Muller, R. N. *Chem. Rev.* **2008**, *108*, 2064–2110.

[33] Neuberger, T.; Schöpf, B.; Hofmann, H.; Hofmann, M.; Rechenberg, B. V. *J Magn. Magn. Mater.* **2005**, *293*, 483–496.

[34] Arruebo, M.; Fernández-Pacheco, R.; Ibarra, M. R.; Santamaría, J. *NanoToday* **2007**, *2*, 22–32.

[35] Cunningham, D.; Littleford, R. E.; Smith, W. E.; Lundahl, P. J.; Khan, I.; McComb, D. W.; Graham, D.; Laforest, N. *Faraday Discuss.* **2006**, *132*, 135–145.

[36] Morel, A.-L.; Nikitenko, S. I.; Gionnet, K.; Wattiaux, A.; Lai-Kee-Him, J.; Labrugere, C.; Chevalier, B.; Deleris, G.; Petibois, C.; Brisson, A.; Simonoff, M. *ACS Nano* **2008**, *2*, 847–856.

[37] Corr, S. A.; Gun'ko, Y. K.; Douvalis, A. P.; Venkatesan, M.; Gunning, R. D.; Nellist, P. D. *J. Phys. Chem. C* **2008**, *112*, 1008–1018.

[38] Wang, Y.; Wong, J. F.; Teng, X.; Lin, X. Z.; Yang, H. *Nano Lett.* **2008**, *3*, 1555–1559.

[39] Sun, S.; Zeng, H. *J. Am. Chem. Soc.* **2002**, *124*, 8204–8205.

[40] Li, Z.; Yi, P. W.; Sun, Q.; Lei, H.; Zhao, H. L.; Zhu, Z. H.; Smith, S. C.; Lan, M. B.; Lu, G. Q. M. *Adv. Funct. Mater.* **2012**, *22*, 2387–2393.

[41] Sun, C.; Du, K.; Fang, C.; Bhattarai, N.; Veiseh, O.; Kievit, F.; Stephen, Z.; Lee, D.; Ellenbogen, R. G.; Ratner, B.; Zhang, M. *ACS. Nano.* **2010**, *4*, 2402–2410.

[42] Park, J.-H.; von Maltzahn, G.; Zhang, L.; Schwartz, M. P.; Ruosahti, E.; Bhatia, S. N.; Sailor, M. J. *Adv. Mater.* **2008**, *20*, 1630–1635.

[43] Kim, J.; Kim, H. S.; Lee, N.; Kim, T.; Kim, H.; Yu, T.; Song, I. C.; Moon, W. K.; Hyeon, T. *Angew. Chem. Int. Ed.* **2008**, *47*, 8438–8441.

[44] Wu, S.; Jiang, W.; Sun, Z.; Dai, J.; Liu, L.; Li, F. *J Magn. Magn. Mater.* **2011**, *323*, 2170–2173.

[45] Marangoni, V. S.; Martins, M. V. A.; Souza, J. A.; Oliveira, O. N.; Zucolotto, V.; Crespilho, F. N. *J. Nanopart. Res.* **2012**, *14*, 769.

[46] Lin, C.-L.; Lee, C.-F.; Chiu, W.-Y. *J. Colloid. Interf. Sci.* **2005**, *291*, 411–420.

[47] Itoh, F.; Satou, M.; Yamazaki, Y. *IEEE T. Magn.* **1977**, *13*, 1385–1387.

[48] Yuen, A. K. L.; Hutton, G. A.; Masters, A. F.; Maschmeyer, T. *Dalton Trans.* **2012**, *41*, 2545–2559.

[49] Chen, L. X.; Liu, T.; Thurnauer, M. C.; Csencsits, R.; Rajh, T. *J. Am. Chem. Soc.* **2004**, *126*, 9938–9939.

[50] Maity, D.; Zoppellaro, G.; Sedenkova, V.; Tucek, J.; Safarova, K.; Polakova, K.; Tomankova, K.; Jiwoky, C.; Stollberger, R.; Machala, L.; Zboril, R. *Chem. Commun.* **2012**, *48*, 11398–11400.

[51] Hou, Y.; Yu, J.; Gao, S. *J. Mater. Chem.* **2003**, *13*, 1983–1987.

[52] Tian, Y.; Yu, B.; Li, X.; Li, K. *J. Mater. Chem.* **2011**, *21*, 2476–2481.

[53] Zhang, T.; Ge, J.; Hu, Y.; Yin, Y. *Nano. Lett.* **2007**, *7*, 3203–3207.

[54] Ge, J.; Hu, Y.; Biasini, M.; Dong, C.; Guo, J.; Beyermann, W. P.; Yin, Y. *Chem. Eur. J.* **2007**, *13*, 7153–7161.

Chapter 5: Investigating magnetic fluid behaviour by varying polyelectrolyte type and chain length

5.1 General introduction and objectives

Polyelectrolytes can be highly versatile with variations in chain size and monomer composition allowing for the further enhancement of the nanocomposites water stability or the addition of functional groups. As shown in the previous chapter the iron oxide particle size, morphology and magnetic properties can change based on the polyelectrolyte bound to the iron oxide surface. The aim of this chapter is to continue exploring polyelectrolyte materials as potential iron oxide stabilisers, specifically looking at affect of the polyelectrolyte nature on the final nanocomposite water stability. The charge and chain length may have a great affect on the nature of the polyelectrolyte binding to the nanoparticle surface. Changing the length of the polyelectrolyte will alter the number of binding sites and how many magnetic nanoparticles can be supported by the polyelectrolyte chain. Varying the charge of the polyelectrolyte chain will affect how the polyelectrolyte binds to the iron oxide surface. Additionally it will also alter the nanocomposites surface charge which dictates the water stability. The effect of charge was seen briefly in chapter 4 when comparing the fully charged strong polyelectrolyte PSSS against the weak polyelectrolyte SPP which is only partially charged in solution. This chapter will further explore the distinction between weak and strong polyelectrolytes, and will also look at the use of cationic polyelectrolytes.

Two different polyelectrolytes with distinct functional groups will be investigated. The first polyelectrolyte will be poly(acrylic acid) (PAA) which contains a negatively charged carboxylic acid binding group. PAA is considered to be a weak polyelectrolyte and is partially ionised in solution.[1,2] The deionised carboxylate groups are available to bind to the iron groups on the particle surface (figure 53). One advantage of PAA is the possibility of carbodiimide coupling, which allows the attachment of linkers and functional groups (i.e.

chemotherapy agents) to the free carboxylic acid groups, which is key to the development of multi-functional nanocomposites.[3,4] The second polyelectrolyte is Poly(diallyldimethylammonium chloride) (pDADMAC) which binds at an alternative site through the polyelectrolyte ammonium groups to the hydroxide groups on the magnetite surface (figure 53). This is a strong cationic polyelectrolyte that is fully deionised in solution and will act as a comparison to the anionic PAA, PSSS and SPP polyelectrolytes explored previously.[5,6] Other groups have used PAA and pDADMAC as iron oxide stabilisers previously but this work aims to expand on this existing knowledge by using these stabilisers in a microwave assisted co-precipitation reaction, and to conduct a systematic study of polyelectrolyte chain length on iron oxide water stability.[7–10]

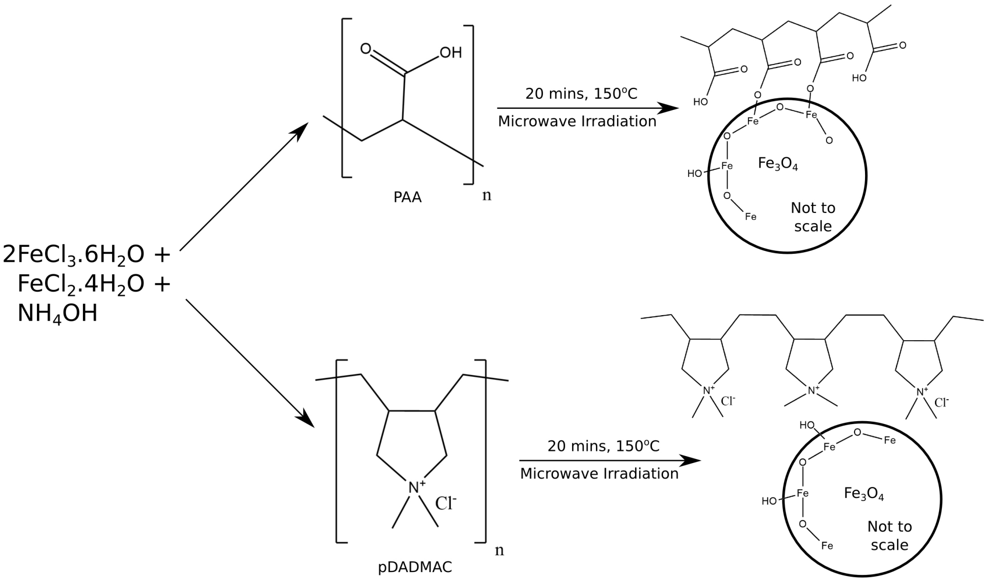

Figure 53: Schematic of the one pot co-precipitation and stabilisation reaction of PAA and pDADMAC on iron oxide nanoparticles. The negatively charged carboxylic acid group of PAA will bind to the positively charged iron groups on the magnetite surface. The positively charged ammonium group of pDADMAC will bind to the magnetite surface via the hydroxide groups.

5.2 Characterisation of polyelectrolyte-Fe_3O_4 nanocomposites

The nanocomposites were prepared in a similar method as discussed in chapter 4. The nanoparticles were stabilised *in situ* via a single microwave-assisted coprecipitation reaction. The reaction conditions were kept at 150°C, at 100 W for 20 minutes (plus ramping time). Three different chain lengths were used for each polyelectrolyte (Table 13). The resulting dried precipitates were characterised with XRD and TGA. The stable and pH neutral dispersions (third to fifth washings) were analysed with FTIR, TEM and DLS.

Table 13: The sample prepared, and polyelectrolyte chain lengths used to stabilise iron oxide particles used in this chapter

Sample Name	Polyelectrolyte Classification	Polyelectrolyte mwt
PAA stabilised nanoparticles		
Sample A	Very low mwt	1,800
Sample B	High mwt	400,000-500,000
Sample C	Very High mwt	1,250,000
pDADMAC stabilised nanoparticles		
Sample D	Low mwt	<100,000
Sample E	Medium mwt	100,000-200,000
Sample F	High mwt	400,000-500,000

5.2.1 Structural characterisation

Powder XRD patterns of the samples identify the iron oxide core and the primary particle size was calculated using the Scherrer equation. Figure 54 shows the patterns for both the PAA-stabilised samples and pDADMAC-stabilised samples, along with the unfunctionalised bare Fe_3O_4 also prepared by the microwave assisted co-precipitation method (green). The patterns match the peaks observed for bare magnetite prepared in chapter 3 along with magnetite standards from the ICSD and reported by other groups.[11–15] The broad peaks indicate that the particles are on the nanoscale with the Scherrer equation determining the crystallites to be between 9-15 nm for the stabilised samples (table 14), which is small enough for the particles to be single domain.[16] There seemed to be little effect of polyelectrolyte length or charge on the primary particle size, with the particles showing the same size irrespective of polyelectrolyte coating.

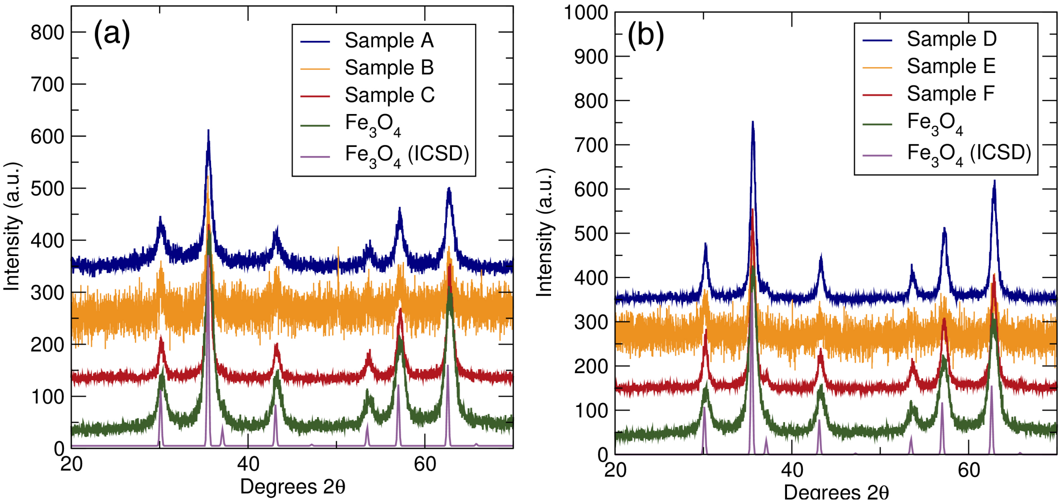

Figure 54: XRD patterns for bare magnetite (green) and magnetite samples stabilised with PAA (image (a) Sample A: blue, Sample B: yellow, Sample C: red) and pDADMAC (image (b) Sample D: blue, Sample E: yellow, Sample F: red). Samples B and E were characterised under different conditions at the University of Glasgow (more information can be found in chapter 2). The pattern for all samples are in good agreement to known magnetite (purple).[11]

Table 14: Primary particle sizes calculated via Scherrer broadening. Polyelectrolyte length or charge seems to have little effect on particle size, with all particles small enough to be single domain.[16]

Sample	**Polyelectrolyte mwt**	**Primary particle size (nm)**
Magnetite	N/A	11.2
PAA stabilised nanoparticles		
Sample A	1,800	13.5
Sample B	400,000-500,000	15.2
Sample C	1,250,000	12.9
pDADMAC stabilised nanoparticles		
Sample D	<100,000	14.1
Sample E	100,000-200,000	9.9
Sample F	400,000-500,000	10.4

5.2.2 Surfactant characterisation

FTIR and TGA spectroscopy was used to confirm the polyelectrolyte binding to the magnetite surface. All samples gave a large Fe-O absorption at 570 cm^{-1} and a small broad band at around 3400 cm^{-1} due to water groups physically adsorbed on the particle surface.[17,18]

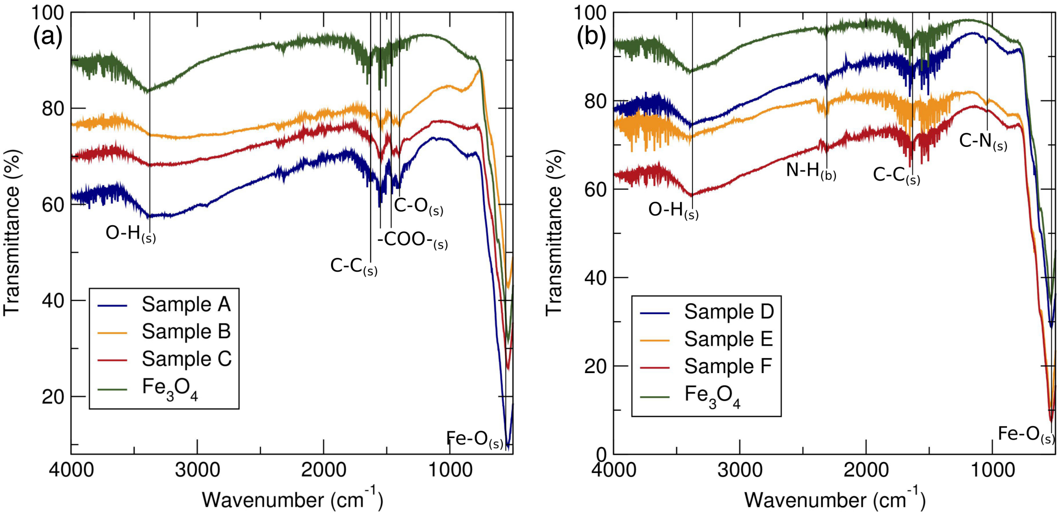

Figure 55: FTIR spectra of magnetic nanocomposites stabilised with PAA (image (a) Sample A: blue, Sample B: yellow, Sample C: red) and pDADMAC (image (b) Sample D: blue, Sample E: yellow, Sample F: red) compared to bare magnetite (green). A series of peaks relating to PAA and pDADMAC indicate successful stabilisation.[19–22]

For the PAA-Fe_3O_4 stabilised samples (Figure 55, (a)), the polyelectrolyte binding is confirmed by the symmetric and asymmetric -COO- vibrations at 1550 and 1390 cm^{-1}. These are ionised carboxylic acid groups, shift from 1600 and 1420 cm^{-1} respectively when bound to the iron oxide surface indicating successful stabilisation. Distinction of these peaks is difficult due to background CO_2 but a clear shifting and addition of peaks can be seen when compared to the bare magnetite spectrum (green). Multiple groups have confirmed this shifting effect and the linking carboxylate peaks at 1550 and 1390 cm^{-1}, with stabilisation further supported by the formation of water stable suspensions.[19–21] Additional unbound C-O stretches occur at 1210 cm^{-1} causing a broadening of this peak and the neighbouring carboxylic acid peaks. The C-C alkane backbone that holds the PAA together gives a signal at 1600 cm^{-1} which has merged with some of the carboxylic acid peaks. The hydroxide group of the carboxylic acid overlaps with the peak for excess water on the magnetite surface at 3400 cm^{-1} while weak C-H stretches can be seen at 2921 cm^{-1} as a slight shoulder. These peaks match with PAA stabilisation reactions found within the literature, but are absent in the bare magnetite samples.[7,23,24] Little difference can be seen between the polyelectrolyte chain lengths in the FTIR spectra, with Sample A showing slightly more pronounced polyelectrolyte peak intensities.

The intensity of the pDADMAC-Fe_3O_4 signals are weak but there are several specific peaks that relate to the polyelectrolyte structure and indicate successful binding. The polyelectrolyte coordinates with the magnetic nanoparticle via the interaction of the polyelectrolyte ammonium group with the hydroxide groups on the iron oxide surface. The formation of the linking N-H bond can be seen with a stretch at 3400 cm^{-1} and a N-H bend at 2326 cm^{-1}. These signals are weak and can overlap with hydroxide peaks at 3400 cm^{-1}, but in samples D and E the N-H bend can clearly be distinguished at 2326 cm^{-1} when compared to bare magnetite (green). Successful stabilisation can also be inferred from the formation of a water stable suspension. Stretches from the anchoring points also support stabilisation with an O-H stretch at 3400 cm^{-1}, Fe-O stretch at 570 cm^{-1} and C-N stretch at 1053 cm^{-1}. Work by several other groups support this binding method by exploring the coordination of other materials containing amide and ammonium groups with iron oxide surfaces.[25,26] There are several other non bonding polyelectrolyte peaks in the spectrum with the C-C backbone of the structure giving a signal at 1650 cm^{-1} and C-H stretches observed at 2941 cm^{-1}. The C-C stretches occur at the same wavenumber as vibrations from background CO_2 (C=O: 1550 cm^{-1}) but the increased intensity supports the presence of polyelectrolyte. The C-H stretches at 2931 cm^{-1} have merged with the ammonium peaks at 3400 cm^{-1} with a broadening of the peak and the formation of a slight shoulder is observed by the overlapping signals. The overall peak assignment matches the pDADMAC magnetite nanoparticles prepared by other groups with the assigned polyelectrolyte peaks absent in the bare magnetite spectrum.[9] Little difference can be seen between the polyelectrolyte chain lengths with all samples showing similar peaks and intensities.

TGA was also used confirm the polyelectrolyte component in the iron oxide composites.The stabilised samples show multiple mass losses. The first mass loss between 60-140°C is due to solvent molecules (i.e. water, acetone and ethanol) trapped on the surface of the nanocomposite. The stabilised samples show a greater mass loss between 200-460°C from the polyelectrolyte coating. The temperature range of the mass loss varies depending on the polyelectrolyte. The PAA samples show losses between 250-460°C (Figure 56, (a)) while the pDADMAC coating is lost over a smaller range of 200-350°C [(Figure 56, (b)]. The very heavy polyelectrolyte chain for sample C resulted in a two stage decomposition of the PAA coating over a range of 250-650°C. The mass loss profiles are similar to what is found the in the literature for PAA or pDADMAC stabilised samples further confirming the results.[7,23,24,27,28]

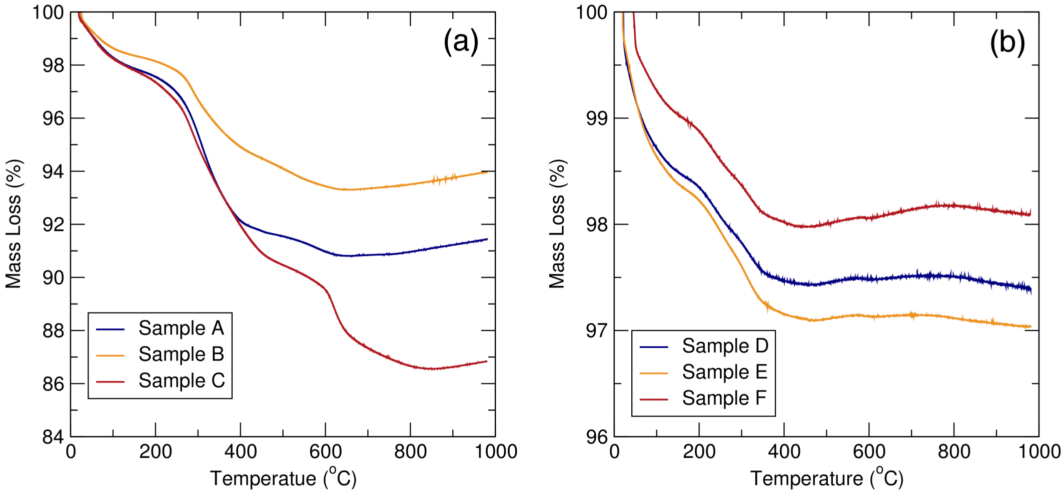

Figure 56: TGA for magnetite nanoparticles stabilised with PAA (image (a) Sample A: blue, Sample B: yellow, Sample C: red) and pDADMAC (image (b) Sample D: blue, Sample E: yellow, Sample F: red). All samples showed a 3 stage mass loss.

The PAA-Fe_3O_4 samples show a large mass loss of between 6-13% (which varies based on chain length), with the pDADMAC-Fe_3O_4 sample showing a loss of just 2.5% irrespective of chain length (table 15). The difference between the TGA profiles is primarily due to the mwt of the polyelectrolyte that is attached but the binding affinity of the polyelectrolyte can also affect the mass profile. Heavy, long chain polyelectrolytes (sample C) will show the greatest mass loss, due to their extreme size and increased mass. For smaller polyelectrolyte chains, binding affinity also begins to affect the TGA profile. Smaller chains are less likely to form loops and folds, and cause reduced steric hinderance, allowing for more chains to bind to the iron oxide surface. This results in the composite supporting more polyelectrolyte mass, despite the lighter individual polyelectrolyte chains. This is best illustrated in the comparison of samples A and B. Sample B contains the heavier polyelectrolyte chains, but has the smallest mass loss in the TGA profile, whereas sample A uses very small PAA chains, but shows the greater mass loss of the two. This is because the very small chain length used in sample A, allows for many polyelectrolyte chains to bind to the composite, compensating for the small individual chain mass. The advantages of using smaller polyelectrolyte chains can also be seen in the TEM and DLS results, which are discussed further into the chapter. These effects are harder to distinguish in the pDADMAC TGA profiles as the mass loss difference between the samples occurs within 1%.

Table 15: Overall Mass losses from the TGA measurements of the stabilised samples.

Sample	Polyelectrolyte mwt	Mass loss (%)
Magnetite	N/A	3.77
PAA stabilised nanoparticles		
Sample A	1,800	8.56
Sample B	400,000-500,000	6.02
Sample C	1,250,000	13.15
pDADMAC stabilised nanoparticles		
Sample D	<100,000	2.60
Sample E	100,000-200,000	2.96
Sample F	400,000-500,000	1.91

5.2.3 Particle size and morphology

Electron microscopy was used to measure the primary particle sizes and morphologies of the iron oxide composites in addition to observing any effects the varying chain length would have on the composite conformation. Primary particle sizes were measured of over 100 nanoparticles, from the TEM images of the composites dried in ambient conditions (Figures 57 and 58). Clustering can be observed due to the drying effects from the preparation of the grids. All samples had a primary particle size under 15 nm (Table 16), making the crystals small enough to be single domain/superparamagnetic.[16,29] The PAA-Fe_3O_4 nanoparticles show a slightly greater size variance (Figure 57) than the pDADMAC-Fe_3O_4 samples (Figure 58) but neither polyelectrolyte or chain length has a significant effect on the primary particle size. The measured sizes are in good agreement with the Scherrer sizes calculated from the XRD patterns. In sample C, unbound material can be seen around the aggregates.

When exposed to an 0.5 T external magnetic field, differences between the polyelectrolyte types and chain lengths become more apparent. All samples formed linear assemblies compared to when dried under ambient conditions as shown in Figures 59 and 60.

Table 16: Particle sizes calculated from TEM images. Assembly widths were measured from particles dried in an external magnetic field.

Sample	**mwt**	**Particle size** (nm)	**S.D** (nm)	**Assembly width** (nm)	**S.D** (nm)
PAA stabilised nanoparticles					
Sample A	1,800	12.6	3.091	84.1	23.1
Sample B	450,000	13.1	2.626	204.3	62.6
Sample C	1,250,000	14.2	3.518	210.2	64.8
pDADMAC stabilised nanoparticles					
Sample D	<100,000	14.5	2.769	81.9	28.3
Sample E	100-200,000	13.7	2.529	78.50	30.50
Sample F	400-500,000	13.9	3.447	44.7	13.5

The PAA-Fe_3O_4 samples showed great variation based on polyelectrolyte molecular weight as shown in Figure 59. Sample A formed thin linear assemblies. As the polyelectrolyte molecular weight (and chain length) increases, these linear assemblies become thicker and agglomerate with little orientation to the external field. PAA is considered a weak polyelectrolyte, and forms loops and folds in solution due to partial ionisation of the polyelectrolyte.[1,2] For sample A, the composite chain is small enough that the formation of loops and folds are minimal resulting in thin linear strands as seen in Figure 59 images (a) and (b). For sample B, the chain is longer and will have more chance to loop and fold. This leads to a thicker polyelectrolyte strand, with less orientation to the external magnetic field. This increase in strand thickness can be seen in the TEM images (images (c) and (d)). Sample C continues to illustrate this point, with the PAA stabiliser being very long in length, maximising the chance for the chain to loop and fold. This translates into thick polyelectrolyte strands (image (f)) with agglomeration between the individual strands (as seen in the TEM images (image (e)). Lin *et al.* also stabilised palladium/iron nanoparticles with a variety of PAA chain lengths (1800-1250,000) confirming the very high mwt chain aggregating and becoming unusable due to the extreme chain length.[19]

The pDADMAC-Fe_3O_4 samples formed very thin linear assemblies (reminiscent of the PSSS-Fe_3O_4 samples in Chapter 4), which aligned in the direction of the applied magnetic field (Figure 60). This was consistent between all pDADMAC-Fe_3O_4 samples with cross linking seen between the strands. Cross linking between the strands increases as the polyelectrolyte molecular weight decreases. These assemblies extend to over 1 μm in length. The formation of the linear assemblies is due to several factors, such as the magnetite/polyelectrolyte ratio and pDADMAC being a strong polyelectrolyte.[5,6] When in solution the pDADMAC chain is fully ionised, with the monomers repelling each other and exposing all of the binding sites. This stops the formation of loops and folds while increasing the opportunities for magnetite nanoparticles to bind to the polyelectrolyte chain. The more magnetite that is supported, the stronger response the composite has in an external magnetic field. As was seen with the PSSS results, this linear conformation increases the composite's surface area, which may ultimately enhance the MRI efficacy. This improved MRI behaviour has been previously reported in the literature and shown in chapter 4.[30]

The distinction between weak and strong polyelectrolytes can clearly be seen comparing Samples B and F, as they were stabilised with polyelectrolytes of a similar molecular weight. Sample B was bound to a weak polyelectrolyte (PAA) and forms thick strands due to the loops and folds (as seen in Figure 59 images (c) and (d)). Conversely Sample F is stabilised with a strong polyelectrolyte unable to loop and fold, forming much thinner single strands in comparison (seen in Figure 60 images (e) and (f)). The thinner assemblies are more desirable in biomedical applications due to the increased surface area and smaller size.

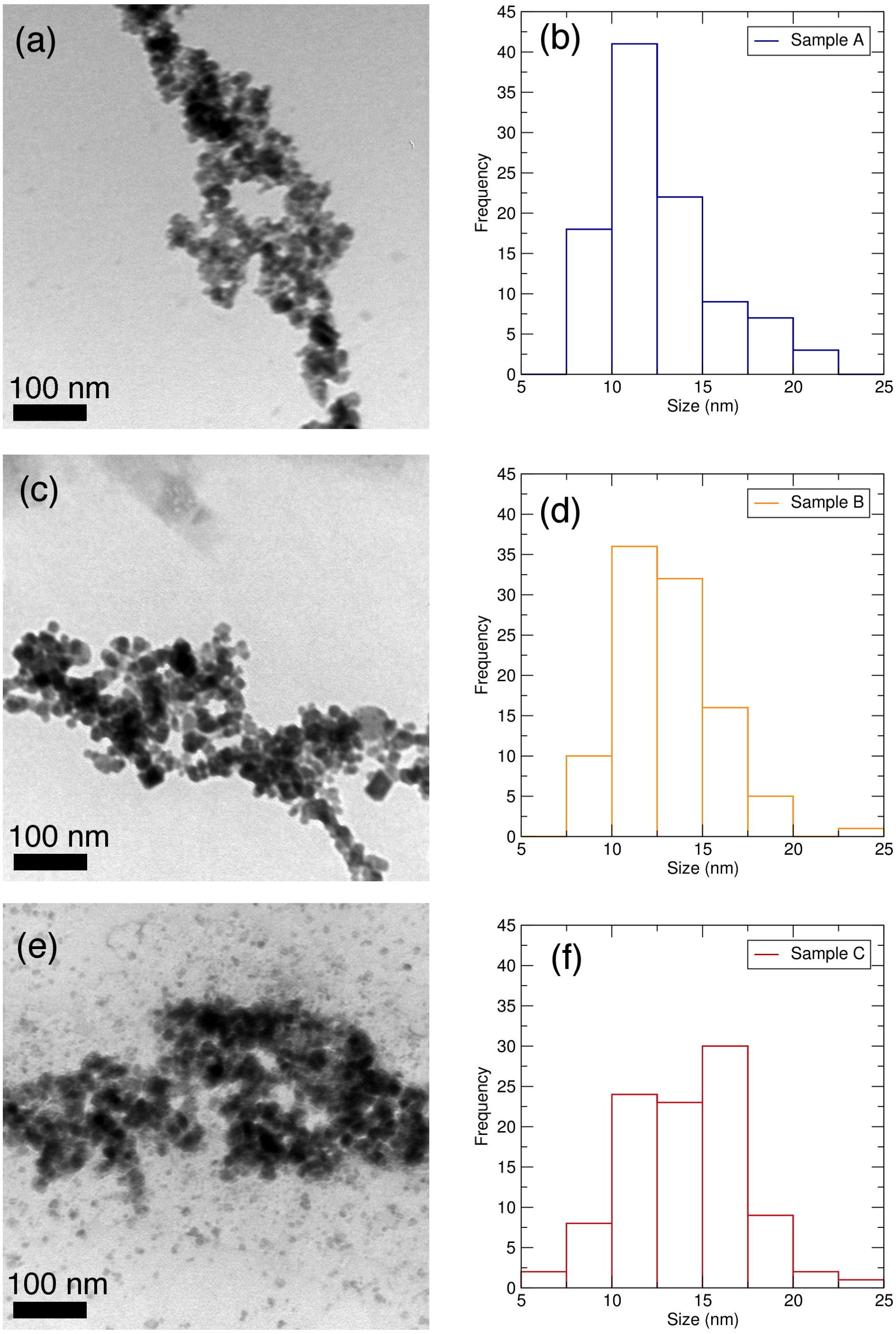

Figure 57: TEM images of PAA-Fe_3O_4 nanoparticles dried under standard conditions. Magnetite nanoparticles were stabilised with a variety of PAA chain lengths (Sample A: (a) and (b), Sample B: (c) and (d), Sample C: (e) and (f)). Little difference between polyelectrolyte chain lengths can be seen on the particle morphology or sizes.

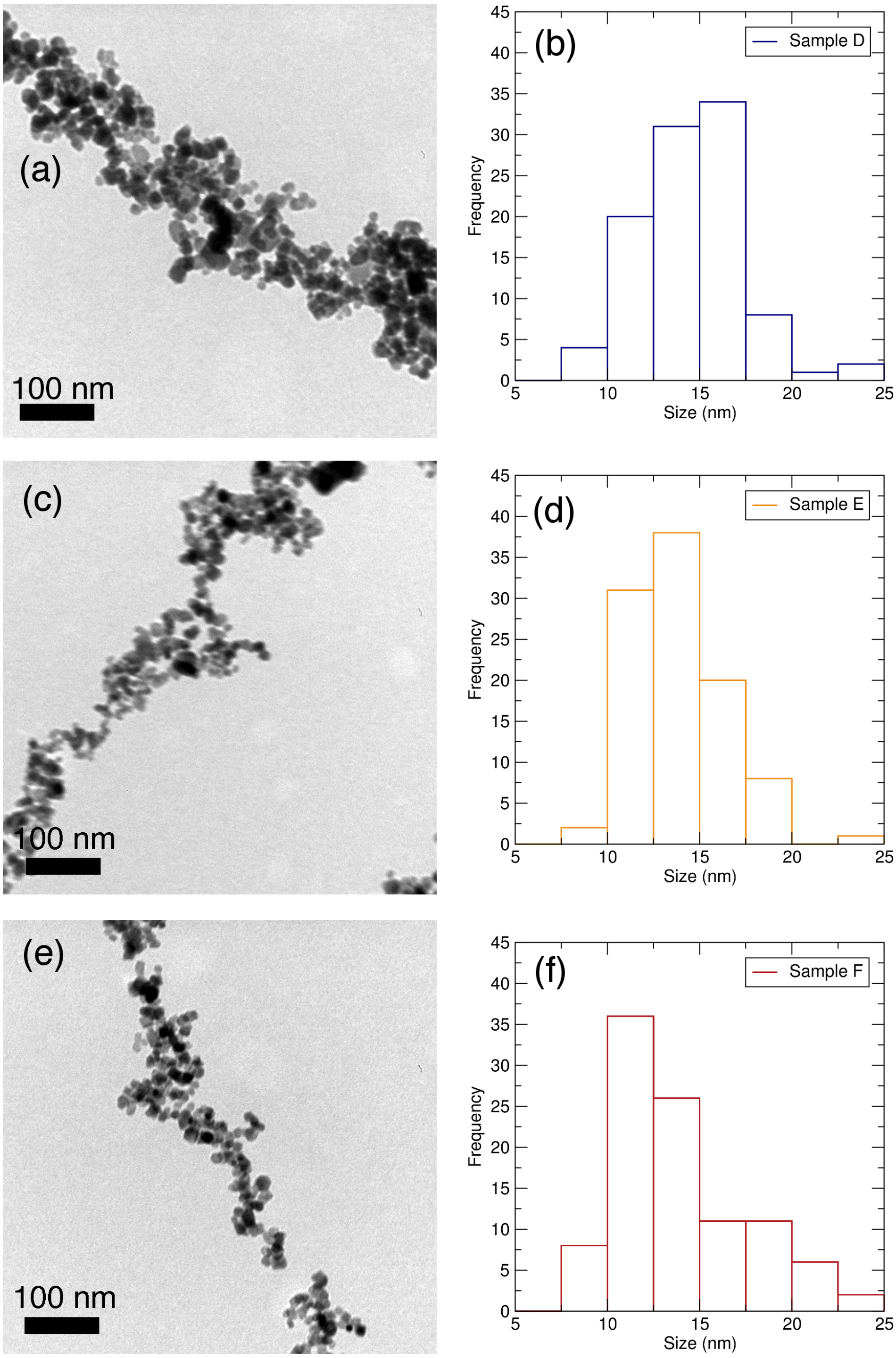

Figure 58: TEM images of pDADMAC-Fe_3O_4 nanoparticles dried under standard conditions. A variety of pDADMAC lengths were used to stabilise the iron oxide cores (Sample D: (a) and (b), Sample E: (c) and (d), Sample F: (e) and (f)). The pDADMAC chain length has little effect on the primary particle size.

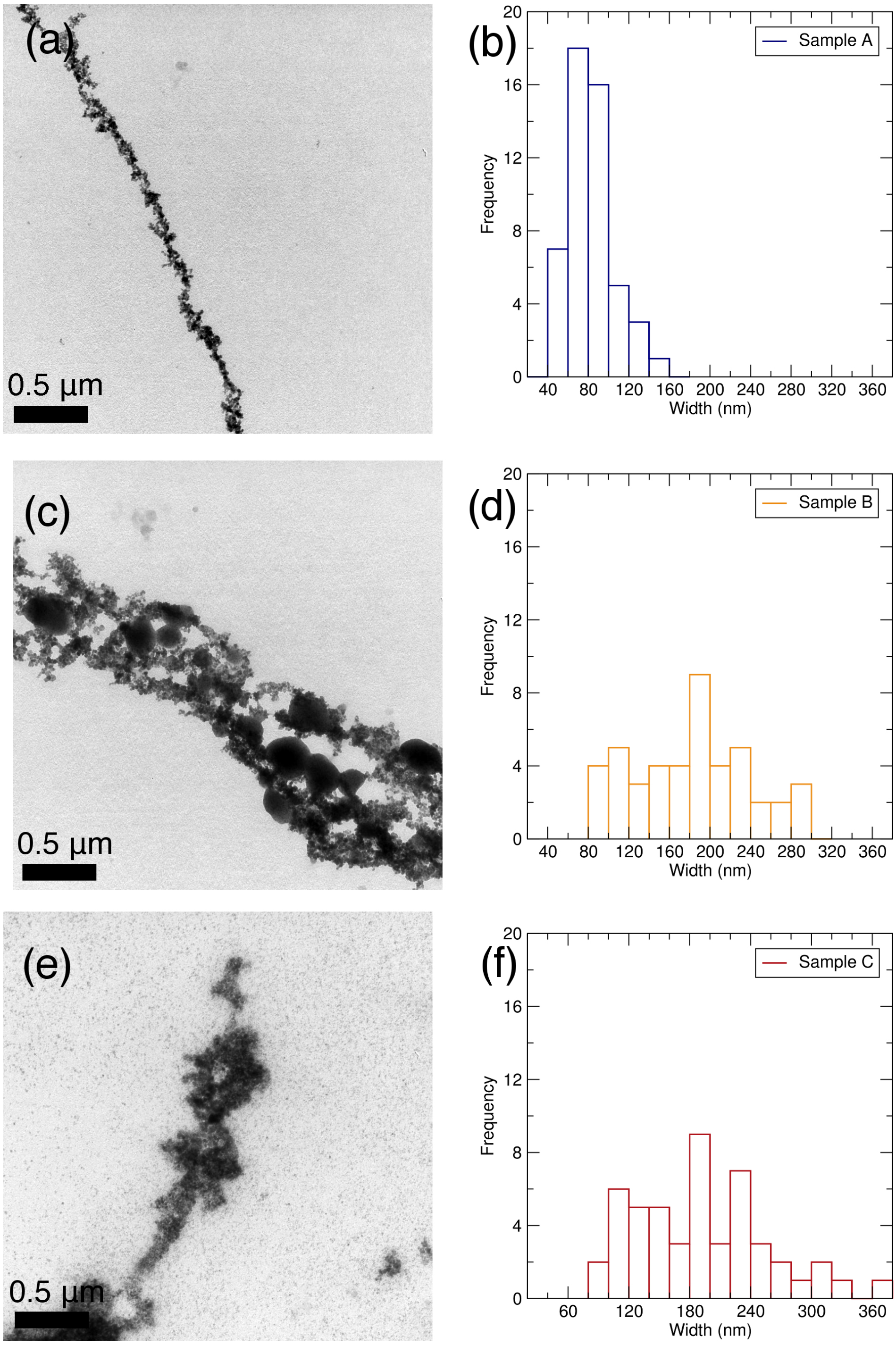

Figure 59: TEM measurements of PAA-Fe_3O_4 nanoparticles forming linear assemblies when dried in an external magnetic field. Three different PAA chain lengths were used to stabilise magnetite (Sample A: (a) and (b), Sample B: (c) and (d), Sample C: (e) and (f)) with significant differences observed between the samples. Strand width increases with chain length.

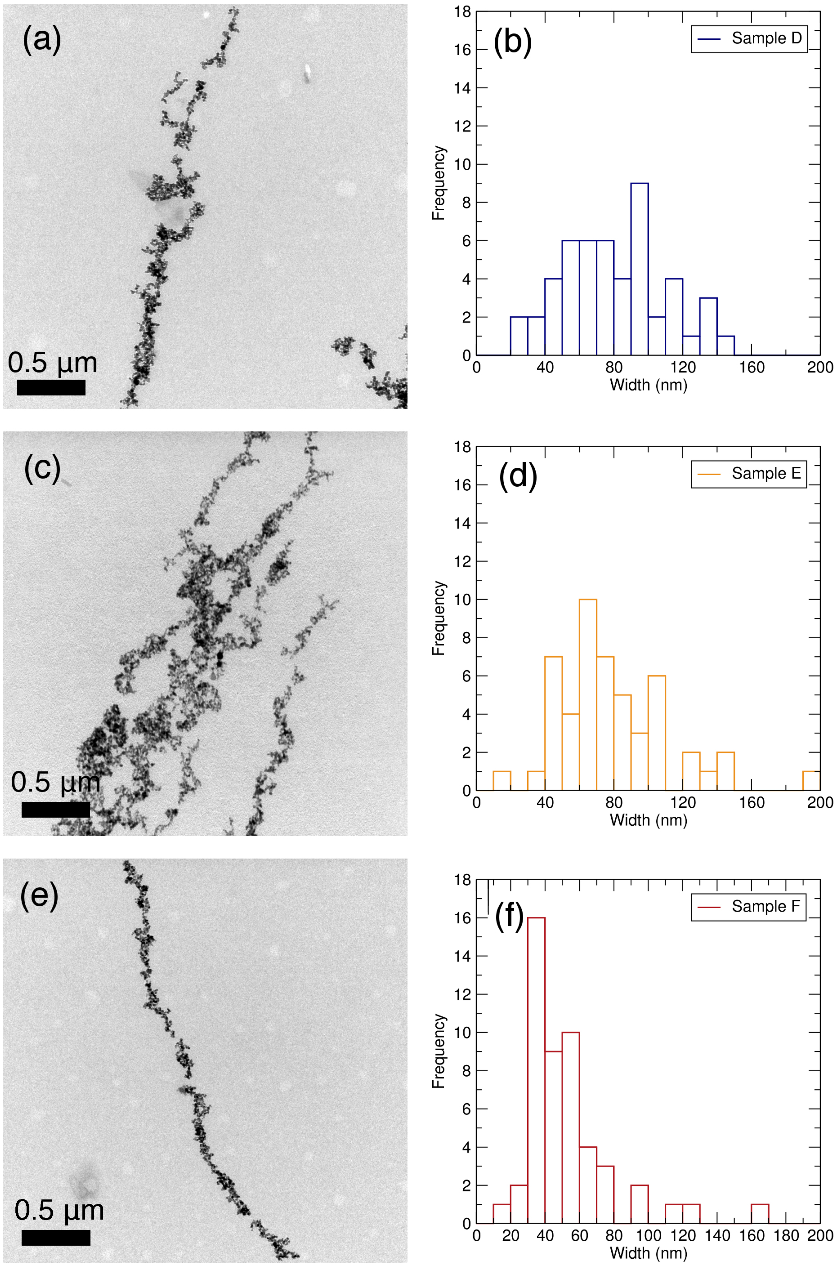

Figure 60: TEM measurements of pDADMAC-Fe_3O_4 nanoparticles forming linear assemblies in an external magnetic field. Different pDADMAC chain lengths were used (Sample D: (a) and (b), Sample E: (c) and (d), Sample F: (e) and (f)). All samples formed linear assemblies over $2\,\mu$m in length. Interchain clustering can be observed in the samples, due to the rigid nature of the polyelectrolyte.

5.2.4 Suspension behaviour

DLS was used to determine the effect of chain length on water stability and composite behaviour. For the majority of samples (excluding sample C) as the particles were washed to pH neutral, the composite is more readily dispersed in water to form a stable suspension. These stable suspensions remained stable even when suspended over a 0.5 T magnet for 24 hours. As the stabilised nanocomposites move towards a neutral pH, the Z-averages and polydispersity indices (PDIs) decrease and the cluster distribution becomes mono-modal, as detailed in Table 17 and Figure 62. The lowest molecular weight samples for both PAA and pDADMAC samples (Sample A and D) gave the best combination of Z-average, PDI values and smallest range of cluster sizes. For both stabilisers as the molecular weight increases, the hydrodynamic radius gets larger and the size distribution also increases, in some cases becoming multimodal (Figures 61 and 62). This is best illustrated with the PAA-Fe_3O_4 stabilised composites, with a significant increase in DLS values as the polyelectrolyte molecular weight increases. Sample C is so unstable that it is crashing out of solution during a measurement and cannot be accurately measured. For most biomedical applications, it is desirable for the particles to be 200 nm or less, with all of the pDADMAC-Fe_3O_4 samples and the PAA Sample A prepared here falling within this size range.[31–33]

A comparison between samples B and F again highlights the distinction between weak and strong polyelectrolytes and the importance of charge in polyelectrolyte stabilisers. Samples B and F are stabilised with different polyelectrolytes but are of the similar molecular weight allowing for the effect of charge to be examined. Sample F has the highest DLS of the pDADMAC-stabilised samples but these values are still significantly less than the PAA stabilised Sample B. TEM images (Figures 60 (e) and 59 (c)) show that Sample F forms thin linear assemblies while Sample B aggregates, forming thick strands due to loops and folds. The formation of the loops and folds also increases the composite size when in solution, resulting in larger DLS values as shown in Table 17. This is responsible for the higher PDI value for sample B, with the formation of loops and folds causing variation in the aggregate sizes. The cationic charge of pDADMAC seems to have little effect on DLS values and composite behaviour, with the equivalent length anionic PSSS sample from Chapter 4 showing similar DLS values (Z-average: 94.7 nm, PDI 0.097) to sample E.

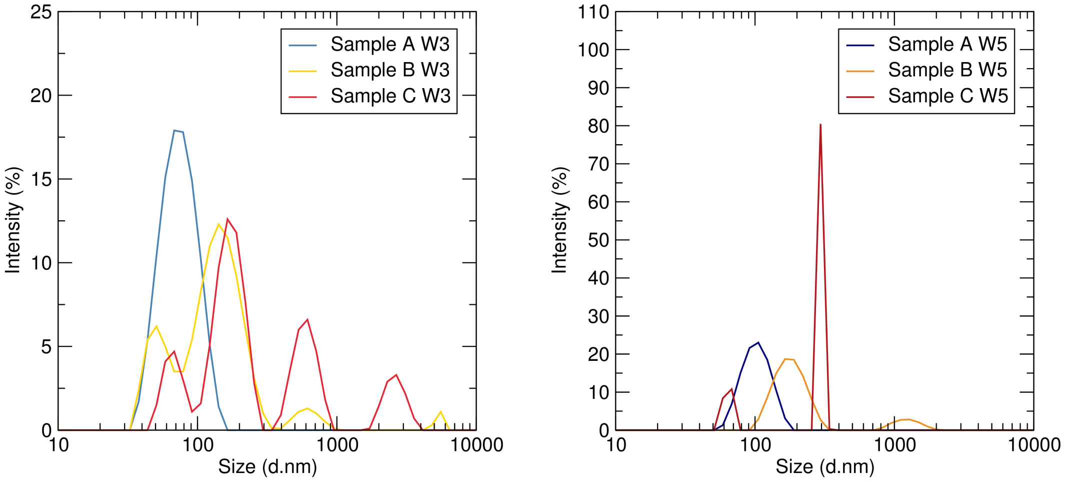

Figure 61: DLS measurements PAA-stabilised magnetite nanoparticles (Sample A: blue, Sample B: yellow, Sample C: red). Measurements were taken for the initial basic washing (washing 3, image (a)) and the pH neutral final washing (washing 5, image (b)). Z-average and PDI values decreased as the sample approached neutrality. Sample C values reflect poor water stability.

The differences in Z-averages and PDIs are reflected in water stability, with the pDADMAC-Fe_3O_4 samples staying in aqueous suspension for over a month and sample D lasting over 6 weeks. The PAA-stabilised nanocomposites show a more varied behaviour, with Sample A being the most stable of all of the prepared samples staying in solution for over 2 months. As the PAA chain increased in size, water stability dropped rapidly with sample B being stable for just under a month and Sample C unable to form a suspension when neutral. As the polyelectrolyte molecular weight increases, the chain length also presumable increases in size. Therefore, the polyelectrolyte can support more iron oxide nanoparticles, increasing the composite mass and decreasing water stability. This effect is most significant with the wide size ranges of the PAA-Fe_3O_4 samples, but the lighter pDADMAC-Fe_3O_4 dispersions also showed a slight increase in stability.

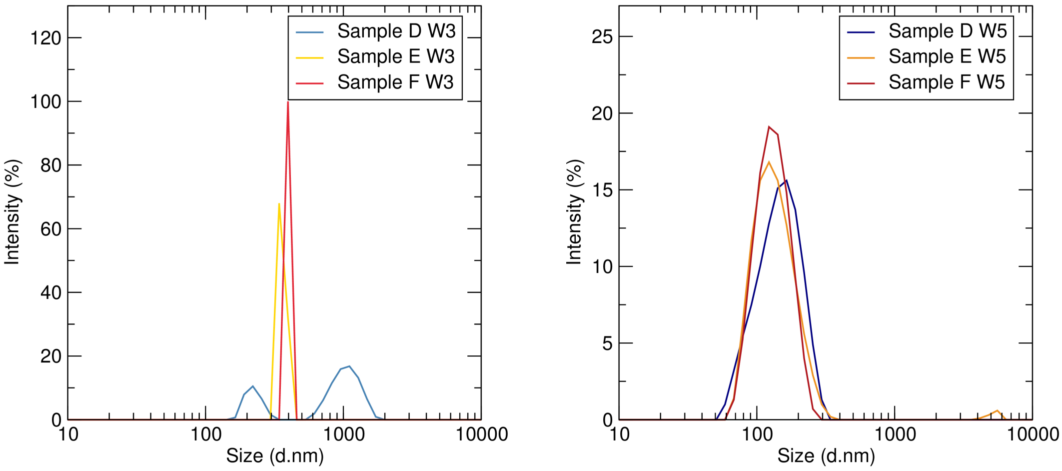

Figure 62: DLS measurements of pDADMAC-stabilised magnetite nanoparticles (Sample D: blue, Sample E: yellow, Sample F: red). Measurements were taken for the initial basic washing (washing 3, left) and for the pH neutral final washing (washing 5, right). All samples decreased in polydispersity and Z-average as they were washed.

The surface charges of the particles were also investigated and the results are recorded in Table 17. The extreme DLS properties of Sample C are due to this sample being unable to form a stable suspension. The pDADMAC-Fe_3O_4 samples give decreased values when compared to other polyelectrolyte stabilised iron oxides, due to the positive charge of the coating. This is indicative of the polyelectrolyte coating binding, as the positive polyelectrolyte charge counteracts the overall negative charge of the iron oxide cores. The decrease in zeta potential is reflected in lower water stability. The decreased values might also suggest incomplete coverage of the particles. Wotschadlo *et al.* prepared iron oxide nanoparticles with pDADMAC stabilised on a carboxymethyldextran shell.[10] They found reduced zeta potentials for the short chain polyelectrolytes indicating incomplete coverage of the nanoparticle cores. Interestingly, those decreased values may improve biological properties though, with extreme surface charges presenting problems for biomedical applications. This is because highly positive coatings can attach non specifically to cells, whereas strongly negatively charged particles are more likely to be taken up by the liver.[34] These particles can still be considered water stable, lasting over a month in solution and the effect of decreased surface charge from the coating has been observed previously by other groups.[35–38]

Table 17: DLS measurements of the pH neutral nanocomposite washings. As the samples were washed, the Z-average and PDI values stabilised. Significant differences can be observed as the chain length increases. The positive charge of the pDADMAC coating is reflected in decreased zeta potentials (Z. Po.) for samples D-F

Sample	**Washing 3**		**Washing 4**		**Washing 5**		**Z. Po.**
	Z-Average (d.nm)	**PDI**	**Z-Average** (d.nm)	**PDI**	**Z-Average** (d.nm)	**PDI**	(mV)
PAA stabilised nanoparticles							
Sample A	64.8	0.176	69.1	0.177	90.74	0.126	-60.0
Sample B	116.3	0.347	405.3	0.986	221.8	0.438	-59.8
Sample C	254.1	0.658	652.4	0.946	1193	1	-63.5
pDADMAC stabilised nanoparticles							
Sample D	799.5	0.752	167.7	0.317	116.4	0.228	-24.7
Sample E	1799.6	0.878	103.1	0.194	122.7	0.091	-37.2
Sample F	1554.6	0.866	387.3	0.448	141.4	0.307	-28.5

5.3 Discussion and conclusions

Regulation of polyelectrolyte molecular weight and charge is key to maximising water stability and controlling composite size. The choice of weak and strong polyelectrolytes also has a large affect in relation to iron oxide stabilisation. These considerations can therefore be vital in optimising iron oxide-polyelectrolyte nanoparticles as water stable magnetic fluids for MR imaging or targeted drug delivery. Both polyelectrolytes explored here have previously been shown to be suitable as stabilisers for iron oxide nanoparticles. However, up to now, there has been no systematic study of their behaviour as a function of molecular weight. Lin *et al.* prepared PAA-Fe_3O_4 demonstrating the formation of a water stable suspension with cluster sizes similar to the materials prepared within this chapter, noting a decrease in M_s values from the stabiliser.[7] Si *et al.* also observed that the PAA stabiliser can have a size inhibiting effect which accounts for the reduction in magnetism.[24] Unfortunately, it has not been possible to measure the magnetic properties of each nanocomposite prepared here due to a SQUID failure. A slight inhibition of magnetisation values for the PAA-Fe_3O_4 would be expected, based on the reports by previous groups.[7,24] Less of a decrease is expected for the pDADMAC-Fe_3O_4 samples though, with Yu *et al.* reporting that the binding of the pDADMAC does not affect the magnetisation of the particles.[39] Despite inhibition from the stabilisers, use of microwave irradiation would ensure that any inhibited crystal growth and decreases in M_s values would be minimal, as illustrated in Chapter 4. Additionally, the formation of linear assemblies when stabilised with pDADMAC or very low mwt PAA chains will also enhance MRI properties, with the work by Park *et al.* identifying that the formation of linear assemblies can increase M_s values and MRI efficacy.[30] Utilising microwave irradiation will ensure a high crystallinity, which is not lost through the stabilisation of the particles. Both PAA and pDADMAC stabilisers also have a combined use in layer-by-layer (LBL) reactions, where the formation of loops and folds is desirable and can be used to control layer thickness.[40–42]

From the results presented here, the most suitable stabiliser for iron oxide nanoparticles would be either the short chain length PAA (sample A) or pDADMAC (sample D) stabiliser. The short chain length is a must, as this keeps the composite weight low, ensuring good water stability and the formation of linear assemblies. Both polyelectrolytes present their own advantages and disadvantages. The formation of linear assemblies with the pDADMAC-Fe_3O_4 particles will enhance magnetic properties and the reduced overall surface charge may facilitate the particles passage through the body.[34] However, this is at a cost to water stability, which is lower than the PAA samples. The water stability of the PAA-Fe_3O_4 samples are dependant on molecular weight. Sample A displays the best water stability of the samples and forms linear assemblies in solution. The other important consideration of PAA is the functionalisation of the unbound carboxylic acid groups. Carboxylic acid can undergo carbodiimide coupling, which is a versatile functionalisation reaction used in the development of multifunctional magnetic nanoparticles.[3,4] Support for carbodiimide coupling allows for the attachment of moieties such as fluorescent tags[43,44] or chemotherapy agents[45,46] drastically expanding the potential of the composite.

From the results obtained in Chapters 4 and 5, one potential area of future work is utilising multiple polyelectrolytes in the preparation of magnetic nanocomposites. The functionalisation options offered by PAA are essential for the continued development of the nanoparticles. Combining this with the PSSS stabiliser (from chapter 4) can add excellent water stability and crystallinity for the foundation of this composite. Shortening the length of the PSSS chain can further increase the nanocomposites water stability. Both materials have displayed a high affinity for iron oxide cores and incorporating both stabilisers into the composite could take advantage of both these materials. This may allow for the further development of the composite into a multifunctional system capable of detecting, targeting, highlighting and then treating cancerous cells.

References

[1] Shiratori, S. S.; Rubner, M. F. *Macromolecules* **2000**, *33*, 4213–4219.

[2] Cranford, S. W.; Ortiz, C.; Buehler, M. J. *Soft Matter* **2010**, *6*, 4175–4188.

[3] Ge, J.; Hu, Y.; Biasini, M.; Dong, C.; Guo, J.; Beyermann, W. P.; Yin, Y. *Chem. Eur. J.* **2007**, *13*, 7153–7161.

[4] Na, H. B.; Palui, G.; Rosenberg, J. T.; Ji, X.; Grant, S. C.; Mattoussi, H. *ACS Nano* **2012**, *6*, 389–399.

[5] Mattison, K. W.; Dubin, P. L.; Brittain, I. J. *J. Phys. Chem. B.* **1998**, *102*, 3830–3836.

[6] Notley, S. M.; Norgren, M. *Biomacromolecules* **2008**, *9*, 2081–2086.

[7] Lin, C.-L.; Lee, C.-F.; Chiu, W.-Y. *J. Colloid. Interf. Sci.* **2005**, *291*, 411–420.

[8] Kim, H.; Dae, H.-M.; Park, C.; Kim, E. O.; Kim, D.; Kim, I.-H.; Kim, Y.-H.; Choi, Y. *J. Mater. Chem.* **2011**, *21*, 7742–7747.

[9] Marangoni, V. S.; Martins, M. V. A.; Souza, J. A.; Jr., O. N. O.; Zucolotto, V.; Crespilho, F. N. *J. Nanopart. Res.* **2012**, *14*, 769.

[10] Wotschadlo, J.; Liebert, T.; Clement, J. H.; Anspach, N.; Höppener, S.; Rudolph, T.; Müller, R.; Schacher, F. H.; Schubert, U. S.; Heinze, T. *Macromol. Biosci* **2013**, *13*, 93–105.

[11] Fleet, M. E. *Acta. Cryst.* **1981**, *B37*, 917–920.

[12] Mikhaylova, M.; Kim, D. K.; Bobrysheva, N.; Osmolowsky, M.; Semenov, V.; Tsakalakos, T.; Muhammed, M. *Langmuir* **2004**, *20*, 2472–2477.

[13] Mahmoudi, M.; Simchi, A.; Milani, A. S.; Stroeve, P. *J. Colloid. Interf. Sci.* **2009**, *336*, 510–518.

[14] Cheng, F.-Y.; Su, C.-H.; Yang, Y.-S.; Yeh, C.-S.; Tsai, C.-Y.; Wu, C.-L.; Wu, M.-T.; Shieh, D.-B. *Biomaterials* **2005**, *26*, 729–738.

[15] Kim, D. K.; Zhang, Y.; Voit, W.; Rao, K. V.; Muhammed, M. *J Magn. Magn. Mater.* **2001**, *225*, 30–36.

[16] Goya, G. F.; Berquó, T. S.; Fonseca, F. C.; Morales, M. P. *J. Appl. Phys.* **2003**, *94*, 3520–3528.

[17] Zaitsev, V. S.; Filimonov, D. S.; Presnyakov, I. A.; Gambino, R. J.; Chu, B. *J. Colloid Inter. Sci.* **1999**, *212*, 49–57.

[18] Hu, L.; Percheron, A.; Chaumont, D.; Brachais, C.-H. *J. Sol-Gel. Sci. Technol.* **2011**, *60*, 198–205.

[19] Lin, Y.-H.; Tseng, H.-H.; Wey, M.-Y.; Lin, M.-D. *Colloid Surface. A* **2009**, *349*, 137–144.

[20] He, F.; Zhao, D.; Liu, J.; Roberts, C. B. *Ind. Eng. Chem. Res.* **2007**, *46*, 29–34.

[21] Lefêvre, G. *Adv. Colloid Interfac.* **2004**, *207*, 109–123.

[22] Dallas, P.; Bourlinos, A. B.; Niarchos, D.; Petridis, D. *J. Mater. Sci.* **2007**, *42*, 4996–5002.

[23] Zhang, T.; Ge, J.; Hu, Y.; Yin, Y. *Nano. Lett.* **2007**, *7*, 3203–3207.

[24] Si, S.; Kotal, A.; Mandal, T. K.; Giri, S.; Nakamura, H.; Kohara, T. *Chem. Mater.* **2004**, *16*, 3489–3496.

[25] Cirtiu, C. M.; Raychoudhury, T.; Ghoshal, S.; Moores, A. *Colloid Surface. A* **2011**, *390*, 95–104.

[26] Ângela L. Andrade,; Fabris, J. D.; Ardisson, J. D.; Valente, M. A.; Ferreira, J. M. F. *J. Nanomater.* **2012**, *2012*, 1–10.

[27] Kumar, S.; Ravikumar, C.; Bandyopadhyaya, R. *Langmuir* **2010**, *26*, 18320–18330.

[28] Zhitomirsky, I.; Niewczas, M.; Petric, A. *Mater. Lett.* **2003**, *57*, 1045–1050.

[29] Morais, P.; Garg, V.; Oliveira, A.; Silva, L.; Azevedo, R.; Silva, A.; Lima, E. *J. Magn. Magn. Mater.* **2001**, *225*, 37–40.

[30] Park, J.-H.; von Maltzahn, G.; Zhang, L.; Schwartz, M. P.; Ruosahti, E.; Bhatia, S. N.; Sailor, M. J. *Adv. Mater.* **2008**, *20*, 1630–1635.

[31] Laurent, S.; Forge, D.; Port, M.; Roch, A.; Robic, C.; Elst, L. V.; Muller, R. N. *Chem. Rev.* **2008**, *108*, 2064–2110.

[32] Neuberger, T.; Schöpf, B.; Hofmann, H.; Hofmann, M.; Rechenberg, B. V. *J Magn. Magn. Mater.* **2005**, *293*, 483–496.

[33] Arruebo, M.; Fernández-Pacheco, R.; Ibarra, M. R.; Santamaría, J. *NanoToday* **2007**, *2*, 22–32.

[34] Berry, C. C. *J. Phys. D: Appl. Phys.* **2009**, *42*, 224003.

[35] Schwarz, S.; Wong, J. E.; Bornemann, J.; Hodenius, M.; Himmelreich, U.; Richtering, W.; Hoehn, M.; Zenke, M.; Hieronymus, T. *Nanomed-Nanotechnol.* **2012**, *8*, 682–691.

[36] Baier, J.; Koetz, J.; Kosmella, S.; Tiersch, B.; Rehage, H. *J. Phys. Chem. B* **2007**, *111*, 8612–8618.

[37] Caruso, F.; Susha, A. S.; Giersig, M.; Möhwald, H. *Adv. Mater.* **1999**, *111*, 950–953.

[38] Zhu, Y.; Da, H.; Yang, X.; Hu, Y. *Colloid Surface A* **2003**, *231*, 123–129.

[39] Yu, C.-J.; Lin, C.-Y.; Liu, C.-H.; Cheng, T.-L.; Tseng, W.-L. *Biosens Bioelectron* **2010**, *26*, 913–917.

[40] Chia, K.-K.; Rubner, M. F.; Cohen, R. E. *Langmuir* **2009**, *25*, 14044–14052.

[41] Kato, N.; Schuetz, P.; Fery, A.; Caruso, F. *Macromolecules* **2002**, *35*, 9780–9787.

[42] Dante, S.; Hou, Z.; Risbud, S.; Stroeve, P. *Langmuir* **1999**, *15*, 2176–2182.

[43] Hu, F.; Li, Z.; Tu, C.; Gao, M. *J. Colloid. Interf. Sci.* **2007**, *311*, 469–474.

[44] Qu, H.; Caruntu, D.; Liu, H.; O'Connor, C. J. *Langmuir* **2011**, *27*, 2271–2278.

[45] Hua, M.-Y.; Yang, H.-W.; Chuang, C.-K.; Tsai, R.-Y.; Chen, W.-J.; Chuang, K.-L.; Chang, Y.-H.; Chuang, H.-C.; Pang, S.-T. *Biomaterials.* **2010**, *31*, 7355–7363.

[46] Dilnawaz, F.; Singh, A.; Mohanty, C.; Sahoo, S. K. *Biomaterials* **2010**, *31*, 3694–3706.

Chapter 6: Functionalisation of magnetic nanocomposites

6.1 General introduction

Previous chapters have demonstrated that microwave irradiation combined with polyelectrolyte stabilisers afford extremely water stable, highly magnetic nanocomposites, which are effective MRI contrast agents. Also, these can support a fluorescent molecule through electrostatic interactions. This chapter will explore the further functionalisation of iron oxide based nanocomposites, detailing a series of reactions to attach functional groups such as polyelectrolytes to maximise water stability, fluorescent molecules for cell imaging and tracking, and targeting compounds to ensure cell specificity to the core magnetic nanoparticles. This is shown for a general case in Figure 63.

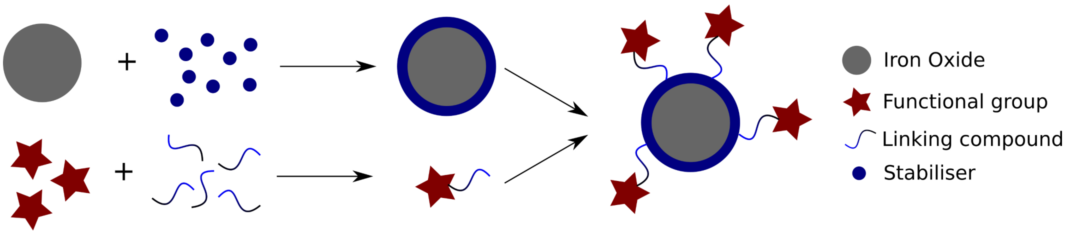

Figure 63: Schematic illustrating the covalent functionalisation of magnetite nanoparticles. A multistep method can allow for stabilisation and subsequent functionalisation.

One promising coupling method is covalent attachment using a carbodiimide coupling, which promotes the formation of a strong amide bond between amine and carboxylic acid groups. This provides a stable linker that will hold the functional group far more securely than electrostatic interactions. A wide range of biomedical materials contains amine or carboxylic acid groups allowing the carbodiimide approach to be used for many reactions.

One such example is dopamine, which contains amine groups that are capable of coupling with carboxylic acid based moieties. Dopamine can also be used as a stabiliser for iron oxide nanoparticles as it is biocompatible and can bestow water stability.[1,2] It can bind to the iron oxide surface via two hydroxide groups, forming a strong bidentate bond which minimises the risk of the stabiliser layer desorbing.[3,4] The amine groups of dopamine provide sites for additional functionality as they can easily undergo carbodiimide coupling.[5,6] To further extend the range of materials that can be bound, the dopamine groups can also be coupled to PAA via carbodiimide coupling. PAA contains carboxylic acid groups which can both bind to dopamine and provide alternative functionalisation sites for materials containing amine groups. When conjugated, the result is a stabiliser material which when bound to the iron oxide, forms a hydrophilic surface rich with amine and carboxylic acid coupling sites.

This chapter focuses on a series of functionalisation reactions to dopamine stabilised magnetic nanoparticles. The individual reactions involve PAA, PSSS, acridine-9-carboxylic acid (A-9-CA) and folic acid (FA), each of which has been chosen to add additional functionality to the underlying particles. The binding of A-9-CA to dopamine stabilised iron oxide nanoparticles has yet to be done, and will demonstrate that versatility of the coupling method. Additionally, folic acid will be bound directly to dopamine stabilised nanoparticles, eliminating the need for linking groups. Finally, a multifunctional platform will be examined to prepare a highly crystalline, water stable magnetic nanocomposite supporting both targeting groups (folic acid) and fluorescent moieties (acridine orange). For all reactions, the iron oxide nanoparticles were first prepared using the co-precipitation reaction with dopamine (or dopamine based composites) bound during precipitation. Selected reactions were repeated using microwave-assisted methods to show the applicability of this method to obtaining multifunctional nanocomposites.

6.1.1 The carbodiimide coupling reaction

In carbodiimide coupling, the carboxylic acid group is activated to form a carboxylic ester (an O-acylisourea intermediate), which will then react with amine groups to form the amide bond.[7] The excess carbodiimide forms a urea derivative, but undesirable urea based products can also form in side reactions between the O-acylisourea intermediate and groups other than the amine linker. If unreacted with the amine group, the intermediate will hydrolyse, reforming the carboxylic acid groups and producing a urea byproduct. To assist in the activation of carboxylic acid groups, N-hydroxysuccimide (NHS) can be used. NHS binds to the carboxylic acid groups to form an NHS ester which is more stable than the O-acylisourea intermediate. This reduces the side product formation and promotes amide bond formation, increasing the reaction efficiency. NHS has to be used in dry conditions though, as NHS esters can hydrolyse in water.[8–10]

The reaction conditions for carbodiimide coupling is dependant on the carbodiimide used. Two of the most common carbodiimides are 1-Ethyl-3-(3-dimethylaminopropyl) carbodiimide (EDCI) and N,N'-Dicyclohexylcarbodiimide (DCC). DCC is the most commonly used carbodiimide and is soluble in organic solvents, making it useful in polymer coupling reactions. However, it is toxic and requires extensive post processing to remove excess DCC and side products from the reaction.[8,11,12] EDCI is a water soluble alternative that that can be used for aqueous coupling reactions and as such is more suited to the development of biological agents.[6,7] Additionally EDCI is non toxic, easily removed by dialysis and can also be used in organic solvents.[5,6] Both carbodiimides will be explored and compared in this chapter to determine the best method to functionalise iron oxide nanoparticles.

6.2 Addition of poly(acrylic acid) to dopamine stabilised iron oxide nanoparticles

The attachment of PAA to dopamine serves a structural purpose rather than a biological one. Dopamine provides free amine groups for carbodiimide coupling, so the addition of PAA will provide alternative carboxylic acid binding sites, extending the range of materials that can be bound to the composite via carbodiimide coupling. The preparation of the magnetite/dopamine/PAA composite was a multistep process. PAA (Mwt 1,800) was bound to free dopamine first via a carbodiimide coupling reaction. The two EDCI-based carbodiimide routes explored here are given in Figure 64, an organic approach based on the work by Na *et al.*, and an aqueous coupling method adapted from the method presented by Wu *et al.*[5,6] The resulting materials were characterised using

FTIR, NMR and UV-Vis spectroscopy to identify which approach best suited iron oxide functionalisation. The organic based reaction formed a vicious dark brown liquid, whereas the aqueous method formed a white powder.

The dopamine/PAA conjugate was then bound to co-precipitated magnetite nanoparticles, in a one step stabilisation reaction. This occurs *in situ*, where the dopamine/PAA conjugate was bound as the iron oxide particles were precipitated (similar to other polyelectrolyte stabilisation reactions). A water stable suspension formed and washings were collected and stored. The material was characterised with XRD, DLS and FTIR spectroscopy.

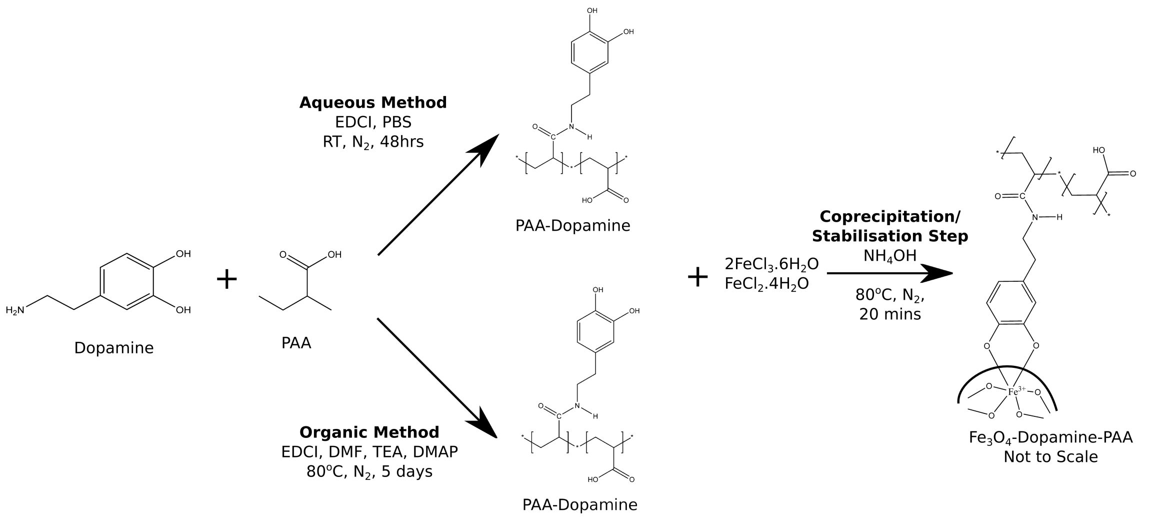

Figure 64: Schematic showing preparation and subsequent functionalisation of magnetite nanoparticles with dopamine/PAA. The dopamine/PAA composite can be linked via an EDCI coupling reaction.

6.2.1 Characterisation of the dopamine/PAA conjugate

First, the dopamine/PAA conjugate was characterised, before iron oxide nanoparticle functionalisation. IR spectroscopy was used to confirm amide bond formation. Figure 65(a) compares the coupled dopamine/PA0A composite (organic reaction: orange, aqueous reaction: green) with free dopamine (black) and free PAA (grey). Amide stretches occur at 1556 cm^{-1}, with a second peak associated with the the carbonyl group at 1630 cm^{-1}. Both stretches are observed for both the organic and aqueous reactions (Figure 65(b)). The peak positions and assignments are in good agreement with other reports in the literature.[5,6,13–15] Aromatic stretches for dopamine are seen at 1456 cm^{-1}, with hydroxide and aromatic C-C stretches of the catechol group resulting in a broad band above 3380 cm^{-1}.[6,16,17] The PAA stabiliser gives carboxylic acid stretches at 1127 and 1730 cm^{-1}, alkane C-H stretches at 2936 cm^{-1} and O-H stretches at 3300 cm-1 which overlap with some dopamine stretches.[18] The water based sample shows more peaks corresponding to the starting materials (i.e. the carboxylic acid stretch at 1127 cm^{-1}), but dopamine and PAA peaks can be observed in the organic sample as well.

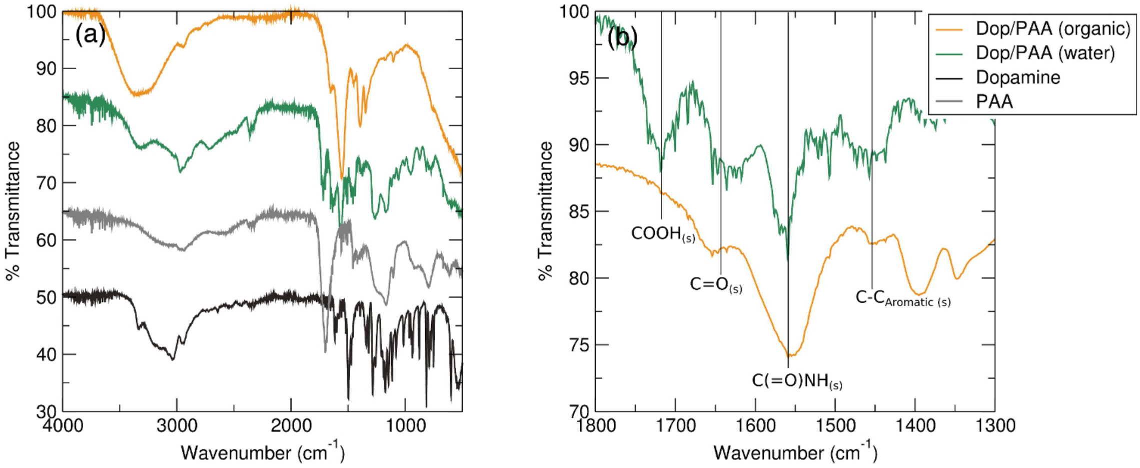

Figure 65: IR spectra of dopamine/PAA coupling reactions (a), with the expected signal area for the amide bond expanded (b). The dopamine/PAA conjugate prepared by the organic carbodiimide reaction is shown in orange, while the dopamine/PAA conjugate from the aqueous carbodiimide reaction is shown in green. The starting materials are also shown (dopamine; black, PAA; grey). The two stretches at 1556 and 1630 cm^{-1} (highlighted in (b)) correspond to the amide bond and the carbonyl group formed during the coupling reaction.

The conjugated π-bonds of dopamine mean UV-vis spectroscopy can be used to confirm the presence of dopamine in the samples. Both the organic and aqueous dopamine/PAA composites show an absorbance peak at 280 nm, seen in Figure 66 and similar to previous reports.[6,19] The peak position also indicates the dopamine component of the sample has not oxidised to quinone, as this would lead to a shift in peak position to 400 nm.[17] Minimising dopamine oxidation is desirable, as oxidation can reduce dopamine's affinity for the iron oxide surface and risk early desorption.[20,21]

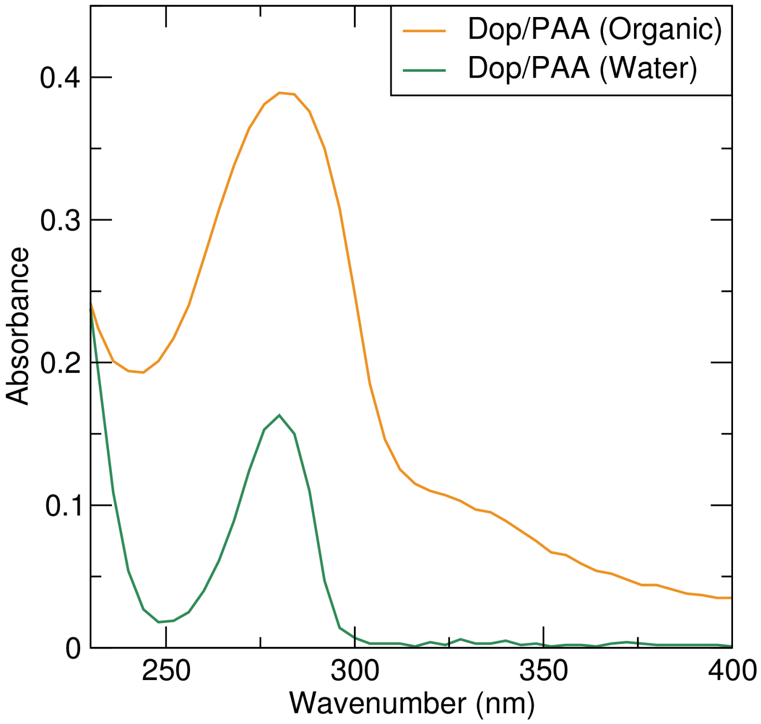

Figure 66: UV-Vis spectra of the dopamine/PAA composite from the organic (orange) and aqueous (green) coupling reactions.

NMR spectroscopy was used to further confirm the coupling reaction and to map the structure of the conjugated components (Figure 67). For pure PAA (purple spectrum), the peaks between 1 ppm and 2.5 ppm relate to the polyelectrolyte alkane backbone. The broadening of the peaks is characteristic of polymers due to the repetition of the signal from the identical monomers. Dopamine shifts are shown in blue and are observed at higher shifts than the PAA component. The dopamine alone presents strong alkane signals at 2.7 ppm and 3 ppm as a series of split peaks with the group of signals centred at 6.7 ppm are characteristic for the catechol aromatic ring.

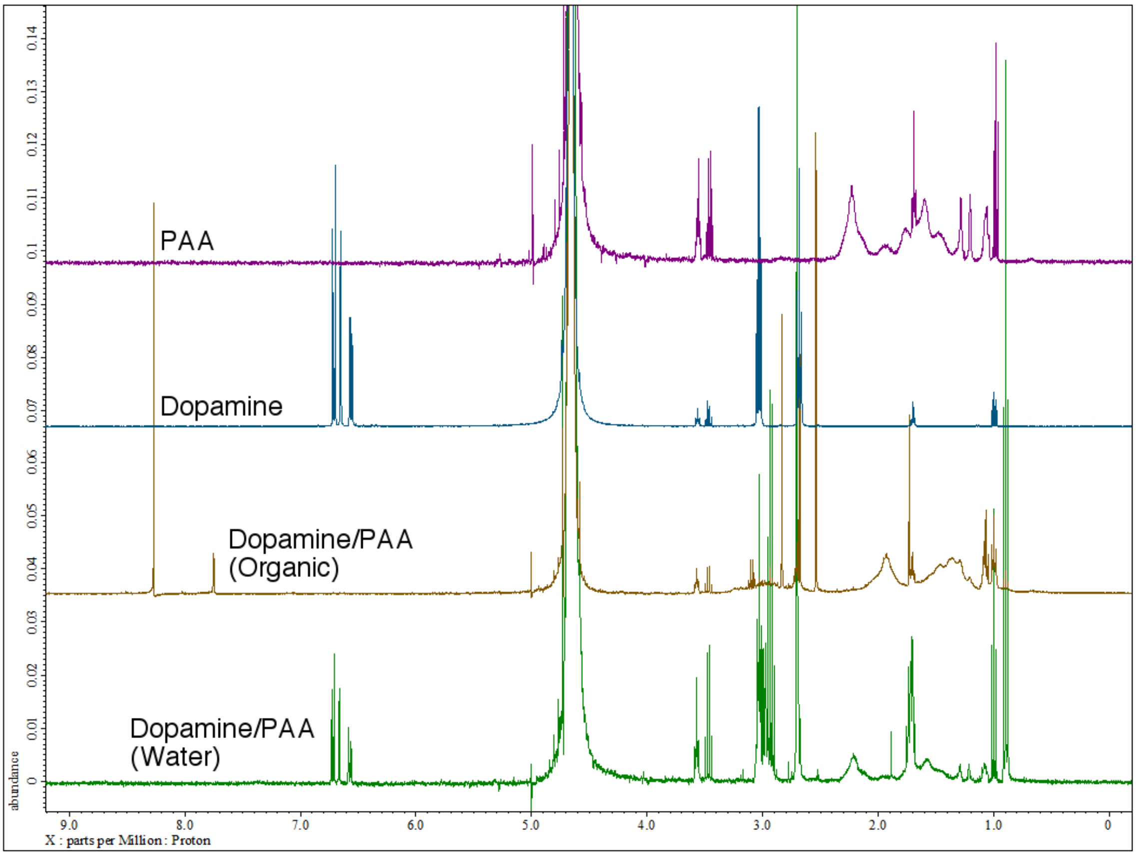

Figure 67: NMR data of the dopamine/PAA composite synthesised via organic (orange) and aqueous (green) methods and the starting materials (dopamine; blue, PAA; purple). Both composites show similarities with the starting materials.

The product from the organic carbodiimide reaction (orange) shows a significant difference compared to the free dopamine sample, with an absence of aromatic peaks at 6.7 ppm which are replaced by two large peaks at 7.7 ppm and 8.3 ppm. The FTIR and UV-Vis results indicate that the aromatic group is still present in the structure but the NMR results suggest an incomplete reaction. These unaccounted peaks could signify an incomplete product or unwanted side products from the reaction. These differences indicate that the organic coupling of dopamine and PAA is unsuitable for further stabilisation and functionalisation of the iron oxide nanoparticles.

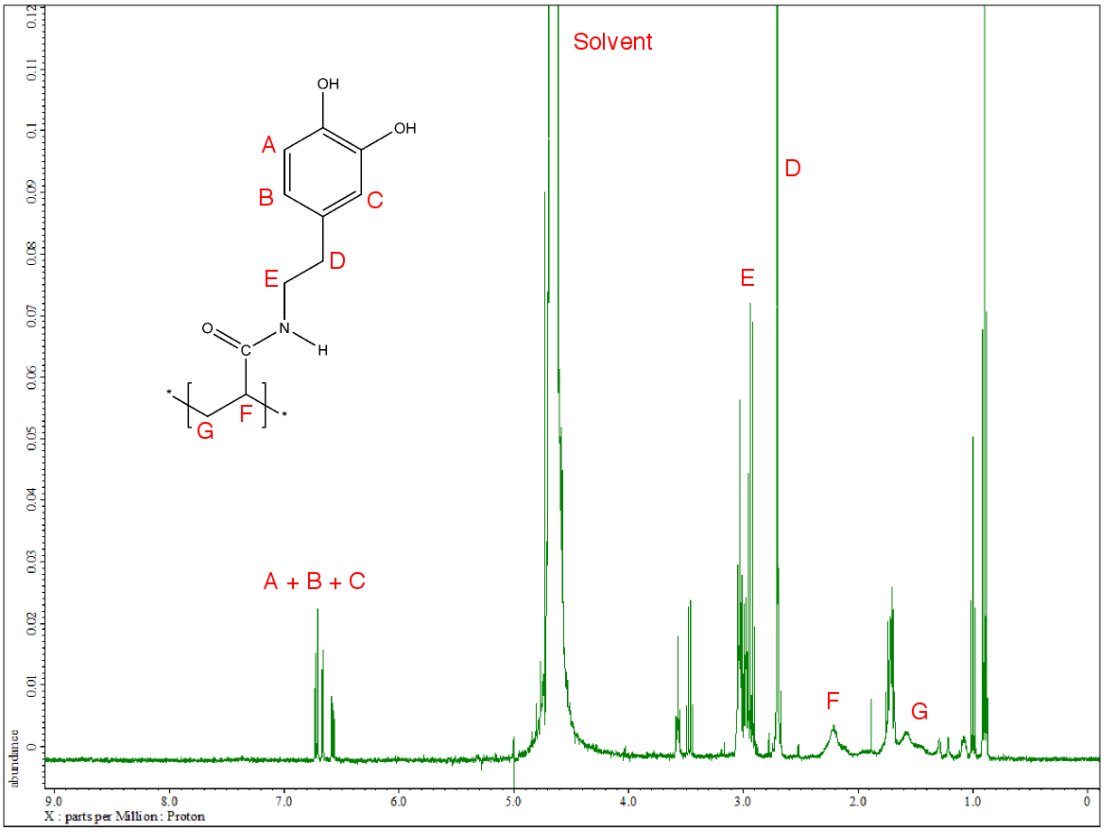

Figure 68: NMR spectrum of the dopamine/PAA composite prepared via the water-based EDCI coupling method. Peak assignments based on shifting and splitting have been calculated with the strongest signals agreeing with the expected structure. Additional unaccounted peaks are present in the spectra which can be attributed to impurities or residual starting materials.

The NMR spectrum for the dopamine/PAA composite prepared by the aqueous method shows peaks for both starting materials, with a slight shifting in peak position, and an assigned spectrum is given in Figure 68. The only discrepancy is the lack of a signal for the proton of the amide bond. The signal is expected to have a high chemical shift at 8ppm, as it is attached to a very electronegative group. The signal could still be present, but as a very weak broad signal which will be difficult to detect from the background noise. The FTIR data shows two distinct amide stretches, indicating the presence of the amide bond, but the NMR data could have further confirmed this. The NMR data does confirm the structure of the dopamine and PAA components of the conjugate though. From these results, the aqueous carbodiimide coupling reaction is the best way to bind PAA to dopamine with both the amide bond and individual components confirmed by FTIR and NMR spectroscopy respectively. The aqueous method is also advantageous as it is more comparable with biological systems requiring less post processing and can be done in the same vessel as the co-precipitation reaction. Stabilising iron oxide nanoparticles with the conjugate, will build upon the work by Wu *et al.*[6] They used the conjugate in electrostatic layer by layer reactions to form extremely stable PAA/PAH multilayers. This work will show that the conjugate can also be used directly in the stabilisation of iron oxide nanoparticles, and will provide multiple different sites for further carbodiimide coupling

6.2.2 Stabilisation of iron oxide nanoparticles with dopamine/PAA conjugate

Using the aqueous carbodiimide coupling method, the dopamine/PAA conjugate was bound to magnetite nanoparticles in a one pot co-precipitation/stabilisation reaction shown in Figure 69. Addition of the conjugate to the iron chloride solution (a) caused the solution to turn a dark green (b), which when precipitated with ammonia formed the characteristic jet black particles (c). The sample was characterised with XRD, FTIR and DLS.

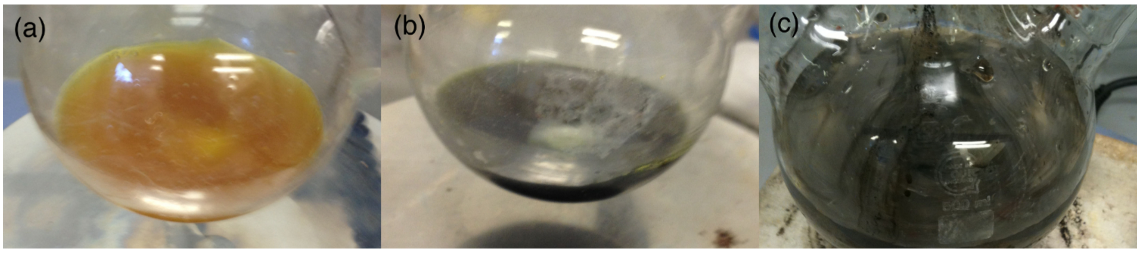

Figure 69: Photos of the co-precipitation/stabilisation reaction of the magnetite/dopamine composite. The starting materials form an orange solution (a), which when exposed to dopamine the solution changes to dark green (b). After addition of ammonium hydroxide a jet black precipitate forms, characteristic of magnetite (c).

Powder XRD patterns were collected to confirm that the organic conjugate coating does not effect the phase of the magnetic core of the sample, with the peak broadening used to calculate the average primary particle size using the Scherrer equation. The patterns for stabilised PAA-Dopamine-Fe_3O_4 composite prepared by coprecipitation (red) are shown in Figure 70. Comparative patterns for bare Fe_3O_4 (grey) and dopamine-stabilised Fe_3O_4 (green) are also shown. The PAA-Dopamine-Fe_3O_4 pattern agrees with the previously prepared magnetite sample (grey) and magnetite standards from the ICSD and previously reported Fe_3O_4 patterns.[22–25] The broad peaks for the PAA-Dopamine-Fe_3O_4 composite suggest small nanoparticles with the Scherrer equation calculating crystallite size as 11.6 nm. These sizes are similar to previously prepared bare Fe_3O_4 (11.2 nm), with the work by Basti *et al.* and Kemikli *et al.* confirming that the dopamine coating has no oxidising/size inhibiting effect on the magnetite crystal structure.[11,16] The crystallite size is small enough for the particles to be single domain and therefore superparamagnetic.[26,27]

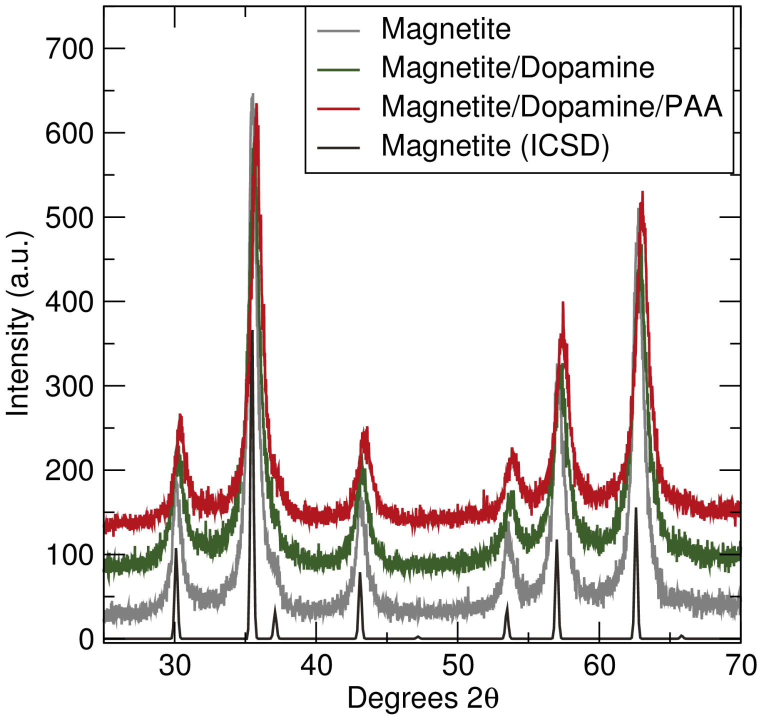

Figure 70: XRD patterns of magnetite stabilised dopamine (dark green) and the dopamine/PAA conjugate (red) prepared by the standard co-precipitation reaction. The stabilised nanocomposites shows no oxidation and matches bare magnetite prepared in the same way (grey) and the ICSD crystal pattern (black).[22]

FTIR spectroscopy was used to further confirm the binding of the organic conjugate to the iron oxide particles and is shown in Figure 71. The IR spectrum for PAA-Dopamine-Fe_3O_4 (red) shows similarities between both bare magnetite (grey) and the dopamine/PAA conjugate (green). The amide peaks at 1549 and 1630 cm^{-1} still persist when bound to the iron oxide surface. Additionally, carboxylic acid and aromatic stretches from the PAA and dopamine components can be seen at 1731 cm^{-1} and 1456 cm^{-1}. The Fe-O stretch is found at 550 cm^{-1}, characteristic for magnetite.[28,29] Dopamine binding can be discerned from the hydroxide peaks above 3000 cm^{-1} with both C-H and O-H stretch exclusive to the catechol group of dopamine. Shultz *et al.* explored the binding of dopamine to iron oxide surfaces using FTIR spectroscopy, noting that the hydroxide peaks at 3300 cm^{-1} shift to the higher wave numbers of 3400-3500 cm^{-1} when bound to the iron oxide surface.[30] This can be seen in Figure 71, with the 3322 cm^{-1} shoulder broadening and shifting to 3429 cm^{-1}. Additionally, the formation of a water stable suspension for the standard co-precipitation of particles and the colour change of the iron chloride starting solution to green indicated dopamine binding.[30] The amide peaks and persistence of PAA peaks after 5 washings also confirms the coupling of PAA to dopamine.

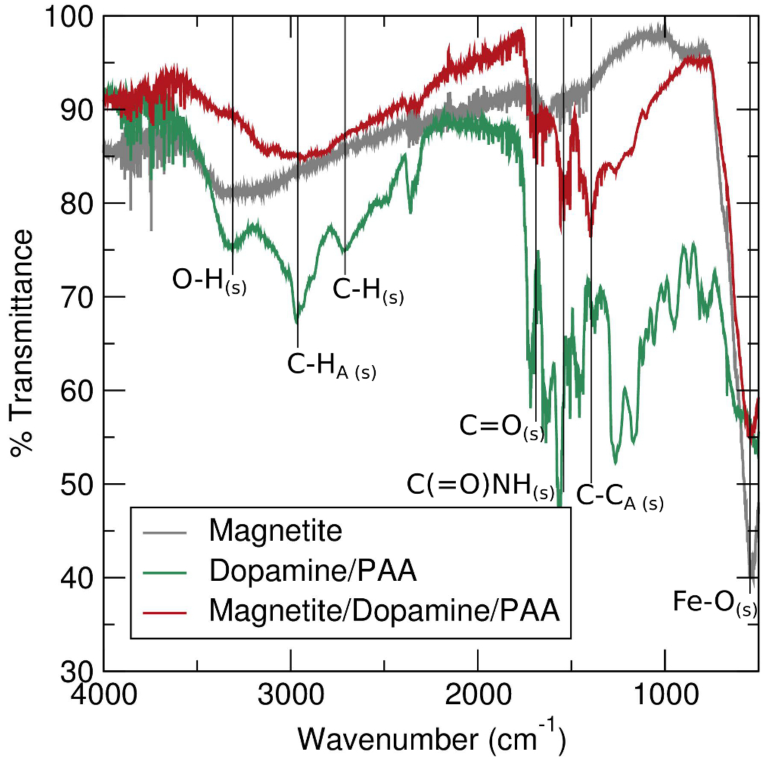

Figure 71: IR spectra of the dopamine/PAA conjugate (green) and magnetite stabilised with the conjugate (red). Peaks with $_A$ signify aromatic peaks.

The aromatic groups of dopamine cannot be confirmed by UV-Vis spectroscopy, as scattering of light by the magnetic cores suppresses the 280 nm absorbance peak (figure 72).

The stabilised co-precipitated particles formed a water stable dispersion which was characterised using DLS to determine the effect of functionalisation on composite size and water stability. As the suspensions become pH neutral, the Z-averages and polydispersities decrease and stabilise. Values are given in Table 18. The addition of the PAA-dopamine conjugate increases the composite cluster distribution when compared to iron oxide nanoparticles stabilised with either PAA or dopamine alone, shown in Figure 73. Despite the increased size distribution, the Z-average of the final washing is under 200 nm making it suitable for biomedical applications.[31–33] The particle surface charges were found to be above -30 mV, indicating high water stability which was confirmed by the particles staying in solution for over a month.[34] These characterisation results show that the dopamine/PAA conjugate has wide range of stabilisation applications in addition to forming LBL assemblies. The material can stabilise and bestow water stability on iron oxide nanoparticles, while presenting a surface rich with amine and carboxylic acid groups for further functionalisation.

Table 18: DLS measurements of magnetite/dopamine/PAA nanocomposite washings. Strongly negative zeta potentials (Z. Po.) values indicate high water stability for the final washing

Sample	**Washing 3**		**Washing 4**		**Washing 5**		**Z. Po.**
	Z-Average (d.nm)	**PDI**	**Z-Average** (d.nm)	**PDI**	**Z-Average** (d.nm)	**PDI**	(mV)
Mag/Dop/PAA	61.98	0.262	103.06	0.161	110.7	0.109	-46.3
Mag/Dop	185.03	0.325	155	0.167	163.83	0.090	-50.8
Mag/PAA	64.8	0.176	69.1	0.177	90.74	0.126	-60.0

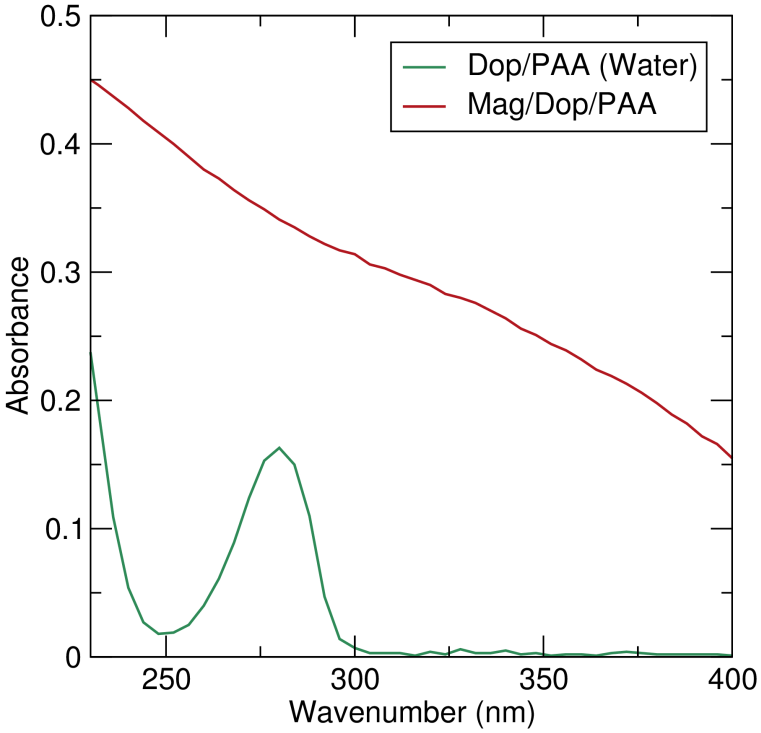

Figure 72: UV-Vis spectra of magnetite stabilised with the dopamine/PAA conjugate (red) along with the unbound dopamine/PAA conjugate (green). Scattering of light by the magnetic cores suppresses the dopamine absorbance at 280 nm.

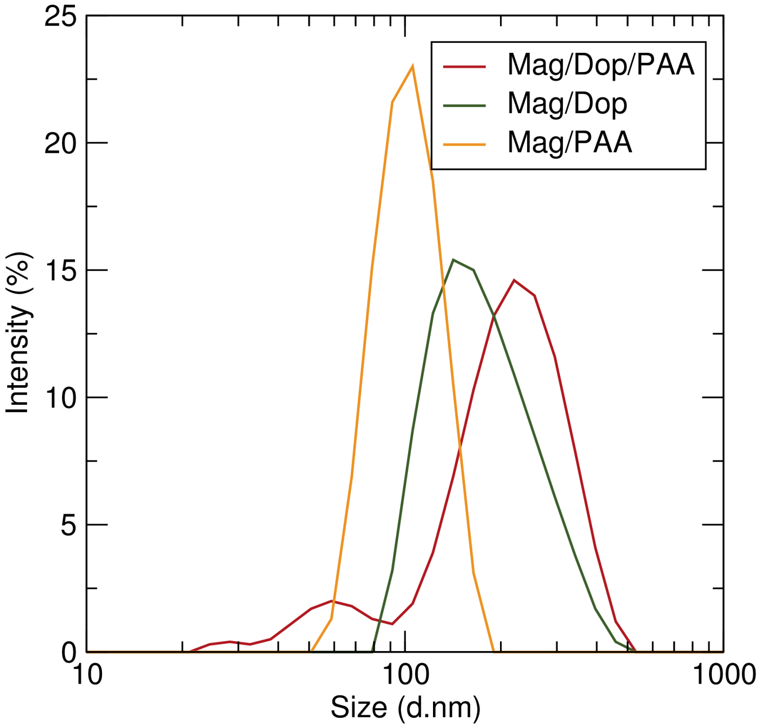

Figure 73: Size distribution of the final washing of the nanocomposites stabilised with either dopamine (olive), PAA (orange) and dopamine/PAA (red) measured using DLS.

6.3 Addition of acridine-9-carboxylic acid to dopamine-stabilised iron oxide nanoparticles

The aqueous carbodiimide coupling reaction can be used to graft a wide range of materials to dopamine, in addition to polyelectrolytes. One such example is fluorescent groups, which can allow the particles to be used in biomedical applications such as cell imaging and cell tracking. Acridine-9-carboxylic acid (A-9-CA) is a highly fluorescent group and was bound to dopamine stabilised nanoparticles instead of PAA. Coupling occurred via the same water based EDCI carbodiimide coupling reaction but PAA was substituted for A-9-CA, shown in Figure 74. One difference from the previous reaction was that A-9-CA was bound to dopamine after it had been used to stabilise magnetite nanoparticles. Binding after stabilisation minimises the risk of dopamine oxidation before it coordinates with the magnetite surface. Fluorescent dyes have been bound to iron oxide nanoparticles before but this work is the first reported approach to directly linking A-9-CA to dopamine stabilised magnetite nanoparticles.[35,36] When the dopamine stabiliser was added to the iron chloride starting solution, a dark green solution formed, which turned jet black on precipitation with ammonia. The sample forms a water stable suspension after several washings with the third to fifth washing collected and stored. The prepared product was characterised with FTIR, DLS, UV-Vis and fluorescence spectroscopy.

FTIR spectroscopy was used to confirm the binding of A-9-CA to the dopamine coating via amide bond formation and the stabilisation of magnetite with dopamine. The two stretches at 1563 and 1650 cm^{-1} signify the formation of the amide bond linking the two components.[13–15] The A-9-CA component shows an C-N vibration at 1263 cm^{-1}, with aromatic stretches at 1056 cm^{-1}, 977 cm^{-1} and 850 cm^{-1} associated with single and conjugated aromatic rings. This assignment is in good agreement to previous reports of acridine compounds.[37,38] Dopamine components can also be identified, with the C-C aromatic stretch identified at 1396 cm^{-1}, and a large broad O-H and C-H stretch at 3300 cm^{-1}, which indicates dopamine binding to the iron oxide surface. The Fe-O stretch is seen at 540 cm^{-1}.

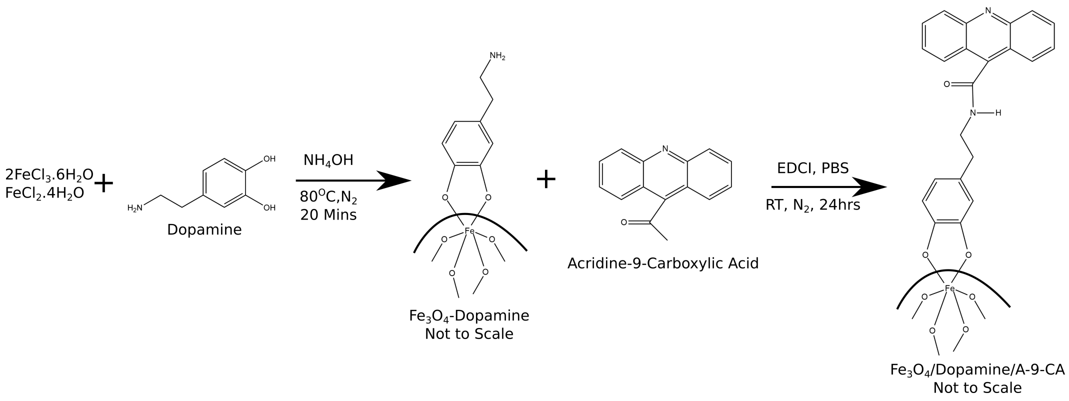

Figure 74: Schematic detailing the preparation of a fluorescent magnetic nanocomposites stabilised with both dopamine and acridine-9-carboxylic acid. This is a multi-step reaction that involves stabilising the magnetite cores with dopamine, before the attachment of A-9-CA via aqueous EDCI coupling.

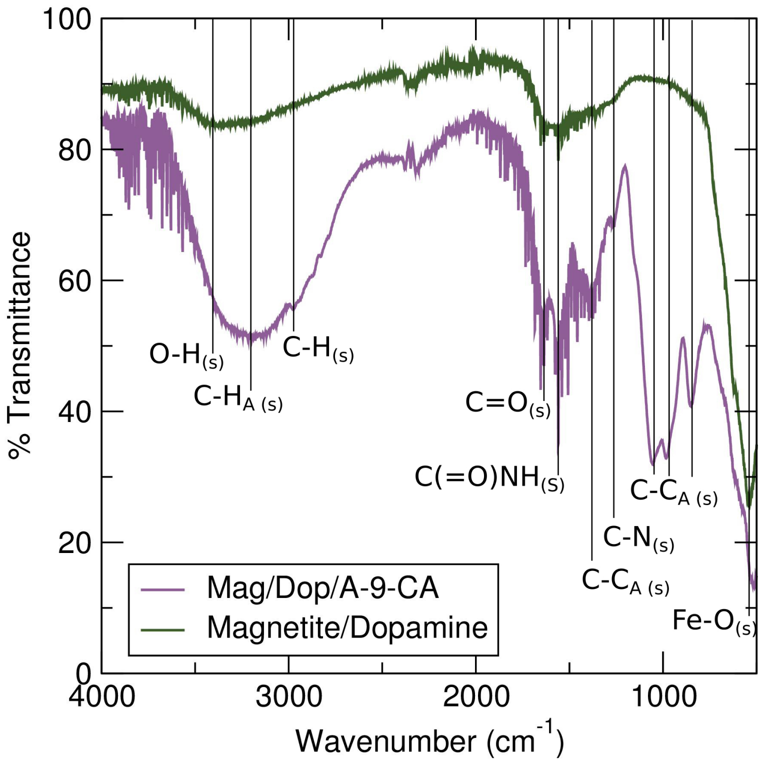

Figure 75: FTIR spectra of magnetite cores stabilised with dopamine (olive) and dopamine/acridine-9-carboxylic acid (violet). $_A$ *signifies aromatic stretches.*

DLS measurements show that the addition of A-9-CA does not drastically affect the cluster size of the composite (Table 19) and that as the sample is washed, the z-average and PDI values stabilise. The addition of A-9-CA does increase the PDI values, indicating an increase in polydispersity. The Z-average values for the composites are below 200 nm making them suitable for biological applications.[31–33] The dispersions display excellent water stability, staying in suspension for over a month. Additionally, the A-9-CA component has little effect on surface charge, with a zeta potential of -53.2 mV to reflect this.[34]

Table 19: DLS measurements of magnetite/dopamine/A-9-CA washings. Negative zeta potentials (Z. Po.) confirm that water stability is not lost through functionalisation with acridine groups.

Sample	**Washing 3**		**Washing 4**		**Washing 5**		**Z. Po.**
	Z-Average (d.nm)	**PDI**	**Z-Average** (d.nm)	**PDI**	**Z-Average** (d.nm)	**PDI**	(mV)
Mag/Dop/A-9-CA	173.9	0.443	97.31	0.116	107.4	0.164	-53.2
Mag/Dop	185.03	0.325	155	0.167	163.83	0.090	-50.8

UV-Vis and fluorescence spectroscopy was used to confirm the presence of the A-9-CA component. UV-Vis measurements show several absorption peaks for the A-9-CA functionalised composite (Figure 76). The two strongest peaks are at 250 nm and 350 nm and are characteristic of the π,π* transition of A-9-CA.[39,40] The π,π* transition is the promotion of electron from the π bonding orbital to the π anti bonding orbital. The transition of the electron back to the bonding orbital, releases the excited energy through a variety of different ways including light. This is an allowed transition and is responsible for the fluorescence of the dye. These peaks agree with the prepared acridine standard and other acridine based fluorescent compounds reported by other groups.[40–42] These peaks are only present for the first two washings of the composite though, with remaining dispersions showing no peaks. As the sample is washed, excess A-9-CA is washed out decreasing the samples absorbance. As more of the composite remains in solution (from washing), the suspended inorganic cores scatter the UV measurement light, resulting in a sloping effect. This sloping effect is undesirable as it can hide the fluorescent signals as seen in dispersions 3-5. The dopamine absorbance at 280 nm also cannot be seen, either merging with the acridine peaks or hidden by the light scattering of the particles.

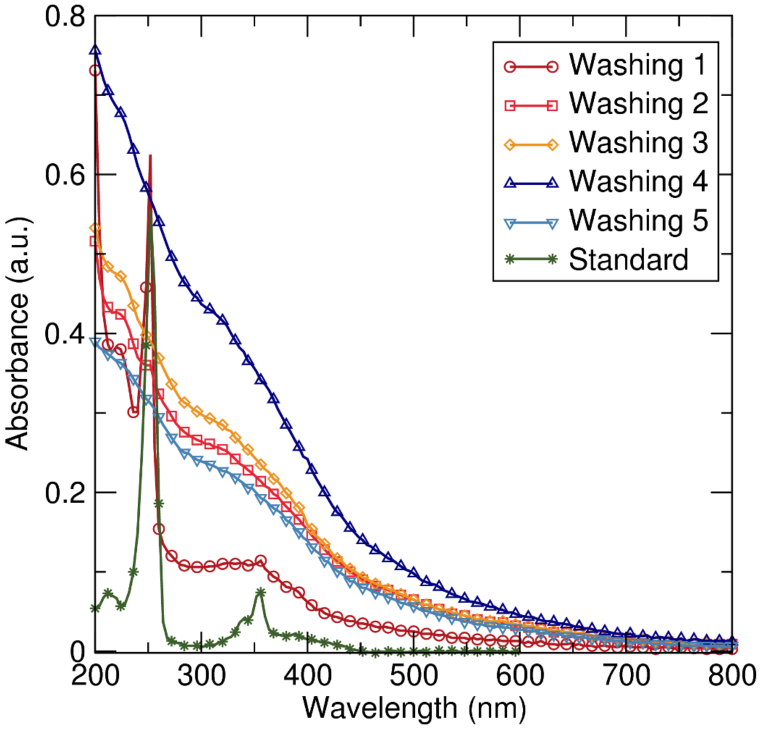

Figure 76: UV-Vis spectra of the washings of the magnetite/dopamine/A-9-CA nanocomposite. The absorbances at 250 nm and 350 nm are characteristic of A-9-CA.[39,40] *As the sample is washed the 350 nm absorbance decreases due to scattering of light by the nanoparticles.*

Fluorescence spectroscopy was employed to measure the emission and excitation profiles of the magnetite/dopamine/A-9-CA washings (figure 77). The emission spectra (Figure 77(b)) were obtained by exciting at 350 nm and corresponding excitation spectra were also collected.The A-9-CA-dopamine-Fe_3O_4 composite show characteristic peaks for acridine groups with an emission peak at 430 nm and an excitation peak 350 nm.[40,43] As the samples are washed, the fluorescent signal decreases. The initial signal decrease is due to unbound A-9-CA being washed out of the composite. The final, neutral sample still displays peaks for A-9-CA indicating the successful coupling to the nanoparticles. The emission intensity is similar to the Rhodamine-B decorated nanocomposite in chapter 4 which indicates potential in confocal measurements.

This is the first example of acridine-9-carboxylic acid being bound to dopamine stabilised iron oxide nanoparticles via an aqueous carbodiimide coupling method. The direct attachment of the fluorescent group leads to a quick and simple coupling reaction that can be done in a single functionalisation step. The formation of the amide bond ensures the dye is securely attached to the composite, as opposed to electrostatic binding. Stabilisation of the iron oxide particles before functionalisation is also a key element of this synthesis method. Stabilising *in situ* allows the magnetic base to be prepared independently to the functionalisation reaction. Microwave assisted co-precipitation methods combined with surface defect coordinating stabilisers (i.e. PSSS or Dopamine) can be used to ensure the magnetic base is highly crystalline, precipitated and stable. Once formed further functionalisation can occur with little effect on the magnetic foundation as it will be interacting with the stabiliser material not the magnetic base.

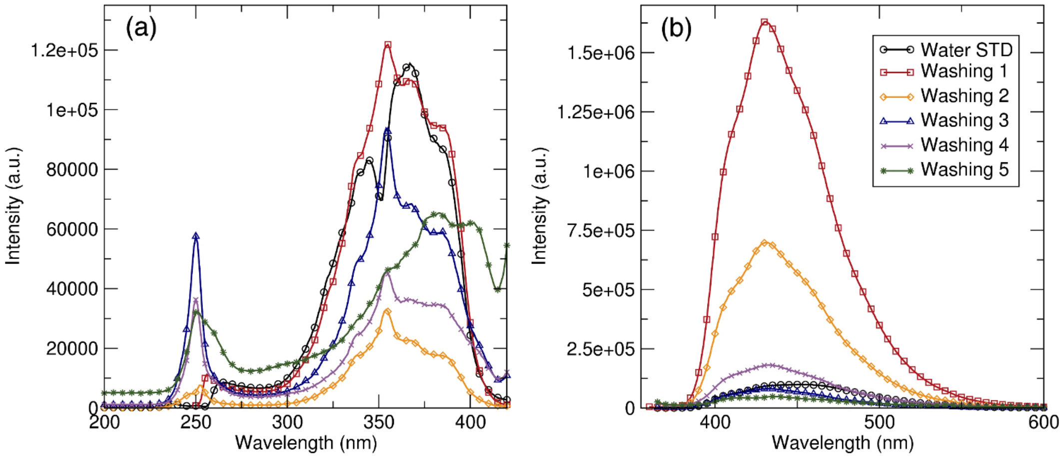

Figure 77: (a) Excitation and (b) emission spectra of magnetite/dopamine/A-9-CA nanocomposites. As the sample is washed, the fluorescence intensities decrease as more unbound acridine is removed from the washings but the final washings still show peaks that are characteristic of the acridine group indicating binding.

6.4 Addition of folic acid to dopamine-stabilised iron oxide nanoparticles

Folic acid is an example of a targeting molecule with a high binding affinity for folate receptors, which are over-expressed in cancerous cells.[8,44] Folic acid contains multiple carboxylic acid binding sites, suitable for carbodiimide coupling. DCC has been used here as the coupling agent in organic conditions, due to the solubility of folic acid. A small excess of DCC was used to ensure that only one of the carboxylic acid sites was activated, and N-

Hydroxysuccinimide (NHS) was used to activate the acid group.[8] Folic acid contains two carboxylic acid groups (labelled α and γ) with the γ group being activated by NHS due to the higher reactivity.[45,46] The reaction follows Figure 78 leading to the formation of a folic acid-N-hydroxysuccinimide (FA-NHS) conjugate. The activation process was based on the work by Chen *et al.* who reported the activation of folic acid with NHS for subsequent binding to an amine-capped silica shell.[44] This work was adapted so the activated folic acid could be stored and bound to dopamine-coated magnetite nanoparticles instead. The activated folic acid formed an orange powder that was characterised with FTIR, UV-Vis and NMR spectroscopy. This activated folic acid was then bound to the dopamine-coated magnetite nanoparticles. A colour change with addition of dopamine to the iron chloride solution was noted and a jet black precipitate formed upon addition of ammonia. A water stable suspension formed after repeated washings which was collected and stored. The final composite was then characterised with FTIR, DLS and UV-Vis spectroscopy.

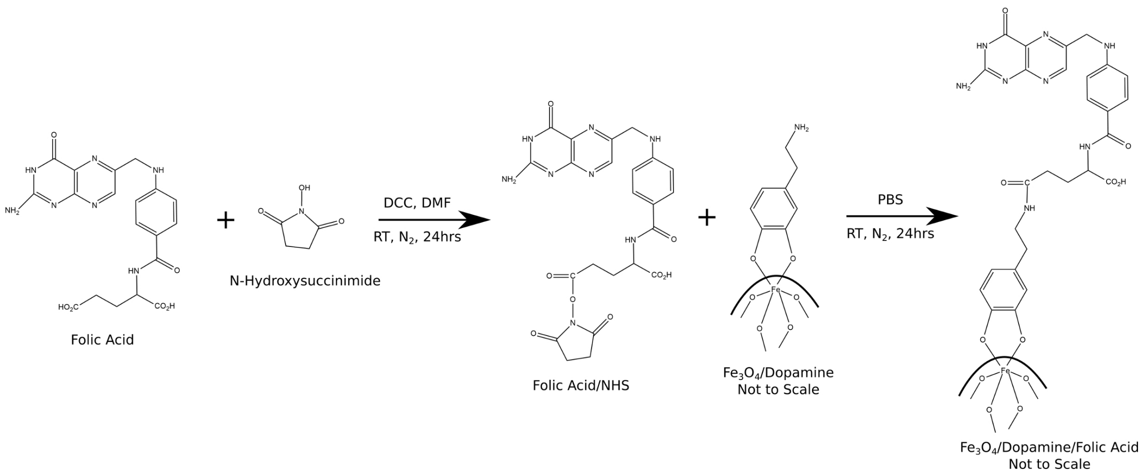

Figure 78: Schematic detailing the preparation of a magnetite nanoparticles containing both dopamine and folic acid for stabilisation and targeting purposes.

6.4.1 Characterisation of the activated FA-NHS conjugate

FTIR was used to confirm the activation of folic acid, but due to the complexity of folic acid, peak assignment can be difficult as below 2000 cm^{-1} it very difficult to distinguish individual peaks. Between the 2000 and 4000 cm^{-1}, similarities between the conjugate and starting materials can be observed (Figure 79).

The FA-NHS conjugate has a large stretch at 3200 cm^{-1} with a smaller shoulder at 2900 cm^{-1}. Folic acid has stretches at 3543, 3412 and 3322 cm^{-1}, which are assigned to O-H stretches and secondary N-H stretches.[47] There is also a broad peak between 3150-2700 cm^{-1} for the alkane and alkene groups of folic acid. NHS has three intense stretches at 3110, 2975 and 2869 cm^{-1} relating to C-H stretches that make up the structure.[48] The FA-NHS conjugate forms a very large broad band, with individual peaks from both of these components seen in this band. The shoulder extending up to 3600 cm^{-1} and the small peak at 3245 cm^{-1} are for the hydroxide and amine groups of folic acid. Smaller shifted peaks seen at 2938 and 2791 cm^{-1} relate to C-H stretches. The shifting effect is indicative of carboxylic acid activation and are in good agreement with previous reports.[49,50]

The absorbing aromatic groups of folic acid can be studied using UV-vis spectroscopy, with a characteristic π-π* absorption peak at 280 nm and n-π* absorption peak 380 nm (Figure 80). These absorbances are in good agreement with the literature.[9,51,52]

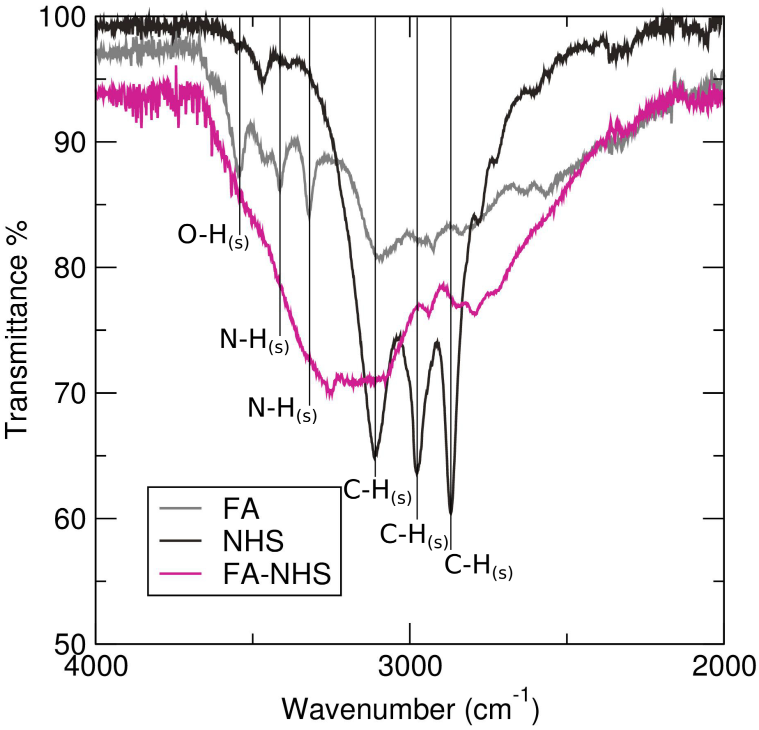

Figure 79: FTIR spectra of FA-NHS (violet) and the starting materials (Folic acid; grey, N-Hydroxysuccinimide; black).

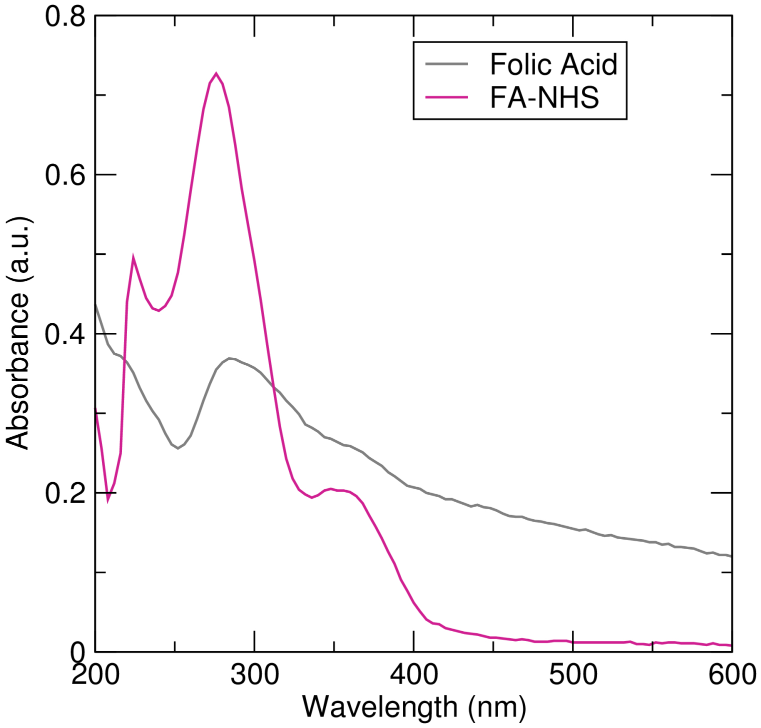

Figure 80: UV-Vis spectra of folic acid-NHS conjugate (violet) and folic acid standard (grey).

The FA-NHS conjugate and starting materials were also characterised using NMR spectroscopy and are shown in Figure 81. The alkane structure of NHS appears as a series of peaks at 2.6 ppm. The folic acid alkane protons are found at 1.6 ppm (A) and 2.0 ppm (B). The aromatic protons are found at 6.6 ppm (D), 7.4 ppm (E) and 7.8 ppm (F). The amine protons have the highest shift at 8.6 ppm (G). Complete peak assignment is not possible, as the D_2O solvent peak hides some of the alkane/amine signals (labelled (S) on the structure). The assigned peaks in the NMR spectrum agrees with the FTIR spectrum confirming the activation of FA with NHS. The signal assignments also agree with literature reports for activated folic acid.[53]

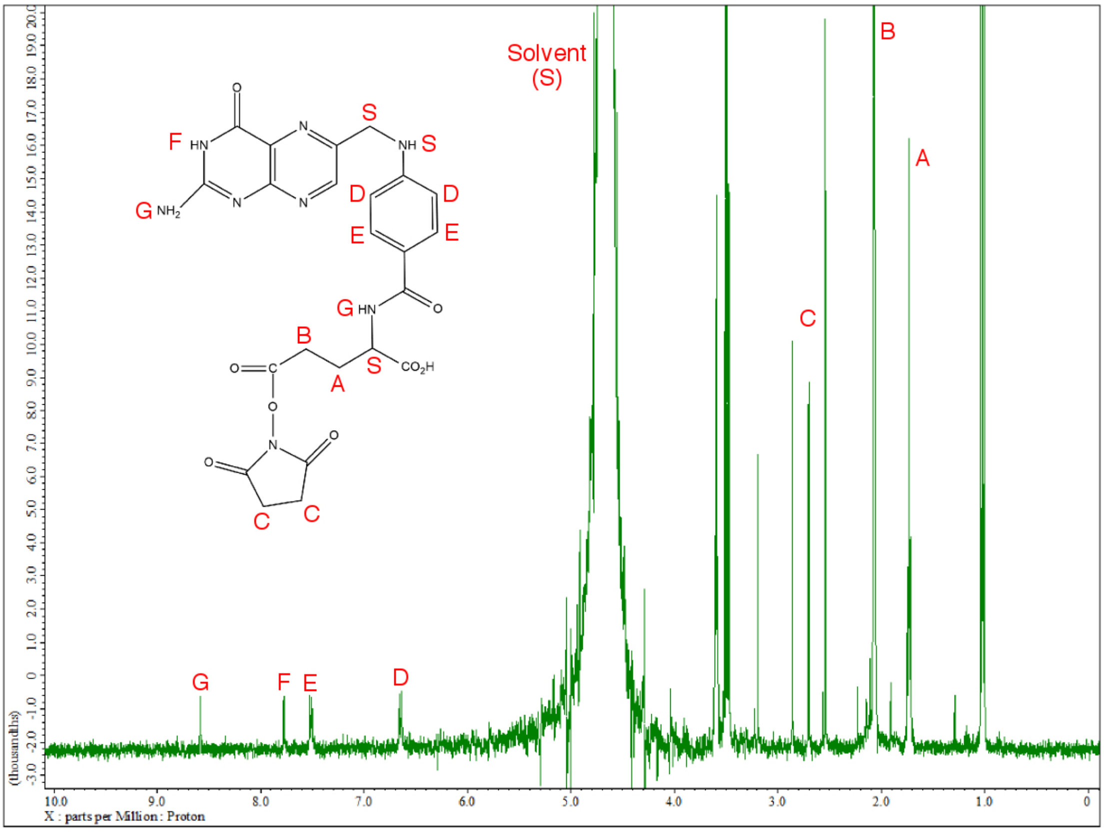

Figure 81: NMR spectra of the FA-NHS conjugate in D_2O. The conjugate shows peaks for both the folic acid and NHS components. Unaccounted peaks suggest the presence of impurities.

6.4.2 Characterisation of the magnetite/dopamine/FA nanocomposite

Figure 82, image (a) compares the FTIR spectra of magnetite nanoparticles functionalised with dopamine, with those functionalised with both dopamine and folic acid. Firstly, a close inspection of the response at 1530 cm^{-1}, shows a slight broadening of the peak for the folic acid functionalised sample. This broadening is due to amide bond linking the folic acid groups to the composite, but it is weak due to the low concentration of folic acid used. This peak is observed in the literature for other folic acid functionalisation reactions and indicates coupling.[10,45,54] The neighbouring peak at 1460 cm^{-1} increases in intensity when folic acid is bound. This is an aromatic stretch which is increased by the aromatic groups in folic acid. Additionally two extra peaks formed at 1050 and 1090 cm^{-1} (image (b)) relate to the folic acid component. These stretches are characteristic of aliphatic amine which is contained in folic acid.

A small set of peaks are observed at 2900 cm^{-1} due to C-H stretches from folic acid. The weak signals is due to the low concentration of folic acid used and suggests there are still free binding sites. The persistence of the folic acid signals after multiple washings indicates the material is securely bound. The folic acid component could not be further confirmed by UV-Vis spectroscopy due to scattering of light from the magnetic cores.

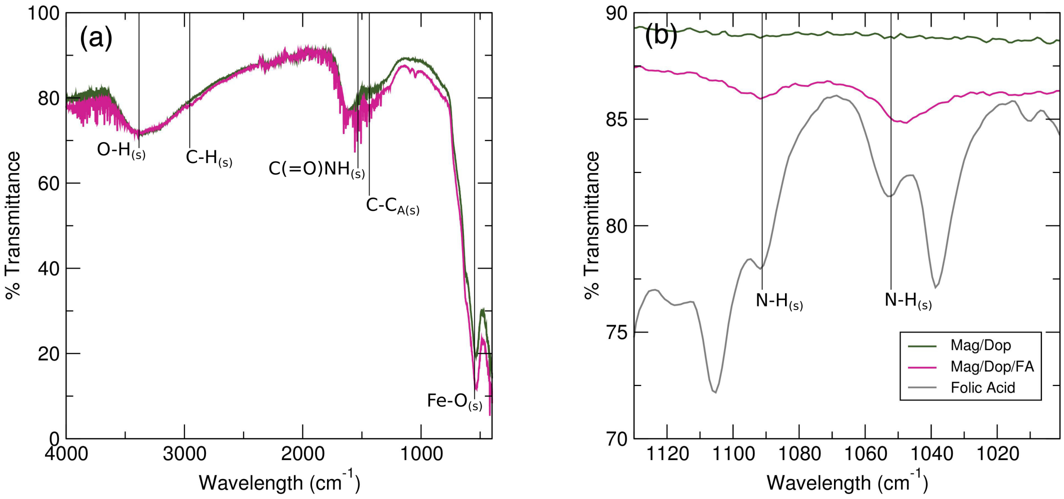

Figure 82: (a) FTIR spectra of magnetite nanoparticles functionalised with folic acid/dopamine conjugate (violet) and dopamine alone (olive). (b) focuses on the 1000-1140 cm^{-1} region, where the composite shows N-H peaks found in the unbound folic acid (grey).

The folic acid bound nanocomposites formed water stable suspensions which were analysed with DLS. The washed suspensions of the nanocomposite display similar DLS properties to previous dopamine stabilised iron oxide nanoparticles. As the sample is washed, the DLS values and the size distribution of the washings become more consistent (Table 20) and the samples stay in suspension for longer. The stabilised composite is slightly larger than previous samples. This is due to the composite supporting larger folic acid molecules. However, the low PDI indicate these are monodisperse dispersions, which is further supported by the monomodal size distribution of the sample seen in Figure 83. The final dispersion has a z-average below 200 nm, making them suitable for biomedical applications.[31–33] The sample also has an high zeta potential (-50.4 mV) indicating good water stability which is reflected in the samples staying in suspension for over a month.[34]

Table 20: DLS measurements of magnetite/dopamine nanoparticles functionalised with folic acid. High water stability is reflected in strong zeta potentials (Z. Po.)

Sample	**Washing 3**		**Washing 4**		**Washing 5**		**Z. Po.**
	Z-Average (d.nm)	**PDI**	**Z-Average** (d.nm)	**PDI**	**Z-Average** (d.nm)	**PDI**	(mV)
Mag/Dop/FA	84.3	0.294	113.8	0.137	150.3	0.092	-50.4
Mag/Dop	185.03	0.325	155	0.167	163.83	0.090	-50.8

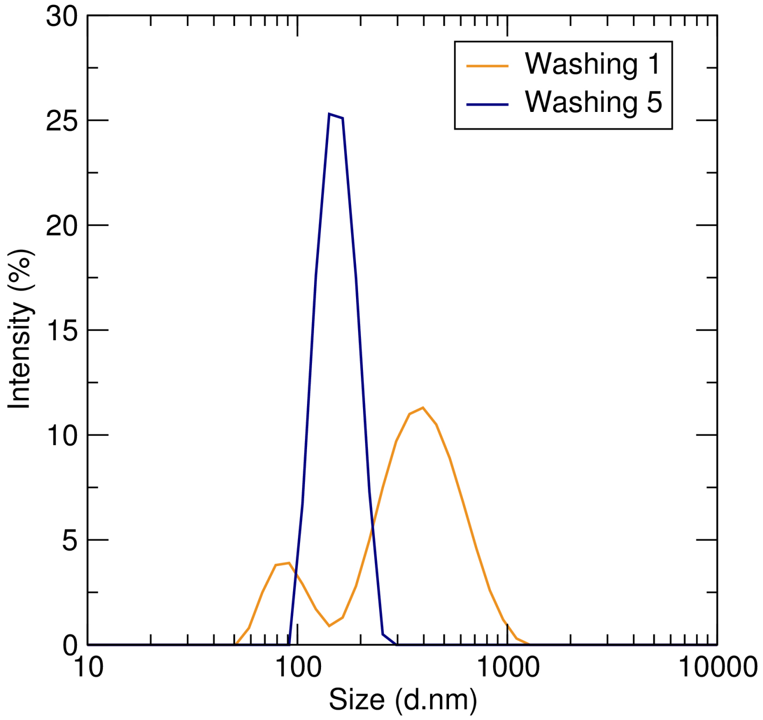

Figure 83: The size distribution of the first and fifth washing of the magnetite/dopamine/folic acid composite, measured using dynamic light scattering. The results show that the size distribution significantly narrows as the particles are washed reflecting the low PDI values measured for the samples.

The characterisation methods confirm that not only is the folic acid bound to dopamine stabilised magnetite nanoparticles, but the addition of this group has little effect on the hydrodynamic properties of the composite. This work is also a first example of folic acid being directly bound to the magnetite/dopamine particles. Commonly folic acid is bound to dopamine groups via a organic linker like PEG or dextran.[55,56] The method outlined here shows that folic acid can be bound directly with the dopamine group, which quickens and simplifies the synthesis process. The folic acid component will complement the magnetic targeting functionality of the iron oxide base, resulting in a highly selective composite. Microwave irradiation can then further enhance the iron oxide crystallinity and magnetism, optimising the targeting capabilities of the material.

6.5 Stabilising iron oxide nanoparticles with dopamine and PSSS

Chapter 4 established PSSS as the best stabiliser for magnetite nanoparticles, resulting in a nanocomposite with excellent DLS values which was water stable for over 2 months. This chapter demonstrates that dopamine provides secure anchoring points for carbodiimide coupling. By binding both PSSS and dopamine onto the iron oxide surface, the excellent water stability of PSSS can be combined with the functionalisation options provided by dopamine. Unlike other functionalisation reactions, carbodiimide coupling is not needed for the attachment of PSSS or dopamine to iron oxide particles, with the stabilisers bound in a one-pot manner during the precipitation of the nanoparticles. The dopamine and PSSS stabilisers were added simultaneously to the iron chloride solution and the schematic is given in Figure 84. The resulting particles formed water stable suspensions and were characterised with XRD, FTIR and DLS.

XRD patterns confirm an iron oxide spinel, shown in Figure 85. This pattern agrees with previously prepared bare magnetite (grey), reports from the literature and the ICSD.[22–25,57] The broad peaks were measured and the average crystallite size and was calculated to be 13 nm, below the critical diameter for superparamagnetic behaviour.[26,27]

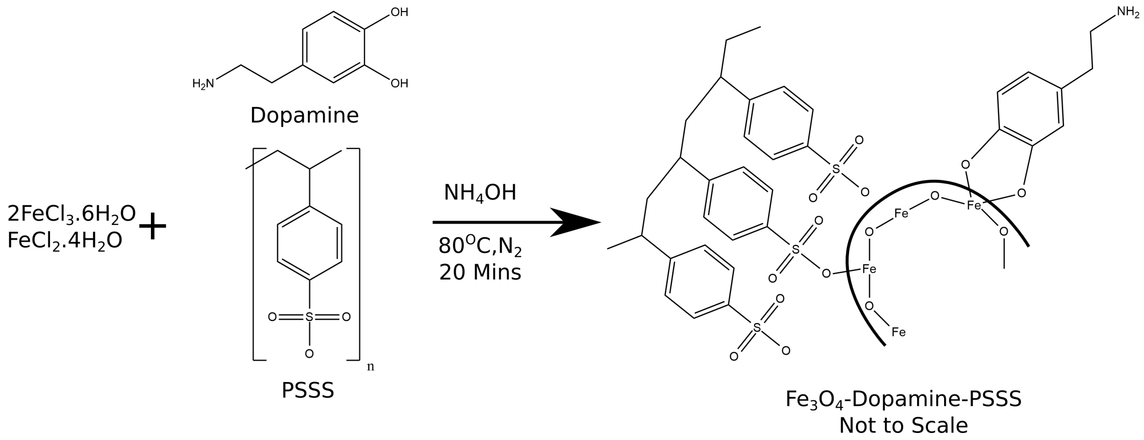

Figure 84: Schematic detailing the one-pot preparation of a magnetite nanoparticles functionalised with both dopamine and PSSS. The dopamine component will allow for further functionalisation while the PSSS stabiliser will enhance the composites water stability.

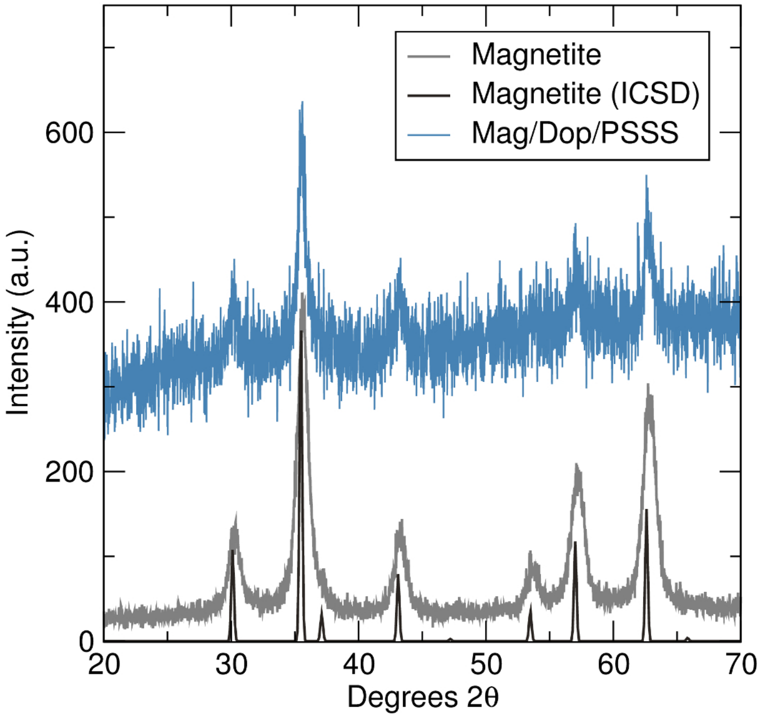

Figure 85: XRD patterns of magnetite nanoparticles stabilised with dopamine and PSSS (light blue). The Mag/Dop/PSSS sample was characterised under different conditions at the University of Glasgow (more information can be found in chapter 2).The stabilised nanocomposites shows no oxidation and matches bare magnetite prepared in the same way (grey) and the ICSD crystal pattern (black).[22]

FTIR spectroscopy confirms the presence of both stabilisers and the iron oxide core, shown in Figure 86. The Fe-O stretch is seen at 535 cm^{-1}. The PSSS coating gives S-O stretches at 825 cm^{-1}, 777 cm^{-1} and R-SO$_2$-OR stretches at 1119 cm^{-1} and 1163 cm^{-1}. The alkane backbone of the polyelectrolyte gives C-H stretches at 1023 and 1001 cm^{-1} with another stretch at 2942 cm^{-1} which has merged with the C-H aromatic dopamine peaks. The PSSS peaks match with previously prepared samples (Chapter 4) and with work done by previous groups.[58–60] Dopamine gives a characteristic broad band between 2500 and 3500 cm^{-1}, relating to both the hydroxide and aromatic groups. A broad C-C aromatic stretch can be seen at 1429 cm^{-1} for the aromatic rings of dopamine

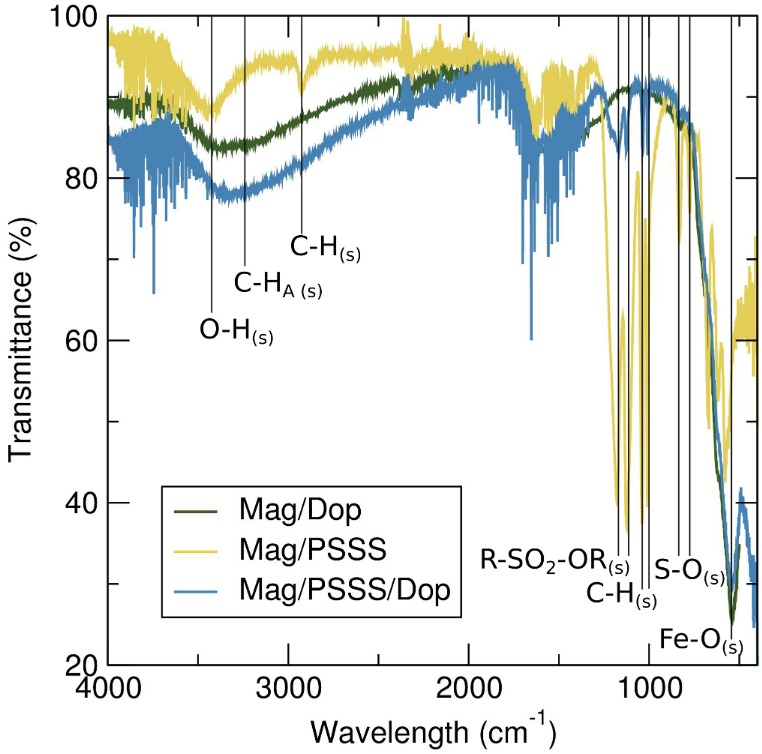

Figure 86: FTIR spectrum of magnetite stabilised with dopamine (olive), PSSS (banana) and PSSS/dopamine simultaneously (blue). $_A$ *indicates an aromatic stretch.*

The composite formed a stable suspension which was investigated using DLS. As with the previous samples stabilised with PSSS, the Z-average and DLS values of the composite become more consistent as the sample is washed (Table 21). Addition of the large polyelectrolyte chain to the composite is reflected in the DLS results, with the suspensions showing increased Z-average values. This polyelectrolyte addition is also reflected in the polydispersity of the sample, with a multimodal distribution of sizes seen in figure 87 for even the final dispersion. The final dispersion has a Z-average below 200 nm though, making it small enough for biological applications.[31–33] The addition of PSSS does improve water stability, with the particles remaining in suspension for over 6 weeks and this is further confirmed with a zeta potential of -58.1 mV.[34]

Table 21: DLS measurements of magnetite/dopamine/PSSS composites. Negative zeta potentials demonstrate the high water stability of the suspensions. High zeta potentials (Z. Po.) indicate good water stability.

Sample	**Washing 3**		**Washing 4**		**Washing 5**		**Z. Po.**
	Z-Average (d.nm)	**PDI**	**Z-Average** (d.nm)	**PDI**	**Z-Average** (d.nm)	**PDI**	(mV)
Mag/Dop/PSSS	172.5	0.280	186.6	0.190	194.5	0.205	-58.1
Mag/Dop	185.03	0.325	155	0.167	163.83	0.090	-50.8
Mag/PSSS	166	0.248	82.78	0.111	94.7	0.097	-41.5

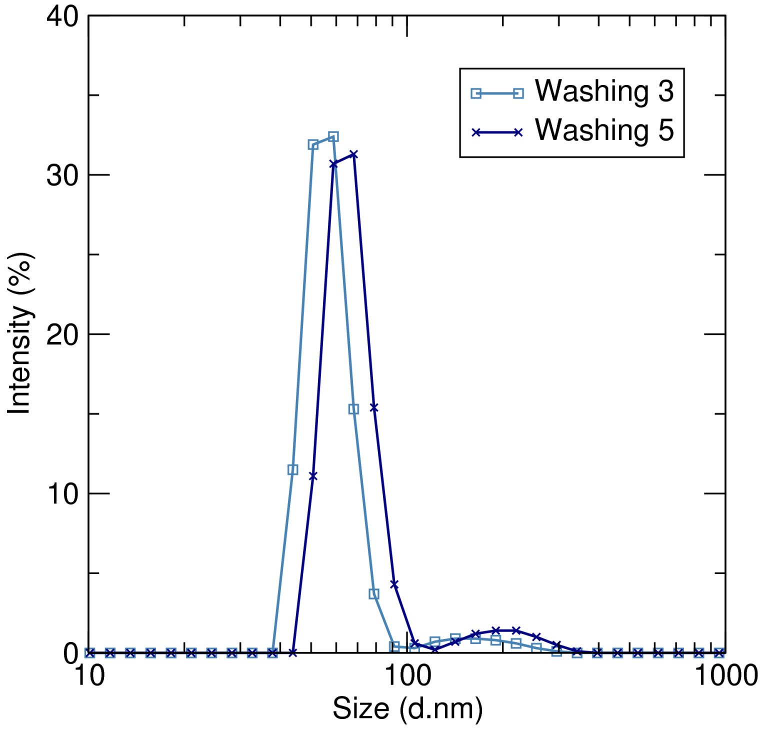

Figure 87: The size distribution of the third and fifth suspensions of the magnetite/dopamine/PSSS nanocomposite. As the sample is washed, little difference can be seen between the cluster distributions. The stabilisation of the composite with two organic stabilisers resulted in a multimodal size distribution even after several washes.

6.6 Developing a multifunctional nanocomposite with fluorescent and targeting capabilities

The final aim of this chapter is to combine several of the stabilisation and functionalisation reactions to produce a multifunctional nanocomposite. Co-precipitated magnetite nanoparticles were stabilised with PSSS and dopamine first to confer water stability and provide anchoring points for further functionalisation. Theses particles were then functionalised with acridine-9-carboxylic acid via carbodiimide coupling. Finally, activated folic acid was attached to the composite via carbodiimide coupling. The resulting composite formed was stable in water and was characterised using XRD, DLS, FTIR, UV-Vis and fluorescence spectroscopy. The reaction was then repeated with microwave irradiation, to ensure this technique can also be used to produce such a multifunctional platform. The resulting microwave assisted composite formed a water stable suspension and was characterised with XRD, FTIR , UV-Vis and fluorescence spectroscopy.

The XRD pattern confirms the iron oxide magnetite spinel for both the co-precipitated sample and the microwave sample (Figure 88). Scherrer broadening gives a primary particle size of 10.38 nm for the standard co-precipitation reaction and 10.22 nm for the microwave sample.

Figure 89 shows the FTIR spectra obtained for the functionalised samples prepared by the standard co-precipitation method. Amide bond stretches are seen at 1563 and 1650 cm^{-1} and Fe-O stretches at 541 cm^{-1}. Between 700 and 1350 cm^{-1} , stretches for the sulfonate group of the PSSS coating can be seen as very sharp well defined peaks. With the addition of A-9-CA and FA, the peaks broaden and shoulders form between the 800-1300 cm^{-1} region. Not only do the sulfonate signals (1119 cm^{-1} and 1163 cm^{-1}) arise in this region but also responses for the aliphatic amines of FA (1050 and 1090 cm^{-1}) and the C-N bond and the aromatic rings of acridine orange (1263 cm^{-1} and 1050-850 cm^{-1}) as well. Comparing the spectra, shows that addition of FA and A-9-CA causes multiple peaks in this area to form one single broad band with several smaller peaks for the individual stretches seen on the band. Previous FTIR results confirm the individual binding of A-9-CA and FA to iron oxide nanoparticles by carbodiimide coupling and this data illustrates that multiple groups can be attached to the same composite. The persistence of the A-9-CA and FA peaks after several washing shows that the moieties are securely bound

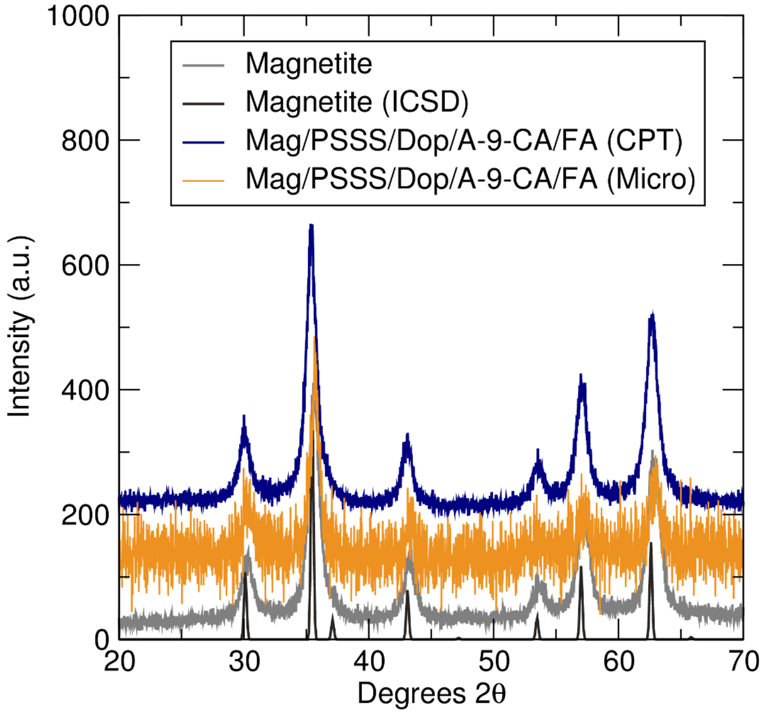

Figure 88: XRD patterns of uncoated magnetite nanoparticles (grey) and magnetite nanoparticles stabilised with PSSS, dopamine, A-9-CA and folic acid prepared with (orange) and without (navy) microwave irradiation. The microwave assisted co-precipitated Mag/PSSS/Dop/A-9-CA/FA sample was characterised under different conditions at the University of Glasgow (more information can be found in chapter 2). The patterns match previous reports for magnetite.[22]

Figure 90 compares the FTIR spectrum of sample prepared by microwave heating, with the sample prepared by conventional heating methods. The microwave assisted sample also shows corresponding peaks to the organic components, and is in good agreement with the standard co-precipitated sample (figure 90). The amide peaks are still present along with the sulphonate, aromatic amine peaks between 750-1200 cm^{-1}. The only major discrepancy is the weaker O-H stretch at 3331 cm^{-1} and the intense two peaks at 2372 and 2332 cm^{-1} which are N-H and C-N stretches relating to the FA and A-9-CA groups. These peaks further confirm the functionalisation reaction and demonstrate that this approach is applicable with microwave heating.

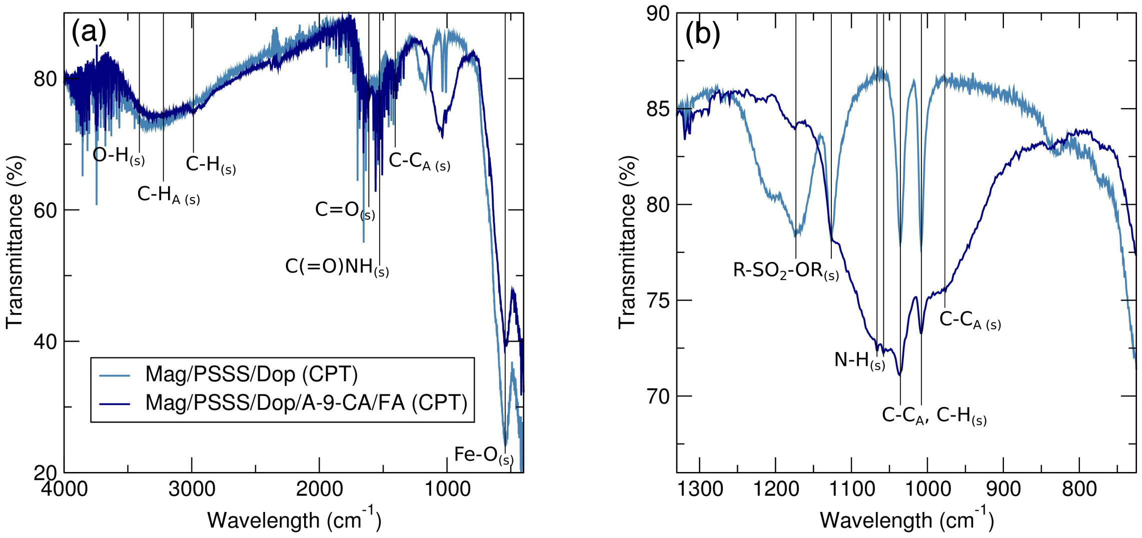

Figure 89: FTIR spectra (image (a)) of magnetite nanoparticles stabilised with PSSS/Dopamine (steel), and PSSS/Dopamine/A-9-CA/Folic acid (navy) prepared by the standard co-precipitation method. Image (b) expands the 700-1350 cm^{-1} region when the organic components are most likely to be seen. Broadening of the 1000 and 1500 cm^{-1} peaks indicates the addition of A-9-CA and folic acid into the sample.

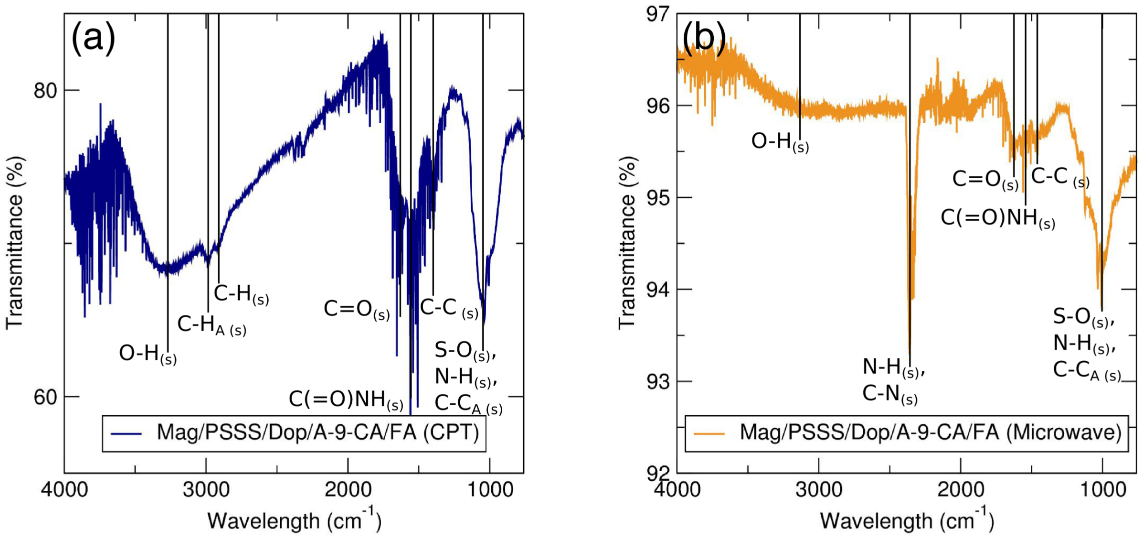

Figure 90: FTIR spectra of magnetite nanoparticles stabilised with PSSS/Dopamine/A-9-CA/Folic acid via co-precipitation using conventional heating methods (image (a) blue) or microwave irradiation (Image b, orange). Similarities can be seen between the samples, with the microwave sample having a weaker O-H stretch, but a very intense set of peaks at 2372 cm^{-1} relating to the N-H and C-N groups of A-9-CA and FA components.

The DLS measurements shows that even with the composite supporting additional functional groups there is little effect to the hydrodynamic radius and polydispersity of the sample. As with previous samples, water stable suspensions formed as the sample was washed and became pH neutral. The aggregate size and polydispersity decreased significantly as the sample was washed, as shown in Table 22. The low PDI indicates mono dispersity which is further confirmed by the size distribution being monomodal in figure 91. The zeta potential is still above the -30mV threshold indicating water stability, which is confirmed by the particles staying in suspension for over 6 weeks.[34]

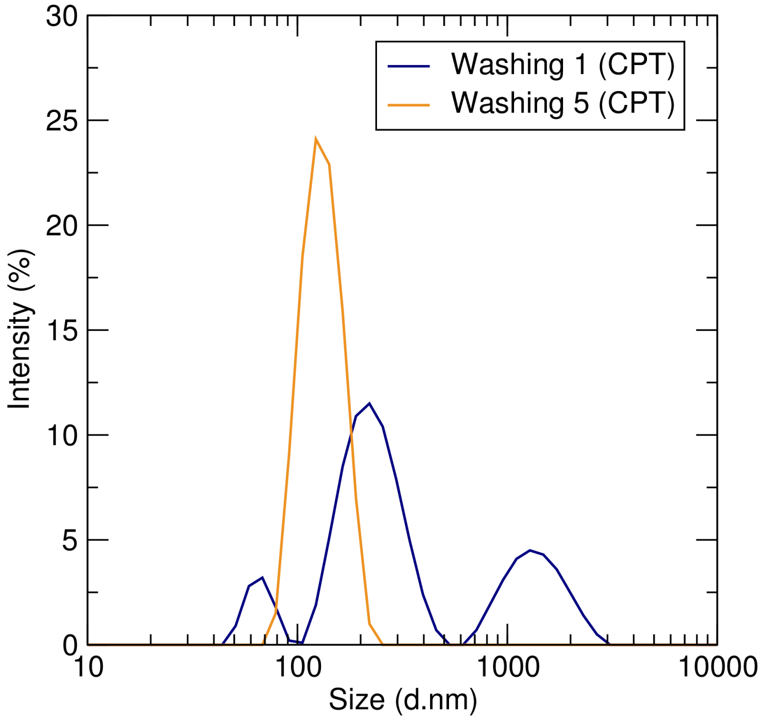

Figure 91: Size distribution of the first and final (fifth) washing of magnetite nanoparticles functionalised with PSSS, dopamine, acridine-9-carboxylic acid and folic acid in aqueous solution measured using dynamic light scattering. As with previous samples, as the material is washed the suspensions become more stable with a monomodal size distribution for the final fifth washing.

Table 22: DLS measurements of magnetite nanoparticles functionalised with PSSS, dopamine, acridine-9-carboxylic acid and folic acid. The high zeta potentials (Z. Po.) indicate good water stability despite the addition of multiple functional groups.

Sample	**Washing 3**		**Washing 4**		**Washing 5**		**Z. Po.**
	Z-Average (d.nm)	**PDI**	**Z-Average** (d.nm)	**PDI**	**Z-Average** (d.nm)	**PDI**	(mV)
Mag/.../AO/FA	123.9	0.137	134.5	0.107	129.7	0.112	-50.5

The first two washings for the standard co-precipitated Magnetite/PSSS/Dopamine/FA/A-9-CA sample show absorption peaks of 280 nm and 350 nm, as seen in Figure 92(a). The absorption at 350 nm is characteristic for the π-π* transition in A-9-CA. The other peak relates to the folic acid component of the composite with the absorbance at 280 nm relating to the π-π* transition of folic acid. Both signals are lost after the 3rd washing and a sloping effect can be seen due to the scattering of light by the nanoparticles. FTIR results suggest that both A-9-CA and FA persist in the washings even after this scattering effect occurs. Similar results are seen for the sample prepared using the microwave assisted method as seen in Figure 92(b).

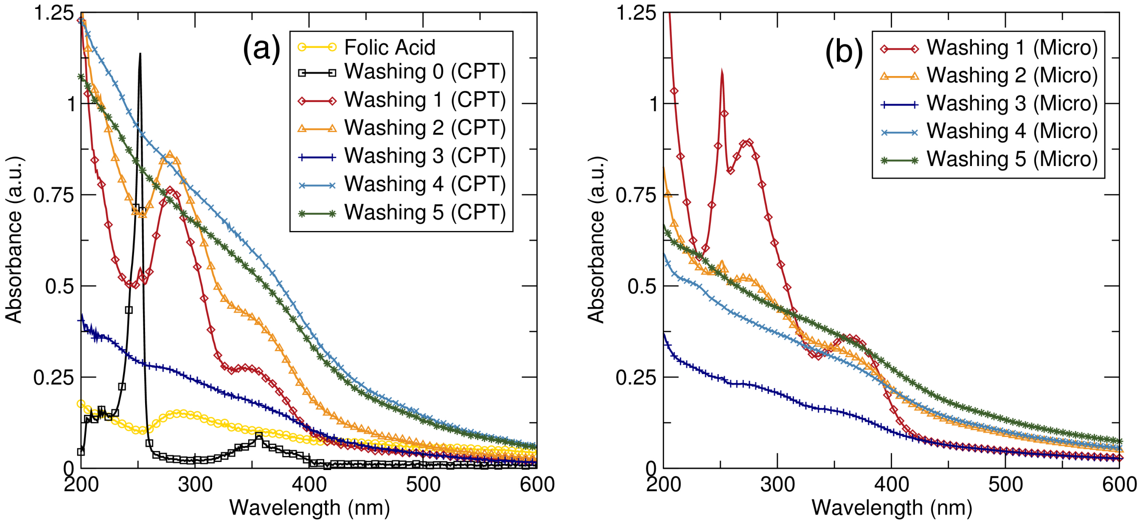

Figure 92: UV-Vis spectra of magnetite/dopamine/PSSS nanoparticles functionalised with acridine orange and folic acid prepared by (a) standard co-precipitation methods and (b) microwave assisted methods.

Fluorescence spectra collected of the final (fifth) washings of both the standard and microwave heated samples reveals the presence of A-9-CA and folic acid in Figure 93. The emission peak is characteristic for A-9-CA at 430 nm, with the corresponding excitation peak 350 nm. Interestingly there is also a second excitation peak in the spectrum at 280 nm, indicative of folic acid acid and confirmed by other literature reports.[9,51,52] The fluorescence signals for both folic acid and acridine-9-carboxylic acid still persist when the reaction method is combined with microwave irradiation. Additionally strong emission signals are seen for the samples after several washing indicating their suitability for confocal applications.

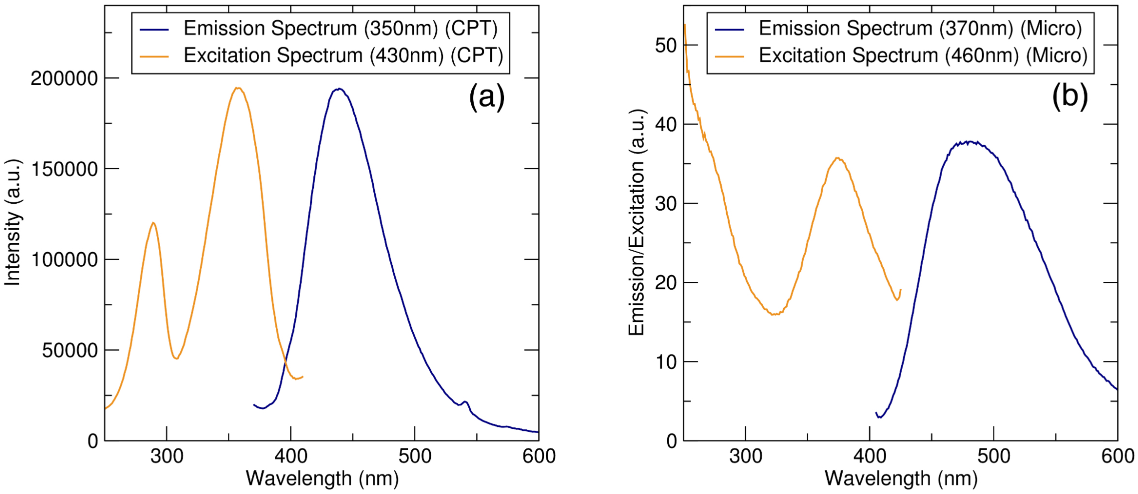

Figure 93: Emission (navy) and excitation (carrot) spectra of final (final) washing of magnetite nanoparticles functionalised with PSSS, Dopamine, A-9-CA and folic acid for the (a) co-precipitated sample (CPT) and (b) the microwave-assisted sample.

The formation of water stable composites indicate successful dopamine and PSSS binding. The enhanced water stability in comparison to magnetite/dopamine samples confirm the attachment of the PSSS stabiliser. The UV-Vis and fluorescence results confirm that the final nanocomposites contain A-9-CA and folic acid. The amide bond formation confirms that this is bound acridine/FA and not free molecules in suspension. The resulting composite is one of the first examples of acridine-9-carboxylic acid and folic acid being grafted onto magnetite/dopamine particles through direct carbodiimide coupling. A-9-CA has yet to be bound to magnetite/dopamine nanoparticles and folic acid is commonly bound using a linker. Not only does this method show that both materials can be bound directly to the dopamine surface layer, but it is quick and facile. This work also shows that the magnetic base can support multiple groups with little sacrifice to water stability or size.

The microwave results show that the groups are firmly bound to the composite. The result is a unique microwave assisted co-precipitated nanocomposite that supports several stabiliser and functional groups such as dopamine, PSSS, A-9-CA and folic acid. These groups have yet to be seen bound to nanoparticles prepared using a microwave assisted co-precipitation method and therefore offer an interesting avenue to further build upon. Microwave heating complements the functionalisation reactions by enhancing the properties of the magnetic base. This will improve the composites selectivity (combined with the folic acid group) and MRI efficacy. This could also enable other biomedical applications such as magnetic hyperthermia.

6.7 Discussion and Conclusions

This chapter demonstrates a facile and safe approach to preparing a range of multifunctional magnetic nanocomposites which encompass fluorescent and targeting moieties. The nanocomposite displays excellent water stability despite supporting additional groups, with the final dispersion showing Z-average, zeta potentials and PDI values well within the limits for biomedical applications.[31–34] Additionally the use of aqueous carbodiimide reactions and the use of NHS activation allows functional groups to be bound to the particles quickly after precipitation with minimal post processing. The flexibility of carbodiimide coupling provides a route to a highly flexible biomedical platform capable of supporting a variety of functional groups. Additionally this is the first example of acridine-9-carboxylic acid and folic acid being bound to highly crystalline microwave assisted co-precipitated magnetic nanoparticles.

Functionalisation was achieved by using the dopamine coating as a anchoring point, but the dopamine coating also offers other advantages in the stabilisation of iron oxide cores. As discussed earlier, the catechol group of dopamine binds with under-coordinated surface oxygen sites to form a strong bidentate bond.[2–4,61] These under-coordinated oxygen sites are surface defects which may reduce the magnetisation of the particles. Therefore, dopamine binding will affect the surface chemistry and therefore the resulting magnetisation of the particles. SQUID measurements are required to confirm this, but the literature suggests that stabilisation can partially realign magnetic spins within the defects and improve the overall particle crystallinity.[4,62] Work by other groups supports this theory, observing no change or even an increase in magnetisation values when a dopamine stabiliser is employed.[63,64] This is significant because microwave irradiation has already been shown to significantly improve crystallinity and this coupled with the dopamine stabiliser could maximise the magnetic potential of the iron oxide cores. PSSS has already been shown to have a crystallinity enhancing effect in Chapter 4 and the dopamine coating would not only complement this effect but also provide a surface for functionalisation.

When compared to nanocomposites prepared by other groups with targeting and luminescent functionalities, several advantages can be seen with this approach (i.e. quicker reaction times and removing the need for linking groups). For example Corato *et al.* bound folic acid and quantum dots to manganese oxide nanoparticles via a series of carbodiimide coupling reactions using an 2,2'-(ethylenedioxy)bis(ethylamine) linker.[65] The nanocomposite was effectively used in confocal microscopy which showed a preferential uptake of the folic acid stabilised materials but the modification of folic acid with a linker is a multistep process involving hazardous chemicals and long reaction times. Zhang *et al.* prepared iron oxide nanoparticles which bound folic acid and fluorescein to a aminopropyl-trimethoxysilane linker via an EDCI coupling reaction which was then attached to the nanocomposite silica surface via a condensation reaction.[54] The particles not only required post processing to coat the nanoparticles with PEG groups making them water stable but also involved multi-step, time-consuming reactions. The work outlined in this chapter has demonstrated the stabilisation of magnetic nanoparticles during co-precipitation and the binding of a functional group to the stabiliser without the need for a linker. Additionally, the microwave assisted co-precipiatation method can also provide water stable suspensions, which retain multifunctional behaviour. Further work is required to confirm the enhanced crystallinity of these samples.

There are still opportunities to optimise this nanocomposite. For example, one interesting avenue is to bind chemotherapy agents (i.e. duoxorubicin, paclitaxel) to the nanocomposite so that they can simultaneously detect and treat cancerous cells. There have been many examples of carbodiimide coupling grafting chemotherapy agents to nanoparticles, indicating that the method presented in this chapter is suitable for the attachment of chemotherapy agents.[13,66]

References

[1] Amstad, E.; Gillich, T.; Bilecka, I.; Textor, M.; Reimhult, E. *Nano Lett.* **2009**, *9*, 4042–4048.

[2] Gu, H.; Yang, Z.; Gao, J.; Chang., C. K.; Xu, B. *J. Am. Chem. Soc.* **2004**, *127*, 34–35.

[3] Xu, C.; Xu, K.; Gu, H.; Zheng, R.; Liu, H.; Zhang, X.; Guo, Z.; Xu, B. *J. Am. Chem. Soc.* **2004**, *126*, 9938–9939.

[4] Chen, L. X.; Liu, T.; Thurnauer, M. C.; Csencsits, R.; Rajh, T. *J. Am. Chem. Soc.* **2004**, *126*, 9938–9939.

[5] Na, H. B.; Palui, G.; Rosenberg, J. T.; Ji, X.; Grant, S. C.; Mattoussi, H. *ACS Nano.* **2012**, *6*, 389–399.

[6] Wu, J.; Zhang, L.; Wang, Y.; Long, Y.; Gao, H.; Zhang, X.; Zhao, N.; Cai, Y.; Xu, J. *Langmuir* **2011**, *27*, 13684–13691.

[7] Nakajima, N.; Ikada, Y. *Bioconjugate Chem.* **1995**, *6*, 123–130.

[8] Kaaki, K.; Hervé-Aubert, K.; Chipter, M.; Shkilnyy, A.; Soucé, M.; Benoit, R.; Paillard, A.; Dubois, P.; Saboungi, M.-L.; Chourpa, I. *Langmuir* **2012**, *28*, 1496–1505.

[9] Oh, J.-M.; Choi, S.-J.; Lee, G.-E.; Han, S.-H.; Choy, J.-H. *Adv. Funct. Mater.* **2009**, *19*, 1617–1624.

[10] Zhang, J.; Ranan, S.; Srivastava, R.; Misra, R. *Acta Biomater.* **2008**, *4*, 40–48.

[11] Kemikli, N.; Kavas, H.; Kazan, S.; Baykal, A.; Ozturk, R. *J. Alloy Compd.* **2010**, *502*, 439–444.

[12] Xie, J.; Xu, C.; Kohler, N.; Hou, Y.; Sun, S. *Adv. Mater* **2007**, *19*, 3163–3166.

[13] Hua, M.-Y.; Yang, H.-W.; Chuang, C.-K.; Tsai, R.-Y.; Chen, W.-J.; Chuang, K.-L.; Chang, Y.-H.; Chuang, H.-C.; Pang, S.-T. *Biomaterials.* **2010**, *31*, 7355–7363.

[14] Sun, C.; Du, K.; Fang, C.; Bhattarai, N.; Veiseh, O.; Kievit, F.; Stephen, Z.; Lee, D.; Ellenbogen, R. G.; Ratner, B.; Zhang, M. *ACS Nano.* **2010**, *4*, 2402–2410.

[15] Harris, J. J.; DeRose, P. M.; Bruening, M. L. *J. Am. Chem. Soc.* **1999**, *121*, 1978–1979.

[16] Basti, H.; Tahar, L. B.; Smiri, L. S.; Herbst, F.; Vaulay, M.-J.; Chau, F.; Ammar, S.; Benderbous, S. *J. Colloid. Interf. Sci.* **2010**, *341*, 248–254.

[17] Shultz, M. D.; Reveles, J. U.; Khanna, S. N.; Carpenter, E. E. *J. Am. Chem. Soc.* **2007**, *129*, 2482–2487.

[18] Lin, C.-L.; Lee, C.-F.; Chiu, W.-Y. *J. Colloid. Interf. Sci.* **2005**, *291*, 411–420.

[19] Xu, C.; Xu, K.; Gu, H.; Zheng, R.; Liu, H.; Zhang, X.; Guo, Z.; Xu, B. *J. Am. Chem. Soc.* **2004**, *126*, 9938–9939.

[20] Álvarez-Paino, M.; Marcelo, G.; Munñoz-Bonilla, A.; Fernández-García, M. *Macromolecules* **2013**, *46*, 2951–2962.

[21] Faure, E.; Falentin-Daudré, C.; Jérôme, C.; Lyskawa, J.; Fournier, D.; Woisel, P.; Detrembleur, C. *Prog. Polym. Sci.* **2013**, *38*, 236–270.

[22] Fleet, M. E. *Acta. Cryst.* **1981**, *B37*, 917–920.

[23] Mikhaylova, M.; Kim, D. K.; Bobrysheva, N.; Osmolowsky, M.; Semenov, V.; Tsakalakos, T.; Muhammed, M. *Langmuir* **2004**, *20*, 2472–2477.

[24] Mahmoudi, M.; Simchi, A.; Milani, A. S.; Stroeve, P. *J. Colloid. Interf. Sci.* **2009**, *336*, 510–518.

[25] Cheng, F.-Y.; Su, C.-H.; Yang, Y.-S.; Yeh, C.-S.; Tsai, C.-Y.; Wu, C.-L.; Wu, M.-T.; Shieh, D.-B. *Biomaterials* **2005**, *26*, 729–738.

[26] Morais, P.; Garg, V.; Oliveira, A.; Silva, L.; Azevedo, R.; Silva, A.; Lima, E. *J. Magn. Magn. Mater.* **2001**, *225*, 37–40.

[27] Goya, G. F.; Berquó, T. S.; Fonseca, F. C.; Morales, M. P. *J. Appl. Phys.* **2003**, *94*, 3520–3528.

[28] Zaitsev, V. S.; Filimonov, D. S.; Presnyakov, I. A.; Gambino, R. J.; Chu, B. *J. Colloid Inter. Sci.* **1999**, *212*, 49–57.

[29] Hu, L.; Percheron, A.; Chaumont, D.; Brachais, C.-H. *J. Sol-Gel. Sci. Technol.* **2011**, *60*, 198–205.

[30] Shultz, M. D.; Reveles, J. U.; Khanna, S. N.; Carpenter, E. E. *J. Am. Chem. Soc.* **2007**, *129*, 2482–2487.

[31] Laurent, S.; Forge, D.; Port, M.; Roch, A.; Robic, C.; Elst, L. V.; Muller, R. N. *Chem. Rev.* **2008**, *108*, 2064–2110.

[32] Neuberger, T.; Schöpf, B.; Hofmann, H.; Hofmann, M.; Rechenberg, B. V. *J Magn. Magn. Mater.* **2005**, *293*, 483–496.

[33] Arruebo, M.; Fernández-Pacheco, R.; Ibarra, M. R.; Santamaría, J. *NanoToday* **2007**, *2*, 22–32.

[34] Cunningham, D.; Littleford, R. E.; Smith, W. E.; Lundahl, P. J.; Khan, I.; McComb, D. W.; Graham, D.; Laforest, N. *Faraday Discuss.* **2006**, *132*, 135–145.

[35] Qu, H.; Caruntu, D.; Liu, H.; OConnor, C. J. *Langmuir* **2011**, *27*, 2271–2278.

[36] Das, M.; Mishra, D.; Dhak, P.; Gupta, S.; Maiti, T. K.; Basak, A.; Pramanik, P. *Small* **2009**, *5*, 2883–2893.

[37] Zimmermann, F.; Hossenfelder, B.; Panitz, J.-C.; Wokaun, A. *J. Phys. Chem.* **1994**, *98*, 12796–12804.

[38] Lagutschenkov, A.; Dopfer, O. *J. Mol. Spectrosc.* **2011**, *30*, 2843–2848.

[39] Ladner, S. J.; Becker, R. S. *J. Phys. Chem.-US* **1963**, *67*, 2481–2486.

[40] Dey, J.; Haynes III, J. L.; Warner, I. M. *J. Phys. Chem. A* **1997**, *101*, 2271–2278.

[41] Hu, F.; Li, Z.; Tu, C.; Gao, M. *J. Colloid. Interf. Sci.* **2007**, *311*, 469–474.

[42] White, E. H.; Roswell, D. F.; Dupont, A. C.; Wilson, A. A. *J. Am. Chem. Soc.* **1987**, *109*, 5189–5196.

[43] Yu, Q.; Wei, Z.-Z.; Li, J.-R.; Hu, T.-L. *J. Mol. Struct.* **2009**, *931*, 68–75.

[44] Chen, D.; Jiang, M.; Li, N.; Gu, H.; Xu, Q.; Ge, J.; Xia, X.; Lu, J. *J. Mater. Chem.* **2010**, *20*, 6422–6429.

[45] Mohaptra, S.; Mallick, S. K.; Maiti, T. K.; Ghosh, S. K.; Pramanik, P. *Nanotechnology* **2007**, *18*, 385102.

[46] Zhang, Z.; Lee, S. H.; Feng, S.-S. *Biomaterials* **2007**, *8*, 1889–1899.

[47] Dutta, R. K.; Sharma, P. K.; Pandey, A. C. *J. Nanopart. Res.* **2010**, *12*, 11211–1219.

[48] Zhang, C.; Luo, N.; Hirt, D. E. *Langmuir* **2006**, *22*, 6851–6857.

[49] Chang, Y.; Liu, N.; Chen, L.; Meng, X.; Liu, Y.; Li, Y.; Wang, J. *J. Mater. Chem.* **2012**, *22*, 9594–9601.

[50] Kohler, N.; Fryxell, G. E.; Zhang, M. *J. Am. Chem. Soc.* **2004**, *126*, 7206–7211.

[51] Maeng, J. H.; Lee, D.-H.; Jung, K. H.; Bae, Y.-H.; Park, I.-S.; Jeong, S.; Jeon, Y.-S.; Shim, C.-K.; Kim, W.; Kim, J.; Lee, J.; Lee, Y.-M.; Kim, J.-H.; Kim, W.-H.; Hong, S.-S. *Biomaterials* **2010**, *31*, 4995–5006.

[52] Wu, H.; Liu, G.; Zhang, S.; Shi, J.; Zhang, L.; Chen, Y.; Chen, F.; Chen, H. *J. Mater. Chem.* **2011**, *21*, 3037–3045.

[53] Lu, T.; Sun, J.; Chen, X.; Zhang, P.; Jing, X. *Macromol. Biosci.* **2009**, *9*, 1059–1068.

[54] Zhang, Y.; Kohler, N.; Zhang, M. *Biomaterials* **2002**, *23*, 1553–1561.

[55] Wang, Z.; Zhu, J.; Chen, Y.; Geng, K.; Qian, N.; Cheng, L.; Lu, Z.; Pan, Y.; Guo, L.; Li, Y.; Gu, H. *RSC Adv.* **2014**, *4*, 7483–7490.

[56] Majd, M. H.; Asgari, D.; Barar, J.; Valizadeh, H.; Kafil, V.; Coukos, G.; Omidi, Y. *J. Drug. Target.* **2013**, *21*, 328–340.

[57] Kim, D. K.; Zhang, Y.; Voit, W.; Rao, K. V.; Muhammed, M. *J Magn. Magn. Mater.* **2001**, *225*, 30–36.

[58] Corr, S. A.; Gun'ko, Y. K.; Tekoriute, R.; Meledandri, C. J.; Brougham, D. F. *J. Phys. Chem. C* **2008**, *112*, 13324–13327.

[59] Isojima, T.; Lattuada, M.; Sande, J. B. V.; Hatton, T. A. *ACS Nano* **2008**, *2*, 1799–1806.

[60] Corr, S. A.; Byrne, S. J.; Tekoriute, R.; Meledandri, C. J.; Brougham, D. F.; Lynch, M.; Kerskens, C.; O'Dwyer, L.; Gun'ko, Y. K. *J. Am. Chem. Soc.* **2008**, *130*, 4214–4215.

[61] Fouineau, J.; Brymora, K.; Ourry, L.; Mammeri, F.; Yaacoub, N.; Calvayrac, F.; Ammar-Merah, S.; Greneche, J.-M. *J. Phys. Chem. C* **2013**, *117*, 14295–14302.

[62] Yuen, A. K. L.; Hutton, G. A.; Masters, A. F.; Maschmeyer, T. *Dalton Trans.* **2012**, *41*, 2545–2559.

[63] Nagesha, D. K.; Plouffe, B. D.; Phan, M.; Lewis, L. H.; Sridhar, S.; Murthy, S. K. *J. Appl. Phys.* **2009**, *105*, 07B317.

[64] Mazur, M.; Barras, A.; Kuncser, V.; Galatanu, A.; Zaitzev, V.; Turcheniuk, K. V.; Woisel, P.; Lyskawa, J.; Laure, W.; Siriwardena, A.; Boukherroub, R.; Szunerits, S. *Nanoscale* **2013**, *5*, 2692–2702.

[65] Corato, R. D.; Bigall, N. C.; Ragusa, A.; Dorfs, D.; Genovese, A.; Marotta, R.; Manna, L.; Pellegrino, T. *ACS Nano* **2011**, *5*, 1109–1121.

[66] Lee, G. Y.; Qian, W. P.; Wang, L.; Wang, Y. A.; Staley, C. A.; Satpathy, M.; Nie, S.; Mao, H.; Yang, L. *ACS Nano* **2013**, *26*, 2078–2089.

Chapter 7: Conclusions and future work

This thesis presents microwave-assisted routes for preparing magnetic nanoparticles and nanocomposite materials. The methods presented are fast, efficient and lead to the production of materials with properties suitable for biomedical applications, including as contrast agents for MR imaging, for cell imaging use and as drug-delivery agents.

A new microwave-assisted co-precipitation technique has been developed which affords highly crystalline magnetic nanoparticles and can be applied to produce a range of ferrite-based nanomaterials. Traditionally, highly crystalline magnetic nanoparticles may be obtained through high temperature decomposition reactions. While effective and controllable, these reactions use organic surfactants and stabilisers during synthesis, which needs to be removed via post processing ligand exchange reactions before the particles can be re-dispersed into aqueous solutions. The microwave heating method detailed here produces particles with M_s values similar to thermal decomposition routes (65.2 emu/g Vs. 60-85 emu/g, respectively) but with the added advantage of reduced reaction times and the possibility of the simultaneous stabilisation of the particles.

Following on from this, a polyelectrolyte surfactant may also be introduced to the synthesis to enhance water stability, as shown in Chapter 4. An advantage of this method is that the synthesis takes place in water, without the need for additional steps to transfer the nanoparticles from organic to aqueous solvents. Iron oxide nanoparticles can be stabilised with hydrophilic polyelectrolytes during the precipitation reaction, eliminating the need for a separate post processing and stabilisation step. This co-precipitation approach has quick synthesis times, which when combined with polyelectrolytes and microwave irradiation allows for the preparation of highly crystalline water stable nanoparticles in under an hour. Interestingly, the magnetic properties also depend on the nature of the surfactant employed, with the polyelectrolyte, PSSS displaying high crystallinity and high M_s values, while the phosphate stabiliser, SPP leads to an irregular nanoparticle shape, which manifests in lower magnetisation saturation values. This water stability coupled with the high crystallinity from microwave heating made the PSSS-Fe_3O_4 nanocomposite an excellent candidate as an MR imaging contrast agent, exceeding other commercial iron oxide based agents. Fluorescent groups, such as the organic dye Rhodamine B, may also be used during synthesis to bind to the polyelectrolyte via electrostatic interactions, allowing for confocal imaging use.

The increase in crystallinity of the iron oxide nanoparticles through the use of microwave-assisted synthesis led to the exploration of a range of polyelectrolyte stabilisers and chain lengths, as discussed in Chapter 5. Here, it has been shown that lower molecular weight polyelectrolytes reduce clustering, maximise water stability and can form linear assemblies in an external magnetic field. Stabilising with highly charged polyelectrolytes also leads to the formation of these linear assemblies. Either cationic or anionic polyelectrolytes can be used to stabilise iron oxide nanoparticles, with strong cationic polyelectrolytes displaying excellent water stability, as shown by DLS measurements. The formation of linear assemblies may also affect the MR imaging properties, as the linear assemblies have a greater surface area to interact with neighbouring protons. Linear assemblies have been explored before in the literature[1] but the advantage of using polyelectrolyte chains is that these assemblies extend to over a micron in length, further increasing the surface area.

Finally, the functionalisation of these iron oxide nanoparticles, in combination with polyelectrolyte stabilisers, has been explored through a series of carbodiimide coupling reactions and dopamine-based linkers. The dopamine anchor strongly coordinates with the iron oxide nanoparticle surface minimising the risk of early desorption of the attached species. A range of molecules including PAA, acridine-9-carboxylic acid and folic acid were bound to the particle surface, which demonstrates the versatility of this approach. Finally, a single nanocomposite comprised of PSSS-stabilised iron oxide nanoparticles, prepared using a microwave-assisted approach, was functionalised via a dopamine surface layer with acridine-9-carboxylic acid to promote fluorescence, and folic acid to enhance targeting. The final nanocomposite was extremely water stable and shown by DLS to be small enough for biological applications. It is reasonable to expect this nanocomposite to show promise as a targeting agent as folic acid is found to specifically target cancerous tissues, while at the same time the MR imaging potential is retained through PSSS surface coverage. In this way, a multifunctional single platform has been prepared using microwave-assisted synthetic approaches, with potential uses in MR imaging, confocal microscopy and drug delivery.

The microwave assisted synthetic route shown here is an excellent method to obtaining highly crystalline ferrite nanoparticles. Further examination of MFe_2O_4 (where M = Mn, Co, Zn) could optimise the magnetic properties of the core nanoparticles and hence the contrast efficacy. For example, manganese ferrite has been reported to display greater relaxivity values when compared with standard iron oxide nanoparticles.[2,3] The route to these ferrite nanoparticles could also be further explored, for example the development of the one-pot co-precipitation reaction using urea as a base which was only briefly tested in Chapter 3. Development of this approach could further reduce reaction times. Performing the reaction under reflux could avoid the reaction of the iron oxide seed particles with carbon dioxide that leads to oxidation and the formation of hematite.[4] By modifying the microwave system, the set up could be altered to allow for reflux during the microwave heating step.

The examination of different stabilisers in combination with microwave assisted synthesis could also provide new nanocomposites with enhanced theranostic properties. For example, recently the highest relaxivity values for iron oxide nanoparticles has been reported by Maity *et al.* who have used terephthalic acid to stabilise iron oxides.[5] Terephthalic acid stabilisers improve relaxivity values by providing π-conjugation paths to allow spin transfer from electrons in the magnetic core to the surrounding water molecules. The stabiliser distributes the charge across a larger group of neighbouring water protons (compared to more traditional stabilisers) increasing the contrast effect. Using this stabiliser on microwave assisted co-precipitated nanoparticles can further increase relaxivity values, as microwave heating will improve the magnetism of the magnetic core, while the stabiliser will better distribute this enhanced charge.

One area of potential future work is to further functionalise the iron oxide nanoparticles with chemotherapy agents via carbodiimide coupling. There are a number of candidate chemotherapy agents used in the treatment of tumours that could be explored, including Paclitaxel,[6] Vincristine[7] and Doxorubicin.[8] Another possibility for cancer treatment is the attachment of photosensitive molecules to the nanoparticle surface for photodynamic therapy. Photodynamic therapy works by exciting photosensitive groups leading to the formation of free radicals.[9] The free radicals are unstable and destroy nearby cells, which when dispersed in cancerous cells can be an effective treatment. Unwanted distribution of the chemotherapy drugs and photosensitive groups in healthy cells is a concern but the targeting functionality of the nanocomposite would ensure that only cancerous cells would be attacked.

To conclude, the synthetic methods presented in this thesis detail a highly flexible route to extremely crystalline iron oxide nanoparticles that display excellent water stability and are capable of being further functionalised with luminescent and targeting groups. This work highlights the importance of microwave irradiation and polyelectrolyte stabilisers in the construction of magnetic nanocomposites. Use of carbodiimide coupling and dopamine coatings allows a wide range of materials to be bound to the composite by a strong amide bond further adding to the potential applications of the nanocomposite. This work not only gives a simple and reliable method for the preparation of multifunctional nanocomposites for use in biomedical applications, but also presents an easily modifiable foundation that can be further enhanced for cancer diagnosis and treatment.

References

[1] Park, J.-H.; von Maltzahn, G.; Zhang, L.; Schwartz, M. P.; Ruosahti, E.; Bhatia, S. N.; Sailor, M. J. *Adv. Mater.* **2008**, *20*, 1630–1635.

[2] Lu, J.; Ma, S.; Sun, J.; Xia, C.; Liu, C.; Wang, Z.; Zhao, X.; Gao, F.; Gong, Q.; Song, B.; Shuai, X.; Ai, H.; Gu, Z. *Biomaterials* **2009**, *30*, 2919–2928.

[3] Lee, J.-H.; Huh, Y.-M.; wook Jun Jung-wook Seo, Y.; tak Jang, J.; Song, H.-T.; Kim, S.; Cho, E.-J.; Yoon, H.-G.; Suh, J.-S.; Cheon, J. *Nat. Med.* **2007**, *13*, 95–99.

[4] Lian, S.; Wang, E.; Kang, Z.; Bai, Y.; Gao, L.; Jiang, M.; Hu, C.; Xu, L. *Solid State Commun.* **2004**, *129*, 485–490.

[5] Maity, D.; Zoppellaro, G.; Sedenkova, V.; Tucek, J.; Safarova, K.; Polakova, K.; Tomankova, K.; Jiwoky, C.; Stollberger, R.; Machala, L.; Zboril, R. *Chem. Commun.* **2012**, *48*, 11398–11400.

[6] Hua, M.-Y.; Yang, H.-W.; Chuang, C.-K.; Tsai, R.-Y.; Chen, W.-J.; Chuang, K.-L.; Chang, Y.-H.; Chuang, H.-C.; Pang, S.-T. *Biomaterials.* **2010**, *31*, 7355–7363.

[7] Webb, M. S.; Saxon, D.; Wong, F. M. P.; Lim, H. J.; Wang, Z.; Bally, M. B.; Choi, L. S. L.; Cullis, P. R.; Mayer, L. D. *Biochim. Biophys. Acta.* **1998**, *1372*, 272–282.

[8] Brulé, S.; Levy, M.; Wilhelm, C.; Letourneur, D.; Gazeau, F.; Méanger, C.; Visage, C. L. *Adv. Mater.* **2011**, *23*, 787–790.

[9] Kloek, J.; Akkermans, W.; van Henegouwen, G. M. J. B. *Photochem. Photobiol.* **1998**, *67*, 150–154.